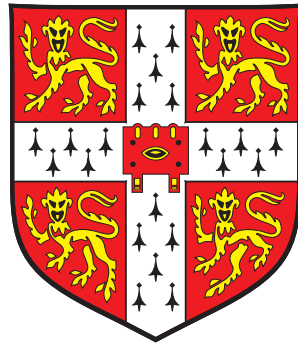


New techniques in NMR spectroscopy

Andrew James Pell



Selwyn College and Department of Chemistry
University of Cambridge

This dissertation is submitted for the degree of Doctor of Philosophy

Declaration

THIS DISSERTATION IS THE RESULT OF MY OWN WORK and includes nothing which is the outcome of work done in collaboration except where specifically indicated in the text. The results outlined have not previously been submitted for a degree, diploma, or other qualification at any university. This dissertation does not exceed the word limit set by the degree committee.

Andrew James Pell
Cambridge, April 2009

Summary

THE WORK DESCRIBED IN THIS THESIS is concerned with the development of new techniques in high-resolution nuclear magnetic resonance (NMR) spectroscopy. These methods were developed with the aim of aiding the structural studies of small-to medium-sized molecules in solution. The basic background theory that is needed to describe the relevant experiments is set out in Chapters 1 and 2.

Conventional proton spectra contain information about the chemical shifts of the spins and the couplings between them. One particular problem that is often encountered is that neighbouring multiplets overlap with each other, thus obscuring this wealth of information. One solution is to obtain a complete separation of the shifts and couplings using an existing experiment known as *J*-spectroscopy, which is described in Chapter 3. An important feature of this experiment is that it provides a broadband proton-decoupled proton spectrum, which contains a single line at each shift. However, the poor lineshape in the spectrum can only be alleviated at the cost of reduced sensitivity and intensity distortions, or complex data processing.

Chapters 4 and 5 describe two new methods for obtaining *J*-spectra that have the absorption-mode lineshape and reliable intensities, which is a much sought-after goal in NMR. The first method is based on an entirely different experiment called anti *z*-COSY. Chapter 4 describes how this experiment is utilized to obtain a decoupled spectrum along with its possible applications, for example to diffusion measurements. The second pulse sequence is proposed in Chapter 5. It is based on a sequence that was proposed by Zanger and Sterk that enables the homonuclear decoupling of different spins in different parts of the sample.

Inverse heteronuclear correlation spectra are often handicapped by low resolution in the indirect dimension. This is because restrictions on the available experiment time usually lead to the data being truncated in this dimension. Chapter 6 investigates the use and limitations of sparse sampling followed by the application of the Maximum Entropy Method in obtaining high resolution in a comparatively short time.

Acknowledgements

FIRSTLY, I WOULD LIKE TO THANK my parents and my brother Matthew for their continual love and encouragement. I would never have got this far without you.

I gratefully acknowledge the past members of the Keeler group for providing very useful help and discussion. Dr Richard Edden deserves a huge thank you for his patient supervision when I first joined the group, in particular for teaching me how to use the spectrometer. The work described in Chapter 4 was done in collaboration with him. My Part III students Nick England, Ben Simmons, Michael Scott, Michael Tayler, and Alex Hermes were welcome additions to the group, particularly for keeping me on my toes with their many incisive questions. I would like to thank Dr Melinda Duer for giving me a desk at which to work in Room 251. Thanks go to my fellow inhabitants – Dr Robin Orr, Dr Robin Stein, Erica Wise, Matthew Ironside, and Dr David Reid – for our many useful discussions and comradeship.

Many of the preliminary experiments were performed at the Laboratory of Molecular Biology. Although none of the spectra made it into this thesis, the time spent there was invaluable. I would therefore like to thank Dr David Neuhaus for a generous allocation of spectrometer time, and Ji-Chun Yang for his technical expertise. I am also grateful to Dr Ulrich Günther at the University of Birmingham for supplying me with the cancer cell extract.

The work described in Chapter 6 was performed using the Azara suite of programs that are available from the Department of Biochemistry. I am indebted to both Dr Daniel Nietlispach and Wayne Boucher for helping me get to grips with the software and for tirelessly answering my many questions about Maximum Entropy.

This research was funded by a Domestic Research Studentship from the University of Cambridge, and a grant from AstraZeneca. My industrial supervisor Dr Andrew Phillips has been a true friend and ally. Thank you.

I have been blessed with many great friends in Selwyn's MCR, without whom I would probably have gone insane. In particular Helen Griffiths, George Roberts, Philip Blakely, Penfold, Andrew Cassidy, Catherine Williams, Alastair Appleton,

Gareth Conduit, James Lawrence, and Isobel Johnston deserve a special mention for putting up with my mood swings and giving me a valuable sense of perspective. I would also like to thank Gareth for his advice on programming.

Finally, I would like to take this opportunity to say a big thank you to my supervisor Dr James Keeler for his supervision, encouragement, and timely criticism over the past seven years.

To Mum, Dad, and Matt

Contents

1	The basics of nuclear magnetic resonance	1
1.1	Spin angular momentum and magnetic moment	1
1.2	The interaction of a single spin with a magnetic field	2
1.2.1	A static magnetic field	2
1.2.2	Time evolution	2
1.2.3	Measurements on a single spin	3
1.3	An ensemble of spins	3
1.3.1	The density operator	4
1.3.2	Time evolution of the density operator	5
1.3.3	The rotating frame of reference	5
1.3.4	The matrix representation of the density operator	7
1.3.5	Time evolution of the density matrix	7
1.3.6	The density operator at thermal equilibrium	9
1.4	The Hamiltonian for a one-spin system	10
1.4.1	The chemical shift	10
1.4.2	Radiofrequency pulses	11
1.5	The basis operators for a one-spin system	14
1.5.1	Cartesian basis operators	14
1.5.2	Single-element basis operators	16
1.6	Relaxation	19
1.7	The Hamiltonian for a two-spin system	20
1.7.1	The free-precession Hamiltonian	20
1.7.2	The weak coupling approximation	21
1.8	Product operators	22
1.8.1	Cartesian operators	23

1.8.2	Single-element basis operators	25
1.8.3	The spin echo	26
1.9	Strong coupling	27
1.9.1	Single-element basis operators	29
1.10	The pulse–acquire experiment	30
1.10.1	The spectrum of a one-spin system	30
1.10.2	The Fourier transform	31
1.10.3	Digital sampling	34
1.10.4	The spectrum of a two-spin system in the weak-coupling approximation	35
1.10.5	The spectrum of a strongly-coupled two-spin system	36
1.11	Weighting functions and sensitivity	38
1.11.1	The convolution theorem	38
1.11.2	Truncation	38
1.11.3	Sensitivity	40
1.12	Two-dimensional NMR	41
1.12.1	Two-dimensional lineshapes	42
1.12.2	Digital sampling in t_1	46
1.12.3	Sensitivity	46
1.12.4	Projections	47
2	Methods of signal selection	49
2.1	Coherence transfer pathways	49
2.2	Phase cycling	50
2.2.1	The phase cycle of a single set of pulses	50
2.2.2	Nested phase cycles	52
2.2.3	EXORCYCLE	53
2.3	Pulsed field gradients	54
2.3.1	Free precession in the presence of a gradient	54
2.3.2	Shaped PFGs	55
2.3.3	Coherence transfer pathway selection	56
2.4	Selective pulses	57
2.4.1	Rectangular selective pulses	57
2.4.2	Shaped pulses	60

2.5	Broadband inversion	61
2.5.1	Adiabatic inversion pulses	62
2.5.2	Adiabatic refocusing	64
2.5.3	Partially adiabatic inversion pulses	66
2.6	Nuclear magnetic resonance imaging	67
2.6.1	Slice-selective pulses	69
2.7	The z -filter	70
2.7.1	The suppression of zero-quantum coherence	72
3	Two-dimensional J-spectroscopy	77
3.1	J -spectroscopy of a weakly-coupled two-spin system	77
3.1.1	Analysis of the pulse sequence	78
3.1.2	Separation of offset and J -coupling	80
3.2	Lineshapes and sensitivity	81
3.2.1	Pseudo-echo weighting	82
3.3	J -spectroscopy of a strongly-coupled two-spin system	86
3.3.1	Analysis of the pulse sequence	86
3.4	Experimental example	88
4	Broadband proton-decoupled proton spectra using z-COSY	91
4.1	Analysis of the pulse sequence	92
4.1.1	The zero-quantum artefacts	95
4.1.2	The diagonal-peak multiplet	96
4.1.3	The cross-peak multiplets	99
4.1.4	Strongly-coupled spin systems	99
4.2	Separation of chemical shifts and couplings	101
4.2.1	Rotating the spectrum	102
4.2.2	Shearing the spectrum	102
4.2.3	Lineshapes in the decoupled spectrum	105
4.2.4	Sensitivity	106
4.3	Anti z -COSY spectra with reduced ω_1 spectral width	107
4.3.1	The diagonal peaks	107
4.3.2	The cross peaks	109
4.3.3	Removal of the cross peaks by symmetrization	111

4.4	Direct suppression of the cross peaks	113
4.4.1	Analysis of the pulse sequences	115
4.5	Experimental verification	119
4.5.1	Anti z -COSY with full spectral width	120
4.5.2	Anti z -COSY with reduced spectral width	123
4.5.3	Anti z -COSY spectra with direct cross-peak suppression	123
4.6	Application to diffusion-ordered spectroscopy	128
4.6.1	The stimulated-echo experiment	128
4.6.2	Convection	130
4.6.3	Eddy currents	132
4.6.4	Homonuclear decoupling	132
4.6.5	Experimental examples	134
4.6.6	Discussion	135
4.7	Application to longitudinal relaxation measurements	140
4.7.1	The inversion–recovery experiment	140
4.7.2	Experimental examples	141
4.8	Application to complex mixtures	142
4.8.1	Experimental example	144
4.9	Conclusion	144
5	Two-dimensional J-spectra with absorption-mode lineshapes	147
5.1	The Zanger–Sterk experiment	148
5.1.1	Analysis of the pulse sequence	148
5.1.2	Lineshapes and the projection	150
5.1.3	Spatially-selective decoupling	151
5.1.4	Spatial inhomogeneity of the gradient and RF field	155
5.1.5	Strong coupling and close-lying multiplets	157
5.1.6	Speeding up acquisition	160
5.1.7	Comparison of the anti z -COSY and Zanger–Sterk pulse sequences	162
5.2	Two-dimensional J -spectra with absorption-mode lineshapes	164
5.2.1	Analysis of the pulse sequences	165
5.2.2	Linewidths in the decoupled spectrum	167
5.3	The absorption-mode J -spectrum of quinine	168

5.4	The effects of strong coupling	172
5.5	The absorption-mode J -spectrum of dehydroisoandrosterone	172
5.6	Conclusion	174
6	High-resolution heteronuclear correlation spectra using the Maximum Entropy Method	177
6.1	Single-bond correlation experiments	179
6.1.1	HMQC of a two-spin system	179
6.1.2	HSQC of a two-spin system	182
6.2	The effects of homonuclear coupling	184
6.2.1	HMQC of a three-spin system	184
6.2.2	HSQC of a three-spin system	186
6.2.3	Discussion	188
6.3	Multiple-bond correlation experiments	188
6.3.1	HMBC of a two-spin system	189
6.3.2	Suppression of unwanted signals using gradient selection	190
6.3.3	HMBC of a three-spin system	191
6.4	Sparse sampling	191
6.4.1	On-grid and off-grid schemes	192
6.4.2	Sensitivity of spectra constructed from sparsely-sampled data	192
6.4.3	Resolution of spectra constructed from sparsely-sampled data	193
6.4.4	Sampling schemes	194
6.5	Spectral reconstruction from sparsely-sampled datasets	195
6.5.1	The Maximum Entropy Method	197
6.5.2	Application of the MEM to two-dimensional spectra	199
6.6	HSQC of dehydroisoandrosterone	199
6.6.1	Exponential sampling	202
6.6.2	Random sampling	203
6.6.3	Effect of the SNR on the MEM spectrum	212
6.6.4	Discussion	212
6.7	HMBC of dehydroisoandrosterone	214
6.8	Conclusion	219
A	Angular momentum	220

A.1	The spin angular momentum operators	220
A.1.1	Eigenfunctions and eigenvalues	220
A.1.2	The raising, lowering, and polarization operators	221
A.1.3	Rotation operators	222
A.2	Superposition states and matrix representations of operators	222
Bibliography		225

Chapter 1

The basics of nuclear magnetic resonance

THE DEVELOPMENT OF NEW TECHNIQUES in nuclear magnetic resonance (NMR) spectroscopy requires an understanding of how nuclear spins interact with magnetic fields. This Chapter describes the dynamics of an ensemble of spins in the presence of a magnetic field using the density operator approach. It is then shown how the theory can predict the form of the NMR spectrum, and how such spectra are recorded and processed. The material presented in this Chapter relies on an understanding of the basic properties of the spin angular momentum operators, which are summarized in Appendix A.

1.1 Spin angular momentum and magnetic moment

Many particles possess an intrinsic angular momentum known as *spin*. The spin angular momentum \mathbf{I} produces a magnetic moment $\boldsymbol{\mu}$ which is given by

$$\boldsymbol{\mu} = \gamma \mathbf{I}.$$

The constant of proportionality γ is known as the *gyromagnetic ratio* and takes a different value for each species of nuclear spin. It proves to be convenient to use a system of units in which the constant \hbar is unity; in this system, angular momentum is dimensionless and energy has frequency units of rad s⁻¹.

The work described in this dissertation deals exclusively with particles of spin $I = \frac{1}{2}$, such as the ¹H and ¹³C nuclei. The following discussion is therefore restricted to such spins.

1.2 The interaction of a single spin with a magnetic field

In this Section, the behaviour of a single spin in the presence of a magnetic field is examined.

1.2.1 A static magnetic field

In the classical limit, the energy of interaction of a spin with an external magnetic field \mathbf{B} is given by $E = -\mu \cdot \mathbf{B}$. The operator that describes this interaction is the Hamiltonian $\hat{\mathcal{H}}$. It has the form

$$\begin{aligned}\hat{\mathcal{H}} &= -\gamma \hat{\mathbf{I}} \cdot \mathbf{B} \\ &= -\gamma \sum_{i=1}^3 B_i \hat{I}_i,\end{aligned}\quad (1.1)$$

where B_i is the component of the magnetic field along the i -axis. Nuclear magnetic resonance experiments are performed in the presence of a static field of magnitude B_0 that is conventionally applied along the z -axis of the laboratory frame of reference. The Hamiltonian is then known as the Zeeman Hamiltonian $\hat{\mathcal{H}}_z$, and is given by

$$\begin{aligned}\hat{\mathcal{H}}_z &= -\gamma B_0 \hat{I}_z \\ &= \omega_0 \hat{I}_z,\end{aligned}\quad (1.2)$$

where we have defined the Larmor frequency as $\omega_0 = -\gamma B_0$.

The eigenfunctions of this Hamiltonian are the Zeeman functions $|I, M\rangle$ which are described in Appendix A. The spin angular momentum quantum number I take integer or half-integer values, and the magnetic quantum number M takes values between $-I$ and $+I$ in integer steps. The Zeeman states have energies $M\omega_0$, and so when an external field is applied they cease to be degenerate, with adjacent levels being separated by ω_0 . The order of the levels depends upon the sign of γ .

1.2.2 Time evolution

The time-evolution of a wavefunction $|\psi(t)\rangle$ is governed by the time-dependent Schrödinger equation:

$$\frac{d|\psi(t)\rangle}{dt} = -i\hat{\mathcal{H}}|\psi(t)\rangle, \quad (1.3)$$

where $\hat{\mathcal{H}}$ is the Hamiltonian. If $\hat{\mathcal{H}}$ is time-independent, the solution to Equation 1.3 is

$$|\psi(t)\rangle = \exp(-i\hat{\mathcal{H}}t)|\psi(0)\rangle. \quad (1.4)$$

The Hamiltonian is Hermitian, so $\hat{U} = \exp(-i\hat{\mathcal{H}}t)$ is a unitary operator which is referred to as the *propagator*.

If the wavefunction is an eigenfunction of $\hat{\mathcal{H}}$, then the solution of Equation 1.4 becomes

$$|\psi(t)\rangle = \exp(-iEt) |\psi(0)\rangle, \quad (1.5)$$

where E is the corresponding energy eigenvalue. The wavefunction in this case simply acquires a phase.

1.2.3 Measurements on a single spin

An observable quantity, such as the magnetic moment, is associated with an operator \hat{A} which must be Hermitian. It is therefore possible to expand the wavefunction as a superposition of a set of linearly independent basis functions $\{|i\rangle\}$ as in Equation A.3. Any such basis can be used, but it proves convenient to use the eigenbasis of \hat{A} . In this case, when the observable is measured, the result will always be one of the corresponding eigenvalues a_i . Assuming that $|\psi(t)\rangle$ is normalized, the probability of returning a particular eigenvalue is given by $|c_i|^2$, where c_i is the coefficient of the state $|i\rangle$ in the superposition. Since it is not possible to predict which eigenvalue will be recorded for any given measurement, it is useful to define the *expectation value* of \hat{A} as

$$\langle \hat{A} \rangle = \langle \psi | \hat{A} | \psi \rangle.$$

The expectation value is simply the average result that is obtained from a series of many such measurements in which the wavefunction $|\psi\rangle$ does not change.

1.3 An ensemble of spins

Nuclear magnetic resonance experiments are performed on samples that contain an *ensemble*, that is a large number, of nuclear spin systems. In order to calculate the value of an observable of the whole sample A_{bulk} , it is necessary to sum the individual contributions from all N spins:

$$A_{\text{bulk}} = \sum_{l=1}^N \langle \hat{A}_l \rangle,$$

where $\langle \hat{A}_l \rangle$ is the expectation value of the corresponding microscopic observable of spin l . For example, the component of the *bulk magnetization* about axis i , M_i , is

given by the sum of the expectation values of the corresponding component of the magnetic moment of each spin:

$$M_i = \gamma \sum_{l=1}^N \langle \psi^{(l)} | \hat{I}_i | \psi^{(l)} \rangle,$$

where $|\psi^{(l)}\rangle$ is the *superposition* wavefunction of the l th spin.

Within the ensemble we can view the spins as being distributed over all the accessible spin states. If the probability of a spin occupying a *state* $|k\rangle$ is p_k , the ensemble average of the expectation value of the microscopic observable is

$$\overline{\langle \hat{A} \rangle} = \sum_{k=1}^n p_k \langle k | \hat{A} | k \rangle, \quad (1.6)$$

where the sum is taken over all n possible spin states, and the overbar denotes the average over the ensemble. As N becomes very large, the measurement of A_{bulk} is accurately assumed to be

$$A_{\text{bulk}} = N \overline{\langle \hat{A} \rangle}.$$

In this Section, it is assumed that the matrix representations of the operators are calculated in the eigenbasis of the relevant Hamiltonian.

1.3.1 The density operator

The calculation in Equation 1.6 can be simplified by inserting two completeness relations, Equation A.2, from which we obtain

$$\begin{aligned} \overline{\langle \hat{A} \rangle} &= \sum_{i,j} \sum_k p_k \langle k | i \rangle \langle i | \hat{A} | j \rangle \langle j | k \rangle \\ &= \sum_{i,j} \langle i | \hat{A} | j \rangle \sum_k p_k \langle j | k \rangle \langle k | i \rangle \\ &= \sum_{i,j} \langle i | \hat{A} | j \rangle \langle j | \hat{\sigma} | i \rangle, \end{aligned} \quad (1.7)$$

where we have introduced the *density operator* $\hat{\sigma}$:

$$\hat{\sigma} = \sum_k p_k |k\rangle \langle k| = \overline{|\psi\rangle \langle \psi|}.$$

Equation 1.7 can now be written in the more succinct form

$$\overline{\langle \hat{A} \rangle} = \text{Tr}(\hat{A} \hat{\sigma}), \quad (1.8)$$

where \hat{A} is the operator for the *microscopic* observable. Once the density operator has been computed, it is possible to calculate the value of *any* bulk observable simply by computing the relevant trace. The trace is taken by first calculating the matrix representation of $\hat{A}\hat{\sigma}$, and then summing the diagonal elements.

1.3.2 Time evolution of the density operator

Using the time-dependent Schrödinger equation, it is possible to derive the Liouville–von Neumann equation, which governs the time evolution of the density operator:

$$\begin{aligned} \frac{d\hat{\sigma}}{dt} &= \frac{d|\psi\rangle\langle\psi|}{dt} \\ &= \frac{d|\psi\rangle}{dt}\langle\psi| + |\psi\rangle\frac{d\langle\psi|}{dt} \\ &= -i\hat{\mathcal{H}}|\psi\rangle\langle\psi| + i|\psi\rangle\langle\psi|\hat{\mathcal{H}} \\ &= -i[\hat{\mathcal{H}}, \hat{\sigma}]. \end{aligned} \quad (1.9)$$

This differential equation has a straightforward solution when $\hat{\mathcal{H}}$ is time independent:

$$\begin{aligned} \hat{\sigma}(t) &= \exp(-i\hat{\mathcal{H}}t)\hat{\sigma}(0)\exp(i\hat{\mathcal{H}}t) \\ &= \hat{U}\hat{\sigma}(0)\hat{U}^{-1}, \end{aligned} \quad (1.10)$$

where \hat{U} is the propagator that was introduced in Section 1.2.2. This transformation is simply a rotation of the density operator about an axis that is defined by $\hat{\mathcal{H}}$.

Over the course of most NMR experiments, the Hamiltonian changes with time, for example when radiofrequency (RF) pulses are applied. However, the experiment can be broken up into sections during each of which the Hamiltonian is constant. A propagator \hat{U}_n can be defined for each of the N sections, so that Equation 1.10 becomes:

$$\hat{\sigma}(t) = (\hat{U}_N\hat{U}_{N-1}\dots\hat{U}_2\hat{U}_1)\hat{\sigma}(0)(\hat{U}_1^{-1}\hat{U}_2^{-1}\dots\hat{U}_{N-1}^{-1}\hat{U}_N^{-1}).$$

1.3.3 The rotating frame of reference

The solution to the Liouville–von Neumann equation in Equation 1.10 is only valid for a Hamiltonian that is time independent. However, there are situations where this is not the case. Fortunately, it may be possible to remove the time dependence of a Hamiltonian $\hat{\mathcal{H}}$ by transforming both the Hamiltonian and density operator into a new frame of reference, which is sometimes referred to as the *interaction frame*.

The Hamiltonian can be written as the sum of two terms:

$$\hat{\mathcal{H}} = \hat{\mathcal{H}}_0 + \hat{\mathcal{H}}_1,$$

where $\hat{\mathcal{H}}_1$ contains all the time dependence, and $\hat{\mathcal{H}}_0$ is time independent. The time dependent part of the Hamiltonian can be rotated by the propagator defined by $\hat{\mathcal{H}}_0$ to give the interaction frame Hamiltonian $\hat{\mathcal{H}}_1^T$:

$$\hat{\mathcal{H}}_1^T = \hat{U}_0^{-1} \hat{\mathcal{H}}_1 \hat{U}_0,$$

where $\hat{U}_0 = \exp(-i\hat{\mathcal{H}}_0 t)$. The interaction frame density operator $\hat{\sigma}^T$ is defined in exactly the same way:

$$\hat{\sigma}^T = \hat{U}_0^{-1} \hat{\sigma} \hat{U}_0.$$

Note that the rotation of the new frame of reference is described by \hat{U}_0 , and so we must apply the *inverse* rotation to the operators.

The equation of motion of this density operator can be derived by taking the time derivative of $\hat{\sigma}^T$:

$$\begin{aligned} \frac{d\hat{\sigma}^T}{dt} &= \frac{d}{dt} (\hat{U}_0^{-1} \hat{\sigma} \hat{U}_0) \\ &= \frac{d\hat{U}_0^{-1}}{dt} \hat{\sigma} \hat{U}_0 + \hat{U}_0^{-1} \hat{\sigma} \frac{d\hat{U}_0}{dt} + \hat{U}_0^{-1} \frac{d\hat{\sigma}}{dt} \hat{U}_0 \\ &= i\hat{\mathcal{H}}_0 \hat{U}_0^{-1} \hat{\sigma} \hat{U}_0 - i\hat{U}_0^{-1} \hat{\sigma} \hat{U}_0 \hat{\mathcal{H}}_0 + \hat{U}_0^{-1} \frac{d\hat{\sigma}}{dt} \hat{U}_0 \\ &= i\hat{U}_0^{-1} [\hat{\mathcal{H}}_0, \hat{\sigma}] \hat{U}_0 + \hat{U}_0^{-1} \frac{d\hat{\sigma}}{dt} \hat{U}_0. \end{aligned}$$

The derivative in the second term can be replaced by the Liouville–von Neumann equation for the laboratory frame density operator:

$$\begin{aligned} \frac{d\hat{\sigma}^T}{dt} &= i\hat{U}_0^{-1} [\hat{\mathcal{H}}_0, \hat{\sigma}] \hat{U}_0 - i\hat{U}_0^{-1} [\hat{\mathcal{H}}_0 + \hat{\mathcal{H}}_1, \hat{\sigma}] \hat{U}_0 \\ &= -i\hat{U}_0^{-1} [\hat{\mathcal{H}}_1, \hat{\sigma}] \hat{U}_0 \\ &= -i\hat{U}_0^{-1} \hat{\mathcal{H}}_1 \hat{\sigma} \hat{U}_0 + i\hat{U}_0^{-1} \hat{\sigma} \hat{\mathcal{H}}_1 \hat{U}_0 \\ &= -i(\hat{U}_0^{-1} \hat{\mathcal{H}}_1 \hat{U}_0)(\hat{U}_0^{-1} \hat{\sigma} \hat{U}_0) + i(\hat{U}_0^{-1} \hat{\sigma} \hat{U}_0)(\hat{U}_0^{-1} \hat{\mathcal{H}}_1 \hat{U}_0) \\ &= -i[\hat{\mathcal{H}}_1^T, \hat{\sigma}^T]. \end{aligned}$$

The interaction frame density operator therefore only evolves under the action of $\hat{\mathcal{H}}_1^T$, which is time independent.

1.3.4 The matrix representation of the density operator

It is implied in Equation 1.8 that it is useful to write the density operator in its matrix form $\sigma_{ij} = \langle i|\hat{\sigma}|j\rangle$, which is referred to as the *density matrix*. For an ensemble of non-interacting spins- $\frac{1}{2}$ the density matrix, when expressed in the $\{|\alpha\rangle, |\beta\rangle\}$ basis, is

$$\sigma = \begin{pmatrix} \overline{c_\alpha c_\alpha^*} & \overline{c_\alpha c_\beta^*} \\ \overline{c_\beta c_\alpha^*} & \overline{c_\beta c_\beta^*} \end{pmatrix}.$$

The numbers c_α and c_β are the coefficients of the expansion $|\psi\rangle = c_\alpha|\alpha\rangle + c_\beta|\beta\rangle$. The bulk z -magnetization can be calculated as follows:

$$\begin{aligned} M_z &= \gamma N \text{Tr}(\hat{I}_z \hat{\sigma}) \\ &= \gamma N \text{Tr} \left[\begin{pmatrix} \frac{1}{2} & 0 \\ 0 & -\frac{1}{2} \end{pmatrix} \begin{pmatrix} \overline{c_\alpha c_\alpha^*} & \overline{c_\alpha c_\beta^*} \\ \overline{c_\beta c_\alpha^*} & \overline{c_\beta c_\beta^*} \end{pmatrix} \right] \\ &= \frac{1}{2} \gamma N \left(\overline{|c_\alpha|^2} - \overline{|c_\beta|^2} \right). \end{aligned}$$

It can be seen that the diagonal elements of $\hat{\sigma}$ determine the value of M_z . The x - and y -components can be calculated in the same way to give:

$$\begin{aligned} M_x &= \frac{1}{2} \gamma N \left(\overline{c_\alpha^* c_\beta} + \overline{c_\beta^* c_\alpha} \right), \\ M_y &= \frac{1}{2} i \gamma N \left(\overline{-c_\alpha^* c_\beta} + \overline{c_\beta^* c_\alpha} \right), \end{aligned}$$

from which it can be seen that they depend upon the off-diagonal elements.

In general, a diagonal element σ_{ii} has the form $\overline{|c_i|^2}$, and therefore can be interpreted as the population of the state $|i\rangle$. The off-diagonal elements σ_{ij} are given by $\overline{c_i c_j^*} = |c_i| |c_j| \exp[i(\phi_i - \phi_j)]$, where ϕ_i is the phase of the coefficient c_i ^{*}.

1.3.5 Time evolution of the density matrix

The effect of a Hamiltonian on the time evolution of the density matrix is described by Equation 1.10 where the propagators are expressed in matrix form. It is necessary to determine the matrix representation of the propagator, which requires the calculation

*Any complex coefficient c_i may be written as the product of a magnitude $|c_i|$ and a phase factor $\exp(i\phi_i)$.

of the exponential of a matrix. This is generally not trivial, the exception being when the matrix is calculated using the eigenbasis of \hat{A} , so that it is diagonal:

$$A_{ij} = a^{(i)} \delta_{ij}.$$

In this case the exponential of A is also diagonal [†]:

$$\begin{aligned} [\exp(A)]_{ij} &= \delta_{ij} + a^{(i)} \delta_{ij} + \frac{1}{2!} (a^{(i)})^2 \delta_{ik} \delta_{kj} + \dots \\ &= \left[1 + a^{(i)} + \frac{1}{2!} (a^{(i)})^2 + \dots \right] \delta_{ij} \\ &= \exp(a^{(i)}) \delta_{ij}. \end{aligned}$$

If we therefore choose the eigenbasis of the Hamiltonian $\hat{\mathcal{H}}$, so that $\mathcal{H}_{ij} = E_i \delta_{ij}$, then the propagator is diagonal:

$$U_{ij} = [\exp(-i\hat{\mathcal{H}}t)]_{ij} = \exp(-iE_i t) \delta_{ij}.$$

The element σ_{ij} is transformed by this propagator to give:

$$\begin{aligned} \sigma_{ij}(t) &= \langle i | \exp(-i\hat{\mathcal{H}}t) \hat{\sigma}(0) \exp(i\hat{\mathcal{H}}t) | j \rangle \\ &= \sum_{k,l} \langle i | \exp(-i\hat{\mathcal{H}}t) | k \rangle \langle k | \hat{\sigma}(0) | l \rangle \langle l | \exp(i\hat{\mathcal{H}}t) | j \rangle \\ &= \sum_{k,l} \exp(-iE_k t) \delta_{ik} \sigma_{kl}(0) \exp(iE_l t) \delta_{lj} \\ &= \sigma_{ij}(0) \exp(i(E_j - E_i)t). \end{aligned} \quad (1.11)$$

Each element of the density matrix therefore acquires a phase that is modulated at a frequency equal to the energy difference of the two connected eigenstates.

For a system of non-interacting spins, there are two energy levels with energies $E_\alpha = +\frac{1}{2}\omega_0$ and $E_\beta = -\frac{1}{2}\omega_0$. Therefore, the two off-diagonal elements evolve as follows:

$$\begin{aligned} \sigma_{12}(t) &= \sigma_{12}(0) \exp(-i\omega_0 t), \\ \sigma_{21}(t) &= \sigma_{21}(0) \exp(+i\omega_0 t), \end{aligned}$$

that is, they evolve at the Larmor frequency.

[†]In this equation we make use of Einstein's summation convention, in which a repeated subscript implies a summation over that index [1].

1.3.6 The density operator at thermal equilibrium

In this Section, we will calculate the form of the density operator at thermal equilibrium for an ensemble of spins that are subject to an external magnetic field B_0 that is applied in the z -direction of the laboratory frame of reference.

In the eigenbasis of the Zeeman Hamiltonian $\hat{\mathcal{H}}_z$, the populations p_i of the spin states $|i\rangle$ are equal to the diagonal elements of the density matrix. At thermal equilibrium, they are given by the Boltzmann distribution:

$$p_i = \frac{1}{Z} \exp\left(-\frac{E_i}{kT}\right),$$

where Z is the partition function which corresponds to the sum of all the population factors:

$$Z = \sum_{i=1}^n \exp\left(-\frac{E_i}{kT}\right).$$

The energy E_i is the eigenvalue of $\hat{\mathcal{H}}_z$ that corresponds to the state $|i\rangle$. The off-diagonal elements all take the form $\overline{|c_i||c_j| \exp[i(\phi_i - \phi_j)]}$. At equilibrium, the phases ϕ_i are randomly distributed resulting in the ensemble average being equal to zero.

The equilibrium density operator $\hat{\sigma}_0$ must therefore be diagonal, with diagonal elements that are given by the Boltzmann distribution. It is therefore given by [2]

$$\hat{\sigma}_0 = \frac{1}{Z} \exp\left(-\frac{\hbar\hat{\mathcal{H}}_z}{kT}\right) = \frac{1}{Z} \exp\left(-\frac{\hbar\omega_0\hat{I}_z}{kT}\right), \quad (1.12)$$

where the factor Z is the sum of the diagonal elements, which is given by the trace

$$Z = \text{Tr} \left[\exp\left(-\frac{\hbar\omega_0\hat{I}_z}{kT}\right) \right].$$

Nuclear magnetic resonance experiments are carried out in the high-temperature limit, such that for all the eigenvalues $\hbar E_i/kT \ll 1$. In this case, we can expand the exponential in Equation 1.12 as a Taylor series [1], and truncate after the second term to give

$$\hat{\sigma}_0 = \frac{1}{Z} \left(\hat{E} - \frac{\hbar\omega_0\hat{I}_z}{kT} \right).$$

As will be shown in Section 1.5.1 the identity operator \hat{E} cannot be observed in an NMR experiment. Furthermore, it commutes with all operators, and so is unchanged by the action of any Hamiltonian. It therefore will not produce any observable

magnetization, and so is omitted from the expression for $\hat{\sigma}_0$. In addition, the factor $\hbar\omega_0/kT$ simply scales the \hat{I}_z term, and is also removed to simplify the results of any calculations. This gives the following simple expression for $\hat{\sigma}_0$:

$$\hat{\sigma}_0 = \hat{I}_z. \quad (1.13)$$

1.4 The Hamiltonian for a one-spin system

In order to calculate the time evolution of an ensemble of spins, it is first necessary to determine the form of the Hamiltonian. A typical NMR experiment is built up from two different elements for which the Hamiltonian is different: delays during which the spins evolve freely, and radiofrequency (RF) pulses.

1.4.1 The chemical shift

When a static field of strength B_0 is applied along the z -axis of the laboratory reference frame, it was shown that the spins precess about this axis at the Larmor frequency $\omega_0 = -\gamma B_0$. This description, however, ignores the fact that spins in different chemical environments actually precess at different frequencies.

The local electron density has the effect of modifying the size of the magnetic field that is experienced by the spins. The resultant magnetic field B_{total} is given by

$$B_{\text{total}} = (1 - \sigma)B_0,$$

where σ is the *chemical shielding constant* that depends upon the precise chemical environment of the spin. The actual Larmor frequency is therefore given by

$$\omega_0 = -\gamma B_{\text{total}} = -\gamma(1 - \sigma)B_0,$$

which also varies with the chemical environment.

For a given nucleus, the Larmor frequency is dependent upon the value of B_0 , which will be different for different spectrometers. Therefore, it is conventional to introduce a frequency scale that is field independent. The *chemical shift* δ (in units of parts per million) is defined as

$$\delta = 10^6 \times \frac{\omega_0 - \omega_{\text{ref}}}{\omega_{\text{ref}}},$$

where ω_{ref} is the Larmor frequency of a nucleus in a reference molecule at the same field strength.

1.4.2 Radiofrequency pulses

In order to observe free precession, it is necessary to generate non-equilibrium magnetization in the transverse plane, or equivalently to create non-zero off-diagonal elements in the density matrix. This is done by applying an RF pulse to the sample. The magnetic field that is thus generated, and therefore the resulting Hamiltonian, is time dependent. The description of how the pulse works is therefore complex. However, the time dependence can be removed by using a frame of reference that rotates relative to the laboratory frame, using the procedure that is described in Section 1.3.3.

The RF Hamiltonian in the rotating frame

The RF pulse generates an oscillating magnetic field $\mathbf{B}_1(t)$ along the x -axis of the laboratory frame. The field is described by

$$\mathbf{B}_1(t) = i2B_1 \cos(\omega_{\text{rf}}t + \phi_{\text{rf}}),$$

where $2B_1$ is the maximum strength of the field, ω_{rf} is the frequency of oscillation, ϕ_{rf} is the initial phase of the field, and i is the unit vector that is parallel to x . Since the field is time dependent the Hamiltonian, $\hat{\mathcal{H}}_{\text{rf}}(t) = -\gamma\hat{\mathbf{I}} \cdot \mathbf{B}_1(t)$, will also vary with time. However, this time dependence can be removed by a transformation into the interaction representation.

The transformation is implemented by firstly decomposing the \mathbf{B}_1 field into two counter-rotating components:

$$\begin{aligned}\mathbf{B}_1^+(t) &= B_1 [\mathbf{i} \cos(\omega_{\text{rf}}t + \phi_{\text{rf}}) + \mathbf{j} \sin(\omega_{\text{rf}}t + \phi_{\text{rf}})], \\ \mathbf{B}_1^-(t) &= B_1 [\mathbf{i} \cos(\omega_{\text{rf}}t + \phi_{\text{rf}}) - \mathbf{j} \sin(\omega_{\text{rf}}t + \phi_{\text{rf}})].\end{aligned}$$

This simplifies any calculations involving a pulse since one of the two fields has a negligible effect on the spins and so can be discarded. The choice of which can be ignored depends on the sign of γ . The Hamiltonian $\hat{\mathcal{H}}_{\text{total}}$ is therefore

$$\hat{\mathcal{H}}_{\text{total}} = \omega_0\hat{I}_z - \gamma\hat{\mathbf{I}} \cdot \mathbf{B}_1^+(t) - \gamma\hat{\mathbf{I}} \cdot \mathbf{B}_1^-(t).$$

To facilitate the transformation $\hat{\mathcal{H}}_{\text{total}}$ is written as the sum of a time independent part

$\hat{\mathcal{H}}_0$ and a time dependent part $\hat{\mathcal{H}}_1$, which are given by

$$\begin{aligned}\hat{\mathcal{H}}_0 &= \omega_{\text{rot}} \hat{I}_z, \\ \hat{\mathcal{H}}_1 &= (\omega_0 - \omega_{\text{rot}}) \hat{I}_z - \gamma B_1 \hat{R}_z (\omega_{\text{rf}} t + \phi_{\text{rf}}) \hat{I}_x \hat{R}_z (\omega_{\text{rf}} t + \phi_{\text{rf}})^{-1} \\ &\quad - \gamma B_1 \hat{R}_z (\omega_{\text{rf}} t + \phi_{\text{rf}})^{-1} \hat{I}_x \hat{R}_z (\omega_{\text{rf}} t + \phi_{\text{rf}}).\end{aligned}$$

The rotating frame is rotating about the z -axis of the laboratory frame at frequency ω_{rot} , which is chosen to be $-\text{sign}(\gamma)\omega_{\text{rf}}$. The Hamiltonian $\hat{\mathcal{H}}_1$ is transformed into the interaction frame of $\hat{\mathcal{H}}_0$ using the propagator $\hat{U}_0 = \hat{R}_z(\omega_{\text{rot}} t + \phi_{\text{rot}})$, where ϕ_{rot} has been included to account for the initial phase of the frame at $t = 0$. This gives

$$\begin{aligned}\hat{\mathcal{H}}_1^T &= (\omega_0 - \omega_{\text{rot}}) \hat{I}_z - \gamma B_1 \hat{R}_z (\omega_{\text{rf}} t - \omega_{\text{rot}} t + \phi_{\text{rf}} - \phi_{\text{rot}}) \hat{I}_x \hat{R}_z (\omega_{\text{rf}} t - \omega_{\text{rot}} t + \phi_{\text{rf}} - \phi_{\text{rot}})^{-1} \\ &\quad - \gamma B_1 \hat{R}_z (\omega_{\text{rf}} t + \omega_{\text{rot}} t + \phi_{\text{rf}} + \phi_{\text{rot}})^{-1} \hat{I}_x \hat{R}_z (\omega_{\text{rf}} t + \omega_{\text{rot}} t + \phi_{\text{rf}} + \phi_{\text{rot}}).\end{aligned}$$

On setting $\omega_{\text{rot}} = -\text{sign}(\gamma)\omega_{\text{rf}}$, one of the RF terms in $\hat{\mathcal{H}}_1^T$ will still be time dependent (the second term for $\gamma > 0$, or the third term for $\gamma < 0$). The magnetic field giving rise to this time dependency is referred to as *non-resonant*, and can be shown to have a negligible effect on the motion of the spins [3]; this term can therefore be deleted, giving

$$\hat{\mathcal{H}}_1^T = (\omega_0 - \omega_{\text{rot}}) \hat{I}_z - \gamma B_1 \hat{R}_z (\phi_p - \phi_{\text{rot}}) \hat{I}_x \hat{R}_z (\phi_p - \phi_{\text{rot}})^{-1},$$

where $\phi_p = -\text{sign}(\gamma)\phi_{\text{rf}}$. Conventionally, $\phi_{\text{rot}} = \pi$ if $\gamma > 0$, or 0 if $\gamma < 0$ [4]. We now define $\omega_1 = |\gamma B_1|$ as the frequency of rotation about the x -axis in the rotating frame, and $\Omega = \omega_0 - \omega_{\text{rot}}$ as the relative Larmor frequency which is known as the offset. The Hamiltonian is (dropping the superscript for brevity):

$$\hat{\mathcal{H}}_1 = \Omega \hat{I}_z + \omega_1 \hat{R}_z (\phi_p) \hat{I}_x \hat{R}_z (\phi_p)^{-1}. \quad (1.14)$$

The phase of the pulse in the rotating frame is ϕ_p : for example, if $\phi_p = 0$ the pulse is applied along x , and if $\phi_p = \pi/2$ the pulse is applied along y .

Hard and soft pulses

From the Hamiltonian in Equation 1.14, it is apparent that the pulse can be described in terms of an *effective magnetic field* B_{eff} that is the resultant of two parts: the B_1 (ω_1) field in the transverse plane, and a reduced magnetic field along z that is given by $\Delta B = -\Omega/\gamma$. This is illustrated in Figure 1.1. The bulk magnetization will precess

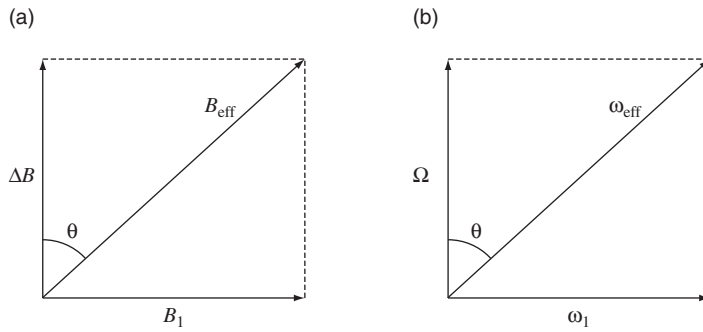


Figure 1.1: The effective magnetic field in the rotating frame. The effective field B_{eff} is the vector sum of the field due to the pulse B_1 and the reduced field along the z -axis ΔB , as shown in (a). The resultant is tilted from z by an angle θ . The same diagram is shown in (b), but in terms of the rotation frequencies.

about the effective field at a frequency that is given by $\omega_{\text{eff}} = |\gamma| B_{\text{eff}}$. This effective frequency, and the angle of tilt of the field from the z -axis θ are given by:

$$\omega_{\text{eff}} = \sqrt{\omega_1^2 + \Omega^2} \quad \tan \theta = \frac{\omega_1}{\Omega}.$$

The Hamiltonian can therefore be rewritten as follows:

$$\begin{aligned} \hat{\mathcal{H}}_1 &= \omega_{\text{eff}} \cos \theta \hat{I}_z + \omega_{\text{eff}} \sin \theta \hat{R}_z(\phi_p) \hat{I}_x \hat{R}_z(\phi_p)^{-1} \\ &= \omega_{\text{eff}} \hat{R}_z(\phi_p) [\hat{I}_z \cos \theta + \hat{I}_x \sin \theta] \hat{R}_z(\phi_p)^{-1} \\ &= \omega_{\text{eff}} \hat{R}_z(\phi_p) \hat{R}_y(\theta) \hat{I}_z \hat{R}_y(\theta)^{-1} \hat{R}_z(\phi_p)^{-1}. \end{aligned} \quad (1.15)$$

A *hard* pulse is defined to have a sufficiently large B_1 so that $\omega_1 \gg |\Omega|$ for the full range of offsets. In this limit, $\omega_{\text{eff}} \approx \omega_1$, and $\theta \approx \pi/2$ for all offsets (so that the effective field lies in the transverse plane), and the Hamiltonian becomes

$$\hat{\mathcal{H}}_{\text{hard}} = \omega_1 \hat{R}_z(\phi_p) \hat{I}_x \hat{R}_z(\phi_p)^{-1}. \quad (1.16)$$

When $\phi_p = 0$ or $\pi/2$ the pulse is along the x or y axis respectively. In these cases, the Hamiltonian takes a very simple form:

$$\hat{\mathcal{H}}_{\text{hard},x} = \omega_1 \hat{I}_x, \quad \hat{\mathcal{H}}_{\text{hard},y} = \omega_1 \hat{I}_y.$$

When we are not in the hard pulse approximation, for example when we wish to excite certain offsets selectively, the full form of the Hamiltonian in Equation 1.15 must be used. In this case, the pulse is referred to as *soft*. The topic of selective excitation will be covered in Section 2.4.

1.5 The basis operators for a one-spin system

It is sometimes convenient to expand the density operator as a linear combination of basis operators $\{\hat{B}_i\}$:

$$\hat{\sigma}(t) = \sum_{i=1}^{n^2} b_i(t) \hat{B}_i, \quad (1.17)$$

where the $b_i(t)$ are time dependent coefficients.

For a system of N coupled spins, $n = 2^N$ basis *functions* are required to compute the matrix representation of $\hat{\sigma}$. Each of the n^2 elements may represent an independent *operator* in the expansion in Equation 1.17, and so the complete operator basis comprises $n^2 = 4^N$ operators. The operators are chosen so that they are normalized and orthogonal, as defined through their *scalar product*:

$$(\hat{B}_i | \hat{B}_j) \equiv \text{Tr}(\hat{B}_i^\dagger \hat{B}_j) = K\delta_{ij}, \quad (1.18)$$

where K is the normalization constant for \hat{B}_i .

This Section is concerned with the operator expansion used to describe the density operator of a one-spin system. There are two such bases that are commonly used, both of which comprise the spin angular momentum operators: the Cartesian operators, and the single-element operators.

1.5.1 Cartesian basis operators

The Cartesian operator basis comprises the Cartesian spin operators and half the identity: $\{\frac{1}{2}\hat{E}, \hat{I}_x, \hat{I}_y, \hat{I}_z\}$. With this basis, the three components of the bulk magnetization \mathbf{M} are proportional to the three coefficients b_x , b_y , and b_z of the expansion

$$\hat{\sigma} = b_E \frac{1}{2} \hat{E} + b_x \hat{I}_x + b_y \hat{I}_y + b_z \hat{I}_z.$$

For example, M_x is given by:

$$\begin{aligned} M_x &= \gamma N \text{Tr}(\hat{I}_x \hat{\sigma}) \\ &= \gamma N b_E \text{Tr}(\hat{I}_x \frac{1}{2} \hat{E}) + \gamma N b_x \text{Tr}(\hat{I}_x \hat{I}_x) + \gamma N b_y \text{Tr}(\hat{I}_x \hat{I}_y) + \gamma N b_z \text{Tr}(\hat{I}_x \hat{I}_z) \\ &= \frac{1}{2} \gamma N b_x, \end{aligned}$$

where we have used the fact that \hat{I}_x is orthogonal to the other members of the basis. Similarly, $M_y = \frac{1}{2} \gamma N b_y$, and $M_z = \frac{1}{2} \gamma N b_z$. In an NMR experiment, we detect only

the transverse magnetization M_x and M_y . For this reason, the only terms in the density operator expansion that are observable are those involving \hat{I}_x and \hat{I}_y .

Both the Hamiltonian and density operator can be expanded in the Cartesian basis, the operators of which obey the cyclic commutation rule of Equation A.1. In this case, the solution to the Liouville–von Neumann equation can be reduced to a simple transformation rule using the following identity [4]:

$$\exp(-i\alpha \hat{I}_i) \hat{I}_j \exp(i\alpha \hat{I}_i) = \cos \alpha \hat{I}_j + \sin \alpha \hat{I}_k,$$

which is more usually written as

$$\hat{I}_j \xrightarrow{\alpha \hat{I}_i} \cos \alpha \hat{I}_j + \sin \alpha \hat{I}_k. \quad (1.19)$$

Free precession

In the rotating frame of reference, the free-precession Hamiltonian is given by $\hat{\mathcal{H}}_{\text{free}} = \Omega \hat{I}_z$. The operators \hat{I}_x and \hat{I}_y precess about z through an angle Ωt , whereas \hat{I}_z is unaffected:

$$\begin{aligned} \hat{I}_x &\xrightarrow{\Omega t \hat{I}_z} \cos(\Omega t) \hat{I}_x + \sin(\Omega t) \hat{I}_y \\ \hat{I}_y &\xrightarrow{\Omega t \hat{I}_z} \cos(\Omega t) \hat{I}_y - \sin(\Omega t) \hat{I}_x \\ \hat{I}_z &\xrightarrow{\Omega t \hat{I}_z} \hat{I}_z. \end{aligned}$$

Radiofrequency pulses

A hard RF pulse about an axis with phase ϕ is represented by the Hamiltonian in Equation 1.16. If the pulse is applied for a time t_p , the propagator is simply the corresponding rotation operator $\hat{R}_\phi(\alpha)$, where $\alpha = \omega_1 t_p$ is the *flip angle*:

$$\begin{aligned} \hat{R}_\phi(\alpha) &= \exp(-i\alpha \hat{R}_z(\phi) \hat{I}_x \hat{R}_z(\phi)^{-1}) \\ &= \hat{R}_z(\phi) \hat{R}_x(\alpha) \hat{R}_z(\phi)^{-1}. \end{aligned}$$

The resulting transformation is described by Equation 1.19. For example, an x -pulse transforms \hat{I}_z according to the following rule:

$$\hat{I}_z \xrightarrow{\alpha \hat{I}_x} \cos \alpha \hat{I}_z - \sin \alpha \hat{I}_y.$$

1.5.2 Single-element basis operators

Each Cartesian basis operator contains contributions from more than one element of the density matrix: for example, in the case of an N -spin system, 2^N elements contribute. This can be useful as the complexity of the calculation does not increase greatly as N increases. However, it is sometimes useful to employ a basis in which each operator represents only a single element; such operators are referred to as *single-element basis operators*.

Coherence order and single-element operators

If the density matrix is written in the eigenbasis of the Zeeman Hamiltonian, we can define a coherence order p of an element σ_{ij} as

$$p = M_i - M_j,$$

where M_i is the magnetic quantum number of the state $|i\rangle$.

For a one-spin system, the elements of the density matrix of a one-spin system have the following coherence orders, which are indicated by the superscript of each element:

$$\sigma = \begin{array}{cc} |\alpha\rangle & |\beta\rangle \\ \begin{matrix} |\alpha\rangle \\ |\beta\rangle \end{matrix} & \left(\begin{array}{cc} \sigma_{11}^{(0)} & \sigma_{12}^{(+1)} \\ \sigma_{21}^{(-1)} & \sigma_{22}^{(0)} \end{array} \right) \end{array}.$$

Therefore, the single-element operators each have a single coherence order. The basis comprises the polarization operators, and the raising and lowering operators: $\{\hat{I}_\alpha, \hat{I}_\beta, \hat{I}_+, \hat{I}_-\}$. \hat{I}_+ and \hat{I}_- have coherence order +1 and -1 respectively, while \hat{I}_α and \hat{I}_β have coherence order zero, and represent the populations of the $|\alpha\rangle$ and $|\beta\rangle$ states.

The explicit expansion of $\hat{\sigma}$ is

$$\hat{\sigma} = b_\alpha \hat{I}_\alpha + b_\beta \hat{I}_\beta + b_+ \hat{I}_+ + b_- \hat{I}_-.$$

The x -magnetization is given by

$$\begin{aligned} M_x &= \gamma N \text{Tr}(\hat{I}_x \hat{\sigma}) \\ &= \gamma N \text{Tr}\left(\frac{1}{2}(\hat{I}_+ + \hat{I}_-) \hat{\sigma}\right) \\ &= \frac{1}{2}\gamma N b_\alpha \text{Tr}(\hat{I}_+ \hat{I}_\alpha) + \frac{1}{2}\gamma N b_\beta \text{Tr}(\hat{I}_+ \hat{I}_\beta) + \frac{1}{2}\gamma N b_+ \text{Tr}(\hat{I}_+ \hat{I}_+) + \frac{1}{2}\gamma N b_- \text{Tr}(\hat{I}_+ \hat{I}_-) \\ &\quad + \frac{1}{2}\gamma N b_\alpha \text{Tr}(\hat{I}_- \hat{I}_\alpha) + \frac{1}{2}\gamma N b_\beta \text{Tr}(\hat{I}_- \hat{I}_\beta) + \frac{1}{2}\gamma N b_+ \text{Tr}(\hat{I}_- \hat{I}_+) + \frac{1}{2}\gamma N b_- \text{Tr}(\hat{I}_- \hat{I}_-) \\ &= \frac{1}{2}\gamma N b_- + \frac{1}{2}\gamma N b_+, \end{aligned}$$

where we have made use of the fact that the basis operators are orthogonal to each other, and so the only non-zero traces are of the products $\hat{I}_+ \hat{I}_-$ and $\hat{I}_- \hat{I}_+$. It can be seen that the expression for M_x contains an equal mixture of the coefficients of the \hat{I}_+ and \hat{I}_- operators. Likewise, the y -magnetization is given by

$$M_y = -\frac{1}{2}i\gamma N b_- + \frac{1}{2}i\gamma N b_+.$$

Conventionally, these two components of the transverse magnetization are combined to form the complex magnetization $M_+ = M_x + iM_y$; this procedure is referred to as *quadrature detection*. The complex magnetization is therefore given by

$$M_+ = \gamma N b_-;$$

that is it depends only on the coefficient for the operator \hat{I}_- . Using quadrature detection, the only part of the density matrix that contributes to the observable magnetization has coherence order -1 . This result can be found more directly by calculating $M_+ = \gamma N \text{Tr}(\hat{I}_+ \hat{\sigma})$.

Free precession

The free-precession Hamiltonian is diagonal in the Zeeman basis, and so the single-element operators simply acquire a phase during free precession, which is given by Equation 1.11. The operator \hat{I}_+ evolves to acquire a phase of $-\Omega t$:

$$\hat{I}_+ \xrightarrow{\hat{\mathcal{H}}_{\text{free}} t} \hat{I}_+ \exp(i(E_\beta - E_\alpha)t) = \hat{I}_+ \exp(-i\Omega t).$$

\hat{I}_- acquires a phase $+\Omega t$, and the polarization operators are unaffected:

$$\hat{I}_- \xrightarrow{\hat{\mathcal{H}}_{\text{free}}t} \hat{I}_- \exp(i\Omega t),$$

$$\hat{I}_\alpha \xrightarrow{\hat{\mathcal{H}}_{\text{free}}t} \hat{I}_\alpha,$$

$$\hat{I}_\beta \xrightarrow{\hat{\mathcal{H}}_{\text{free}}t} \hat{I}_\beta.$$

Radiofrequency pulses

The effect of RF pulses on the single-element operators can be calculated using the pulse propagator $\hat{R}_\phi(\alpha)$. For example, \hat{I}_+ is transformed into:

$$\begin{aligned} & \left(\hat{R}_z(\phi) \hat{R}_x(\alpha) \hat{R}_z(\phi)^{-1} \right) \hat{I}_+ \left(\hat{R}_z(\phi) \hat{R}_x(\alpha) \hat{R}_z(\phi)^{-1} \right)^{-1} \\ &= \begin{pmatrix} \cos \frac{1}{2}\alpha & -ie^{-i\phi} \sin \frac{1}{2}\alpha \\ -ie^{i\phi} \sin \frac{1}{2}\alpha & \cos \frac{1}{2}\alpha \end{pmatrix} \begin{pmatrix} 0 & 1 \\ 0 & 0 \end{pmatrix} \begin{pmatrix} \cos \frac{1}{2}\alpha & ie^{-i\phi} \sin \frac{1}{2}\alpha \\ ie^{i\phi} \sin \frac{1}{2}\alpha & \cos \frac{1}{2}\alpha \end{pmatrix} \\ &= \begin{pmatrix} \frac{1}{2}ie^{i\phi} \sin \alpha & \cos^2 \frac{1}{2}\alpha \\ e^{2i\phi} \sin^2 \frac{1}{2}\alpha & -\frac{1}{2}ie^{i\phi} \sin \alpha \end{pmatrix} \\ &= \hat{I}_+ \cos^2 \frac{1}{2}\alpha + \hat{I}_- e^{2i\phi} \sin^2 \frac{1}{2}\alpha + \frac{1}{2}ie^{i\phi} \sin \alpha (\hat{I}_\alpha - \hat{I}_\beta). \end{aligned}$$

This calculation can be repeated for all the operators to give the following set of transformations:

$$\hat{I}_+ \xrightarrow{\alpha \hat{I}_\phi} \hat{I}_+ \cos^2 \frac{1}{2}\alpha + \hat{I}_- e^{2i\phi} \sin^2 \frac{1}{2}\alpha + \frac{1}{2}ie^{i\phi} \sin \alpha (\hat{I}_\alpha - \hat{I}_\beta), \quad (1.20)$$

$$\hat{I}_- \xrightarrow{\alpha \hat{I}_\phi} \hat{I}_- \cos^2 \frac{1}{2}\alpha + \hat{I}_+ e^{-2i\phi} \sin^2 \frac{1}{2}\alpha - \frac{1}{2}ie^{-i\phi} \sin \alpha (\hat{I}_\alpha - \hat{I}_\beta), \quad (1.21)$$

$$\hat{I}_\alpha \xrightarrow{\alpha \hat{I}_\phi} \hat{I}_\alpha \cos^2 \frac{1}{2}\alpha + \hat{I}_\beta \sin^2 \frac{1}{2}\alpha + \frac{1}{2}i \sin \alpha (e^{-i\phi} \hat{I}_+ - e^{i\phi} \hat{I}_-), \quad (1.22)$$

$$\hat{I}_\beta \xrightarrow{\alpha \hat{I}_\phi} \hat{I}_\beta \cos^2 \frac{1}{2}\alpha + \hat{I}_\alpha \sin^2 \frac{1}{2}\alpha - \frac{1}{2}i \sin \alpha (e^{-i\phi} \hat{I}_+ - e^{i\phi} \hat{I}_-). \quad (1.23)$$

For an x -pulse, these relations become:

$$\begin{aligned}\hat{I}_+ &\xrightarrow{\alpha\hat{I}_x} \hat{I}_+ \cos^2 \frac{1}{2}\alpha + \hat{I}_- \sin^2 \frac{1}{2}\alpha + \frac{1}{2}i \sin \alpha (\hat{I}_\alpha - \hat{I}_\beta), \\ \hat{I}_- &\xrightarrow{\alpha\hat{I}_x} \hat{I}_- \cos^2 \frac{1}{2}\alpha + \hat{I}_+ \sin^2 \frac{1}{2}\alpha - \frac{1}{2}i \sin \alpha (\hat{I}_\alpha - \hat{I}_\beta), \\ \hat{I}_\alpha &\xrightarrow{\alpha\hat{I}_x} \hat{I}_\alpha \cos^2 \frac{1}{2}\alpha + \hat{I}_\beta \sin^2 \frac{1}{2}\alpha + \frac{1}{2}i \sin \alpha (\hat{I}_+ - \hat{I}_-), \\ \hat{I}_\beta &\xrightarrow{\alpha\hat{I}_x} \hat{I}_\beta \cos^2 \frac{1}{2}\alpha + \hat{I}_\alpha \sin^2 \frac{1}{2}\alpha - \frac{1}{2}i \sin \alpha (\hat{I}_+ - \hat{I}_-).\end{aligned}$$

1.6 Relaxation

Equation 1.11 predicts that once the density operator has been perturbed into a non-equilibrium state, the off-diagonal elements will continue to evolve indefinitely. However, this is not the case as the system will eventually return to its equilibrium configuration via a process known as relaxation.

Relaxation is caused by the random variation of the local magnetic fields experienced by the nuclear spins. These fields originate from a number of sources which involve the orientation-dependent interactions of the spin with neighbouring nuclei, and the surrounding electrons; the fluctuations are caused by molecular tumbling. The work described in this dissertation does not require a detailed theoretical account of relaxation, and so a phenomenological description will suffice. There are two relaxation processes for an ensemble of non-interacting spins- $\frac{1}{2}$, both of which follow first-order kinetics.

The first of these is *transverse relaxation*, which causes the off-diagonal elements of the density operator, and hence the transverse magnetization, to decay to zero. The off-diagonal elements are multiplied by an assumed exponential decay, which is characterized by a time constant T_2 . For example, the transverse magnetization decays according to

$$\begin{aligned}M_x(t) &= M_x(0) \exp(-t/T_2) \\ M_y(t) &= M_y(0) \exp(-t/T_2).\end{aligned}$$

The second process is *longitudinal relaxation*, which is responsible for returning the populations of the spin states to their equilibrium values as given by the Boltzmann distribution. This process is assumed to be exponential and is characterized by a time

constant T_1 . It causes the z -magnetization to relax according to

$$M_z(t) = (M_z(0) - M_0) \exp(-t/T_1) + M_0. \quad (1.24)$$

1.7 The Hamiltonian for a two-spin system

The basis functions for a two-spin system are found by taking the direct product of two one-spin bases:

$$\{|\alpha_1\rangle, |\beta_1\rangle\} \otimes \{|\alpha_2\rangle, |\beta_2\rangle\} = \{|\alpha_1\alpha_2\rangle, |\alpha_1\beta_2\rangle, |\beta_1\alpha_2\rangle, |\beta_1\beta_2\rangle\},$$

where the subscript denotes the spin label. For brevity, the subscripts are omitted and the new *product basis* is written as $\{|\alpha\alpha\rangle, |\alpha\beta\rangle, |\beta\alpha\rangle, |\beta\beta\rangle\}$. This is the eigenbasis of the Zeeman Hamiltonian for two non-interacting spins:

$$\hat{\mathcal{H}}_{z,2\text{spins}} = \omega_0^{(1)} \hat{I}_{1z} + \omega_0^{(2)} \hat{I}_{2z},$$

which describes the interaction of the two spins with the external field B_0 . The operator \hat{I}_{ia} represents the component of the spin i angular momentum about axis a , and $\omega_0^{(i)}$ is the Larmor frequency of spin i . In this basis the density operator takes the following form:

$$\sigma = \begin{pmatrix} & |\alpha\alpha\rangle & |\alpha\beta\rangle & |\beta\alpha\rangle & |\beta\beta\rangle \\ |\alpha\alpha\rangle & \left(\begin{array}{cccc} \sigma_{11}^{(0)} & \sigma_{12}^{(+1)} & \sigma_{13}^{(+1)} & \sigma_{14}^{(+2)} \\ \sigma_{21}^{(-1)} & \sigma_{22}^{(0)} & \sigma_{23}^{(0)} & \sigma_{24}^{(+1)} \\ \sigma_{31}^{(-1)} & \sigma_{32}^{(0)} & \sigma_{33}^{(0)} & \sigma_{34}^{(+1)} \\ \sigma_{41}^{(-2)} & \sigma_{42}^{(-1)} & \sigma_{43}^{(-1)} & \sigma_{44}^{(0)} \end{array} \right) & , \end{pmatrix}$$

where the superscripts give the coherence order of each element.

1.7.1 The free-precession Hamiltonian

The free-precession Hamiltonian for a two-spin system is

$$\hat{\mathcal{H}}_{\text{free}} = \Omega_1 \hat{I}_{1z} + \Omega_2 \hat{I}_{2z} + 2\pi J_{12} \hat{\mathbf{I}}_1 \cdot \hat{\mathbf{I}}_2,$$

where $\hat{\mathbf{I}}_i$ is the total spin angular momentum operator for spin i , and Ω_i is the offset of spin i . The first two terms are due to the interaction of each spin with the reduced field

ΔB , i.e. they represent the Zeeman interaction in the rotating frame. The third term arises as the two spins interact with each other in a process that is referred to as scalar coupling or J -coupling; the coupling constant J_{12} (in Hz) is a measure of the strength of the interaction.

The matrix representation of $\hat{\mathcal{H}}_{\text{free}}$ in the product basis is

$$\hat{\mathcal{H}}_{\text{free}} = \frac{1}{2} \begin{pmatrix} \Omega_1 + \Omega_2 + \pi J_{12} & 0 & 0 & 0 \\ 0 & \Omega_1 - \Omega_2 - \pi J_{12} & 2\pi J_{12} & 0 \\ 0 & 2\pi J_{12} & -\Omega_1 + \Omega_2 - \pi J_{12} & 0 \\ 0 & 0 & 0 & -\Omega_1 - \Omega_2 + \pi J_{12} \end{pmatrix}.$$

$\hat{\mathcal{H}}_{\text{free}}$ is *not* diagonal in the product basis, and so it is no longer true that each element of $\hat{\sigma}$ simply acquires a phase during free precession. In order to continue, it is necessary to do one of two things: either make an approximation so that $\hat{\mathcal{H}}_{\text{free}}$ is diagonal in this basis, or find an alternative basis in which $\hat{\mathcal{H}}_{\text{free}}$ is diagonal.

1.7.2 The weak coupling approximation

The non-zero off-diagonal elements of $\hat{\mathcal{H}}_{\text{free}}$ are due to the $\hat{I}_{1x}\hat{I}_{2x}$ and $\hat{I}_{1y}\hat{I}_{2y}$ parts of the coupling term. If these parts are removed, then $\hat{\mathcal{H}}_{\text{free}}$ will become diagonal. This can be achieved by using the secular approximation, which states that an off-diagonal element can be set to zero provided it is much less than the difference between the two diagonal elements it connects. In this case, the condition which has to be satisfied is $|\Omega_1 - \Omega_2| \gg |\pi J_{12}|$, i.e. that the difference between the Larmor frequencies is much greater than the value of the coupling constant. This is the *weak coupling approximation*. Using this, the matrix $\mathcal{H}_{\text{free}}^{\text{WC}}$ is now diagonal:

$$\mathcal{H}_{\text{free}}^{\text{WC}} = \frac{1}{2} \begin{pmatrix} \Omega_1 + \Omega_2 + \pi J_{12} & 0 & 0 & 0 \\ 0 & \Omega_1 - \Omega_2 - \pi J_{12} & 0 & 0 \\ 0 & 0 & -\Omega_1 + \Omega_2 - \pi J_{12} & 0 \\ 0 & 0 & 0 & -\Omega_1 - \Omega_2 + \pi J_{12} \end{pmatrix}.$$

This corresponds to the matrix representation of the truncated Hamiltonian $\hat{\mathcal{H}}_{\text{free}}^{\text{WC}}$ which is given by

$$\hat{\mathcal{H}}_{\text{free}}^{\text{WC}} = \Omega_1 \hat{I}_{1z} + \Omega_2 \hat{I}_{2z} + 2\pi J_{12} \hat{I}_{1z} \hat{I}_{2z}.$$

The rotation operator for a two-spin system is given by the direct product of two one-spin rotation operators. For example, $\hat{R}_x(\alpha)$ is given by

$$\hat{R}_x(\alpha) = \exp(-i\alpha \hat{I}_{1x}) \otimes \exp(-i\alpha \hat{I}_{2x}).$$

The matrix representation is calculated using the one-spin rotation matrices in Equation A.5:

$$\hat{R}_x(\alpha) = \begin{pmatrix} c^2 & -ics & -ics & -s^2 \\ -ics & c^2 & -s^2 & -ics \\ -ics & -s^2 & c^2 & -ics \\ -s^2 & -ics & -ics & c^2 \end{pmatrix},$$

where $c = \cos \frac{1}{2}\alpha$ and $s = \sin \frac{1}{2}\alpha$.

The use of the weak coupling approximation allows calculations to be simplified using the Cartesian and single-element basis operators in the same way as for a one-spin system. These *product operators* are described in Section 1.8. This approximation is always valid for heteronuclear spin pairs, as the Larmor frequencies are separated by hundreds of MHz, whereas the coupling constant is at most a few hundred Hz. However, this condition may not be met for homonuclear spin pairs. In such cases, it is necessary to employ the full form of the Hamiltonian. How this is done is described in Section 1.9.

1.8 Product operators

In the weak-coupling approximation, the basis operators for a two-spin system are found by taking all possible products of the spin-one operators with the spin-two operators [5].

Table 1.1: The Cartesian product operators for a weakly coupled two-spin system.

description	operators
identity	$\frac{1}{2}\hat{E}$
z -magnetization	$\hat{I}_{1z}, \hat{I}_{2z}$
longitudinal two-spin order	$2\hat{I}_{1z}\hat{I}_{2z}$
single quantum, in phase	$\hat{I}_{1x}, \hat{I}_{1y}, \hat{I}_{2x}, \hat{I}_{2y}$
single quantum, anti phase	$2\hat{I}_{1x}\hat{I}_{2z}, 2\hat{I}_{1y}\hat{I}_{2z}, 2\hat{I}_{1z}\hat{I}_{2x}, 2\hat{I}_{1z}\hat{I}_{2y}$
multiple quantum	$2\hat{I}_{1x}\hat{I}_{2x}, 2\hat{I}_{1x}\hat{I}_{2y}, 2\hat{I}_{1y}\hat{I}_{2x}, 2\hat{I}_{1y}\hat{I}_{2y}$

1.8.1 Cartesian operators

The full set of Cartesian product operators for two spins is given by[‡]

$$2 \times \left\{ \frac{1}{2}\hat{E}_1, \hat{I}_{1x}, \hat{I}_{1y}, \hat{I}_{1z} \right\} \otimes \left\{ \frac{1}{2}\hat{E}_2, \hat{I}_{2x}, \hat{I}_{2y}, \hat{I}_{2z} \right\}.$$

In writing these operators the direct product is usually omitted, along with the \hat{E}_i , to give the full set of sixteen product operators in Table 1.1. The operator $\frac{1}{2}\hat{E}$ can be ignored since, as before, it does not produce any observable magnetization. \hat{I}_{iz} represents the z -magnetization of spin i . \hat{I}_{ix} and \hat{I}_{iy} represent the ‘in-phase’ x - and y -magnetization on spin i , and are the only observable terms in the expansion. $2\hat{I}_{ix}\hat{I}_{jz}$ and $2\hat{I}_{iy}\hat{I}_{jz}$ represent ‘anti-phase’ magnetization which is not directly observable; however, anti phase operators evolve into the observable in phase operators during free precession. The terms ‘in phase’ and ‘anti phase’ will be explained in Section 1.8.2. The operators $2\hat{I}_{ix}\hat{I}_{jx}$, $2\hat{I}_{ix}\hat{I}_{jy}$, and $2\hat{I}_{iy}\hat{I}_{jy}$ each represent an equal mixture of zero and double-quantum coherence and are not observable, and $2\hat{I}_{iz}\hat{I}_{jz}$ is a form of non-equilibrium z -magnetization that is referred to as longitudinal two-spin order.

Double- and zero-quantum coherence

Sometimes we wish to select pure double-quantum (DQ) or zero-quantum (ZQ) coherence rather than the mixture represented by operators such as $2\hat{I}_{1x}\hat{I}_{2x}$. It therefore proves useful to define the operators $\hat{D}Q_x$ and $\hat{D}Q_y$ which represent pure DQ

[‡]The factor of 2 is for normalization purposes. The normalization constant K in Equation 1.18 is 2^{N-2} for Cartesian operators, and 1 (regardless of the value of N) for single-element operators.

coherence, and \hat{ZQ}_x and \hat{ZQ}_y which represent pure ZQ coherence. They are given by

$$\begin{aligned}\hat{DQ}_x &\equiv 2\hat{I}_{1x}\hat{I}_{2x} - 2\hat{I}_{1y}\hat{I}_{2y} \\ \hat{DQ}_y &\equiv 2\hat{I}_{1x}\hat{I}_{2y} + 2\hat{I}_{1y}\hat{I}_{2x} \\ \hat{ZQ}_x &\equiv 2\hat{I}_{1x}\hat{I}_{2x} + 2\hat{I}_{1y}\hat{I}_{2y} \\ \hat{ZQ}_y &\equiv 2\hat{I}_{1y}\hat{I}_{2x} - 2\hat{I}_{1x}\hat{I}_{2y}.\end{aligned}$$

Using these definitions it is easy to see that, for example, $2\hat{I}_{1x}\hat{I}_{2x}$ is an equal mixture of DQ and ZQ coherence:

$$2\hat{I}_{1x}\hat{I}_{2x} = \frac{1}{2}(\hat{DQ}_x + \hat{ZQ}_x).$$

Free precession

The three terms in $\hat{\mathcal{H}}_{\text{free}}^{\text{WC}}$ commute with each other, and so the effect of each on the product operators can be calculated sequentially. Evolution due to the offsets of both spins can be calculated exactly as for a one-spin system, and evolution under the J -coupling causes a transformation similar to Equation 1.19. For example, \hat{I}_{1x} transforms as follows:

$$\hat{I}_{1x} \xrightarrow{2\pi J_{12}\hat{I}_{1z}\hat{I}_{2z}t} \hat{I}_{1x} \cos(\pi J_{12}t) + 2\hat{I}_{1y}\hat{I}_{2z} \sin(\pi J_{12}t).$$

The DQ and ZQ coherence operators evolve to give simple transformations. For example, \hat{DQ}_x and \hat{ZQ}_x are rotated into \hat{DQ}_y and \hat{ZQ}_y respectively [6]:

$$\begin{aligned}\hat{DQ}_x &\xrightarrow{\hat{\mathcal{H}}_{\text{free},\text{WC}}t} \hat{DQ}_x \cos(\Omega_1 + \Omega_2)t + \hat{DQ}_y \sin(\Omega_1 + \Omega_2)t \\ \hat{ZQ}_x &\xrightarrow{\hat{\mathcal{H}}_{\text{free},\text{WC}}t} \hat{ZQ}_x \cos(\Omega_1 - \Omega_2)t + \hat{ZQ}_y \sin(\Omega_1 - \Omega_2)t.\end{aligned}$$

Double-quantum coherence evolves at the DQ frequency $\Omega_1 + \Omega_2$, and ZQ coherence evolves at the ZQ frequency $\Omega_1 - \Omega_2$.

Radiofrequency pulses

The Hamiltonian for a hard x -pulse is

$$\hat{\mathcal{H}}_{\text{hard},x} = \omega_1 \hat{F}_x,$$

where $\hat{F}_x = \hat{I}_{1x} + \hat{I}_{2x}$. The two terms commute, and so the effect of the pulse on each spin can be computed sequentially.

Table 1.2: The single-element product operators for a weakly coupled two-spin system.

coherence order, p	operators
z	$\hat{I}_{1\alpha}\hat{I}_{2\alpha}, \hat{I}_{1\alpha}\hat{I}_{2\beta}, \hat{I}_{1\beta}\hat{I}_{2\alpha}, \hat{I}_{1\beta}\hat{I}_{2\beta}$
0	$\hat{I}_{1+}\hat{I}_{2-}, \hat{I}_{1-}\hat{I}_{2+}$
-1	$\hat{I}_{1-}\hat{I}_{2\alpha}, \hat{I}_{1-}\hat{I}_{2\beta}, \hat{I}_{1\alpha}\hat{I}_{2-}, \hat{I}_{1\beta}\hat{I}_{2-}$
+1	$\hat{I}_{1+}\hat{I}_{2\alpha}, \hat{I}_{1+}\hat{I}_{2\beta}, \hat{I}_{1\alpha}\hat{I}_{2+}, \hat{I}_{1\beta}\hat{I}_{2+}$
-2	$\hat{I}_{1-}\hat{I}_{2-}$
+2	$\hat{I}_{1+}\hat{I}_{2+}$

1.8.2 Single-element basis operators

The entire set of single-element product operators is given by the direct product of the one-spin single-element operators. The sixteen operators are given in Table 1.2. Each represents a single element of the density matrix, and so can be assigned a single coherence order. It is possible to assign a very simple interpretation to each operator, as the two spins can be treated independently. For example, $\hat{I}_{1-}\hat{I}_{2\beta}$ represents a -1 coherence on spin one, in which spin two is present in the $|\beta\rangle$ state, and $\hat{I}_{1\beta}\hat{I}_{2\alpha}$ represents the population of the level $|\beta\alpha\rangle$, i.e. when spin one is in the $|\beta\rangle$ state and spin two is in the $|\alpha\rangle$ state.

Free precession

The Hamiltonian $\hat{\mathcal{H}}_{\text{free}}^{\text{WC}}$ is diagonal, and so each operator acquires a phase during a period of free precession. For example, $\hat{I}_{1-}\hat{I}_{2\beta}$ represents the element σ_{42} , and evolves at the frequency $E_2 - E_4$ to give

$$\hat{I}_{1-}\hat{I}_{2\beta} \xrightarrow{\hat{\mathcal{H}}_{\text{free,WC}} t} \hat{I}_{1-}\hat{I}_{2\beta} \exp(i(\Omega_1 - \pi J_{12})t).$$

Relationship to Cartesian operators

In Section 1.8.1 the Cartesian product operators were defined according to the type of coherence they represent. These properties can be properly understood by writing them in terms of the single-element operators.

For example, the operator \hat{I}_{1x} is given by

$$\hat{I}_{1x}\hat{E}_2 = \frac{1}{2}(\hat{I}_{1+}\hat{I}_{2\alpha} + \hat{I}_{1+}\hat{I}_{2\beta}) + \frac{1}{2}(\hat{I}_{1-}\hat{I}_{2\alpha} + \hat{I}_{1-}\hat{I}_{2\beta}).$$

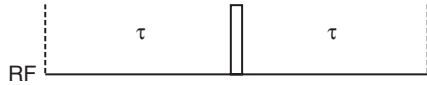


Figure 1.2: The pulse sequence for the spin echo.

The first two terms have coherence order +1, and the last two have coherence order -1. The two observable terms, with coherence order -1, have intensities of the same sign, and are described as being in phase. By contrast, the operator $2\hat{I}_{1x}\hat{I}_{2z}$ can be expanded as

$$2\hat{I}_{1x}\hat{I}_{2z} = \frac{1}{2}(\hat{I}_{1+}\hat{I}_{2\alpha} - \hat{I}_{1+}\hat{I}_{2\beta}) + \frac{1}{2}(\hat{I}_{1-}\hat{I}_{2\alpha} - \hat{I}_{1-}\hat{I}_{2\beta}).$$

In this case, the two observable terms have opposite signs, and so are referred to as being in anti phase.

The multiple-quantum operator $2\hat{I}_{1x}\hat{I}_{2x}$ can also be shown to contain DQ and ZQ coherences in equal amounts. It is expanded as

$$2\hat{I}_{1x}\hat{I}_{2x} = \frac{1}{2}(\hat{I}_{1+}\hat{I}_{2+} + \hat{I}_{1-}\hat{I}_{2-}) + \frac{1}{2}(\hat{I}_{1+}\hat{I}_{2-} + \hat{I}_{1-}\hat{I}_{2+}).$$

The first two terms have coherence orders +2 and -2, and so represent pure DQ coherence, whereas the last two terms have coherence order zero. Furthermore, it is possible to show that the DQ and ZQ operators defined in Section 1.8.1 represent pure DQ and ZQ coherence. In terms of the single-element operators, they are given by

$$\begin{aligned}\hat{DQ}_x &= \hat{I}_{1+}\hat{I}_{2+} + \hat{I}_{1-}\hat{I}_{2-} \\ \hat{DQ}_y &= -i\hat{I}_{1+}\hat{I}_{2+} + i\hat{I}_{1-}\hat{I}_{2-} \\ \hat{ZQ}_x &= \hat{I}_{1+}\hat{I}_{2-} + \hat{I}_{1-}\hat{I}_{2+} \\ \hat{ZQ}_y &= -i\hat{I}_{1+}\hat{I}_{2-} + i\hat{I}_{1-}\hat{I}_{2+}.\end{aligned}$$

1.8.3 The spin echo

The pulse sequence for the homonuclear spin echo experiment is shown in Figure 1.2 [7]. It consists of a 180° pulse that is sandwiched by two delays of equal duration τ . The sequence is an important building block for many experiments as the state of the system at the end of the sequence is independent of the offset, but not the coupling. This can be seen for a two-spin system by considering the effect of the sequence on

the operator $\hat{I}_{1+}\hat{I}_{2\alpha}$, which represents +1 coherence on spin one with spin two in the $|\alpha\rangle$ state.

The operator acquires a phase during the first delay to give

$$\hat{I}_{1+}\hat{I}_{2\alpha} \exp(-i(\Omega_1 + \pi J_{12})\tau).$$

The effect of the 180° pulse is calculated from Equations 1.20–1.23 in which $\alpha = \pi$ and $\phi = 0$. The operator \hat{I}_{1+} is transformed into \hat{I}_{1-} , and $\hat{I}_{2\alpha}$ becomes $\hat{I}_{2\beta}$ giving

$$\hat{I}_{1-}\hat{I}_{2\beta} \exp(-i(\Omega_1 + \pi J_{12})\tau);$$

the sign of the coherence order is changed to -1 , and the polarization of spin two is inverted from $|\alpha\rangle$ to $|\beta\rangle$. Evolution during the second delay gives

$$\hat{I}_{1-}\hat{I}_{2\beta} \exp(-i(\Omega_1 + \pi J_{12})\tau) \exp(i(\Omega_1 - \pi J_{12})\tau) = \hat{I}_{1-}\hat{I}_{2\beta} \exp(-2i\pi J_{12}\tau).$$

The final phase is independent of Ω_1 , and so we say that the offset has been refocused. This is a consequence of the change in the sign of the spin-one coherence order from +1 to -1 by the 180° pulse. The coupling, however, evolves throughout the sequence; this is due to the additional change in the polarization of the passive spin.

1.9 Strong coupling

In the case of homonuclear spin systems there will be situations where the condition $|\Omega_1 - \Omega_2| \gg |\pi J_{12}|$ is not valid, even at high field. In such cases it is necessary to use the full J -coupling Hamiltonian, and a full density matrix calculation must be carried out, in contrast to the simple product operator calculations of Section 1.8.

To calculate the effect of free precession under this Hamiltonian, we need to diagonalize the Hamiltonian by applying a rotation of the form

$$\hat{\mathcal{H}}_{\text{free}}^{\text{SC}} = \hat{U}\hat{\mathcal{H}}_{\text{free}}\hat{U}^{-1},$$

where $\hat{\mathcal{H}}_{\text{free}}^{\text{SC}}$ is the Hamiltonian in the new basis. The new basis functions will be given by

$$\hat{U} \begin{pmatrix} |\alpha\alpha\rangle \\ |\alpha\beta\rangle \\ |\beta\alpha\rangle \\ |\beta\beta\rangle \end{pmatrix}.$$

Since $\hat{\mathcal{H}}_{\text{free}}$ is diagonal save for the central 2×2 block, it follows that U will have the form

$$U = \begin{pmatrix} 1 & 0 & 0 & 0 \\ 0 & \cos \theta & \sin \theta & 0 \\ 0 & -\sin \theta & \cos \theta & 0 \\ 0 & 0 & 0 & 1 \end{pmatrix}. \quad (1.25)$$

We only need to diagonalize the central block, and the transformation gives us

$$\begin{aligned} & \begin{pmatrix} \cos \theta & \sin \theta \\ -\sin \theta & \cos \theta \end{pmatrix} \begin{pmatrix} \Delta - k & 2k \\ 2k & -\Delta - k \end{pmatrix} \begin{pmatrix} \cos \theta & -\sin \theta \\ \sin \theta & \cos \theta \end{pmatrix} \\ &= \begin{pmatrix} \Delta \cos 2\theta + k(2 \sin 2\theta - 1) & 2k \cos 2\theta - \Delta \sin 2\theta \\ 2k \cos 2\theta - \Delta \sin 2\theta & -\Delta \cos 2\theta - k(2 \sin 2\theta + 1) \end{pmatrix}, \end{aligned}$$

where $\Delta = \frac{1}{2}(\Omega_1 - \Omega_2)$ and $k = \frac{1}{2}\pi J_{12}$. The off-diagonal elements will be zero provided θ is given by:

$$\tan 2\theta = \frac{2k}{\Delta} = \frac{2\pi J_{12}}{\Omega_1 - \Omega_2}.$$

The diagonal elements can now be calculated, which gives the following matrix representation of $\hat{\mathcal{H}}_{\text{free}}^{\text{SC}}$:

$$\mathcal{H}_{\text{free}}^{\text{SC}} = \frac{1}{2} \begin{pmatrix} \Omega_1 + \Omega_2 + \pi J_{12} & 0 & 0 & 0 \\ 0 & C - \pi J_{12} & 0 & 0 \\ 0 & 0 & -C - \pi J_{12} & 0 \\ 0 & 0 & 0 & -\Omega_1 - \Omega_2 + \pi J_{12} \end{pmatrix},$$

where

$$C = \sqrt{(\Omega_1 - \Omega_2)^2 + (2\pi J_{12})^2}.$$

The new basis is given by

$$\{|aa\rangle, \cos \theta |a\beta\rangle + \sin \theta |\beta\alpha\rangle, -\sin \theta |a\beta\rangle + \cos \theta |\beta\alpha\rangle, |\beta\beta\rangle\}.$$

To calculate the form of the NMR spectrum, all the relevant operators must be transformed into this basis. The rotation operator for an x -pulse is therefore given by

$$R_x^{\text{SC}}(\alpha) = UR_x(\alpha)U^{-1}$$

$$= \begin{pmatrix} c^2 & -icsu & -icsv & -s^2 \\ -icsu & 1 - s^2 u^2 & -s^2 uv & -icsu \\ -icsv & -s^2 uv & 1 - s^2 v^2 & -icsv \\ -s^2 & -icsu & -icsv & c^2 \end{pmatrix},$$

where $u = \cos\theta + \sin\theta$ and $v = \cos\theta - \sin\theta$. The matrix representation of the observable \hat{F}_+ is transformed in the same way to give

$$F_+^{\text{SC}} = UF_+U^{-1}$$

$$= \begin{pmatrix} 0 & u & v & 0 \\ 0 & 0 & 0 & u \\ 0 & 0 & 0 & v \\ 0 & 0 & 0 & 0 \end{pmatrix}.$$

1.9.1 Single-element basis operators

It is possible to construct a set of single-element operators in the strong coupling basis. It should be emphasized that they are *not* products of the one-spin operators, as the two spins can no longer be treated independently. In the notation of Thripplleton *et al.* [8], the single-element operators representing the four -1 coherences are

$$\left\{ \hat{I}_{1-}\hat{I}_{2\alpha} \right\} \quad \left\{ \hat{I}_{1-}\hat{I}_{2\beta} \right\} \quad \left\{ \hat{I}_{1\alpha}\hat{I}_{2-} \right\} \quad \left\{ \hat{I}_{1\beta}\hat{I}_{2-} \right\}.$$

The notation represents the relationship of these operators to the product operators in the weak coupling basis, while the difference is acknowledged by the use of braces. For example, $\left\{ \hat{I}_{1-}\hat{I}_{2\beta} \right\} \rightarrow \hat{I}_{1-}\hat{I}_{2\beta}$ as we move to the weak coupling approximation.

Each element of $\hat{\sigma}$ which represents single-quantum coherence can no longer be described as a coherence that is solely present on one spin. However, for a modest degree of strong coupling we can view, for example, the operator $\left\{ \hat{I}_{1-}\hat{I}_{2\beta} \right\}$ as representing a coherence that is *mainly* present on spin one.

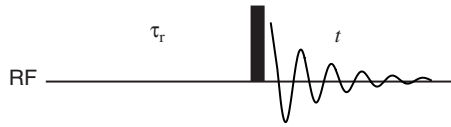


Figure 1.3: The pulse sequence for the pulse–acquire experiment. The 90° pulse is represented by a filled rectangle.

1.10 The pulse–acquire experiment

The simplest NMR experiment is the pulse–acquire sequence, which is shown in Figure 1.3. It comprises three parts: a delay τ_r to allow the system to relax back to its equilibrium configuration, a 90° pulse which rotates the z -magnetization to the transverse plane, and a detection period t during which the signal is acquired. In this Section, we will derive the form of the observable signal for a one-spin system, a two-spin system using the weak-coupling approximation, and a two-spin system taking account of strong coupling. The form of the spectrum will be calculated using the *Fourier transform*.

1.10.1 The spectrum of a one-spin system

The equilibrium density operator is unchanged by the transformation into the rotating frame, and is given by Equation 1.13: $\hat{\sigma}_0 = \hat{I}_z$. The 90° pulse rotates this operator onto the $-y$ axis:

$$\hat{I}_z \xrightarrow{(\pi/2)\hat{I}_x} -\hat{I}_y.$$

During the detection period, $-\hat{I}_y$ evolves under the offset to give

$$-\hat{I}_y \xrightarrow{\Omega t \hat{I}_z} -\hat{I}_y \cos(\Omega t) + \hat{I}_x \sin(\Omega t).$$

This is rewritten in terms of \hat{I}_+ and \hat{I}_- to give

$$\frac{1}{2}i(\hat{I}_+ - \hat{I}_-) \cos(\Omega t) + \frac{1}{2}(\hat{I}_+ + \hat{I}_-) \sin(\Omega t) = \frac{1}{2}i\hat{I}_+ e^{-i\Omega t} - \frac{1}{2}i\hat{I}_- e^{i\Omega t}.$$

Quadrature detection is employed, in which both the x and y components of the magnetization are detected, and combined to give the complex magnetization M_+ . The observable signal $s(t)$ is therefore given by

$$\begin{aligned} s(t) &= \gamma N \text{Tr}(\hat{I}_+ \hat{\sigma}) \\ &= -\frac{1}{2}i\gamma N e^{i\Omega t}. \end{aligned} \tag{1.26}$$

Using quadrature detection, the only part of the density matrix which contributes to the observed signal has coherence order -1 .

In addition to acquiring a phase, the signal will also decay due to the effects of relaxation that were discussed in Section 1.6. To account for this, the oscillating function in Equation 1.26 is multiplied by a decay envelope $s_e(t)$ to give

$$s(t) = A s_e(t) e^{i\Omega t}, \quad (1.27)$$

where for clarity we have introduced the scaling factor $A = -\frac{1}{2}i\gamma\mathcal{N}$. This does not alter the form of the spectrum, and so henceforth it will be omitted. This decaying and oscillating signal is referred to as the *free induction decay*, (FID). As was explained in Section 1.6, the decay envelope is assumed to take the form of an exponential $\exp(-t/T_2)$.

1.10.2 The Fourier transform

The time-domain signal $s(t)$ is converted into a frequency-domain spectrum $S(\omega)$ by processing with a Fourier transform. The continuous Fourier transform and its inverse are defined by:

$$S(\omega) = \int_{-\infty}^{\infty} s(t) \exp(-i\omega t) dt \quad (1.28)$$

$$s(t) = \frac{1}{2\pi} \int_{-\infty}^{\infty} S(\omega) \exp(i\omega t) d\omega. \quad (1.29)$$

Assuming an exponential decay of the signal, the Fourier transform of the FID in Equation 1.27 is given by[§]

$$\begin{aligned} S(\omega) &= \int_0^{\infty} \exp(i\Omega t) \exp(-t/T_2) \exp(-i\omega t) dt \\ &= \frac{T_2}{1 + i(\omega - \Omega)T_2}. \end{aligned}$$

This is the complex *Lorentzian* lineshape, which can be decomposed into its real and imaginary parts to give

$$S(\omega) = \mathcal{A}_\Omega(\omega) + i\mathcal{D}_\Omega(\omega),$$

[§]Conventionally, the point $t = 0$ is taken to be immediately after the pulse, and so no data are recorded for negative times. The FID is therefore defined as $s(t) = 0$ for $t < 0$, and $s(t) = \exp(i\Omega t) \exp(-t/T_2)$ for $t \geq 0$.

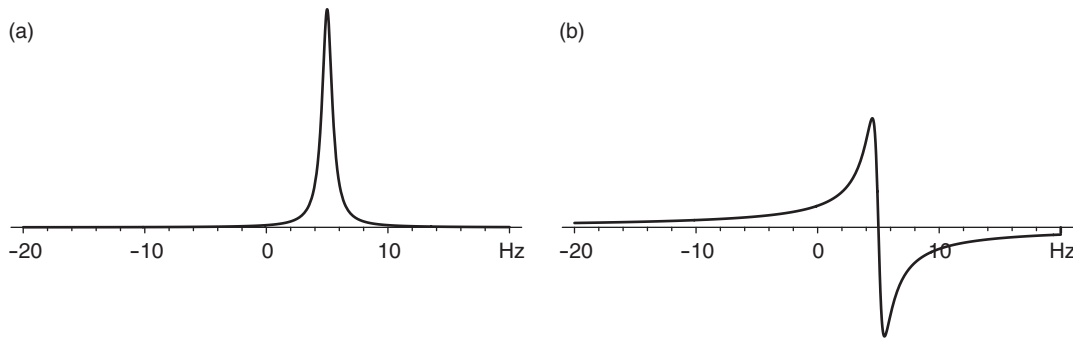


Figure 1.4: The real and imaginary part of the spectrum of a one-spin system, assuming an exponentially-decaying FID. The real part, shown in (a) is an absorption-mode Lorentzian. The dispersion mode, shown in (b), is the imaginary part of the spectrum. The parameters are: $\Omega/(2\pi) = 5$ Hz, and $T_2 = 1/\pi$ s giving a linewidth of 1 Hz.

where $\mathcal{A}_\Omega(\omega)$ is the *absorption-mode* Lorentzian, and $\mathcal{D}_\Omega(\omega)$ is the *dispersion-mode* Lorentzian. Their mathematical forms are

$$\mathcal{A}_\Omega(\omega) = \frac{T_2}{1 + (\omega - \Omega)^2 T_2^2} \quad \mathcal{D}_\Omega(\omega) = \frac{-(\omega - \Omega)T_2^2}{1 + (\omega - \Omega)^2 T_2^2},$$

which are plotted in Figure 1.4; (a) shows the absorption-mode lineshape, and (b) shows the dispersion mode. Both lineshapes are centred on $\omega = \Omega$; the absorption mode is symmetric, and the dispersion mode is anti-symmetric. The absorption mode is narrower than the dispersion mode and is always positive, and so is clearly the preferable lineshape. Therefore, it is conventional to display the part of the spectrum that contains the absorption-mode, which in this case is the real part.

However, the time-domain data that are acquired experimentally often contain phase errors, giving an FID of the form $e^{i\phi_{\text{err}}} e^{i\Omega t} e^{-t/T_2}$, where ϕ_{err} is the phase error. The real part of the resulting spectrum will contain a lineshape that is a mixture of absorption and dispersion modes. Fortunately, the phase error can be removed approximately by multiplying the spectrum by a phase factor $e^{i\phi_{\text{corr}}}$; ϕ_{corr} is the sum of a frequency-independent phase correction ϕ_0 and a first-order frequency-dependent phase correction $\phi_1 = \lambda\omega$. The multiplication of the spectrum by the frequency-independent phase correction factor is equivalent to multiplying the FID by the same factor. Multiplying the spectrum by the first-order phase correction, however, corresponds to performing a left shift or right shift to the components of the FID. The values of ϕ_0 and λ are adjusted interactively to give the required result.

The *linewidth* of the absorption-mode peak is defined as the full-width at half-maximum (FWHM). It is easy to show that this is given by $2/T_2$ in rad s⁻¹. Therefore, as T_2 increases, the signal decays less rapidly and the linewidth decreases.

Inhomogeneous broadening

In practice the applied magnetic field is not uniform but varies with position within the sample. Therefore, spins in different parts of the sample will have different offsets and the lineshape in the spectrum will be a superposition of Lorentzians with different peak positions. The result is that the FID appears to decay more rapidly with an envelope function that, in most cases, is no longer exponential. The peaks in the spectrum therefore have a linewidth that is greater than $2/T_2$, and do not have a Lorentzian lineshape. Despite the decay not being exponential, it is common to account for the extra line broadening by including a second exponential decay factor with a time constant T_2^\dagger . This gives

$$\begin{aligned}s(t) &= \exp(i\Omega t) \exp(-t/T_2) \exp(-t/T_2^\dagger) \\ &= \exp(i\Omega t) \exp(-t/T_2^*).\end{aligned}$$

The time constant T_2^* is the apparent decay constant, and is given by

$$\frac{1}{T_2^*} = \frac{1}{T_2} + \frac{1}{T_2^\dagger},$$

giving an overall linewidth of $2/T_2^*$. The constant T_2 describes the natural decay of the signal, which results in what is known as the *homogeneous* part of the linewidth. The part of the linewidth that is due to field inhomogeneity is described as *inhomogeneous* broadening, and is characterized by the time constant T_2^\dagger .

Peak integrals

The integral of the peak in the spectrum can be calculated as follows:

$$\begin{aligned}\int_{-\infty}^{\infty} S(\omega) d\omega &= \int_{-\infty}^{\infty} d\omega \int_{-\infty}^{\infty} dt s(t) \exp(-i\omega t) \\ &= \int_{-\infty}^{\infty} dt s(t) \int_{-\infty}^{\infty} d\omega \exp(-i\omega t) \\ &= 2\pi \int_{-\infty}^{\infty} dt s(t) \delta(t) \\ &= 2\pi s(0),\end{aligned}$$

where $\delta(t)$ is the Dirac delta function [1]. The integral is proportional to the first recorded point in the time domain, which is independent of the form of the envelope function $s_e(t)$. Therefore, the spectrum has the useful property that the integral of each peak corresponds to the number of spins in each chemical environment; the spectrum is said to be *quantitative*. This property is used extensively in spectral assignment and for determining the relative concentrations of the components of a mixture.

1.10.3 Digital sampling

In practice the FID is sampled at a regular interval Δt , which is known as the *dwell time*. This places a limit on the maximum offset Ω_N (known as the Nyquist frequency) that is properly represented by the data: the rate of sampling must be twice the maximum offset. In angular frequency units, this gives

$$\frac{1}{\Delta t} = \frac{\Omega_N}{\pi}.$$

Since the signal is digitized, the continuous Fourier transform in Equation 1.28 must be replaced by a discrete Fourier transform:

$$S\left(\frac{l}{M\Delta t}\right) = \sum_{k=0}^{M-1} s(k\Delta t) \exp(-i2\pi kl/M),$$

where M is the number of points that is sampled.

As explained in the previous Section, we employ quadrature detection in acquiring the FID. This gives us a signal of the form $\exp(i\Omega t)$, from which we are able to determine the sign of Ω . The range of frequencies that is properly represented therefore runs from $-\Omega_N$ to $+\Omega_N$. The Nyquist condition is now

$$\frac{1}{\Delta t} = \frac{\Delta\Omega}{2\pi},$$

where Δt is interval between samples containing complex pairs of points, and the spectral width $\Delta\Omega$ is the range of properly-represented frequencies.

If a component of the FID oscillates at a frequency Ω_{old} that lies outside the spectral width, this signal will not be properly represented by the digitized data. The component appears to oscillate at an offset Ω_{new} which does lie inside the spectral window. The new offset is found by adding an integer multiple n of the spectral width to Ω_{old} :

$$\Omega_{\text{new}} = \Omega_{\text{old}} + n\Delta\Omega,$$

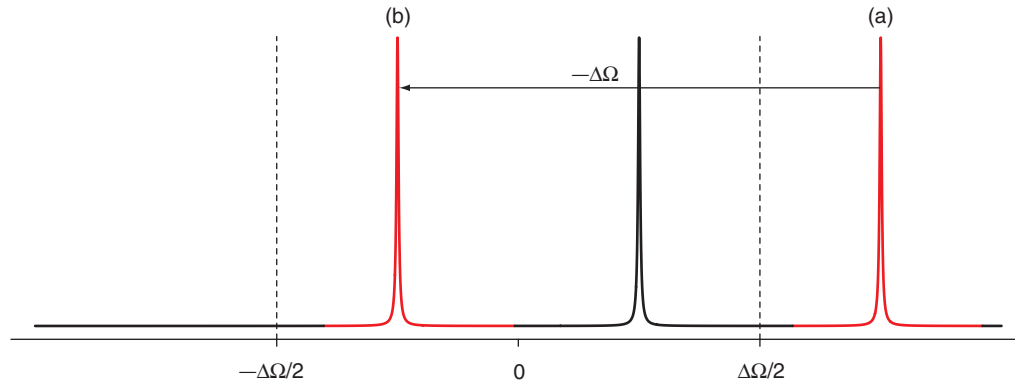


Figure 1.5: Illustration of folding in a spectrum acquired with quadrature detection. The offset of the black peak already lies within the spectral window. The red peak in position (a) lies outside the spectral window, and so is shifted by $-\Delta\Omega$ back into the spectrum to position (b) (so that $n = -1$).

The value that n takes is the one for which $|\Omega_{\text{new}}| < \Delta\Omega/2$ [¶]. The peak in the resulting spectrum is therefore translated into the window by an integral multiple of the spectral width. This process is referred to as *folding*, and is illustrated in Figure 1.5.

1.10.4 The spectrum of a two-spin system in the weak-coupling approximation

For a homonuclear two-spin system, the equilibrium density operator is given by the sum of the z spin operators: $\hat{\sigma}_0 = \hat{I}_{1z} + \hat{I}_{2z}$. The 90° pulse rotates each operator to the $-y$ axis:

$$\hat{I}_{1z} + \hat{I}_{2z} \xrightarrow{(\pi/2)\hat{F}_x} -\hat{I}_{1y} - \hat{I}_{2y}.$$

It proves useful to change from the Cartesian basis to the single-element basis:

$$\begin{aligned} -\hat{I}_{1y} - \hat{I}_{2y} &\equiv -\hat{I}_{1y}\hat{E}_2 - \hat{E}_1\hat{I}_{2y} \\ &= \frac{1}{2}i(\hat{I}_{1+} - \hat{I}_{1-})(\hat{I}_{2\alpha} + \hat{I}_{2\beta}) \\ &\quad + \frac{1}{2}i(\hat{I}_{1\alpha} + \hat{I}_{1\beta})(\hat{I}_{2+} - \hat{I}_{2-}). \end{aligned}$$

The observable magnetization is computed from the trace

$$s(t) = \gamma N \text{Tr}(\hat{F}_+ \hat{\sigma}),$$

where $\hat{F}_+ = \hat{I}_{1+}\hat{I}_{2\alpha} + \hat{I}_{1+}\hat{I}_{2\beta} + \hat{I}_{1\alpha}\hat{I}_{2+} + \hat{I}_{1\beta}\hat{I}_{2+}$. The only terms of the density operator that contribute have coherence order -1 ; therefore, we shall retain only these terms during

[¶]The integer n may be positive or negative.

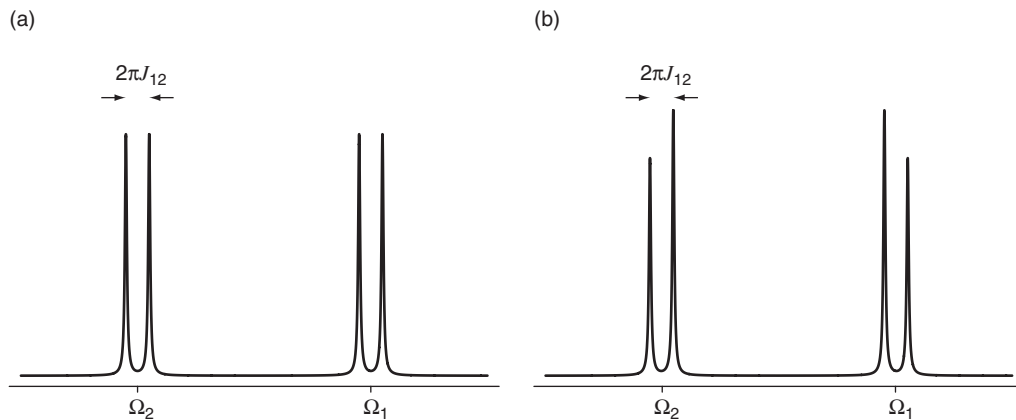


Figure 1.6: Comparison of the spectra of a two-spin system that have been calculated with and without taking account of the effects of strong coupling. Spectrum (a) was calculated using the weak coupling approximation, and (b) was calculated taking account of strong coupling. The spectral parameters are the same for both calculations: $2\pi J_{12}$ and $\Omega_1 - \Omega_2$ are in the ratio 1:10.

the period of free precession. Each of these four terms acquires a phase to give

$$\begin{aligned} & -\frac{1}{2}i\hat{I}_{1-}\hat{I}_{2\alpha} \exp [i(\Omega_1 + \pi J_{12})t] - \frac{1}{2}i\hat{I}_{1-}\hat{I}_{2\beta} \exp [i(\Omega_1 - \pi J_{12})t] \\ & - \frac{1}{2}i\hat{I}_{1\alpha}\hat{I}_{2-} \exp [i(\Omega_2 + \pi J_{12})t] - \frac{1}{2}i\hat{I}_{1\beta}\hat{I}_{2-} \exp [i(\Omega_2 - \pi J_{12})t]. \end{aligned}$$

The evaluation of the trace gives the FID which is, omitting the factor of $-\frac{1}{2}i\gamma\mathcal{N}$,

$$s(t) = \exp [i(\Omega_1 + \pi J_{12})t] + \exp [i(\Omega_1 - \pi J_{12})t] + \exp [i(\Omega_2 + \pi J_{12})t] + \exp [i(\Omega_2 - \pi J_{12})t].$$

Inclusion of an exponential relaxation decay, followed by Fourier transformation produces four peaks in the real part of the spectrum:

$$\mathcal{A}_{\Omega_1+\pi J_{12}}(\omega) + \mathcal{A}_{\Omega_1-\pi J_{12}}(\omega) + \mathcal{A}_{\Omega_2+\pi J_{12}}(\omega) + \mathcal{A}_{\Omega_2-\pi J_{12}}(\omega).$$

The first two peaks form a doublet that is centred on the offset of spin one, and the second two peaks comprise the spin-two doublet. The splitting in both doublets is given by the value of the coupling constant $2\pi J_{12}$, and all four lines have the same intensity. The spectrum is shown in Figure 1.6 (a).

1.10.5 The spectrum of a strongly-coupled two-spin system

Unfortunately, there are no shortcuts to calculating the form of an NMR spectrum in the strong coupling basis, such as the use of product operators, and so a complete

density matrix calculation is needed. They are in general very cumbersome and time-consuming to perform. However, the pulse–acquire experiment is relatively straightforward to evaluate.

The equilibrium density operator in the strong coupling basis is still $\hat{I}_{1z} + \hat{I}_{2z}$ as it is invariant under the transformation described by \hat{U} . So,

$$\sigma_0 = \begin{pmatrix} 1 & 0 & 0 & 0 \\ 0 & 0 & 0 & 0 \\ 0 & 0 & 0 & 0 \\ 0 & 0 & 0 & -1 \end{pmatrix}.$$

The 90° pulse produces the following density matrix:

$$R_x^{\text{SC}}(\pi/2)\sigma_0R_x^{\text{SC}}(\pi/2)^{-1} = \begin{pmatrix} 0 & \frac{1}{2}\text{i}u & \frac{1}{2}\text{i}v & 0 \\ -\frac{1}{2}\text{i}u & 0 & 0 & \frac{1}{2}\text{i}u \\ -\frac{1}{2}\text{i}v & 0 & 0 & \frac{1}{2}\text{i}v \\ 0 & -\frac{1}{2}\text{i}u & -\frac{1}{2}\text{i}v & 0 \end{pmatrix},$$

which is a mixture of $+1$ and -1 coherences as in the weak coupling calculation. However, unlike the latter case, the eight coherences are not excited with the same intensity. During the period of free precession, each element acquires a phase. The observable signal is given by (omitting the factor $-\frac{1}{2}\text{i}\gamma N$ and ignoring relaxation)

$$\begin{aligned} s(t) &= (1 - \sin 2\theta) \exp \left[\text{i} \frac{1}{2} (\Omega_1 + \Omega_2 + C + 2\pi J_{12}) t \right] \\ &+ (1 + \sin 2\theta) \exp \left[\text{i} \frac{1}{2} (\Omega_1 + \Omega_2 + C - 2\pi J_{12}) t \right] \\ &+ (1 + \sin 2\theta) \exp \left[\text{i} \frac{1}{2} (\Omega_1 + \Omega_2 - C + 2\pi J_{12}) t \right] \\ &+ (1 - \sin 2\theta) \exp \left[\text{i} \frac{1}{2} (\Omega_1 + \Omega_2 - C - 2\pi J_{12}) t \right]. \end{aligned}$$

The spectrum is shown in Figure 1.6 (b).

1.11 Weighting functions and sensitivity

Prior to performing the Fourier transform, the FID is often multiplied by a weighting function $w(t)$ either to increase the resolution or sensitivity of the final spectrum. In addition, if the FID is truncated, the resulting lineshape contains unwanted artefacts, and so it is often necessary to apply a weighting function to cause the FID to decay artificially.

1.11.1 The convolution theorem

A time-domain function $h(t)$ can sometimes be expressed as the product of two functions $f(t)$ and $g(t)$:

$$h(t) = f(t)g(t).$$

The Fourier transform of $h(t)$, $H(\omega)$, is then given by the *convolution* of the Fourier transforms of $f(t)$ and $g(t)$, $F(\omega)$ and $G(\omega)$:

$$H(\omega) = \frac{1}{2\pi} F(\omega) * G(\omega), \quad (1.30)$$

where the convolution of $F(\omega)$ with $G(\omega)$ is defined as

$$F(\omega) * G(\omega) = \int_{-\infty}^{\infty} F(u)G(\omega - u)du.$$

Equation 1.30 is known as the convolution theorem.

1.11.2 Truncation

The FID is said to be truncated when acquisition stops before the signal has decayed to within the level of the noise. This is represented mathematically by multiplying the full FID $s(t)$ by a top-hat function $T(t)$ which is defined as

$$T(t) = \begin{cases} \frac{1}{2t^{\max}}, & |t| \leq t^{\max} \\ 0, & \text{otherwise} \end{cases},$$

where t^{\max} is the acquisition time. The spectrum is therefore given by the convolution of the Fourier transform of $s(t)$ with the Fourier transform of $T(t)$:

$$S(\omega) = \frac{1}{2\pi} [\mathcal{A}_\Omega(\omega) + i\mathcal{D}_\Omega(\omega)] * \int_{-\infty}^{\infty} T(t) \exp(-i\omega t) dt.$$

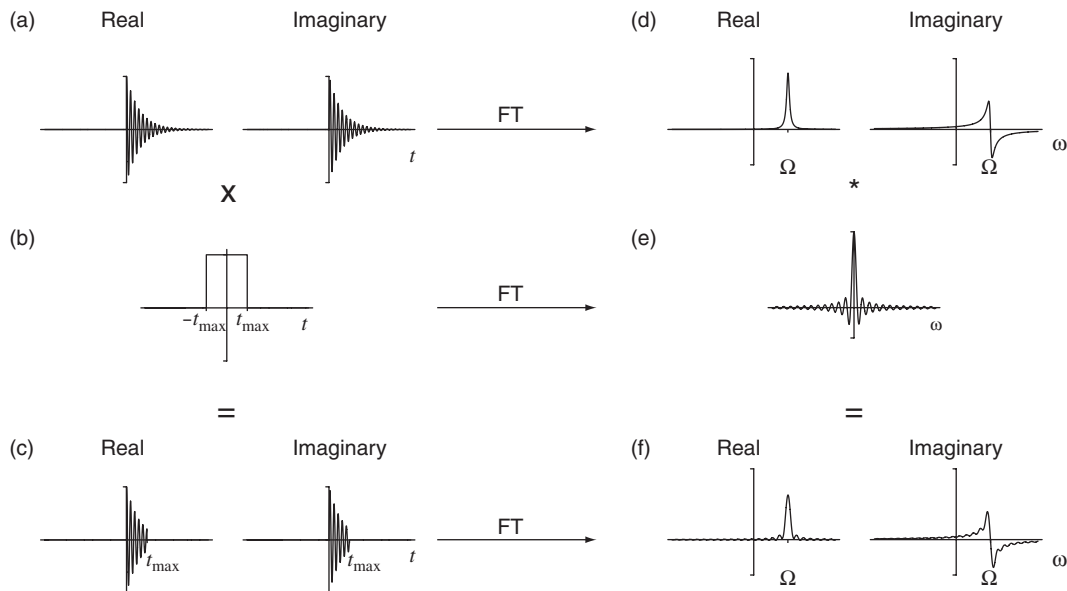


Figure 1.7: Illustration of the convolution theorem as applied to a truncated FID. The real and imaginary parts of an untruncated FID are shown in (a). Multiplication by a top-hat function (b) gives the truncated FID in (c). Fourier transformation of (c) gives the spectrum in (f) which exhibits the sinc wiggles. This spectrum is also given by the convolution of the spectra in (d) and (e). Part (d) shows the Fourier transform of the untruncated FID, and contains the absorption and dispersion mode lineshapes in the real and imaginary parts. The sinc function in (e) is the Fourier transform of the top-hat function.

The integral is a sinc function:

$$\begin{aligned} \int_{-\infty}^{\infty} T(t) \exp(-i\omega t) dt &= \frac{1}{2t^{\max}} \int_{-t^{\max}}^{t^{\max}} \exp(-i\omega t) dt \\ &= \frac{\sin(\omega t^{\max})}{\omega t^{\max}}. \end{aligned}$$

Figure 1.7 illustrates the convolution theorem as applied to a truncated FID, and also shows the lineshape that results from the convolution of the sinc function with the Lorentzian.

The linewidth of the central lobe of the sinc function is $3.791/t^{\max}$ rad s⁻¹ (or $0.603/t^{\max}$ Hz), and so convolution of this with a Lorentzian produces a peak with a linewidth that is greater than the natural linewidth $2/T_2$. In addition, there are oscillating artefacts on either side of the central lobe which are known as ‘sinc wiggles’, whose intensities (relative to the intensity of the central lobe) are governed by the decay envelope $1/(\omega t^{\max})$.

Conventionally, this problem is dealt with in one of two ways. Increasing the acquisition time decreases the linewidth of the sinc function, and reduces the intensities of the truncation artefacts. This latter effect is observed since, for a given frequency ω , the envelope $1/(\omega t^{\max})$ decreases in intensity with increasing t^{\max} . As the acquisition time increases, and the signal decays into the noise, the resulting lineshape tends to the absorption-mode Lorentzian with the natural linewidth. If, however, the acquisition time cannot be increased, for example due to constraints on the experiment time, the sinc wiggles can be removed by multiplying the FID by a decaying weighting function. This has the effect of artificially causing the signal to decay to zero at the end of acquisition, and therefore suppresses the sinc wiggles. However, it also increases the linewidth in the spectrum.

1.11.3 Sensitivity

This thesis describes the development of two new experiments which have intrinsically low sensitivity compared to the conventional ${}^1\text{H}$ experiment. It therefore will prove profitable to be able to compare the signal-to-noise ratios (SNRs) of these experiments. We will derive the relevant expressions in this Section [9].

The signal

This analysis is valid for an FID containing a single component that has been weighted by a function $w(t)$. The FID is composed of M points acquired out to a maximum time of t^{\max} ; the number of scans is n . The spectrum is calculated from the discrete Fourier transform. However, a good approximation is obtained from the integral

$$S(\omega) = n \frac{M}{t^{\max}} \int_0^{t^{\max}} s_e(t) \exp(i\Omega t) w(t) \exp(-i\omega t) dt.$$

The peak height is given by $S(\Omega)$:

$$\begin{aligned} S(\Omega) &= n \frac{M}{t^{\max}} \int_0^{t^{\max}} s_e(t) w(t) dt \\ &= n M \overline{sw}, \end{aligned}$$

where

$$\overline{sw} = \frac{1}{t^{\max}} \int_0^{t^{\max}} s_e(t) w(t) dt$$

is the average of the weighted envelope.

The noise

The noise is principally due to the thermal motion of electrons in the metal coil used in the probe plus noise added by the RF receiver. It is assumed to be white noise with a zero mean of intensities. After weighting, the root mean square (RMS) amplitude $\sigma_n(t)$ is given by

$$\sigma_n(t) = \sqrt{F}\rho_n|w(t)|,$$

where ρ_n is the square root of the frequency-independent power spectral density for white random noise, and F is the bandwidth of receiver in Hz. The latter is set to the spectral width Δf so that any noise components at frequencies outside the spectral window are not folded into the spectrum.

As a consequence of Parseval's theorem [1], the RMS noise in the spectrum σ_N is obtained by summing all nM noise samples in the time domain. This gives

$$\sigma_N = \sqrt{nM\Delta f}\rho_n(\overline{w^2})^{\frac{1}{2}},$$

where

$$\overline{w^2} = \frac{1}{t^{\max}} \int_0^{t^{\max}} w(t)^2 dt.$$

The spectral width is given by $\Delta f = 1/\Delta t = M/t^{\max}$. The RMS noise is therefore

$$\sigma_N = M \sqrt{\frac{n}{t^{\max}}} \rho_n(\overline{w^2})^{\frac{1}{2}}.$$

The signal-to-noise ratio

The SNR is given by

$$\frac{S(\Omega)}{2\sigma_N} = \sqrt{nt^{\max}} \frac{1}{2\rho_n} \frac{\overline{sw}}{(\overline{w^2})^{\frac{1}{2}}}.$$

It can be seen that it is independent of both the number of points M in the FID and the sampling interval Δt ; however, it does depend upon the acquisition time t^{\max} . The SNR increases with the square root of the number of scans, so that if we wish to double the SNR, the number of scans must increase by a factor of four.

1.12 Two-dimensional NMR

As molecules become larger, the one-dimensional NMR spectra become more complicated and therefore more difficult to assign. One common problem is that neigh-

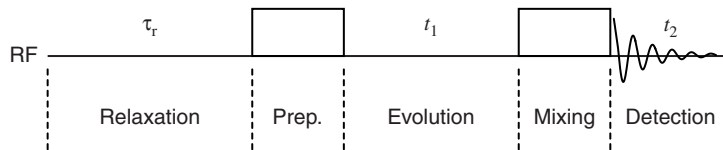


Figure 1.8: Schematic pulse sequence for a two-dimensional experiment. After a delay τ_r which allows the system to relax to equilibrium, the preparation period generates coherences. These evolve during the evolution period t_1 , before the following period mixes the elements of the density matrix. The signal is then acquired in real time during the detection period t_2 .

bouring multiplets tend to overlap. One solution to this problem, first suggested by Jeener [10], is to extend the spectrum into a second frequency dimension.

The pulse sequence for a typical two-dimensional experiment comprises five parts, as shown in Figure 1.8 [11]. The first part is a relaxation delay that allows the system to relax back to its equilibrium configuration. This is followed by an *preparation* period, which is a sequence of RF pulses designed to excite coherences. The coherences then evolve during an *evolution* period t_1 . This is normally a delay during which the elements of the density matrix evolve under the free precession Hamiltonian and acquire phases that depend on t_1 . The next period causes mixing between some terms of the density operator, an example of which is *coherence transfer*, where coherence is transferred from one spin to another. Finally, the observable signal is recorded during the detection period t_2 . The delay t_1 is initially set to zero, and the pulse sequence is executed, resulting in a single FID acquired as a function of t_2 . The experiment is then repeated several times with the value of t_1 incremented for each. This results in a two-dimensional time-domain matrix $s(t_1, t_2)$, which is Fourier transformed in both dimensions to yield a two-dimensional frequency-domain spectrum $S(\omega_1, \omega_2)$.

1.12.1 Two-dimensional lineshapes

The two-dimensional datasets that are acquired during an experiment can be separated into two groups: those which are phase modulated in t_1 , and those which are amplitude modulated in t_1 . Evolution during t_1 gives the signal a t_1 -dependent phase factor in the former, while in the latter the t_1 -dependence affects the amplitude.

If the experiment requires that p -quantum coherence is selected during t_1 , there are two coherence orders that can be acquired: $+p$ and $-p$. Selection of only one of these results in a phase-modulated signal, and selection of both with equal weighting gives

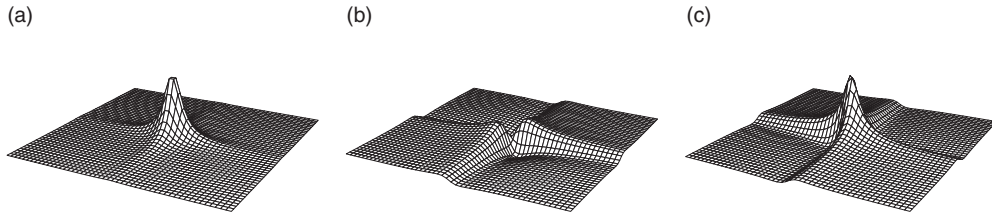


Figure 1.9: Lineshapes in a two-dimensional spectrum. The double absorption-mode lineshape is shown in (a), and the double dispersion-mode is shown in (b). The difference between the two, shown in (c), is the undesirable phase-twist lineshape.

an amplitude-modulated signal. In all cases, only the $p = -1$ pathway is acquired during the detection period, so the signal is always phase-modulated during t_2 .

Phase-modulated data

A coherence that is phase modulated by an offset $\Omega^{(1)}$ during t_1 , and which is phase modulated by $\Omega^{(2)}$ during t_2 is represented by the following FID:

$$s(t_1, t_2) = \exp(i\Omega^{(1)}t_1) \exp(-t_1/T_2^{(1)}) \exp(i\Omega^{(2)}t_2) \exp(-t_2/T_2^{(2)}),$$

where $T_2^{(i)}$ is the decay time constant during t_i . This type of FID is obtained by acquiring a single coherence order $-p$ during t_1 . The two-dimensional Fourier transform is defined as

$$S(\omega_1, \omega_2) = \int_{-\infty}^{\infty} \int_{-\infty}^{\infty} s(t_1, t_2) \exp(-i\omega_1 t_1) \exp(-i\omega_2 t_2) dt_1 dt_2.$$

When applied to the phase-modulated dataset, we obtain

$$[\mathcal{A}_{\Omega^{(1)}}(\omega_1) + i\mathcal{D}_{\Omega^{(1)}}(\omega_1)] [\mathcal{A}_{\Omega^{(2)}}(\omega_2) + i\mathcal{D}_{\Omega^{(2)}}(\omega_2)],$$

which can be separated into its real and imaginary parts:

$$\begin{aligned} & [\mathcal{A}_{\Omega^{(1)}}(\omega_1)\mathcal{A}_{\Omega^{(2)}}(\omega_2) - \mathcal{D}_{\Omega^{(1)}}(\omega_1)\mathcal{D}_{\Omega^{(2)}}(\omega_2)] \\ & + i [\mathcal{A}_{\Omega^{(1)}}(\omega_1)\mathcal{D}_{\Omega^{(2)}}(\omega_2) + \mathcal{D}_{\Omega^{(1)}}(\omega_1)\mathcal{A}_{\Omega^{(2)}}(\omega_2)]. \end{aligned} \quad (1.31)$$

The real part of the spectrum contains the *phase-twist* lineshape [12] (shown in Figure 1.9 (c)), which is the difference between the double absorption-mode and double dispersion-mode lineshapes that are shown in (a) and (b) respectively. It is a very

undesirable lineshape as the dispersive component is very broad, and contains negative regions. The imaginary part also contains a dispersive component.

The more desirable double absorption-mode lineshape can be obtained by acquiring, in a separate experiment, the second coherence order $+p$ during t_1 [13, 14]. The two signals are

$$\begin{aligned}s_N(t_1, t_2) &= \exp(-i\Omega^{(1)}t_1) \exp(-t_1/T_2^{(1)}) \exp(i\Omega^{(2)}t_2) \exp(-t_2/T_2^{(2)}) \\ s_P(t_1, t_2) &= \exp(+i\Omega^{(1)}t_1) \exp(-t_1/T_2^{(1)}) \exp(i\Omega^{(2)}t_2) \exp(-t_2/T_2^{(2)}).\end{aligned}$$

$s_N(t_1, t_2)$ is the echo, or N-type, dataset and is recorded by selecting the $+p$ coherence pathway during t_1 ; $s_P(t_1, t_2)$ is the anti-echo, or P-type, dataset and represents the $-p$ coherence pathway during t_1 .

The two datasets are processed as follows. Firstly, both are Fourier transformed with respect to t_2 only to give

$$\begin{aligned}\tilde{s}_N(t_1, \omega_2) &= \exp(-i\Omega^{(1)}t_1) \exp(-t_1/T_2^{(1)}) [\mathcal{A}_{\Omega^{(2)}}(\omega_2) + i\mathcal{D}_{\Omega^{(2)}}(\omega_2)] \\ \tilde{s}_P(t_1, \omega_2) &= \exp(+i\Omega^{(1)}t_1) \exp(-t_1/T_2^{(1)}) [\mathcal{A}_{\Omega^{(2)}}(\omega_2) + i\mathcal{D}_{\Omega^{(2)}}(\omega_2)].\end{aligned}$$

The two datasets are then combined to give two new datasets that are cosine and sine-modulated during t_1 :

$$\begin{aligned}\tilde{s}_c(t_1, \omega_2) &= \frac{1}{2} (\tilde{s}_P(t_1, \omega_2) + \tilde{s}_N(t_1, \omega_2)) \\ &= \cos(\Omega^{(1)}t_1) \exp(-t_1/T_2^{(1)}) [\mathcal{A}_{\Omega^{(2)}}(\omega_2) + i\mathcal{D}_{\Omega^{(2)}}(\omega_2)] \\ \tilde{s}_s(t_1, \omega_2) &= \frac{1}{2i} (\tilde{s}_P(t_1, \omega_2) - \tilde{s}_N(t_1, \omega_2)) \\ &= \sin(\Omega^{(1)}t_1) \exp(-t_1/T_2^{(1)}) [\mathcal{A}_{\Omega^{(2)}}(\omega_2) + i\mathcal{D}_{\Omega^{(2)}}(\omega_2)].\end{aligned}$$

We then discard the imaginary parts, and combine to real parts to recreate a phase-modulated dataset in t_1 :

$$\begin{aligned}\tilde{s}(t_1, \omega_2) &= \text{Re}(\tilde{s}_c(t_1, \omega_2)) + i\text{Re}(\tilde{s}_s(t_1, \omega_2)) \\ &= \exp(+i\Omega^{(1)}t_1) \exp(-t_1/T_2^{(1)}) \mathcal{A}_{\Omega^{(2)}}(\omega_2).\end{aligned}\tag{1.32}$$

Finally, the second Fourier transform results in the double absorption-mode lineshape in the real part of the spectrum:

$$\text{Re}(S(\omega_1, \omega_2)) = \mathcal{A}_{\Omega^{(1)}}(\omega_1) \mathcal{A}_{\Omega^{(2)}}(\omega_2).$$

Amplitude-modulated data

Some pulse sequences naturally give the sum of the N- and P-type datasets in a single experiment, resulting in an amplitude-modulated dataset. One example is a cosine-modulated signal, which takes the form

$$s_c(t_1, t_2) = \cos(\Omega^{(1)}t_1) \exp(-t_1/T_2^{(1)}) \exp(i\Omega^{(2)}t_2) \exp(-t_2/T_2^{(2)}).$$

Applying a two-dimensional Fourier transform and taking the real part gives the following spectrum:

$$\frac{1}{2} [\mathcal{A}_{\Omega^{(1)}}(\omega_1) \mathcal{A}_{\Omega^{(2)}}(\omega_2) - \mathcal{D}_{\Omega^{(1)}}(\omega_1) \mathcal{D}_{\Omega^{(2)}}(\omega_2)] + \frac{1}{2} [\mathcal{A}_{-\Omega^{(1)}}(\omega_1) \mathcal{A}_{\Omega^{(2)}}(\omega_2) - \mathcal{D}_{-\Omega^{(1)}}(\omega_1) \mathcal{D}_{\Omega^{(2)}}(\omega_2)].$$

Since the cosine can be written as $\frac{1}{2} [\exp(+i\Omega^{(1)}t_1) + \exp(-i\Omega^{(1)}t_1)]$, there are two peaks: one is located at $(\omega_1, \omega_2) = (\Omega^{(1)}, \Omega^{(2)})$, and the second is at $(\omega_1, \omega_2) = (-\Omega^{(1)}, \Omega^{(2)})$. In addition to possessing the phase-twist lineshape, the spectrum does not have frequency discrimination in the ω_1 dimension.

The double absorption-mode lineshape can be obtained very easily; we simply discard the imaginary part of the data after the Fourier transform with respect to t_2 , giving

$$\tilde{s}_c(t_1, \omega_2) = \cos(\Omega^{(1)}t_1) \exp(-t_1/T_2^{(1)}) \mathcal{A}_{\Omega^{(2)}}(\omega_2). \quad (1.33)$$

Then Fourier transformation with respect to t_1 gives, in the real part of the spectrum,

$$\text{Re}(S(\omega_1, \omega_2)) = \frac{1}{2} \mathcal{A}_{\Omega^{(1)}}(\omega_1) \mathcal{A}_{\Omega^{(2)}}(\omega_2) + \frac{1}{2} \mathcal{A}_{-\Omega^{(1)}}(\omega_1) \mathcal{A}_{\Omega^{(2)}}(\omega_2).$$

However, we still lack frequency discrimination. This can be achieved by recording a second dataset that is sine-modulated in t_1 , $s_s(t_1, t_2)$:

$$s_s(t_1, t_2) = \sin(\Omega^{(1)}t_1) \exp(-t_1/T_2^{(1)}) \exp(i\Omega^{(2)}t_2) \exp(-t_2/T_2^{(2)}).$$

The real part of the t_2 Fourier transform is

$$\tilde{s}_s(t_1, \omega_2) = \sin(\Omega^{(1)}t_1) \exp(-t_1/T_2^{(1)}) \mathcal{A}_{\Omega^{(2)}}(\omega_2).$$

This dataset can now be combined with its cosine-modulated counterpart in Equation 1.33 to give a phase-modulated dataset in exactly the same way as is shown in Equation 1.32. The real part of the t_1 Fourier transform then gives a double absorption-mode lineshape with frequency discrimination:

$$\text{Re}(S(\omega_1, \omega_2)) = \mathcal{A}_{\Omega^{(1)}}(\omega_1) \mathcal{A}_{\Omega^{(2)}}(\omega_2).$$

This procedure is referred to as the States–Haberkorn–Ruben (SHR) method [15].

1.12.2 Digital sampling in t_1

In one-dimensional spectroscopy, the separation of data points in the FID Δt was governed by the spectral width via the Nyquist condition. The same considerations apply in both dimensions in two-dimensional spectroscopy: the sampling interval in t_i , Δt_i , is given by

$$\frac{1}{\Delta t_i} = \frac{\Delta\Omega_i}{2\pi},$$

where $\Delta\Omega_i$ is the spectral width in the ω_i dimension.

1.12.3 Sensitivity

The SNR of a two-dimensional spectrum can be calculated in exactly the same way as for a one-dimensional spectrum, as was described in Section 1.11.3 [9]. It is assumed that the FID contains a single component that was sampled with M_1 data points in t_1 , and M_2 points in t_2 ; the maximum time that was attained in each dimension is t_1^{\max} and t_2^{\max} respectively.

The peak height is given by

$$S(\Omega^{(1)}, \Omega^{(2)}) = nM_1 M_2 \overline{sw},$$

where

$$\overline{sw} = \frac{1}{t_1^{\max}} \frac{1}{t_2^{\max}} \int_0^{t_1^{\max}} \int_0^{t_2^{\max}} s_e(t_1, t_2) w(t_1, t_2) dt_1 dt_2$$

The decay envelope is $s_e(t_1, t_2)$ and this has been weighted with a function $w(t_1, t_2)$.

The RMS noise in the weighted time domain is

$$\sigma_n(t_1, t_2) = \sqrt{F} \rho_n |w(t_1, t_2)|.$$

The receiver bandwidth is set to the spectral width in t_2 , $\Delta f_2 = 1/\Delta t_2 = M_2/t_2^{\max}$. In the frequency domain, the RMS noise σ_N is found by summing over all the time-domain points:

$$\sigma_N = M_2 \sqrt{\frac{nM_1}{t_2^{\max}}} (\overline{w^2})^{\frac{1}{2}} \rho_n,$$

where

$$\overline{w^2} = \frac{1}{t_1^{\max}} \frac{1}{t_2^{\max}} \int_0^{t_1^{\max}} \int_0^{t_2^{\max}} w(t_1, t_2)^2 dt_1 dt_2.$$

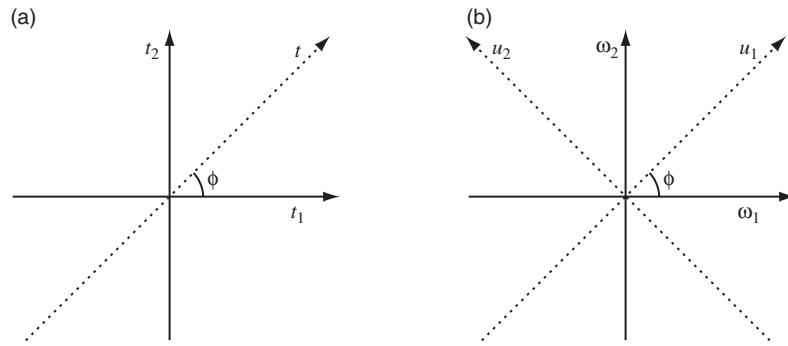


Figure 1.10: The projection–slice theorem. The time domain is shown in (a), and the frequency domain is shown in (b). The projection of a two-dimensional spectrum onto an axis u_1 that is inclined by ϕ to ω_1 can be calculated by extracting a slice from the time domain along an axis t that is inclined by the same angle to t_1 , and performing a one-dimensional Fourier transform.

The SNR is therefore given by

$$\frac{S(\Omega^{(1)}, \Omega^{(2)})}{2\sigma_N} = \sqrt{nM_1 t_2^{\max}} \frac{1}{2\rho_n} \frac{\overline{sw}}{\left(\overline{w^2}\right)^{\frac{1}{2}}}. \quad (1.34)$$

1.12.4 Projections

Much of the work described in this thesis is concerned with calculating the projection of a two-dimensional spectrum onto a particular axis. In order to determine an expression for the lineshape and linewidth of a peak in the projection, it proves very useful to use the *projection–slice theorem* [16].

The projection–slice theorem

The projection–slice theorem can be used to calculate projections of a spectrum onto an axis that passes through the origin, and is inclined at an angle ϕ to the ω_1 axis. We therefore define a pair of axes u_1 and u_2 as follows:

$$\begin{aligned} u_1 &= \omega_1 \cos \phi + \omega_2 \sin \phi \\ u_2 &= -\omega_1 \sin \phi + \omega_2 \cos \phi. \end{aligned}$$

This axis system is illustrated in Figure 1.10 (b).

The projection onto u_1 , $P(u_1)$, is calculated by integrating over u_2 , giving

$$\begin{aligned} P(u_1) &= \int_{-\infty}^{\infty} S(\omega_1, \omega_2) du_2 \\ &= \int_{-\infty}^{\infty} S(u_1 \cos \phi - u_2 \sin \phi, u_1 \sin \phi + u_2 \cos \phi) du_2. \end{aligned}$$

Without loss of generality, we shall set $\phi = 0$, and calculate the projection onto ω_1 ^{||}. The spectrum $S(\omega_1, \omega_2)$ is given by the Fourier transform of the two-dimensional time domain. The projection is then calculated by integrating over ω_2 as follows:

$$\begin{aligned} P(\omega_1) &= \int_{-\infty}^{\infty} d\omega_2 \int_{-\infty}^{\infty} dt_1 \int_{-\infty}^{\infty} dt_2 s(t_1, t_2) \exp(-i\omega_1 t_1) \exp(-i\omega_2 t_2) \\ &= \int_{-\infty}^{\infty} dt_1 \exp(-i\omega_1 t_1) \int_{-\infty}^{\infty} dt_2 s(t_1, t_2) \int_{-\infty}^{\infty} d\omega_2 \exp(-i\omega_2 t_2) \\ &= \int_{-\infty}^{\infty} dt_1 \exp(-i\omega_1 t_1) \int_{-\infty}^{\infty} dt_2 s(t_1, t_2) 2\pi\delta(t_2) \\ &= 2\pi \int_{-\infty}^{\infty} dt_1 \exp(-i\omega_1 t_1) s(t_1, 0), \end{aligned} \tag{1.35}$$

where $\delta(t)$ is the Dirac delta function. Therefore, the projection onto the ω_1 axis can be calculated by firstly extracting the one-dimensional slice $t_2 = 0$ from the time domain and applying a Fourier transform. This projection can therefore be recorded by acquiring the first complex data point of each t_1 increment.

In general, the projection onto the u_1 axis that is inclined by ϕ relative to ω_1 is calculated by Fourier transformation of the one-dimensional slice in the time domain that is inclined by the same angle to t_1 (as is shown in Figure 1.10 (a)). For example, the projection onto ω_2 is found by recording the first FID of the two-dimensional time-domain.

It should be noted that this theorem is only valid if the time domain is processed only by the double Fourier transform; if any other manipulations are carried out, for example discarding the imaginary part, the relationship in Equation 1.35 no longer applies.

^{||}The following argument is also valid for an arbitrary angle ϕ , since we simply transform $s(t_1, t_2)$ into a new axis system.

Chapter 2

Methods of signal selection

THE DENSITY OPERATOR that is generated at each stage of a pulse sequence will, in general, comprise many coherences of different orders. Usually, only a subset of these is needed to produce the required spectrum. The remaining terms may give rise to unwanted peaks, and so must be suppressed. Unwanted coherences that have different coherence orders to the wanted terms at certain stages of the sequence may be removed by applying one or both of two long-established methods: *phase cycling* and *pulsed field gradients*. However, for some experiments the unwanted and wanted coherences have the same order at all times, and so must be suppressed using alternative methods.

2.1 Coherence transfer pathways

Each pulse in a sequence may convert a term in the density operator expansion into one or more terms of different coherence order. Therefore a coherence that is present at the end of the sequence will, in general, have passed through a series of different coherence orders during the sequence. Each set of coherence orders is referred to as a *coherence transfer pathway* (CTP). In many experiments the density operator follows a number of such CTPs, of which it may be desirable to select only a subset. Other CTPs may produce unwanted peaks or phase distortions in the spectrum, and so must be suppressed.

The established methods of CTP selection stem from the idea that coherences of different orders respond differently to a rotation about the z -axis. If we rotate an

operator $\hat{\sigma}^{(p)}$ with coherence order p about z through an angle ϕ , we obtain

$$\begin{aligned}\hat{R}_z(\phi)\hat{\sigma}^{(p)}\hat{R}_z(\phi)^{-1} &= \exp(-i\phi\hat{F}_z)|i\rangle\langle j|\exp(i\phi\hat{F}_z) \\ &= \exp(-i\phi M_i)|i\rangle\langle j|\exp(i\phi M_j) \\ &= \exp(-i\phi(M_i - M_j))|i\rangle\langle j| \\ &= \exp(-i\phi p)\hat{\sigma}^{(p)}.\end{aligned}$$

We have written $\hat{\sigma}^{(p)}$ in terms of the basis functions as $|i\rangle\langle j|$. Since these functions have been chosen to be eigenfunctions of $\hat{\mathcal{H}}_{\text{free}}$, they are also eigenfunctions of $\hat{F}_z = \sum_{i=1}^N \hat{I}_{iz}$ as the two operators commute. The eigenvalues of the latter are the magnetic quantum numbers M_i . The operator has therefore acquired a phase which is proportional to p . This property is exploited by both phase cycling and pulse field gradient coherence order selection techniques.

2.2 Phase cycling

Phase cycling is a method used to separate parts of the density operator which experience different *changes* in coherence order at certain stages of the sequence. The pulse sequence is repeated a number of times with a variation in the phases of one or more of the pulses. This results in each individual FID acquiring a different phase for each repetition of the sequence. It is also possible to change the receiver phase, which results in a second phase factor being introduced during acquisition. The key point is that the receiver phase can be varied so that the overall phase factor of the required CTPs is the same for each FID. Therefore when the FIDs are added, the wanted signal components are retained and the others are cancelled. The combination of pulse and receiver phases that is used during the course of the experiment is referred to as a *phase cycle*.

2.2.1 The phase cycle of a single set of pulses

In this Section, the phase cycle for a single block of pulses, or pulse-sequence element, is discussed. The overall effect of this set of pulses on the density operator can be represented by an overall Hamiltonian $\hat{\mathcal{H}}$ [5]. In general, when applied to $\hat{\sigma}^{(p)}$ it will generate an operator that is a mixture of coherence orders q_i :

$$\hat{\sigma}^{(p)} \xrightarrow{\hat{\mathcal{H}}_t} \sum_i \hat{\sigma}^{(q_i)}.$$

If the phases of all the pulses are shifted by ϕ_{pul} , the Hamiltonian becomes

$$\hat{R}_z(\phi_{\text{pul}})\hat{\mathcal{H}}\hat{R}_z(\phi_{\text{pul}})^{-1}.$$

The phase-shifted Hamiltonian transforms $\hat{\sigma}^{(p)}$ as follows:

$$\begin{aligned} & \exp(-i\hat{R}_z(\phi_{\text{pul}})\hat{\mathcal{H}}\hat{R}_z(\phi_{\text{pul}})^{-1}t)\hat{\sigma}^{(p)}\exp(+i\hat{R}_z(\phi_{\text{pul}})\hat{\mathcal{H}}\hat{R}_z(\phi_{\text{pul}})^{-1}t) \\ = & \hat{R}_z(\phi_{\text{pul}})\exp(-i\hat{\mathcal{H}}t)\left\{\hat{R}_z(\phi_{\text{pul}})^{-1}\hat{\sigma}^{(p)}\hat{R}_z(\phi_{\text{pul}})\right\}\exp(+i\hat{\mathcal{H}}t)\hat{R}_z(\phi_{\text{pul}})^{-1} \\ = & \exp(ip\phi_{\text{pul}})\hat{R}_z(\phi_{\text{pul}})\exp(-i\hat{\mathcal{H}}t)\hat{\sigma}^{(p)}\exp(+i\hat{\mathcal{H}}t)\hat{R}_z(\phi_{\text{pul}})^{-1} \\ = & \exp(ip\phi_{\text{pul}})\sum_i\hat{R}_z(\phi_{\text{pul}})\hat{\sigma}^{(q_i)}\hat{R}_z(\phi_{\text{pul}})^{-1} \\ = & \exp(ip\phi_{\text{pul}})\sum_i\hat{\sigma}^{(q_i)}\exp(-iq_i\phi_{\text{pul}}). \end{aligned}$$

Each term of the density operator expansion has acquired a phase $-\Delta p_i\phi_{\text{pul}}$ which depends on the change in coherence order $\Delta p_i = q_i - p$ caused by $\hat{\mathcal{H}}$, and the phase of the sequence ϕ_{pul} . This phase factor propagates through the rest of the pulse sequence unchanged.

If the receiver phase is ϕ_{rec} the signal is multiplied by a second phase factor $\exp(-i\phi_{\text{rec}})$. The experiment is repeated n times with a different combination of pulse and receiver phases for each scan, and the FIDs are added together to give the following signal:

$$s = s_0 \sum_{k=0}^{n-1} \exp\left(-i\left(\Delta p\phi_{\text{pul}}^{(k)} + \phi_{\text{rec}}^{(k)}\right)\right), \quad (2.1)$$

where s_0 is the signal obtained from a single scan, and $\phi_{\text{pul}}^{(k)}$ and $\phi_{\text{rec}}^{(k)}$ are the pulse and receiver phases in the k th scan.

Conventionally, the n pulse phases are chosen to be equally spaced around a whole rotation of 2π . They are therefore given by

$$\phi_{\text{pul}}^{(k)} = \frac{2\pi k}{n}. \quad (2.2)$$

If the receiver phases satisfy

$$\phi_{\text{rec}}^{(k)} = -\Delta p\phi_{\text{pul}}^{(k)}, \quad (2.3)$$

Equation 2.1 becomes

$$s = ns_0, \quad (2.4)$$

i.e. the signal adds on each scan. This means that a change of coherence order of Δp has been selected.

It is now necessary to determine the fate of other CTPs which experience a change in coherence order of $\Delta p + l$. Substituting this into Equation 2.1 and applying the condition in Equation 2.3 gives

$$\begin{aligned} s &= s_0 \sum_{k=0}^{n-1} \exp(-il\phi_{\text{pul}}^{(k)}) \\ &= s_0 \sum_{k=0}^{n-1} \exp(-i2\pi kl/n). \end{aligned}$$

The sum can be solved to give

$$\begin{aligned} s &= s_0 \frac{1 - \exp(-i2\pi l)}{1 - \exp(-i2\pi l/n)} \\ &= \begin{cases} ns_0, & l = mn \\ 0, & \text{otherwise} \end{cases}, \end{aligned}$$

where m is also an integer.

To summarize, if we design a phase cycle of n steps to select a change of coherence order Δp , then changes of $\Delta p \pm n, \Delta p \pm 2n, \Delta p \pm 3n, \dots$ will also be selected, but the others will not.

2.2.2 Nested phase cycles

If there is more than one pulse-sequence element that requires phase cycling, their phases must be incremented independently. For example, suppose there are two such elements A and B for which the desired changes in coherence order are Δp_A and Δp_B . The phases of the two elements are cycled independently in n_A and n_B steps respectively. The phase of sequence A is cycled through a complete rotation of 2π during which the phase of B remains constant. The phase of B is then incremented to its second value at which it remains constant whilst we record a further n_A experiments in which A is cycled through a complete rotation. This pattern is repeated until B has also been cycled through a complete rotation. Therefore, A completes n_B cycles, whilst B completes one.

The total number of steps in the combined phase cycle is therefore $n_A n_B$. The

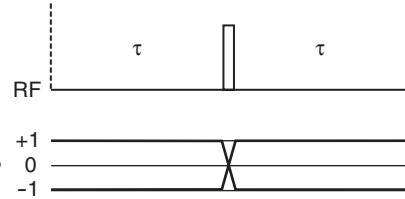


Figure 2.1: The pulse sequence for the spin echo. The three lines beneath the sequence labelled $p = +1$, 0, and -1 indicate the possible coherence orders at each stage of the sequence. The bold lines show the two required CTPs.

pulse phases $\phi_{\text{pul},A}^{(k)}$ and $\phi_{\text{pul},B}^{(k)}$ and receiver phases $\phi_{\text{rec}}^{(k)}$ take the following values:

$$\begin{aligned}\phi_{\text{pul},A}^{(k)} &= \frac{2\pi k}{n_A} \\ \phi_{\text{pul},B}^{(k)} &= \frac{2\pi}{n_B} \text{floor}\left(\frac{k}{n_A}\right) \\ \phi_{\text{rec}}^{(k)} &= -\Delta p_A \phi_{\text{pul},A}^{(k)} - \Delta p_B \phi_{\text{pul},B}^{(k)},\end{aligned}$$

where k runs from 0 to $n_A n_B - 1$, and the function $\text{floor}(x)$ is the integer part of x .

2.2.3 EXORCYCLE

One example of phase cycling is the coherence-order selection on the 180° pulse in a spin echo, as illustrated in Figure 2.1. When the pulse is applied to single-quantum coherence, the required CTPs change coherence order from $+1$ to -1 (since the ideal pulse transforms \hat{I}_+ completely into \hat{I}_-) and *vice versa*, i.e. $\Delta p = \pm 2$. If there were no pulse imperfections and the B_1 field were large enough so that the effective field lies along x across the whole spectrum, then both pathways would be selected unambiguously, and no unwanted CTPs would be generated. However, in practice there will be pulse imperfections, and so other pathways will be generated. To select both wanted CTPs, a four-step phase cycle is required in which the pulse phase is incremented in steps of $\pi/2$. The pulse and receiver phases, which are given by Equations 2.2 and 2.3, are:

$$\begin{aligned}\phi_{\text{pul}} &= 0, \pi/2, \pi, 3\pi/2 \\ \phi_{\text{rec}} &= 0, \pi, 0, \pi.\end{aligned}$$

This phase cycle is referred to as EXORCYCLE [17].

2.3 Pulsed field gradients

It is often the case that the number of scans required to achieve an adequate SNR is less than the number required to complete the phase cycle. For this reason pulsed field gradients (PFGs) are employed as an alternative method of CTP selection as they can select the required CTPs in a single scan.

A PFG generates a spatially inhomogeneous magnetic field \mathbf{B}_g . In this dissertation, \mathbf{B}_g is assumed to vary linearly in the z direction only; the field is therefore given by

$$B_g(z) = Gz,$$

where G is the field gradient. The point $z = 0$ is defined to be the centre of the sample, at which $B_g(0) = 0$.

2.3.1 Free precession in the presence of a gradient

In the presence of a PFG, the free-precession Hamiltonian $\hat{\mathcal{H}}_{\text{free},g}$ is

$$\hat{\mathcal{H}}_{\text{free},g} = \hat{\mathcal{H}}_{\text{free}} + \hat{\mathcal{H}}_g(z),$$

where $\hat{\mathcal{H}}_{\text{free}}$ is the free-precession Hamiltonian in the absence of a gradient, and $\hat{\mathcal{H}}_g(z)$ is the position-dependent term that accounts for the PFG. The latter is given by

$$\hat{\mathcal{H}}_g(z) = -\gamma G z \hat{F}_z.$$

Each spin therefore evolves at an offset that depends on z ; for example, the position-dependent offset for spin i is $\Omega_i - \gamma G z$. The sample can be divided into thin transverse slices (isochromats) within each of which the offsets are constant. During a PFG, the magnetization vectors from each isochromat precess at slightly different frequencies, and thus acquire spatially-dependent phases. After the PFG, it is found that the phases cancel each other to a large extent, and so the magnetization from the whole sample is attenuated, or dephased.

The spatially dependent Hamiltonian $\hat{\mathcal{H}}_g(z)$ commutes with $\hat{\mathcal{H}}_{\text{free}}$, and so its effect on the density operator can be calculated separately. The propagator is the z -rotation operator $\hat{R}_z(-\gamma G z t)$. The initial state $\hat{\sigma}^{(p)}(0)$ has coherence order p and is rotated to give $\hat{\sigma}^{(p)}(t, z)$, which is given by

$$\begin{aligned} \hat{\sigma}^{(p)}(t, z) &= \hat{R}_z(-\gamma G z t) \hat{\sigma}^{(p)}(0) \hat{R}_z(-\gamma G z t)^{-1} \\ &= \exp(i p \gamma G z t) \hat{\sigma}^{(p)}(0). \end{aligned} \tag{2.5}$$

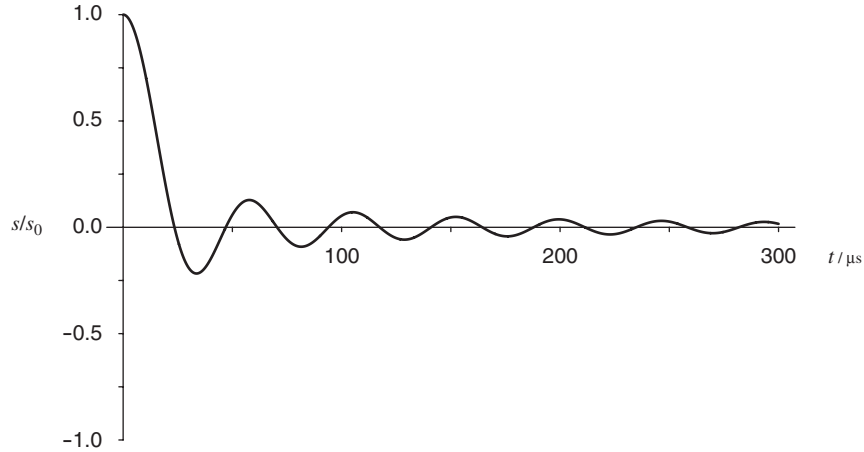


Figure 2.2: The signal attenuation s/s_0 due to a rectangular PFG as a function of duration. The intensity of the unattenuated signal is s_0 , and the parameters are: $p = -1$, $\gamma = 26752.2 \text{ rad s}^{-1}\text{G}^{-1}$, $G = 10 \text{ G cm}^{-1}$, and $L = 1.0 \text{ cm}$.

The gradient therefore imparts a spatially-dependent phase of $\phi(z) = pyGzt$.

The density operator of the whole sample can be calculated by integrating Equation 2.5 with respect to z over the sample length L . This gives

$$\begin{aligned}
 \hat{\sigma}^{(p)}(t) &= \frac{1}{L} \int_{-L/2}^{L/2} \hat{\sigma}^{(p)}(t, z) dz \\
 &= \frac{1}{L} \int_{-L/2}^{L/2} \exp(ipyGzt) \hat{\sigma}^{(p)}(0) dz \\
 &= \frac{\sin \frac{1}{2}pyGLt}{\frac{1}{2}pyGLt} \hat{\sigma}^{(p)}(0).
 \end{aligned} \tag{2.6}$$

The signal due to the density operator is therefore dephased according to a sinc function, which is shown in Figure 2.2.

2.3.2 Shaped PFGs

The PFG that has been described so far has a rectangular time profile; that is, the gradient is constant for the duration of the pulse. The discontinuities in the magnitude of the gradient that are present whilst the PFG is switched on and off produce a rapidly-changing magnetic field which induces eddy currents in the surrounding metal of the probe. In turn, the induced currents produce a magnetic field that affects the evolution of the spins, possibly resulting in distorted spectra.

One way in which the size of the eddy currents can be reduced is to use a gradient time profile $G(t)$ that turns on and off more smoothly. The Hamiltonian is now time-dependent, and so the solution to the Liouville–von Neumann equation in Equation 1.10 no longer applies. However, since $\hat{\mathcal{H}}_g$ commutes with itself at all times, the solution still has a relatively simple form:

$$\hat{\sigma}(t) = \hat{U}\hat{\sigma}(0)\hat{U}^{-1},$$

where

$$\begin{aligned}\hat{U} &= \exp\left(-i \int_0^t \hat{\mathcal{H}}_g(t') dt'\right) \\ &= \exp\left(i\gamma z \hat{F}_z \int_0^t G(t') dt'\right) \\ &= \exp\left(is\gamma G z t \hat{F}_z\right).\end{aligned}$$

In the last line we have introduced the *shape factor* s which is given by

$$s = \frac{1}{Gt} \int_0^t G(t') dt',$$

where G is the maximum amplitude of the gradient. The shape factor is the fraction of the area under a shaped PFG compared to a rectangular gradient profile with the same maximum strength and duration. The spatially-dependent phase that is imparted on $\hat{\sigma}^{(p)}(0)$ is now

$$\phi(z) = s p \gamma G z t.$$

One common shape for a PFG is the half-sine bell. Its mathematical form is

$$G(t) = G \sin\left(\frac{\pi t}{\delta}\right),$$

where δ is the length of the PFG. The shape factor is $2/\pi$.

2.3.3 Coherence transfer pathway selection

Equation 2.6 indicates that all coherences of non-zero coherence order are dephased in the presence of a PFG. However, it is possible to refocus some of the coherences by subsequently applying one or more PFGs. The refocusing condition is that the sum of the spatially-dependent phases at the end of the sequence must be zero:

$$\sum_k \phi^{(k)}(z) = 0, \tag{2.7}$$

where $\phi^{(k)}(z)$ is the phase due to the k th PFG in the sequence. Assuming that the coherence is present on the same species of spin throughout the sequence (so that γ is unchanged) and that all the PFGs have the same shape factor, the refocusing condition becomes

$$\sum_k p^{(k)} G^{(k)} \delta^{(k)} = 0, \quad (2.8)$$

where $\delta^{(k)}$ is the duration of the k th PFG. For example, if there are two PFGs, the following ratio of coherence orders will be selected:

$$\frac{p^{(1)}}{p^{(2)}} = -\frac{G^{(2)} \delta^{(2)}}{G^{(1)} \delta^{(1)}}.$$

Any other CTPs that do not satisfy Equation 2.8 will remain dephased.

2.4 Selective pulses

Many of the standard NMR experiments use non-selective RF pulses to excite the whole spectrum uniformly. However, there are some situations where it is useful to excite a small range of frequencies, say a single multiplet. This selective excitation is usually achieved by employing low-power pulses.

2.4.1 Rectangular selective pulses

The simplest selective pulse has a rectangular time profile, i.e. the B_1 field is constant. For a one-spin system, the Hamiltonian for this pulse is (from Equation 1.15)

$$\hat{\mathcal{H}}_{\text{sel}} = \omega_{\text{eff}} \hat{R}_y(\theta) \hat{I}_z \hat{R}_y(\theta)^{-1},$$

where we have assumed that the B_1 field is along x . The pulse can be represented by a propagator $\hat{R}_\theta(\alpha)$ which represents a rotation about an axis that is inclined from z by angle θ (the angle by which the effective field \mathbf{B}_{eff} is tilted), through an angle $\alpha = \omega_{\text{eff}} t_p$. It is given by

$$\hat{R}_\theta(\alpha) = \hat{R}_y(\theta) \hat{R}_z(\alpha) \hat{R}_y(\theta)^{-1}.$$

The effect of the pulse on an initial density operator $\hat{\sigma}(0)$ is calculated from

$$\hat{\sigma}(t_p) = \hat{R}_\theta(\alpha) \hat{\sigma}(0) \hat{R}_\theta(\alpha)^{-1}. \quad (2.9)$$

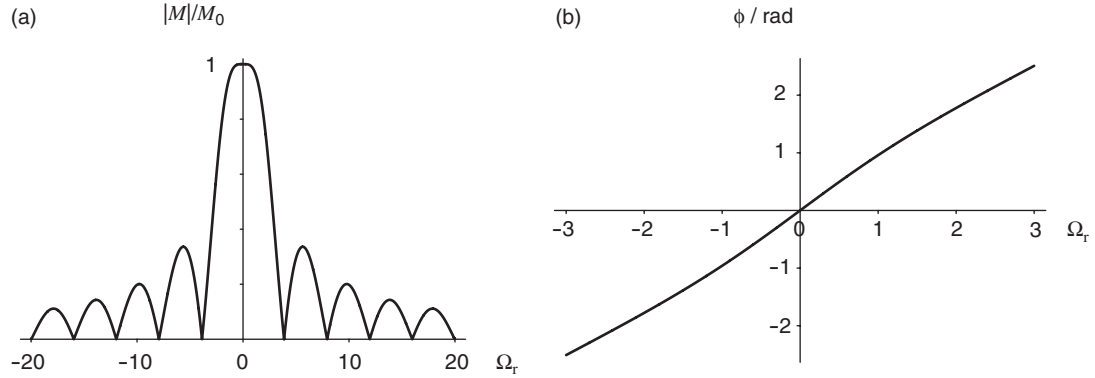


Figure 2.3: Excitation profile of a rectangular pulse with an on-resonance flip angle of $\alpha_0 = \pi/2$ plotted as a function of Ω_r . The value of the absolute magnetization is shown in (a), and its phase is shown in (b).

Selective excitation

Starting from the equilibrium density operator $\hat{\sigma}_0$ the components of the magnetization which are calculated using Equation 2.9 are:

$$\begin{aligned} M_x/M_0 &= \Omega_r \left(\frac{1 - \cos(\alpha_0 \sqrt{1 + \Omega_r^2})}{1 + \Omega_r^2} \right), \\ M_y/M_0 &= -\frac{\sin(\alpha_0 \sqrt{1 + \Omega_r^2})}{\sqrt{1 + \Omega_r^2}}, \\ M_z/M_0 &= \frac{\Omega_r^2 + \cos(\alpha_0 \sqrt{1 + \Omega_r^2})}{1 + \Omega_r^2}, \end{aligned}$$

where α_0 is the flip angle on-resonance, and $\Omega_r = \Omega/\omega_1$ is the relative offset. Figure 2.3 shows the absolute value of the magnetization $|M|$ in (a) and its phase ϕ in (b), which are defined as

$$|M| = \sqrt{M_x^2 + M_y^2} \quad \tan \phi = \frac{M_y}{M_x},$$

as a function of Ω_r after a 90° selective pulse. Together, these plots form the *excitation profile* of the pulse.

The range of offsets for which the excitation gives 90% of the maximum intensity is $-1.58\omega_1 < \Omega < +1.58\omega_1$. Outside this range, the magnitude of the transverse magnetization falls off rapidly as the rotation axis moves closer to the z -axis. However,

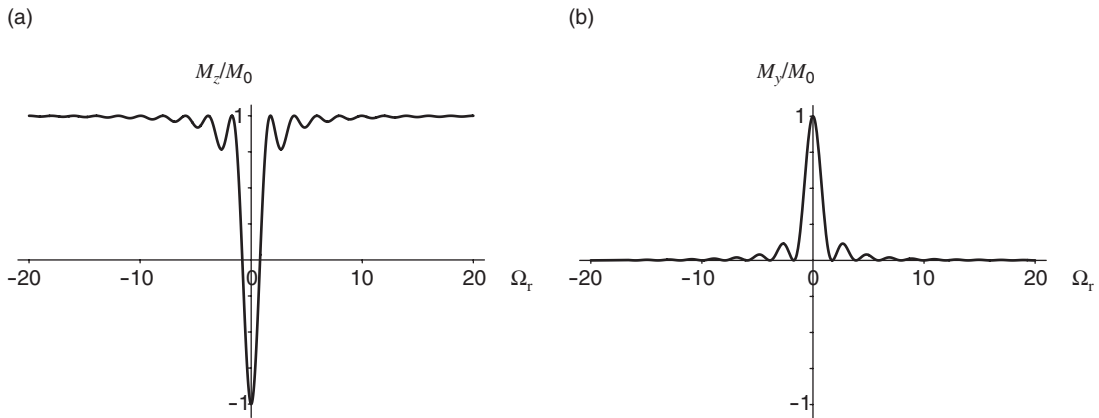


Figure 2.4: The inversion and excitation profiles of pulse-sequence elements containing a 180° rectangular pulse. The inversion profile is calculated by applying the pulse to equilibrium z -magnetization, and is shown in (a). The plot in (b) shows the y -magnetization following the application of the same pulse to the $-y$ -magnetization that is present immediately after a hard 90° pulse along x .

there are two drawbacks to using this pulse for selective excitation. Firstly, the actual envelope of the excitation is broader than the central lobe. This envelope varies as Ω_r^{-1} and contains a series of ‘sinc lobes’ which are due to the discontinuities in the time profile of the B_1 field at $t = 0$ and $t = t_p$. Secondly, the phase of the excited magnetization is offset-dependent, and so each peak in the spectrum will have a different phase.

Selective inversion

The same pulse can also be used to achieve selective inversion of the equilibrium z -magnetization by using an on-resonance flip angle of 180° ; the resulting *inversion profile* is shown in Figure 2.4 (a). The range of offsets for which the efficiency of the inversion is 90% is $-0.23\omega_1 < \Omega < +0.23\omega_1$, which is rather smaller than the region of efficient excitation of the 90° pulse. There are also sinc lobes present in the inversion profile, but they are less pronounced than those in the excitation profile in Figure 2.3 (a).

Selective excitation using a soft 180° pulse

Selective excitation can also be achieved by applying a hard 90° pulse followed by a selective 180° pulse. The density operator after the hard pulse is $-\hat{I}_y$. Subsequently

applying the selective pulse gives the following x and y -magnetization:

$$\begin{aligned} M_x/M_0 &= \Omega_r \frac{\sin(\alpha_0 \sqrt{1 + \Omega_r^2})}{\sqrt{1 + \Omega_r^2}}, \\ M_y/M_0 &= -\cos(\alpha_0 \sqrt{1 + \Omega_r^2}). \end{aligned}$$

As yet, we have no selectivity since the hard pulse excited all frequencies. However, this problem is solved simply by applying EXORCYCLE to the selective pulse; the component of the magnetization that experiences a coherence order change of ± 2 is therefore selected. Applying this phase cycle now gives the following x and y -magnetization:

$$\begin{aligned} M_x/M_0 &= 0, \\ M_y/M_0 &= \frac{\sin^2(\frac{1}{2}\alpha_0 \sqrt{1 + \Omega_r^2})}{\sqrt{1 + \Omega_r^2}}. \end{aligned}$$

M_y is plotted in Figure 2.4 (b). We have now achieved frequency selectivity and, since $M_x = 0$, the phase is constant across all offsets.

The inversion profile in Figure 2.4 (a) and the excitation profile in (b) are related to each other as follows. If we define $f_{\text{inv}}(\Omega_r)$ as the former, and $f_{\text{refoc}}(\Omega_r)$ as the latter, then it can be seen that

$$f_{\text{refoc}}(\Omega_r) = \frac{1}{2} \{1 - f_{\text{inv}}(\Omega_r)\}.$$

2.4.2 Shaped pulses

The excitation and inversion profiles of the rectangular pulse all exhibit the broad envelope with the sinc lobes which result in offsets far off-resonance experiencing a significant excitation. The presence of these undesirable lobes is due to the discontinuities in the B_1 field at the start and end of the pulse. Alternative excitation and inversion profiles can be generated by employing a pulse profile in which the B_1 field increases smoothly from zero at the start, and decreases back to zero at the end.

For such a pulse, the Hamiltonian is time-dependent (and does not commute with itself at different times), and so there is no longer a straightforward analytical solution to the Liouville–von Neumann equation. The excitation profiles have to be determined numerically using a simulation program such as SIMPSON [18, 19] or SPINEVOLUTION [20].

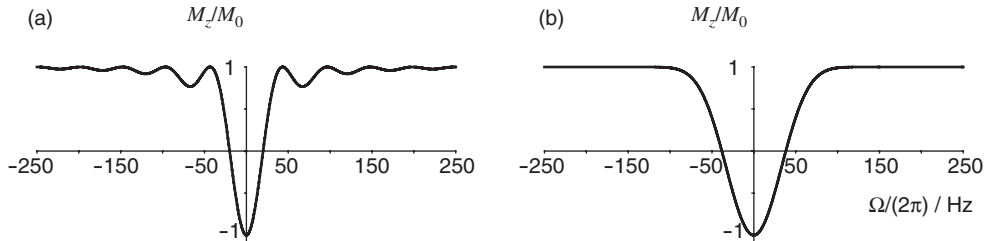


Figure 2.5: Inversion profiles of a rectangular and Gaussian pulse with on-resonance flip angles of 180° . Both pulses have a duration of 20 ms. The inversion profile of the rectangular pulse, which was calculated with $\omega_1/(2\pi) = 25 \text{ Hz}$, is shown in (a). The inversion profile of the Gaussian pulse is shown in (b), and was calculated using a maximum $\omega_1/(2\pi)$ of 60.7 Hz. The pulse time profile was truncated at 1% of its maximum value.

A simple choice of shaped pulse is the Gaussian [21]. Figure 2.5 compares the inversion profiles of a rectangular pulse (a) and a Gaussian pulse (b) of flip angle 180° , and equal duration. Both were simulated using SPINEVOLUTION [20]. The inversion profile of the Gaussian pulse has a broader central lobe, but the excitation envelope tails off more rapidly than for the rectangular pulse.

2.5 Broadband inversion

It is often desirable to be able to invert the z -magnetization over a wide range of offsets (*broadband inversion*). Standard hard 180° pulses may not give adequate results for two reasons.

Firstly, as the offset increases the effective field becomes tilted further towards the z -axis; the resulting trajectory of the magnetization is such that the end point lies further and further from $-z$. The region of offsets over which we obtain 90% inversion was calculated in Section 2.4.1; for a pulse with $\omega_1/(2\pi) = 20 \text{ kHz}$ this offset range is 9.2 kHz. For ^1H at 500 MHz, the 10 ppm range is equivalent to 5 kHz, and so this inversion performance may well be adequate. However, ^{13}C nuclei at 125 kHz have an offset range of 25 kHz (200 ppm), and so a pulse with a larger ω_1 is required.

Secondly, in practice the B_1 field is spatially inhomogeneous, and so each slice of the sample experiences a pulse of a slightly different flip angle. This means that it is not possible to calibrate the pulse length to give perfect inversion over the whole sample, even on-resonance.

When the 180° is used as a refocusing element, the effects of offset and inhomogeneity are reduced.

geneity can be mitigated by using standard CTP selection methods. However, these cannot be used to achieve improved population inversion, and so other methods are necessary. The work in this thesis makes extensive use of swept-frequency pulses, which are the subject of this Section.

2.5.1 Adiabatic inversion pulses

One commonly used method for achieving efficient inversion across the whole spectrum is to employ a swept-frequency 180° pulse, such as the CHIRP pulse [22–24]. In this pulse the RF field has a constant amplitude, and a frequency $\omega_{\text{rf}}(t)$ that is swept across the whole spectrum at a constant rate, starting far off-resonance on one side, and finishing far off-resonance on the other side. If the field is swept sufficiently slowly, so that it satisfies the adiabatic condition, the pulse achieves broadband inversion.

The accelerating and tilting frames of reference

The frequency of the field changes linearly, which suggests that the swept pulse is most easily described in an accelerating frame of reference in which B_1 field is always aligned along x . The frequency $\omega_{\text{rf}}(t)$ starts at a negative offset that is far off-resonance, and so the effective field \mathbf{B}_{eff} is initially aligned along $+z$. As the frequency approaches zero, $\Delta\mathbf{B}$ is reduced until it is zero exactly on resonance. Afterwards, as the field is swept through the positive frequencies, $\Delta\mathbf{B}$ grows along the $-z$ axis until, far off-resonance, \mathbf{B}_{eff} is aligned along $-z$. The effective field therefore rotates about the y axis from $+z$ to $-z$ as shown in Figure 2.6. If the rotation of \mathbf{B}_{eff} about y is sufficiently slow, the magnetization vector will follow the field from its initial position along z to its final position along $-z$.

This behaviour is more easily explained by using a tilting frame of reference (x', y', z') [25,26], where the accelerating frame is rotated about its y -axis at frequency $\omega_{\text{add}}(t)$, which matches the rate at which \mathbf{B}_{eff} is rotated about y . The Hamiltonian can be written as the sum of two parts: $\hat{\mathcal{H}} = \hat{\mathcal{H}}_0 + \hat{\mathcal{H}}_1$, where

$$\begin{aligned}\hat{\mathcal{H}}_0 &= \omega_{\text{add}}(t)\hat{I}_y \\ \hat{\mathcal{H}}_1 &= \omega_{\text{eff}}(t)\hat{R}_y(\theta(t))\hat{I}_z\hat{R}_y(\theta(t))^{-1} - \omega_{\text{add}}(t)\hat{I}_y.\end{aligned}$$

As is described in Section 1.3.3, the term $\hat{\mathcal{H}}_1$ can be transformed into the interaction

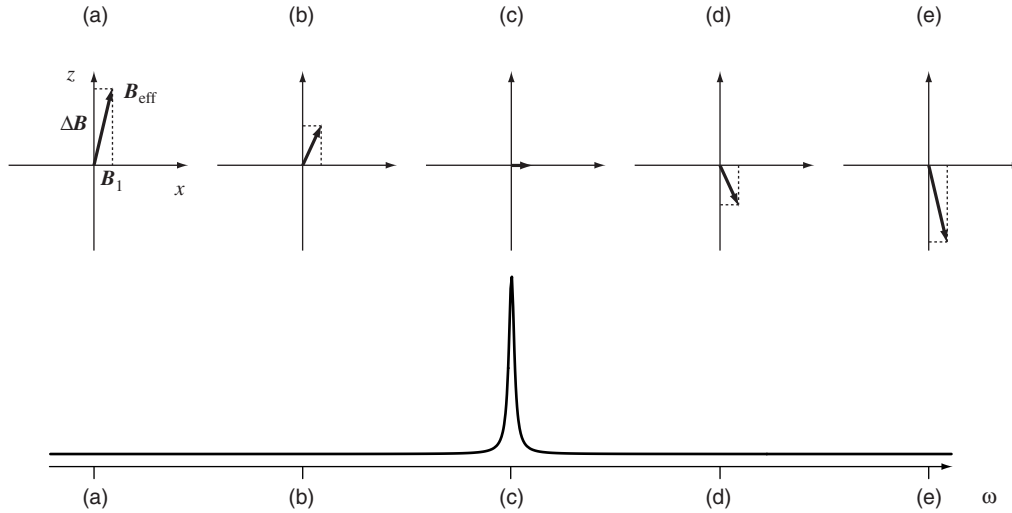


Figure 2.6: The effective field of the CHIRP at different times. The field \mathbf{B}_{eff} is shown at five different points (a)–(e). The diagrams in (a) and (e) show the field when the sweep is far off-resonance, and (c) when the field is on-resonance.

frame of $\hat{\mathcal{H}}_0$ using the propagator

$$\hat{U}_0 = \exp\left(-i\hat{I}_y \int_0^t \omega_{\text{add}}(t') dt'\right).$$

If we set $\omega_{\text{add}}(t) = d\theta(t)/dt$, the result is

$$\begin{aligned}\hat{\mathcal{H}}_1^T &= \omega_{\text{eff}}(t)\hat{I}_z - \omega_{\text{add}}(t)\hat{I}_y \\ &= \omega_{\text{total}}(t)\hat{R}_x(\xi)\hat{I}_z\hat{R}_x(\xi)^{-1},\end{aligned}$$

where

$$\omega_{\text{total}} = \sqrt{\omega_{\text{eff}}^2 + \omega_{\text{add}}^2}, \quad \text{and} \quad \tan \xi = \frac{\omega_{\text{add}}}{\omega_{\text{eff}}}.$$

This indicates that, in the tilting frame, the magnetization precesses about a magnetic field $\mathbf{B}_{\text{total}}$ that is the resultant of the effective field \mathbf{B}_{eff} that is along z' and a field \mathbf{B}_{add} that is along the $-y'$ axis. The magnitudes of the fields B_{add} and B_{total} are given by:

$$B_{\text{add}} = \omega_{\text{add}}/|\gamma| \quad B_{\text{total}} = \omega_{\text{total}}/|\gamma|.$$

If the pulse is adiabatic, so that $\omega_{\text{add}}(t) \ll \omega_{\text{eff}}(t)$, the z -magnetization will remain parallel to the effective field. Therefore, in the *accelerating* frame, it will follow the

effective field from $+z$ to $-z$. The frequency $\omega_{\text{add}}(t)$ is given by

$$\begin{aligned}\omega_{\text{add}}(t) &= \frac{d\theta(t)}{dt} \\ &= \frac{d}{dt} \tan^{-1} \left(\frac{\omega_1}{\Omega - \omega_{\text{rf}}(t)} \right) \\ &= \frac{\omega_s}{t_p} \frac{\omega_1}{\omega_1^2 + (\Omega - \omega_{\text{rf}}(t))^2},\end{aligned}$$

where ω_s is the range of frequencies that is swept through in time t_p . The frequency ω_{add} has its greatest value when the sweep is on-resonance with the spins ($\omega_{\text{rf}}(t) = \Omega$), i.e.

$$\omega_{\text{add}}^{\text{on res.}} = \frac{\omega_s}{t_p} \frac{1}{\omega_1}.$$

In this case, the adiabatic condition becomes

$$\frac{\omega_s}{t_p} \ll \omega_1^2. \quad (2.10)$$

The strength of the field therefore needs to be high enough to satisfy Equation 2.10. Provided that this condition is met, it is found that the efficiency of the inversion is independent of ω_1 , and so the sweep is very tolerant to RF inhomogeneity.

It is found in practice that a better inversion profile is obtained if the RF amplitude is smoothed both at the beginning and end of the pulse; ω_1 is increased slowly from zero to its maximum value at the beginning, and decreased back to zero at the end [24]. This ensures that, at the beginning of the pulse, \mathbf{B}_{eff} lies along $+z$ irrespective of how far off resonance the value of $\omega_{\text{rf}}(0)$ is set; likewise, at the end of the pulse, \mathbf{B}_{eff} lies along $-z$. Typically, up to 20% of the duration of the pulse may be smoothed in this way. A simulation of a typical inversion profile is shown in Figure 2.7. The range of offsets over which complete inversion is achieved is larger than for a hard 180° pulse of the same RF field. However, this increase in the bandwidth must be bought at the price of an increase in the duration of the pulse.

2.5.2 Adiabatic refocusing

The linear frequency sweep is achieved in practice by giving the phase of the RF pulse a quadratic time dependence. The transmitter frequency sweeps from $-\omega_s/2$ at $t = 0$ to $+\omega_s/2$ at $t = t_p$. Therefore at an arbitrary time t it is given by

$$\omega_{\text{rf}}(t) = \omega_s \left(\frac{t}{t_p} - \frac{1}{2} \right). \quad (2.11)$$

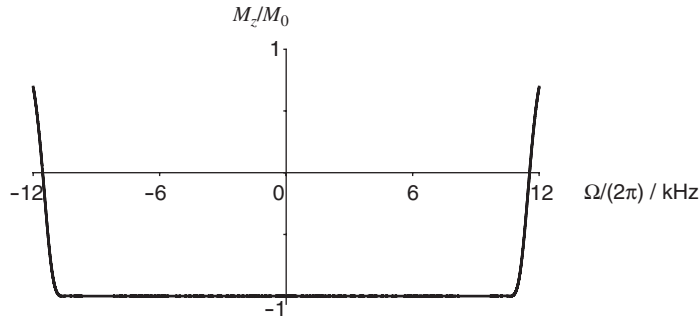


Figure 2.7: Simulated inversion profile of an adiabatic CHIRP pulse. The pulse parameters are: $\omega_s/(2\pi) = 24 \text{ kHz}$, $\omega_1/(2\pi) = 1.5 \text{ kHz}$, and $t_p = 24 \text{ ms}$. The first and last 10% of the RF amplitude profile were smoothed by multiplication by a sine wave.

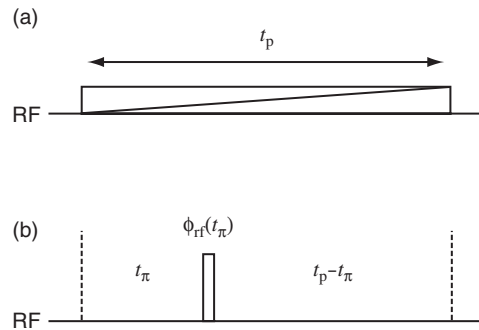


Figure 2.8: The hard-pulse model of a swept-frequency 180° pulse. The swept pulse is shown in (a) as an unfilled rectangle with a diagonal stroke. This can be modelled as a hard 180° pulse with an offset-dependent timing t_π and phase $\phi_{rf}(t_\pi)$, as shown in (b).

The phase of RF field $\phi_{rf}(t)$ is then given by

$$\begin{aligned}\phi_{rf}(t) &= \int_0^t \omega_{rf}(t') dt' \\ &= \frac{\omega_s}{2} \left(\frac{t^2}{t_p} - t \right),\end{aligned}\quad (2.12)$$

which has a quadratic time dependence.

To facilitate calculations involving a swept pulse acting on transverse magnetization, it proves useful to model the sweep according to Figure 2.8. We assume that firstly the RF field has no effect on the magnetization when off-resonance, and secondly, when the sweep is on-resonance at time t_π , the 180° rotation is instantaneous. Therefore, the model for the sweep comprises a delay t_π followed by a hard 180° pulse

of phase $\phi_{\text{rf}}(t_\pi)$ (which is equal to the instantaneous phase of the swept pulse at $t = t_\pi$) and a second delay $t_p - t_\pi$.

We can now calculate the effect of a sweep on the operator \hat{I}_+ . During the first period of free precession, \hat{I}_+ acquires a phase to give

$$\hat{I}_+ \exp(-i\Omega t_\pi).$$

The 180° pulse transforms \hat{I}_+ according to Equation 1.20 to give

$$\hat{I}_- \exp(-i\Omega t_\pi) \exp(i2\phi_{\text{rf}}(t_\pi)).$$

Finally, evolution during $t_p - t_\pi$ gives

$$\hat{I}_- \exp(-i\Omega t_\pi) \exp(i2\phi_{\text{rf}}(t_\pi)) \exp(i\Omega(t_p - t_\pi)) = \hat{I}_- \exp(i\Omega(t_p - 2t_\pi)) \exp(i2\phi_{\text{rf}}(t_\pi)),$$

from which it is seen that the effective evolution time is $t_p - 2t_\pi$, i.e. the evolution of the offset has been partially refocused by a spin echo of length $2t_\pi$. The value of t_π can be calculated from Equation 2.11 by setting $\omega_{\text{rf}}(t_\pi) = \Omega$. The phase acquired by the operator is therefore

$$\Omega(t_p - 2t_\pi) + 2\phi_{\text{rf}}(t_\pi) = -\frac{(4\Omega^2 + \omega_s^2)t_p}{4\omega_s},$$

which varies as Ω^2 .

The frequency-dependent phase can be refocused by applying a second swept pulse; this introduces a second frequency-dependent phase which cancels the first exactly, and returns the initial operator:

$$\begin{aligned} & \hat{I}_+ \exp(i\Omega(t_p - 2t_\pi)) \exp(i2\phi_{\text{rf}}(t_\pi)) \exp(-i\Omega(t_p - 2t_\pi)) \exp(-i2\phi_{\text{rf}}(t_\pi)) \\ &= \hat{I}_+. \end{aligned}$$

2.5.3 Partially adiabatic inversion pulses

There is a second class of swept-frequency 180° pulses, known as *broadband inversion pulses* (BIPs), for which the transmitter frequency is swept in a partially-adiabatic manner [27]. In other words, the magnetization is aligned with the effective field for only part of the pulse duration.

The phase-time profile is divided into regions that are numerically optimized separately to achieve inversion over a defined range of offsets and RF field strengths

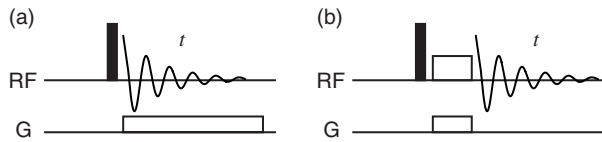


Figure 2.9: Pulse sequences for basic imaging experiments. The line labelled ‘G’ gives the timings of the magnetic field gradients. The sequence in (a) is designed to broaden the spectrum into an image of the sample. It achieves this with a magnetic field gradient applied during acquisition. The sequence in (b) selectively excites a slice of the sample. A selective 180° pulse (indicated by the unfilled rectangle on the RF channel) is applied simultaneously to a gradient.

(thus accounting for inhomogeneity). Each region of the phase profile is fitted to a cubic time function, and so the transmitter offset is swept non-linearly. It has been shown that these BIPs are able to give efficient inversion over a wider range of offsets and have a greater tolerance to RF inhomogeneity than adiabatic pulses, despite the pulse length of the former being much lower. A typical pulse length and field strength are 100 μs and 20 kHz.

Broadband inversion pulses are labelled according to BIP-*a*-*b*-*c*, where *a* is the pulse flip angle for a conventional rectangular pulse of the same duration and field strength. The range of offsets and percentage deviation of the RF field for which we get 99% inversion are given by $b = 100 \times \Delta B/B_1^0$ and $B_1^0(1 \pm c/100)$, where B_1^0 is the nominal RF field strength.

2.6 Nuclear magnetic resonance imaging

Nuclear magnetic resonance imaging is an extension of NMR which is used to determine a spatial image of a sample [28]. In its simplest form, we apply a magnetic field gradient during acquisition; the pulse sequence is shown in Figure 2.9 (a). In Section 2.3.1, it was shown that in the presence of a gradient, each spin evolves at a modified offset Ω_z . For a one-spin system, the Hamiltonian is

$$\hat{\mathcal{H}}_g = \Omega_z \hat{I}_z,$$

where $\Omega_z = \Omega - \gamma G z$; the spins therefore precess at a frequency that depends on their *z*-coordinate. The amplitude of the signal from each slice of the sample depends upon the number spins present in that slice, which is given by $\rho(z) dz$, where $\rho(z)$ is the *spin density*.

The time-domain signal $s(t, z)$ that is acquired from a slice at position z is given by

$$s(t, z) = \exp(i(\Omega - \gamma G z)t) \exp(-t/T_2) \rho(z) dz.$$

The FID that is acquired from the whole sample is therefore

$$\begin{aligned} s(t) &= \int_{-L/2}^{L/2} \exp(i(\Omega - \gamma G z)t) \exp(-t/T_2) \rho(z) dz \\ &= \exp(i\Omega t) \exp(-t/T_2) \times \int_{-L/2}^{L/2} \exp(-i\gamma G z t) \rho(z) dz. \end{aligned}$$

It is a product of two functions, and so $S(\omega)$ is the convolution of their Fourier transforms. The Fourier transform of the z -independent part $\exp(i\Omega t) \exp(-t/T_2)$ is a Lorentzian, and this is convoluted with the Fourier transform of the integral over the sample, which gives the following expression for $S(\omega)$:

$$\begin{aligned} S(\omega) &= \frac{1}{2\pi} [\mathcal{A}_\Omega(\omega) + i\mathcal{D}_\Omega(\omega)] * \left[\int_{-\infty}^{\infty} dt \exp(-i\omega t) \int_{-L/2}^{L/2} dz \exp(-i\gamma G z t) \rho(z) \right] \\ &= \frac{1}{2\pi} [\mathcal{A}_\Omega(\omega) + i\mathcal{D}_\Omega(\omega)] * \left[\int_{-L/2}^{L/2} dz \rho(z) \int_{-\infty}^{\infty} dt \exp(-i(\omega + \gamma G z)t) \right] \\ &= [\mathcal{A}_\Omega(\omega) + i\mathcal{D}_\Omega(\omega)] * \left[\int_{-L/2}^{L/2} dz \rho(z) \delta(\omega + \gamma G z) \right] \\ &= [\mathcal{A}_\Omega(\omega) + i\mathcal{D}_\Omega(\omega)] * \left[\frac{1}{\gamma G} \rho\left(\frac{-\omega}{\gamma G}\right) \right], \end{aligned}$$

where $\delta(x)$ is the Dirac delta function. The Lorentzian is convoluted with $\frac{1}{\gamma G} \rho\left(\frac{-\omega}{\gamma G}\right)$, which represents the spin density function converted to a frequency scale. When the sample is homogeneous, as is the case for all the samples used in the work described in this thesis, $\rho(z) = 1/L$, and the spectrum becomes

$$S(\omega) = [\mathcal{A}_\Omega(\omega) + i\mathcal{D}_\Omega(\omega)] * \left[\frac{1}{\gamma GL} T\left(\frac{-\omega}{\gamma G}\right) \right],$$

where $T\left(\frac{-\omega}{\gamma G}\right)$ is a top-hat function which is defined as

$$T\left(\frac{-\omega}{\gamma G}\right) = \begin{cases} 1, & -\frac{1}{2}\gamma GL \leq \omega \leq +\frac{1}{2}\gamma GL \\ 0, & \text{otherwise} \end{cases}.$$

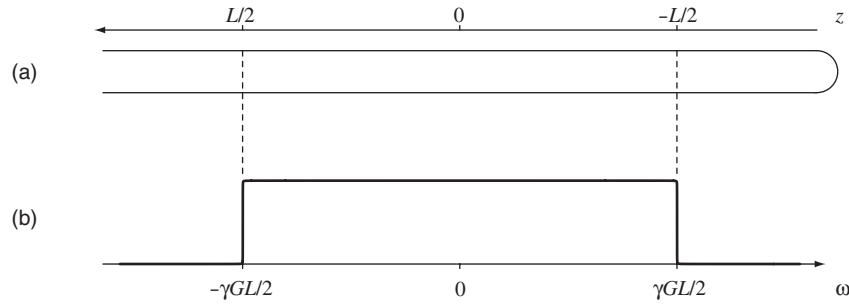


Figure 2.10: Illustration of a one-dimensional image along the z -axis of a homogeneous sample. The offset Ω is zero. A schematic of the sample is shown in (a), with the region contributing to the signal (between $-\frac{1}{2}L$ and $\frac{1}{2}L$) indicated by the dashed lines. The spectrum is shown in (b). Spins that are located at position z in the sample give a signal at frequency $-\gamma Gz$. The ratio of the width of the image to the width of the absorption-mode Lorentzian is 12773:1, and so the effect of the convolution cannot be seen.

The spins that are present at position z produce a signal that is centred at frequency $\Omega - \gamma Gz$ in the spectrum. The extreme edges of the sample, located at $z = +L/2$ and $z = -L/2$, therefore give signals that correspond to extremities of the image, which have frequencies $\Omega - \gamma GL/2$ and $\Omega + \gamma GL/2$. The width of the gradient-broadened image is therefore γGL . A schematic of a typical homogeneous sample is shown in Figure 2.10 (a), and the corresponding spectrum is shown in (b).

2.6.1 Slice-selective pulses

In Section 2.4 the idea of selective excitation was introduced, whereby it is possible to employ low-power RF pulses to excite spins over a small range of frequencies, whilst leaving the others unaffected. This idea can be combined with spatial imaging to enable the selective excitation of the spins in a single *slice* of the sample.

A typical pulse sequence is shown in Figure 2.9 (b). The selective 180° pulse is designed to invert a range of offsets ω_B (often referred to as the bandwidth) that is centred on Ω_0 . However, in the presence of the gradient, the offsets are proportional to z , and so we excite a slice of width $\Delta z = \omega_B/(\gamma G)$ that is centred on $z_0 = -\Omega_0/(\gamma G)$. The position of the slice is varied by adjusting the offset at which the selective pulse is applied, and the width of the slice is varied by adjusting the bandwidth.

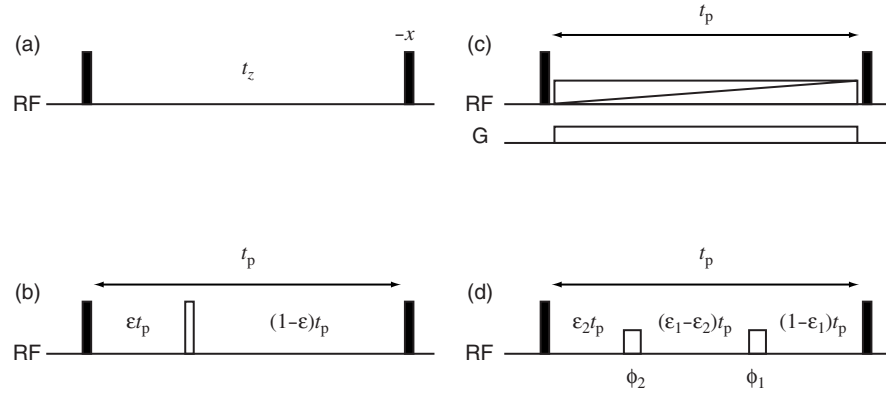


Figure 2.11: The various forms of the z -filter. The basic z -filter is shown in (a), in which the experiment is repeated with different values of t_z to suppress the ZQ coherence. A modified z -filter with a hard 180° pulse with variable timing is shown in (b). Suppression of the ZQ coherence can be achieved in a single scan using the filter in (c). The hard 180° pulse is replaced with a simultaneous swept-frequency 180° pulse and gradient. This last element can be modelled using the sequence in (d), in which the sweep is replaced with the two selective 180° pulses indicated by the unfilled rectangles. The first selective pulse acts on spin two only, and the second acts on spin one only (assuming that $\Omega_1 > \Omega_2$). Unless otherwise stated, all pulses are along x .

2.7 The z -filter

The z -filter is a pulse-sequence element that is used to purge terms from the expansion of the density operator that would otherwise introduce phase errors into the spectrum [29]. It is an important component of many two-dimensional experiments [30–32] and forms the basis of the work described in Chapter 4. The pulse sequence is shown in Figure 2.11 (a). It comprises two 90° pulses which flank a delay t_z . Standard coherence order selection methods are employed to select coherence order zero between the two pulses.

We will calculate the effect it has on the following density operator:

$$\hat{\sigma}(0) = c_{1x}\hat{I}_{1x} + c_{1y}\hat{I}_{1y},$$

which represents a combination of the two in-phase operators on spin one with coefficients c_{1x} and c_{1y} . Allowing this operator to evolve during the detection period will give an FID that contains two components that are 90° out of phase with each other. If the signal arising from \hat{I}_{1y} is phase-corrected to give an absorption-mode lineshape, the signal arising from \hat{I}_{1x} will be in dispersion. However, this unwanted

component is removed by the z -filter. The $90^\circ(x)$ pulse rotates \hat{I}_{1y} to \hat{I}_{1z} and leaves \hat{I}_{1x} unchanged to give

$$c_{1x}\hat{I}_{1x} + c_{1y}\hat{I}_{1z}.$$

Conventional coherence order selection is used to select coherence order zero, and so we only retain the z -magnetization. Finally, the $90^\circ(-x)$ pulse rotates this surviving term back to the y -axis to give

$$c_{1y}\hat{I}_{1y}.$$

The Fourier transform of the FID resulting from this operator will give a spectrum in the pure absorption mode.

However, there is a problem with the conventional z -filter. For coupled spin systems, the first 90° pulse generates ZQ coherence. Since this coherence has the same coherence order as z -magnetization, it is impossible to separate the two by using phase cycling or PFGs alone.

The ZQ coherence arises from anti-phase operators such as $2\hat{I}_{1x}\hat{I}_{2z}$ which are assumed to be present at the start of the filter. The first 90° pulse gives a mixture of DQ and ZQ coherence:

$$-2\hat{I}_{1x}\hat{I}_{2y} = -\frac{1}{2}(\hat{D}Q_y - \hat{Z}Q_y).$$

The DQ coherence is removed by coherence selection, leaving the ZQ term, which then evolves during the delay t_z at the ZQ frequency:

$$\frac{1}{2}\hat{Z}Q_y \xrightarrow{\hat{\mathcal{H}}_{\text{free}}t_z} \frac{1}{2}\hat{Z}Q_y \cos(\Omega_1 - \Omega_2)t_z - \frac{1}{2}\hat{Z}Q_x \sin(\Omega_1 - \Omega_2)t_z.$$

The last pulse generates the following:

$$\begin{aligned} & \frac{1}{2}[-2\hat{I}_{1z}\hat{I}_{2x} + 2\hat{I}_{1x}\hat{I}_{2z}] \cos(\Omega_1 - \Omega_2)t_z \\ & - \frac{1}{2}[2\hat{I}_{1x}\hat{I}_{2x} + 2\hat{I}_{1z}\hat{I}_{2z}] \sin(\Omega_1 - \Omega_2)t_z. \end{aligned}$$

The only observable terms are the anti-phase operators $2\hat{I}_{1z}\hat{I}_{2x}$ and $2\hat{I}_{1x}\hat{I}_{2z}$. Both represent x -magnetization and will give rise to a dispersive signal in the spectrum when \hat{I}_{1y} is phased to absorption. The term $2\hat{I}_{1x}\hat{I}_{2z}$ is a coherence on spin one, and so will give a dispersive anti-phase doublet on spin one. However, $2\hat{I}_{1z}\hat{I}_{2x}$ is a spin two coherence; this is an example of coherence transfer, where the anti-phase spin one coherence that was present before the z -filter has been partially transferred to the other spin. The resulting peaks are often called zero-quantum artefacts.

2.7.1 The suppression of zero-quantum coherence

Zero-quantum coherence and z -magnetization cannot be separated by conventional coherence-selection techniques, as both share the same coherence order of zero. However, there is a difference between the two forms of magnetization that allows the former to be suppressed; ZQ coherence evolves during a delay, whereas z -magnetization does not.

There are two types of suppression scheme, *multiple scan* and *single scan*, that both exploit this property of the ZQ coherence. In the multiple-scan suppression scheme, the experiment is repeated a number of times with a variation of the delay during which the coherence evolves. The coherence thus acquires a different phase in each experiment, and these phases result in the signal cancelling when the signal is summed. The single-scan technique uses the same idea, except that the ZQ coherence acquires a different phase in *different parts of the sample*, and so suppression is achieved in a single experiment.

Multi-scan suppression

The simplest method of suppression is to repeat the experiment a number of times with different values of t_z [33]. The N spectra are then summed, resulting in a net cancellation of the factors of $\cos[(\Omega_1 - \Omega_2)t_z^{(i)}]$, where $t_z^{(i)}$ is the value of t_z in the i th scan. The ZQ coherence is thus attenuated. The attenuation factor $A_{\text{multi},1}$ is given by

$$A_{\text{multi},1} = \frac{1}{N} \sum_{i=0}^{N-1} \cos[(\Omega_1 - \Omega_2)t_z^{(i)}].$$

This factor is plotted in Figure 2.12 (a) as a function of $\Omega_1 - \Omega_2$ for eight scans in which the values of $t_z^{(i)}$ are equally-spaced between 0 and 24 ms.

A variation of this idea is given in Figure 2.11 (b). The variable delay $t_z^{(i)}$ is replaced by a fixed element of duration t_p which contains a hard 180° pulse with a variable position. The timing of the 180° pulse within the element is given by εt_p where ε can take values between 0 and 1, and so it creates a spin echo of duration $2\varepsilon t_p$. Starting from $2\hat{I}_{1x}\hat{I}_{2z}$, the observable signal due to the presence of ZQ coherence during the filter is

$$-\frac{1}{2} [2\hat{I}_{1z}\hat{I}_{2x} - 2\hat{I}_{1x}\hat{I}_{2z}] \cos[(\Omega_1 - \Omega_2)(1 - 2\varepsilon)t_p];$$

the ZQ offset is refocused during the spin echo, and then evolves during the remaining delay $(1 - 2\varepsilon)t_p$.

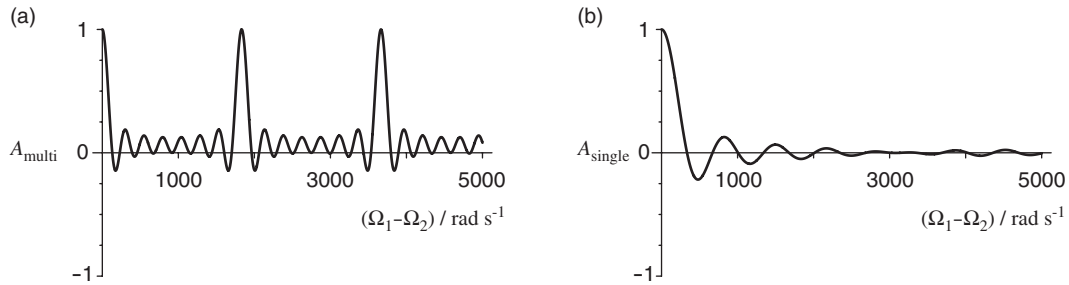


Figure 2.12: Attenuation curves generated by the different methods used for the suppression of ZQ coherence. The curve in (a) was generated using the multiple-scan method in Figure 2.11 (a) using eight values of t_z that are equally spaced between 0 and 24 ms. An identical attenuation curve is generated by using the method in Figure 2.11 (b) with eight scans in which ε takes equally spaced values between 0 and 0.5, and $t_p = 24$ ms. The attenuation curve in (b) was calculated using the approximation in Figure 2.11 (d) to the single-scan method in (c). The parameters are: $\Omega_2 = 0$, $t_p = 24$ ms, $\omega_s/(2\pi) = 24$ kHz, $\gamma = 26752.2 \text{ rad s}^{-1} \text{ G}^{-1}$, $G = 2.2 \text{ G cm}^{-1}$, and $L = 1.0 \text{ cm}$. The offset of spin one was varied from 0 to 5000 rad s^{-1} .

The experiment is repeated multiple times, with a variation in the value of ε . The value of ε is varied between 0 and 0.5, rather than between 0 and 1. The reason for this is that the z -filter in which the 180° pulse occurs at time t_π is exactly the same as one in which the pulse occurs at time $t_p - t_\pi$: in the first case, the spin echo is of duration $2t_\pi$ at the *beginning* of the filter, whilst in the second case the echo is of the same duration at the *end* of the filter. In both cases, the phase acquired by the ZQ coherence is the same. When the spectra are summed, there is a net cancellation in the intensities of the signals from the ZQ coherence. The attenuation factor $A_{\text{multi},2}$ is

$$A_{\text{multi},2} = \frac{1}{N} \sum_{i=0}^{N-1} \cos \left[(\Omega_1 - \Omega_2)(1 - 2\varepsilon_i) t_p \right],$$

where ε_i is the value of ε in the i th scan.

If both z -filters are applied so that both ε_i and $t_z^{(i)}$ are increased by a constant amount for each experiment, the number of experiments is the same for each, and t_p in the second method is equal to the maximum value of t_z in the first, $A_{\text{multi},2} \equiv A_{\text{multi},1}$. Therefore the plot in Figure 2.12 (a) could also have been generated with the second method using eight scans in which the values of ε_i are equally-spaced between 0 and 0.5, and $t_p = 24$ ms.

These methods suffer from two drawbacks. Firstly, it is evident that it is not

possible to suppress all ZQ artefacts equally well. Artefacts associated with certain ZQ frequencies will fall on nulls in the attenuation curve, resulting in complete suppression, whilst others will fall on maxima. If the ZQ frequencies are unknown before the experiment is run, as is usually the case, it is evident that the degree of suppression depends largely on luck. In particular, there are some frequencies for which the phases acquired in each scan are the same, and so there is no cancellation on summing the spectra—these frequencies are indicated by the points at which the attenuation factor is equal to one. Secondly, the repetition of the whole experiment will increase the experiment time, giving a prohibitively long experiment in some cases.

Single-scan suppression

Thrippleton *et al.* introduced a method that gives excellent suppression in a *single scan* [34, 35]. The element in the z -filter that contains the 180° pulse with a variable timing is replaced by a swept-frequency 180° pulse that is applied in the presence of a magnetic field gradient, as shown in Figure 2.11 (c). Conventionally, the swept pulse sweeps through the frequencies in the spectrum, resulting in spins of different offsets experiencing the 180° pulse at different times. In the presence of the gradient, the offsets are position-dependent, and so spins in different slices of the sample experience the pulse at different times. On summing the signal over the whole sample, it is found that there is a net attenuation of the ZQ coherence.

The simplest way of calculating the effect of the sweep-gradient element is to use the hard pulse model that was introduced in Section 2.5.2. Using this model all the spins in each slice of the sample experience the 180° pulse at the same time irrespective of their offsets. However, this is only true if the gradient term in the free-precession Hamiltonian dominates the chemical shift term, so that $|\gamma G_z| \gg |\Omega|$ for all the offsets. This is certainly not the case as the size of the gradient is limited by the range of offsets that are fully inverted by the swept pulse; for the inversion profile in Figure 2.7, the maximum value of $\gamma GL/(2\pi)$ is 21.2 kHz.

A better model is shown in Figure 2.11 (d). Rather than using one hard pulse, we employ two selective pulses that act on each of the two spins separately; the timing of the spin- i pulse is given by $\varepsilon_i t_p$ where ε_i is given by setting $\omega_{\text{rf}}(\varepsilon_i t_p) = \Omega_i - \gamma G_z$ in

Equation 2.11. This gives

$$\varepsilon_i = \frac{\Omega_i - \gamma G_z}{\omega_s} + \frac{1}{2}.$$

If we assume that $\Omega_1 > \Omega_2$, then $\varepsilon_1 > \varepsilon_2$. The phase of the spin- i selective pulse ϕ_i is given by $\phi_{\text{rf}}(\varepsilon_i t_p)$ in Equation 2.12:

$$\phi_i = \frac{\omega_s}{2} (\varepsilon_i^2 - \varepsilon_i) t_p.$$

We can now calculate the effect of this element on $2\hat{I}_{1x}\hat{I}_{2z}$. The ZQ term arising from the first pulse is $\frac{1}{2}\hat{Z}Q_y$, which evolves under the ZQ frequency during the first delay $\varepsilon_2 t_p$ to give

$$\frac{1}{2}\hat{Z}Q_y \cos [(\Omega_1 - \Omega_2) \varepsilon_2 t_p] - \frac{1}{2}\hat{Z}Q_x \sin [(\Omega_1 - \Omega_2) \varepsilon_2 t_p].$$

During the gradient the offsets are z -dependent; however, this dependence cancels when the difference between the two offsets is taken. The first 180° pulse is applied to spin two with phase ϕ_2 , and has the effect of converting $\hat{Z}Q_y$ and $\hat{Z}Q_x$ into $\hat{D}Q_y$ and $\hat{D}Q_x$ to give

$$\frac{1}{2}\hat{D}Q_y \cos [(\Omega_1 - \Omega_2) \varepsilon_2 t_p + 2\phi_2] - \frac{1}{2}\hat{D}Q_x \sin [(\Omega_1 - \Omega_2) \varepsilon_2 t_p + 2\phi_2].$$

Both operators evolve under the z -dependent DQ frequency $\Omega_1 + \Omega_2 - 2\gamma G_z$ during the second delay $(\varepsilon_1 - \varepsilon_2)t_p$. This results in

$$\begin{aligned} & \frac{1}{2}\hat{D}Q_y \cos [\Omega_1 \varepsilon_1 t_p + \Omega_2 (\varepsilon_1 - 2\varepsilon_2) t_p - 2\gamma G_z (\varepsilon_1 - \varepsilon_2) t_p + 2\phi_2] \\ & - \frac{1}{2}\hat{D}Q_x \sin [\Omega_1 \varepsilon_1 t_p + \Omega_2 (\varepsilon_1 - 2\varepsilon_2) t_p - 2\gamma G_z (\varepsilon_1 - \varepsilon_2) t_p + 2\phi_2]. \end{aligned}$$

The selective 180° pulse that is applied to spin one converts both operators back into ZQ coherence, giving

$$\begin{aligned} & - \frac{1}{2}\hat{Z}Q_y \cos [\Omega_1 \varepsilon_1 t_p + \Omega_2 (\varepsilon_1 - 2\varepsilon_2) t_p - 2\gamma G_z (\varepsilon_1 - \varepsilon_2) t_p + 2(\phi_2 - \phi_1)] \\ & - \frac{1}{2}\hat{Z}Q_x \sin [\Omega_1 \varepsilon_1 t_p + \Omega_2 (\varepsilon_1 - 2\varepsilon_2) t_p - 2\gamma G_z (\varepsilon_1 - \varepsilon_2) t_p + 2(\phi_2 - \phi_1)]. \end{aligned}$$

Evolution during the final delay $(1 - \varepsilon_1)t_p$ gives

$$\begin{aligned} & - \frac{1}{2}\hat{Z}Q_y \cos [\Omega_1 (1 - 2\varepsilon_1) t_p - \Omega_2 (1 - 2\varepsilon_2) t_p + 2\gamma G_z (\varepsilon_1 - \varepsilon_2) t_p + 2(\phi_2 - \phi_1)] \\ & + \frac{1}{2}\hat{Z}Q_x \sin [\Omega_1 (1 - 2\varepsilon_1) t_p - \Omega_2 (1 - 2\varepsilon_2) t_p + 2\gamma G_z (\varepsilon_1 - \varepsilon_2) t_p + 2(\phi_2 - \phi_1)]. \end{aligned}$$

Only the first term is transformed into observable magnetization, and so the second term can be discarded. The explicit z -dependence of the coefficient of $-\frac{1}{2}Z\hat{Q}_y$, $c(z)$, is found by substituting in the expressions for ε_i and ϕ_i . The resulting expression is

$$c(z) = \cos \left[\frac{(\Omega_1 - \Omega_2)(\Omega_1 + \Omega_2 - 2\gamma G z)t_p}{\omega_s} \right].$$

The attenuation factor A_{single} is the integral of $c(z)$ over the sample, which is

$$\begin{aligned} A_{\text{single}} &= \frac{1}{L} \int_{-L/2}^{L/2} c(z) dz \\ &= \cos \left[\frac{(\Omega_1^2 - \Omega_2^2)t_p}{\omega_s} \right] \operatorname{sinc} \left[\frac{\gamma GL(\Omega_1 - \Omega_2)t_p}{\omega_s} \right]. \end{aligned} \quad (2.13)$$

A representative attenuation curve is plotted in Figure 2.12 (b). The degree of suppression is greater for all the offsets that fall beyond the first lobe of the sinc function, as can be seen by comparing this plot to the multiple-scan attenuation curve in (a). Most importantly there are no non-zero offsets for which the ZQ coherence is not at least partially dephased, as there are for the multiple-scan method.

The cosine factor in Equation 2.13 gives the relative intensity of the ZQ coherence at the end of the z -filter in the absence of a gradient. It is simply an oscillation, and does not result in any dephasing. The factor that is responsible for the suppression is the decay envelope $(\gamma GL(\Omega_1 - \Omega_2)t_p/\omega_s)^{-1}$ in the sinc function, which decreases as the ZQ frequency $\Omega_1 - \Omega_2$ becomes larger. For lower ZQ frequencies, the degree of the attenuation is lower as the range of spatially-dependent phases across the whole sample is smaller.

Chapter 3

Two-dimensional *J*-spectroscopy

CONVENTIONAL ONE-DIMENSIONAL ^1H NMR SPECTRA contain information about the offsets (chemical shifts) of the spins, and the *J*-couplings between them. While this information is very useful for assigning the spectrum, there are many examples of spectra where neighbouring multiplets overlap with each other, making the assignment very difficult if not impossible. For instance, this problem is often encountered in the assignment of the individual components of a complex mixture.

One way of circumventing this problem is to employ a method which gives a spectrum in which there is a complete separation of the offsets and the *J*-couplings. In principle such a method would allow the acquisition of a one-dimensional ^1H spectrum that is broadband homonuclear-decoupled, i.e. a spectrum in which there is only a single line at each offset. The original method for obtaining this separation is known as *J*-spectroscopy [36]. This experiment has the advantage that it is very simple to implement; however, it has not been widely used owing to two problems. Firstly, the peaks in the spectrum have an unfavourable lineshape, which can only be removed at the expense of sensitivity and the introduction of intensity distortions, or complex data processing. Secondly, the presence of strong coupling results in extra peaks, thus adding unwanted complexity to the spectrum. Nevertheless, the work described in this thesis uses *J*-spectroscopy as a starting point, and so the basic experiment will be described.

3.1 *J*-spectroscopy of a weakly-coupled two-spin system

In this Section, the basic *J*-spectroscopy pulse sequence will be analyzed for two weakly-coupled spins, and the steps needed to separate the offsets and couplings and obtain the decoupled spectrum will be outlined.

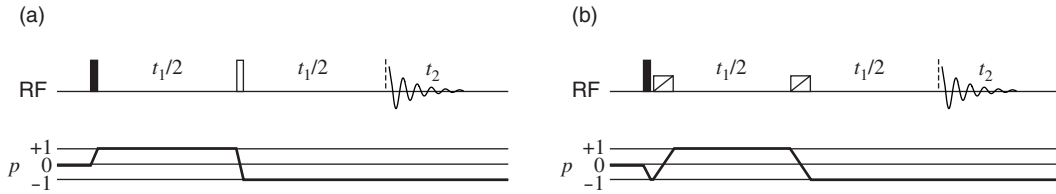


Figure 3.1: The pulse sequences and CTPs for J -spectroscopy. The basic sequence is shown in (a), which uses a hard 180° pulse in the spin echo. The sequence in (b) uses a pair of swept-frequency 180° pulses. Two such pulses are needed so that the phase errors generated by the first are refocused by the second.

3.1.1 Analysis of the pulse sequence

The pulse sequence and CTP for basic J -spectroscopy are shown in Figure 3.1 (a). The sequence comprises a simple spin echo during t_1 , which is followed immediately by acquisition with no mixing period. The spectrum of a weakly-coupled two-spin system can be calculated easily by using a basis operator approach. Since the structures of the multiplets are of great interest, we shall proceed using the single-element operators.

The 90° pulse rotates the equilibrium density operator to the $-y$ -axis as follows:

$$\begin{aligned} \hat{I}_{1z} + \hat{I}_{2z} &\xrightarrow{(\pi/2)\hat{F}_x} -\hat{I}_{1y} - \hat{I}_{2y} \\ &\equiv -\hat{I}_{1y}\hat{E}_2 - \hat{E}_1\hat{I}_{2y} \\ &= \frac{1}{2}i(\hat{I}_{1+} - \hat{I}_{1-})(\hat{I}_{2\alpha} + \hat{I}_{2\beta}) + \frac{1}{2}i(\hat{I}_{1\alpha} + \hat{I}_{1\beta})(\hat{I}_{2+} - \hat{I}_{2-}). \end{aligned}$$

Only the terms with coherence order +1 are retained, as only these give observable signal during t_2 . These four terms evolve during the first half of the spin echo to give

$$\begin{aligned} &\frac{1}{2}i\hat{I}_{1+}\hat{I}_{2\alpha} \exp[-i(\Omega_1 + \pi J_{12})t_1/2] + \frac{1}{2}i\hat{I}_{1+}\hat{I}_{2\beta} \exp[-i(\Omega_1 - \pi J_{12})t_1/2] \\ &+ \frac{1}{2}i\hat{I}_{1\alpha}\hat{I}_{2+} \exp[-i(\Omega_2 + \pi J_{12})t_1/2] + \frac{1}{2}i\hat{I}_{1\beta}\hat{I}_{2+} \exp[-i(\Omega_2 - \pi J_{12})t_1/2]. \end{aligned}$$

The 180° pulse converts \hat{I}_{i+} to \hat{I}_{i-} and changes the polarization of the passive spin. The transformed operators then evolve during the second half of the spin echo to give

$$\begin{aligned} &\frac{1}{2}i\hat{I}_{1-}\hat{I}_{2\beta} \exp[-i\pi J_{12}t_1] + \frac{1}{2}i\hat{I}_{1-}\hat{I}_{2\alpha} \exp[+i\pi J_{12}t_1] \\ &+ \frac{1}{2}i\hat{I}_{1\beta}\hat{I}_{2-} \exp[-i\pi J_{12}t_1] + \frac{1}{2}i\hat{I}_{1\alpha}\hat{I}_{2-} \exp[+i\pi J_{12}t_1]; \end{aligned}$$

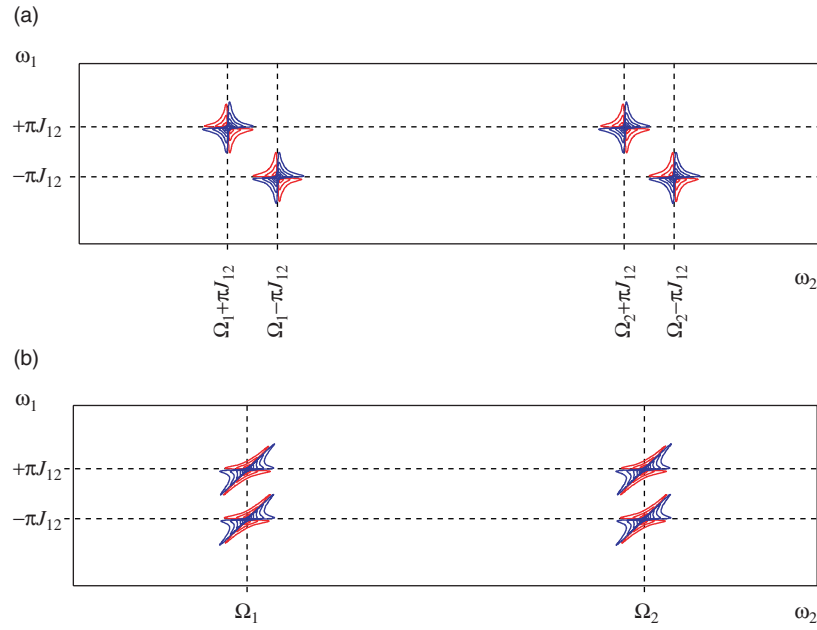


Figure 3.2: Two-dimensional J -spectra of a weakly-coupled two-spin system. The J -spectrum is shown in (a), in which the multiplets are centred on $\omega_1 = 0$, and lie parallel to the main diagonal. Shearing this spectrum by -45° , as explained in the text, produces the spectrum in (b) which has a complete separation of offsets and J -couplings. The peaks in the J -spectrum have the phase-twist lineshape. Contours of positive intensity are blue, and negative contours are red.

the offset has been refocused, while the coupling has evolved throughout. Finally, each term evolves during the detection period t_2 . The final density operator is

$$\begin{aligned} & \frac{1}{2}i\hat{I}_{1-}\hat{I}_{2\beta} \exp[-i\pi J_{12}t_1] \exp[i(\Omega_1 - \pi J_{12})t_2] \\ & + \frac{1}{2}i\hat{I}_{1-}\hat{I}_{2\alpha} \exp[+i\pi J_{12}t_1] \exp[i(\Omega_1 + \pi J_{12})t_2] \\ & + \frac{1}{2}i\hat{I}_{1\beta}\hat{I}_{2-} \exp[-i\pi J_{12}t_1] \exp[i(\Omega_2 - \pi J_{12})t_2] \\ & + \frac{1}{2}i\hat{I}_{1\alpha}\hat{I}_{2-} \exp[+i\pi J_{12}t_1] \exp[i(\Omega_2 + \pi J_{12})t_2]. \end{aligned}$$

The J -spectrum contains four peaks which are grouped into two doublets, one associated with each spin. Both doublets are centred on $\omega_1 = 0$ in the indirect dimension, and are centred on the offset of the spin in the ω_2 dimension. The result is that the doublets are aligned at 45° , running parallel to the main diagonal $\omega_1 = \omega_2$, as shown in the spectrum in Figure 3.2 (a).

This is a general result for a spin system of any size. The offset will be refocused in t_1 , and so each multiplet will be centred on zero in the ω_1 dimension. The position of

each component in this dimension is therefore equal to its ω_2 frequency with the offset term removed, and so each multiplet will be aligned parallel to the main diagonal.

Refocusing of the inhomogeneous line broadening

In one-dimensional NMR spectra, the non-uniformity of the magnetic field B_0 results in spins in different parts of the sample precessing at different offsets. This adds an inhomogeneous contribution to the linewidth, as was discussed in Section 1.10.2. The spin echo in *J*-spectroscopy refocuses *all* the offsets, and so the inhomogeneous decay is removed from the FID in the t_1 dimension. Hence, the decay of the signal in this dimension is due solely to the natural decay constant T_2 , and the linewidths in ω_1 will only have a homogeneous contribution. If the inhomogeneity is significant, *J*-spectroscopy will give an increase in resolution of the multiplets in this dimension when compared to the one-dimensional spectrum. In ω_2 the linewidths will still possess an inhomogeneous contribution.

3.1.2 Separation of offset and *J*-coupling

It is relatively straightforward to obtain a spectrum in which the offsets and couplings are completely separated; the *J*-spectrum is simply tilted, or sheared, by -45° .

The shearing process is illustrated in Figure 3.3 on a schematic two-dimensional spectrum of spectral widths $\Delta\Omega_1$ and $\Delta\Omega_2$ in the ω_1 and ω_2 dimensions. For a shear that is applied parallel to the ω_2 axis, each data point is translated in this dimension by an amount $\Delta\omega_2$ that is proportional to its ω_1 coordinate:

$$\Delta\omega_2 = \kappa\omega_1,$$

where the constant of proportionality κ is the *shear rate*. The ω_2 axis is invariant under this transformation, and is referred to as the *shear axis*. The rectangular spectral window in (a) is sheared to give the parallelogram in (b). The shear can also be described in terms of an angle ξ , which is given by

$$\tan\xi = \kappa.$$

The grey regions in (b) have been moved outside of the original spectral window. It is conventional to move these regions back inside the rectangular window by translating the points by an amount $\pm\Delta\Omega_2$ to give the spectrum in (c); this is analogous to the process of folding that was discussed in Section 1.10.3.

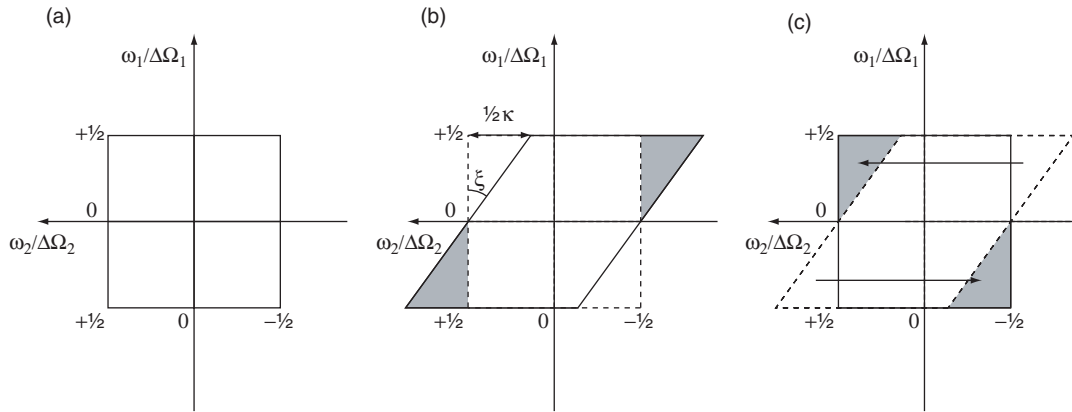


Figure 3.3: Illustration of the shear process on a schematic spectrum. The rectangular dataset in (a) is sheared parallel to the ω_2 axis to give (b), in which the spectral window is a parallelogram. The grey regions have been translated outside the original rectangular window. Conventionally, they are folded back inside to give the spectrum in (c). Note that, as represented in this diagram, both κ and ξ are negative.

Shearing the J -spectrum in Figure 3.2 (a), using a shear rate of $\kappa = -1$ (or shear angle $\xi = -45^\circ$) gives the spectrum in (b). The offsets and couplings have been completely separated: the former are contained in ω_2 , and the latter are contained in ω_1 . The decoupled spectrum is obtained, in principle, simply by summing the spectrum over ω_1 , and the multiplet structures are found by taking a cross-section parallel to ω_1 at the offset of the active spin in ω_2 .

3.2 Lineshapes and sensitivity

The first serious problem that has been mentioned is the lineshape in the two-dimensional spectrum. As can be seen from the CTP in Figure 3.1, only a single pathway is acquired in t_1 and so the data must be phase-modulated in this dimension. A two-dimensional Fourier transform of this data will therefore give a spectrum with the phase-twist lineshape. This lineshape is not suitable for high-resolution spectroscopy because of the broad tails and the negative regions of the dispersive parts. The dispersive parts of neighbouring peaks tend to overlap, thus negating the higher resolution that J -spectroscopy is supposed to provide.

A further difficulty with the phase-twist lineshape is that its projection onto the 45° axis is identically zero. This can be proved as follows. The multiplets are

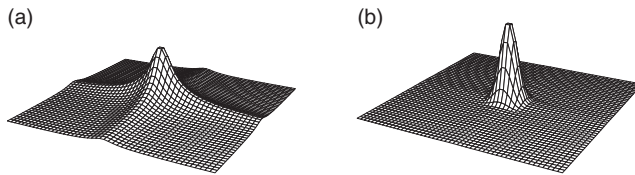


Figure 3.4: The lineshapes observed in two-dimensional J -spectra. Conventional J -spectra are presented as magnitude calculations, giving the lineshape shown in (a) which has broad dispersive tails. Pseudo-echo weighting in both dimensions gives the lineshape in (b), which exhibits much improved resolution. Both lineshapes were calculated with $T_2^{(1)} = T_2^{(2)} = 1/\pi$ s. The parameters for the weighting function are $\lambda^{(1)} = \lambda^{(2)} = \pi$ s $^{-1}$, and $\mu^{(1)} = \mu^{(2)} = 4$ s $^{-2}$.

aligned parallel to the main diagonal of the spectrum, and so in order to obtain the decoupled spectrum we must project onto the anti-diagonal $\omega_1 = -\omega_2$. According to the projection–slice theorem in Section 1.12.4, this projection is mathematically equivalent to extracting the slice from the time domain along $t_1 = -t_2$ and performing a one-dimensional Fourier transform. However, the FID is zero for negative times and so the only non-zero point in this slice is located at the origin; the Fourier transform of this slice (and hence the projection) is therefore zero [37].

The original solution to this problem was to calculate the magnitude spectrum. The lineshape is, from Equation 1.31,

$$|S(\omega_1, \omega_2)| = \sqrt{\frac{\{\mathcal{A}_{\Omega^{(1)}}(\omega_1)\mathcal{A}_{\Omega^{(2)}}(\omega_2) - \mathcal{D}_{\Omega^{(1)}}(\omega_1)\mathcal{D}_{\Omega^{(2)}}(\omega_2)\}^2}{\{\mathcal{A}_{\Omega^{(1)}}(\omega_1)\mathcal{D}_{\Omega^{(2)}}(\omega_2) + \mathcal{D}_{\Omega^{(1)}}(\omega_1)\mathcal{A}_{\Omega^{(2)}}(\omega_2)\}^2}};$$

this is plotted in Figure 3.4 (a). The projection is now non-zero, but the dispersive component still gives a very broad lineshape.

3.2.1 Pseudo-echo weighting

It is possible to eliminate the dispersion mode from the lineshape by shaping the decay envelope of the FID so that it is symmetrical. The idea is based on the observation that a time-domain function that is even about the origin has a Fourier transform that contains no imaginary part [1]. For example, in one dimension, the following FID

$$s(t) = \frac{1}{2} \exp(i\Omega t) \exp(-|t|/T_2)$$

has an envelope that is symmetrical about the origin* and forms what is referred to as a complete echo. The Fourier transform of this function is the pure absorption-mode lineshape:

$$S(\omega) = \mathcal{A}_\Omega(\omega).$$

In practice, it is not possible to record a signal for negative time. However, an absorption-mode signal can be obtained for phase modulated data by applying a weighting function to the FID which produces an envelope that is symmetrical about some time $t = t'$. The weighted FID is known as a *pseudo echo* [38]. The most commonly-used weighting function is a combination of a rising exponential and a Gaussian which, in one dimension, takes the form

$$w(t) = \exp\left(\lambda t - \mu\left(t - \frac{1}{2}t^{\max}\right)^2\right), \quad (3.1)$$

where λ and μ are positive parameters. The product of this function with a conventional, exponentially-decaying FID is

$$s(t)w(t) = \exp\left((\lambda - 1/T_2)t - \mu\left(t - \frac{1}{2}t^{\max}\right)^2\right)\exp(i\Omega t).$$

If we set $\lambda = 1/T_2$, the decay envelope becomes a Gaussian that is centred on $t' = \frac{1}{2}t^{\max}$, whose width is decreased by increasing μ . The value of μ is increased until the intensity of the FID at $t = 0$ and $t = t^{\max}$ has decayed to the point where there is no truncation. An example of a one-dimensional FID is shown in Figure 3.5 (a). The application of the weighting function gives the FID in (b), which is shaped to a symmetrical envelope. It is still necessary to calculate the magnitude spectrum, as the weighting function introduces a phase error across the spectrum. However, the spectrum now contains a narrow line as the dispersive component of the lineshape has been eliminated.

In two-dimensional spectroscopy, we shape the time domain to a pseudo echo in both t_1 and t_2 . The weighting function is

$$w(t_1, t_2) = \exp\left(\lambda^{(1)}t_1 - \mu^{(1)}\left(t_1 - \frac{1}{2}t_1^{\max}\right)^2\right)\exp\left(\lambda^{(2)}t_2 - \mu^{(2)}\left(t_2 - \frac{1}{2}t_2^{\max}\right)^2\right),$$

where $\lambda^{(i)}$ and $\mu^{(i)}$ are the parameters in the t_i dimension. The resulting magnitude spectrum is shown in Figure 3.4 (b). There is a substantial improvement in resolution. Pseudo-echo weighting is illustrated with the two-spin spectrum in Figure 3.6. The

*This function is defined for both positive *and* negative times.

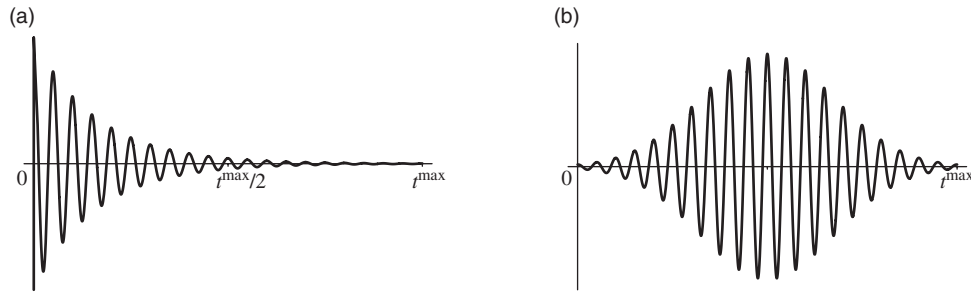


Figure 3.5: Illustration of pseudo-echo weighting in one dimension. A conventional one-dimensional FID acquired out to a maximum time t^{\max} is shown in (a). Applying the weighting function in Equation 3.1 with $\lambda = 1/T_2$ gives the FID in (b). The vertical scale of (b) is expanded by a factor of 50 relative to (a).

two-dimensional spectrum is shown in (a), the sheared spectrum is shown in (b), and its projection in (c).

Sensitivity

The price to be paid for the increase in resolution is a decrease in the SNR. This comes about because the weighting function reduces the intensity of the signal at the beginning of the FID, where the SNR in the time domain is highest. The reduction in the SNR can be calculated using Equation 1.34, by comparing the SNRs of the spectrum of the weighted signal, with the spectrum of the unweighted signal. The ratio of the two SNRs is

$$\frac{\text{SNR}(\text{weighted})}{\text{SNR}(\text{unweighted})} = \frac{\overline{sw}}{\overline{s}(\overline{w^2})^{1/2}},$$

where \overline{s} is equal to \overline{sw} in the absence of a weighting function. If we set the parameters to those used for the plot in Figure 3.4 (b), this ratio is 1.3%.

This represents a substantial degradation of the sensitivity, which is one of the principal drawbacks of this method. The second disadvantage is that there are no single values of $\lambda^{(i)}$ and $\mu^{(i)}$ that are optimum for all the peaks in the spectrum. The result is that the loss of intensity is not uniform for all the peaks; it depends upon the linewidth, with broader peaks experiencing greater losses than narrower peaks. There are two consequences: firstly, the peak integrals in the decoupled projection no longer correspond to the number of protons in each chemical environment; secondly very broad peaks, such as those due to rapidly-exchanging protons, tend to be lost in the

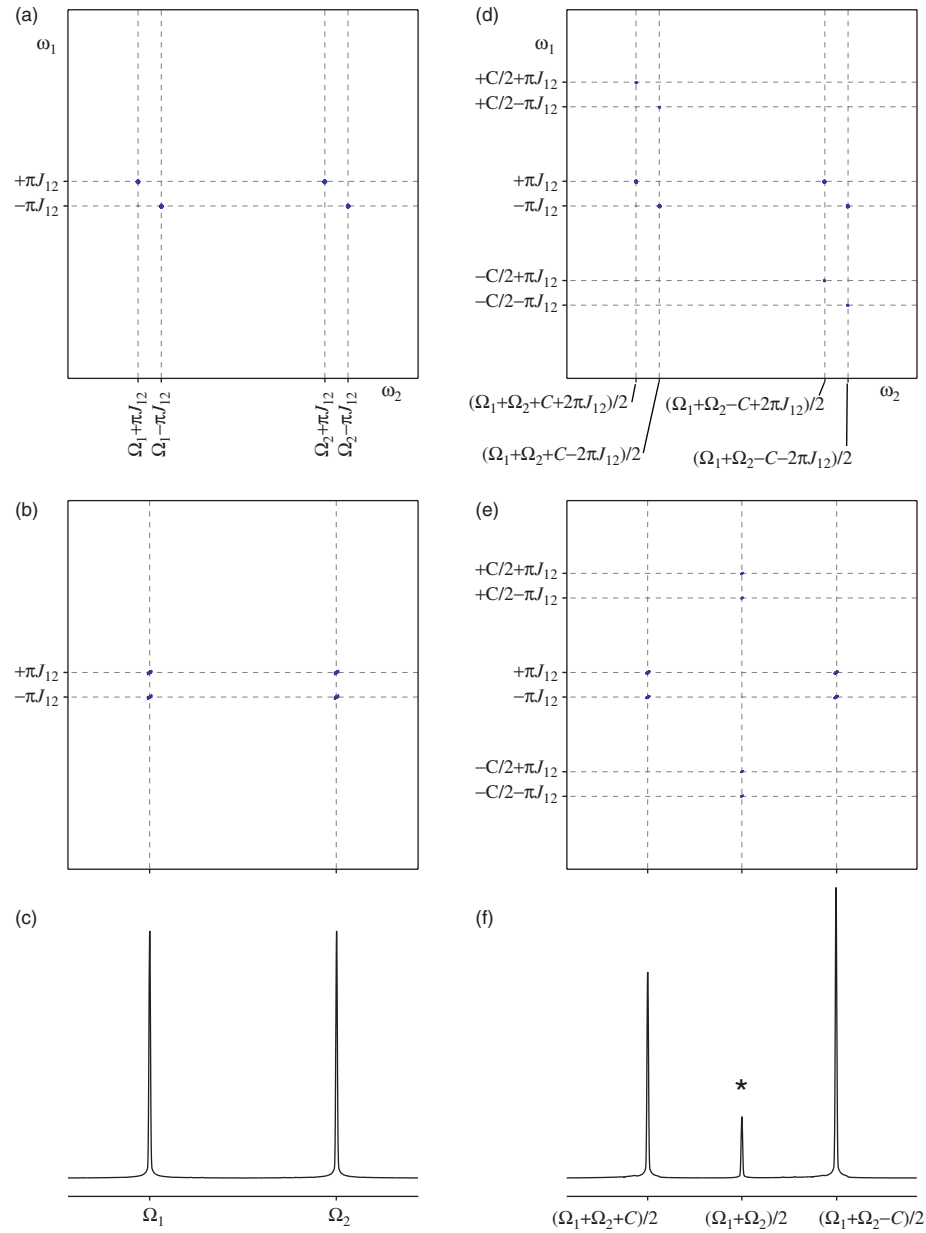


Figure 3.6: Magnitude J -spectra of two-spin systems processed with pseudo-echo weighting. The two-dimensional spectrum of a weakly-coupled system is shown in (a), which is sheared to give (b). The decoupled spectrum is the projection of (b) onto ω_2 , and is shown in (c). The J -spectrum of a strongly-coupled system is shown in (d), which is sheared to give spectrum (e), and projected to give (f). The strong coupling peak is labelled with an $*$.

noise.

Despite the shortcomings of conventional J -spectroscopy, the basic idea of obtaining a complete separation of offsets and couplings is very appealing, and so various methods have been proposed to try to solve the lineshape problem [39–50].

3.3 J-spectroscopy of a strongly-coupled two-spin system

A second problem with J -spectroscopy is that the presence of strong coupling introduces extra peaks into the spectrum [51–53]. These peaks are often referred to as ‘strong coupling artefacts’. However, such a term is misleading as it implies that the peaks should not be present. In fact, they arise because of genuine responses of the spin system, but are certainly unwanted. The important features of these peaks can be determined from a full density matrix calculation on a strong-coupled two-spin system.

3.3.1 Analysis of the pulse sequence

The extra peaks arise because of a mixing effect of the 180° pulse that does not affect weakly-coupled spins. The rotation matrix for a 180° pulse in the weak-coupling basis is given by

$$R_x(\pi) = \begin{pmatrix} 0 & 0 & 0 & -1 \\ 0 & 0 & -1 & 0 \\ 0 & -1 & 0 & 0 \\ -1 & 0 & 0 & 0 \end{pmatrix}.$$

A transformation under this matrix has the effect of converting one element of the density operator wholly into another single element: for example, $\hat{I}_{1+}\hat{I}_{2\alpha}$ is transformed into $\hat{I}_{1-}\hat{I}_{2\beta}$. In the strong-coupling basis, however, the rotation has the following matrix representation:

$$R_x^{SC}(\pi) = \begin{pmatrix} 0 & 0 & 0 & -1 \\ 0 & -\sin 2\theta & -\cos 2\theta & 0 \\ 0 & -\cos 2\theta & \sin 2\theta & 0 \\ -1 & 0 & 0 & 0 \end{pmatrix}.$$

Under this transformation, the four single-element operators with coherence order +1 that are present during the first half of t_1 are transformed as follows:

$$\begin{aligned}\{\hat{I}_{1+}\hat{I}_{2\alpha}\} &\xrightarrow{\pi\hat{F}_x} \cos 2\theta \{\hat{I}_{1-}\hat{I}_{2\beta}\} - \sin 2\theta \{\hat{I}_{1\beta}\hat{I}_{2-}\} \\ \{\hat{I}_{1+}\hat{I}_{2\beta}\} &\xrightarrow{\pi\hat{F}_x} \cos 2\theta \{\hat{I}_{1-}\hat{I}_{2\alpha}\} + \sin 2\theta \{\hat{I}_{1\alpha}\hat{I}_{2-}\} \\ \{\hat{I}_{1\alpha}\hat{I}_{2+}\} &\xrightarrow{\pi\hat{F}_x} \cos 2\theta \{\hat{I}_{1\beta}\hat{I}_{2-}\} + \sin 2\theta \{\hat{I}_{1-}\hat{I}_{2\beta}\} \\ \{\hat{I}_{1\beta}\hat{I}_{2+}\} &\xrightarrow{\pi\hat{F}_x} \cos 2\theta \{\hat{I}_{1\alpha}\hat{I}_{2-}\} - \sin 2\theta \{\hat{I}_{1-}\hat{I}_{2\alpha}\},\end{aligned}$$

where the significance of the curly braces is explained in Section 1.9.1. The first two transformations are analogous to a coherence transfer from spin one to spin two. However, the concept of ‘coherence transfer’ is meaningless in this case as the two strongly-coupled spins cannot be viewed as being separate. Nevertheless, if the degree of strong coupling is not too high, we can view these transformations as a partial transfer from coherence that is *mainly* present on spin one to a coherence that is *mainly* present on spin two.

We can determine the positions of the extra peaks in the spectrum. For example, the operator $\{\hat{I}_{1+}\hat{I}_{2\alpha}\}$ acquires the following phase factor during the first half of t_1 :

$$\{\hat{I}_{1+}\hat{I}_{2\alpha}\} \exp \left[-i\frac{1}{4}(\Omega_1 + \Omega_2 + C + 2\pi J_{12}) t_1 \right],$$

where the quantity C is defined in Section 1.9. Following the 180° pulse, each of the two new operators acquires a different phase during the rest of t_1 to give

$$\begin{aligned}&\cos 2\theta \{\hat{I}_{1-}\hat{I}_{2\beta}\} \exp [-i\pi J_{12}t_1] \\ &- \sin 2\theta \{\hat{I}_{1\beta}\hat{I}_{2-}\} \exp \left[-i\left(\frac{1}{2}C + \pi J_{12}\right) t_1 \right].\end{aligned}$$

The offset of the first term is refocused, and the corresponding peak appears at $(\omega_1, \omega_2) = (-\pi J_{12}, \frac{1}{2}(\Omega_1 + \Omega_2 + C - 2\pi J_{12}))$. This peak also appears in the spectrum of the weakly-coupled spin system, and so is referred to as ‘normal’ (N). The second peak appears at $(\omega_1, \omega_2) = \left(-\frac{1}{2}C - \pi J_{12}, \frac{1}{2}(\Omega_1 + \Omega_2 - C - 2\pi J_{12})\right)$. It does not appear in the weak coupling calculation, and is therefore a strong coupling peak (S).

The full form of the spectrum is determined by a full density matrix calculation, the results of which are presented in Table 3.1. The corresponding spectrum is shown in

Table 3.1: The peak positions and intensities in the J -spectrum of a strongly-coupled two-spin system. The peaks that are labelled ‘N’ have a one-to-one correspondence to the peaks that appear in the spectrum of the weakly-coupled spin system. Those labelled ‘S’, on the other hand, only appear as a result of strong coupling.

peak type (N/S)	ω_1 frequency	ω_2 frequency	complex intensity
N	$+\pi J_{12}$	$\frac{1}{2}(\Omega_1 + \Omega_2 + C + 2\pi J_{12})$	$\frac{1}{2}i \cos^2 2\theta$
N	$-\pi J_{12}$	$\frac{1}{2}(\Omega_1 + \Omega_2 + C - 2\pi J_{12})$	$\frac{1}{2}i \cos^2 2\theta$
N	$+\pi J_{12}$	$\frac{1}{2}(\Omega_1 + \Omega_2 - C + 2\pi J_{12})$	$\frac{1}{2}i \cos^2 2\theta$
N	$-\pi J_{12}$	$\frac{1}{2}(\Omega_1 + \Omega_2 - C - 2\pi J_{12})$	$\frac{1}{2}i \cos^2 2\theta$
S	$\frac{1}{2}C + \pi J_{12}$	$\frac{1}{2}(\Omega_1 + \Omega_2 + C + 2\pi J_{12})$	$\frac{1}{2}i \sin 2\theta(-1 + \sin 2\theta)$
S	$\frac{1}{2}C - \pi J_{12}$	$\frac{1}{2}(\Omega_1 + \Omega_2 + C - 2\pi J_{12})$	$\frac{1}{2}i \sin 2\theta(1 + \sin 2\theta)$
S	$-\frac{1}{2}C + \pi J_{12}$	$\frac{1}{2}(\Omega_1 + \Omega_2 - C + 2\pi J_{12})$	$\frac{1}{2}i \sin 2\theta(1 + \sin 2\theta)$
S	$-\frac{1}{2}C - \pi J_{12}$	$\frac{1}{2}(\Omega_1 + \Omega_2 - C - 2\pi J_{12})$	$\frac{1}{2}i \sin 2\theta(-1 + \sin 2\theta)$

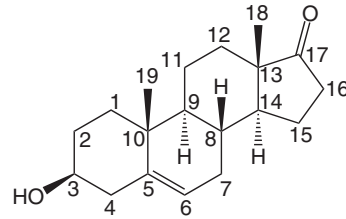


Figure 3.7: The chemical structure of the steroid dehydroisoandrosterone, with the labels used for the assignment.

Figure 3.6 (d). When the spectrum is sheared, as is shown in (e), the strong-coupling peaks line up so that they lie at the same ω_2 frequency, which is the average of the two offsets, $\frac{1}{2}(\Omega_1 + \Omega_2)$. They therefore project to give an ‘artefact’ that lies at this frequency, as is shown in the projection in (f).

3.4 Experimental example

The problems with conventional J -spectroscopy are well-illustrated with the spectrum of the steroid dehydroisoandrosterone, the structure of which is shown in Figure 3.7. The conventional J -spectrum was acquired with the pulse sequence in Figure 3.1 (b) which employs two swept-frequency 180° pulses, so that the frequency-dependent

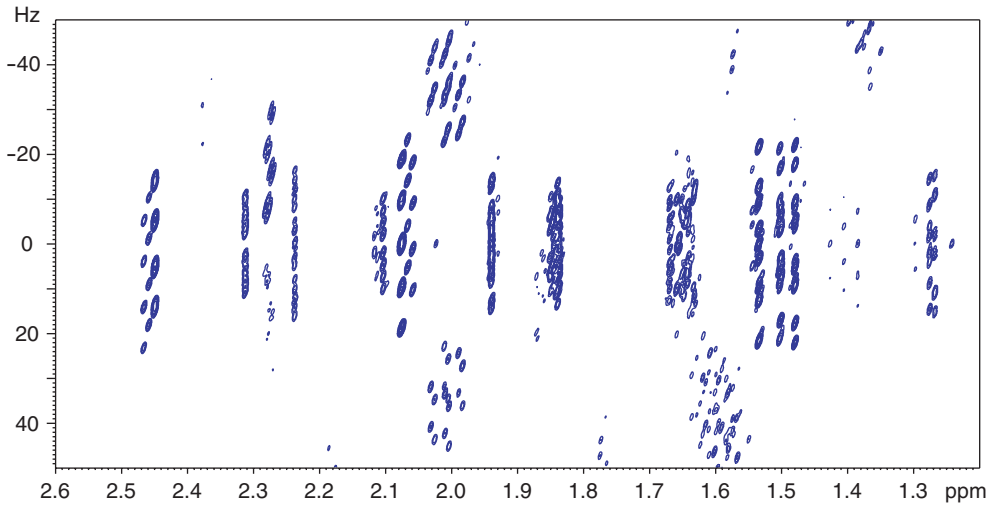


Figure 3.8: A region of the sheared magnitude J -spectrum of dehydroisoandrosterone. Note that the strong-coupling artefacts lying on top of the wanted multiplet to the far left do not appear to have symmetrically-related partners. This is due to their folding in ω_1 , and the subsequent shear not pairing up the artefacts.

phase errors that are introduced by the first are refocused by the second. The swept pulse that was used is BIP-720-25-40 which has a B_1 field of 20 kHz, and a duration of 100 μ s [27]. The spectral widths in ω_2 and ω_1 are 2561 Hz and 100 Hz respectively; the acquisition time in t_2 was 1.60 s, and 200 t_1 increments were acquired, giving a t_1^{\max} of 2.0 s. Thirty scans per increment were recorded to obtain a usable SNR.

The two-dimensional data were processed with pseudo-echo weighting in both dimensions, and the magnitude spectrum was calculated, a region of which is shown in Figure 3.8. The spectrum exhibits the expected separation of offsets and couplings, but also contains numerous strong-coupling artefacts. The decoupled spectrum is shown in Figure 3.9 (b), along with the conventional spectrum in (a) for comparison. The strong-coupling artefacts project to give a series of extra peaks which serve to complicate the spectrum. In addition, it can be seen that there is a great variation in the values of the integrals relative to those in the conventional spectrum. In particular, the broad peak due to water is completely absent from the decoupled spectrum. This reflects the severity of the weighting function.

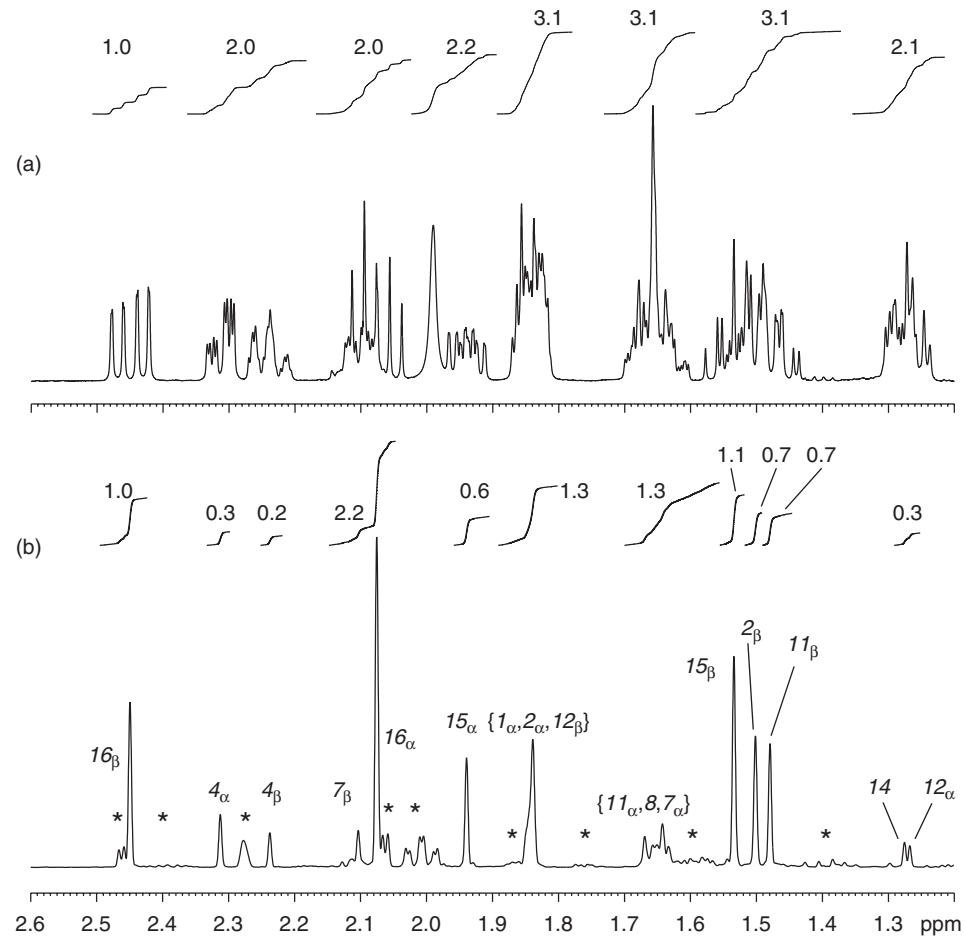


Figure 3.9: One-dimensional spectra of dehydroisoandrosterone. The conventional spectrum is shown in (a), and the projection of the *J*-spectrum in Figure 3.8 is shown in (b). The strong-coupling artefacts in the latter are labelled *, and the assignment is given in italics. For both spectra, the values of the integrals are given relative to the resonance on the far left. Note that the broad water peak at 1.99 ppm in (a) is missing from (b).

Chapter 4

Broadband proton-decoupled proton spectra using z-COSY

THREE ARE MANY POSSIBLE APPLICATIONS for an experiment that achieves the complete separation of offsets and couplings. These include the separation of the components of a mixture by diffusion measurements, the determination of relaxation parameters, and the study of mixtures arising from metabolomics. The conventional *J*-spectroscopy pulse sequence delivers this separation, but suffers from the considerable disadvantage of producing spectra that contain the phase-twist lineshape. Existing solutions to this problem are unsatisfactory either because they result in a significant loss of sensitivity and intensity distortions, or require very complex data processing [39–50].

In this Chapter, a completely new method for obtaining the separation of offsets and couplings is presented. It has the distinct advantage over previous methods that the peaks in the spectrum automatically have the absorption-mode lineshape, and retain their natural intensities. There is therefore no need for specialized data processing, with the result that the decoupled spectrum can be obtained relatively simply.

The experiment upon which this method is based is anti *z*-COSY [32], the pulse sequence of which is shown in Figure 4.1 (a). The mixing period is a *z*-filter in which the flip angles of the two pulses are $180^\circ + \beta$ and β where β is small, i.e. 20° or less. The resulting spectrum contains two kinds of multiplet: diagonal-peak multiplets and cross-peak multiplets. The former are due to coherence that remains on the same spin during t_1 and t_2 , while the latter arise because of coherence transfer and thus indicate the presence of *J*-coupling between the two spins.

If we consider the diagonal peaks only, then each multiplet contains the same number of components as the conventional one-dimensional spectrum and can be

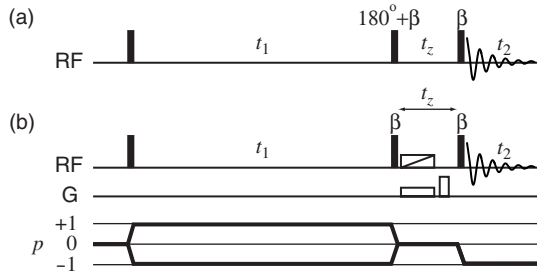


Figure 4.1: Pulse sequences for anti z -COSY. The basic sequence is shown in (a). The mixing period is a z -filter that comprises two pulses of flip angle $\pi + \beta$ and β , where β is small, which sandwich a short delay of duration t_z . The sequence in (b) incorporates the swept-frequency 180° pulse and gradient combination which dephases the ZQ coherence present during t_z . The second gradient is a homospoil which dephases all coherences of non-zero order.

projected to give a decoupled spectrum. The cross peaks however are superfluous for this application and are actually unwanted, rather like the strong-coupling peaks in J -spectra.

In this Chapter we calculate the form of the anti z -COSY spectrum, describe how to obtain the offset-coupling separation, and present two methods for suppressing the cross peaks [54]. We then describe how the decoupled spectra thus obtained can be applied to diffusion measurements, relaxation experiments, and metabonomics.

The work described in this Chapter was carried out in collaboration with Dr Richard Edden during the course of his Ph.D [55].

4.1 Analysis of the pulse sequence

The pulse sequence will be analyzed in this Section. It is sufficient to use a three-spin system as it demonstrates all the relevant properties of the pulse sequence. Since we are interested in the detailed structures of the multiplets, it is convenient to use the single-element operators.

The initial state is chosen to be equilibrium magnetization on spin one, \hat{I}_{1z} . The 90° pulse generates $-\hat{I}_{1y}$ which can be expanded in terms of the single-element operators to give

$$\begin{aligned} & \frac{1}{2}i(\hat{I}_{1+}\hat{I}_{2\alpha}\hat{I}_{3\alpha} + \hat{I}_{1+}\hat{I}_{2\alpha}\hat{I}_{3\beta} + \hat{I}_{1+}\hat{I}_{2\beta}\hat{I}_{3\alpha} + \hat{I}_{1+}\hat{I}_{2\beta}\hat{I}_{3\beta}) \\ - & \frac{1}{2}i(\hat{I}_{1-}\hat{I}_{2\alpha}\hat{I}_{3\alpha} + \hat{I}_{1-}\hat{I}_{2\alpha}\hat{I}_{3\beta} + \hat{I}_{1-}\hat{I}_{2\beta}\hat{I}_{3\alpha} + \hat{I}_{1-}\hat{I}_{2\beta}\hat{I}_{3\beta}). \end{aligned}$$

The terms containing \hat{I}_{1+} will produce the N-type spectrum, and those containing \hat{I}_{1-} will produce the P-type spectrum.

Each of these terms evolves at its characteristic frequency during t_1 to give

$$\begin{aligned} \pm \frac{1}{2}i\hat{I}_{1\pm}\hat{I}_{2\alpha}\hat{I}_{3\alpha} &\quad \pm \frac{1}{2}i\hat{I}_{1\pm}\hat{I}_{2\alpha}\hat{I}_{3\alpha} \exp[\mp i(\Omega_1 + \pi J_{12} + \pi J_{13})t_1] \\ \pm \frac{1}{2}i\hat{I}_{1\pm}\hat{I}_{2\alpha}\hat{I}_{3\beta} &\xrightarrow{\mathcal{H}_{\text{free}, t_1}} \pm \frac{1}{2}i\hat{I}_{1\pm}\hat{I}_{2\alpha}\hat{I}_{3\beta} \exp[\mp i(\Omega_1 + \pi J_{12} - \pi J_{13})t_1] \\ \pm \frac{1}{2}i\hat{I}_{1\pm}\hat{I}_{2\beta}\hat{I}_{3\alpha} &\quad \pm \frac{1}{2}i\hat{I}_{1\pm}\hat{I}_{2\beta}\hat{I}_{3\alpha} \exp[\mp i(\Omega_1 - \pi J_{12} + \pi J_{13})t_1] \\ \pm \frac{1}{2}i\hat{I}_{1\pm}\hat{I}_{2\beta}\hat{I}_{3\beta} &\quad \pm \frac{1}{2}i\hat{I}_{1\pm}\hat{I}_{2\beta}\hat{I}_{3\beta} \exp[\mp i(\Omega_1 - \pi J_{12} - \pi J_{13})t_1]. \end{aligned}$$

The first mixing pulse can be treated as two separate, consecutive pulses of flip angles π and β respectively. The 180° pulse changes both the coherence order of spin one from $+1$ to -1 (and *vice versa*) and the polarization of the passive spins, giving

$$\begin{aligned} \pm \frac{1}{2}i\hat{I}_{1\mp}\hat{I}_{2\beta}\hat{I}_{3\beta} \exp[\mp i(\Omega_1 + \pi J_{12} + \pi J_{13})t_1] \\ \pm \frac{1}{2}i\hat{I}_{1\mp}\hat{I}_{2\beta}\hat{I}_{3\alpha} \exp[\mp i(\Omega_1 + \pi J_{12} - \pi J_{13})t_1] \\ \pm \frac{1}{2}i\hat{I}_{1\mp}\hat{I}_{2\alpha}\hat{I}_{3\beta} \exp[\mp i(\Omega_1 - \pi J_{12} + \pi J_{13})t_1] \\ \pm \frac{1}{2}i\hat{I}_{1\mp}\hat{I}_{2\alpha}\hat{I}_{3\alpha} \exp[\mp i(\Omega_1 - \pi J_{12} - \pi J_{13})t_1]. \end{aligned} \tag{4.1}$$

The transformation laws for a pulse of flip angle β are given by Equations 1.20–1.23. Since β is small, the factor $\sin^2 \frac{1}{2}\beta$ (which is $O(\beta^2)$) is approximately zero, and so the transformation laws can be approximated as

$$\begin{aligned} \hat{I}_{i+} &\xrightarrow{\beta\hat{I}_{ix}} \hat{I}_{i+}c^2 + \frac{1}{2}iS(\hat{I}_{i\alpha} - \hat{I}_{i\beta}), \\ \hat{I}_{i-} &\xrightarrow{\beta\hat{I}_{ix}} \hat{I}_{i-}c^2 - \frac{1}{2}iS(\hat{I}_{i\alpha} - \hat{I}_{i\beta}), \\ \hat{I}_{i\alpha} &\xrightarrow{\beta\hat{I}_{ix}} \hat{I}_{i\alpha}c^2 + \frac{1}{2}iS(\hat{I}_{i+} - \hat{I}_{i-}), \\ \hat{I}_{i\beta} &\xrightarrow{\beta\hat{I}_{ix}} \hat{I}_{i\beta}c^2 - \frac{1}{2}iS(\hat{I}_{i+} - \hat{I}_{i-}), \end{aligned}$$

where $c = \cos \frac{1}{2}\beta$, and $S = \sin \beta$.

The β pulse generates terms of all possible coherence orders (from $+3$ to -3). Terms of non-zero coherence order are removed by conventional coherence order selection methods, while the ZQ coherence is dephased by the single-scan method

discussed in Section 2.7.1. The remaining z -magnetization comprises eight terms, which are

$$\begin{aligned} & \frac{1}{4}S c^4 (\hat{I}_{1\alpha} \hat{I}_{2\beta} \hat{I}_{3\beta} - \hat{I}_{1\beta} \hat{I}_{2\beta} \hat{I}_{3\beta}) \exp [\mp i(\Omega_1 + \pi J_{12} + \pi J_{13}) t_1] \\ & \frac{1}{4}S c^4 (\hat{I}_{1\alpha} \hat{I}_{2\beta} \hat{I}_{3\alpha} - \hat{I}_{1\beta} \hat{I}_{2\beta} \hat{I}_{3\alpha}) \exp [\mp i(\Omega_1 + \pi J_{12} - \pi J_{13}) t_1] \\ & \frac{1}{4}S c^4 (\hat{I}_{1\alpha} \hat{I}_{2\alpha} \hat{I}_{3\beta} - \hat{I}_{1\beta} \hat{I}_{2\alpha} \hat{I}_{3\beta}) \exp [\mp i(\Omega_1 - \pi J_{12} + \pi J_{13}) t_1] \\ & \frac{1}{4}S c^4 (\hat{I}_{1\alpha} \hat{I}_{2\alpha} \hat{I}_{3\alpha} - \hat{I}_{1\beta} \hat{I}_{2\alpha} \hat{I}_{3\alpha}) \exp [\mp i(\Omega_1 - \pi J_{12} - \pi J_{13}) t_1]. \end{aligned}$$

The operators $\hat{I}_{1\mp}$ are transformed into $\hat{I}_{1\alpha}$ and $\hat{I}_{1\beta}$ with equal intensities, and the passive spins remain in the same spin states.

The final β pulse generates the following set of observable terms. There are four spin-one diagonal peaks:

$$\begin{aligned} & -\frac{1}{4}iS^2 c^8 \hat{I}_{1-} \hat{I}_{2\beta} \hat{I}_{3\beta} \exp [\mp i(\Omega_1 + \pi J_{12} + \pi J_{13}) t_1] \\ & -\frac{1}{4}iS^2 c^8 \hat{I}_{1-} \hat{I}_{2\beta} \hat{I}_{3\alpha} \exp [\mp i(\Omega_1 + \pi J_{12} - \pi J_{13}) t_1] \\ & -\frac{1}{4}iS^2 c^8 \hat{I}_{1-} \hat{I}_{2\alpha} \hat{I}_{3\beta} \exp [\mp i(\Omega_1 - \pi J_{12} + \pi J_{13}) t_1] \\ & -\frac{1}{4}iS^2 c^8 \hat{I}_{1-} \hat{I}_{2\alpha} \hat{I}_{3\alpha} \exp [\mp i(\Omega_1 - \pi J_{12} - \pi J_{13}) t_1]; \end{aligned}$$

eight cross peaks between spins one and two:

$$\begin{aligned} & \frac{1}{8}iS^2 c^8 (\hat{I}_{1\alpha} \hat{I}_{2-} \hat{I}_{3\beta} - \hat{I}_{1\beta} \hat{I}_{2-} \hat{I}_{3\beta}) \exp [\mp i(\Omega_1 + \pi J_{12} + \pi J_{13}) t_1] \\ & \frac{1}{8}iS^2 c^8 (\hat{I}_{1\alpha} \hat{I}_{2-} \hat{I}_{3\alpha} - \hat{I}_{1\beta} \hat{I}_{2-} \hat{I}_{3\alpha}) \exp [\mp i(\Omega_1 + \pi J_{12} - \pi J_{13}) t_1] \\ & -\frac{1}{8}iS^2 c^8 (\hat{I}_{1\alpha} \hat{I}_{2-} \hat{I}_{3\beta} - \hat{I}_{1\beta} \hat{I}_{2-} \hat{I}_{3\beta}) \exp [\mp i(\Omega_1 - \pi J_{12} + \pi J_{13}) t_1] \\ & -\frac{1}{8}iS^2 c^8 (\hat{I}_{1\alpha} \hat{I}_{2-} \hat{I}_{3\alpha} - \hat{I}_{1\beta} \hat{I}_{2-} \hat{I}_{3\alpha}) \exp [\mp i(\Omega_1 - \pi J_{12} - \pi J_{13}) t_1]; \end{aligned}$$

and eight cross peaks between spins one and three:

$$\begin{aligned} & \frac{1}{8}iS^2 c^8 (\hat{I}_{1\alpha} \hat{I}_{2\beta} \hat{I}_{3-} - \hat{I}_{1\beta} \hat{I}_{2\beta} \hat{I}_{3-}) \exp [\mp i(\Omega_1 + \pi J_{12} + \pi J_{13}) t_1] \\ & -\frac{1}{8}iS^2 c^8 (\hat{I}_{1\alpha} \hat{I}_{2\beta} \hat{I}_{3-} - \hat{I}_{1\beta} \hat{I}_{2\beta} \hat{I}_{3-}) \exp [\mp i(\Omega_1 + \pi J_{12} - \pi J_{13}) t_1] \\ & \frac{1}{8}iS^2 c^8 (\hat{I}_{1\alpha} \hat{I}_{2\alpha} \hat{I}_{3-} - \hat{I}_{1\beta} \hat{I}_{2\alpha} \hat{I}_{3-}) \exp [\mp i(\Omega_1 - \pi J_{12} + \pi J_{13}) t_1] \\ & -\frac{1}{8}iS^2 c^8 (\hat{I}_{1\alpha} \hat{I}_{2\alpha} \hat{I}_{3-} - \hat{I}_{1\beta} \hat{I}_{2\alpha} \hat{I}_{3-}) \exp [\mp i(\Omega_1 - \pi J_{12} - \pi J_{13}) t_1]. \end{aligned}$$

Every peak in the N-type spectrum is matched by a peak in the P-type spectrum with the same intensity, but opposite sense of modulation during t_1 . Therefore, the two datasets can be combined to give a pure-phase spectrum with frequency discrimination in ω_1 . Furthermore, both the diagonal peaks and cross peaks have the same phase in both dimensions, and so the spectrum can be phased to give the double absorption-mode lineshapes for *all* the peaks.

4.1.1 The zero-quantum artefacts

Before going on to look at the final spectrum in detail, we will consider the effect of the ZQ coherence that is present during t_z should it not be suppressed. The starting point is Equation 4.1, which gives the state of the system before the first β pulse. The ZQ terms with the greatest intensities that are generated by this pulse arise from spin one being unchanged, and either of the two passive spins being converted to \hat{I}_{i+} or \hat{I}_{i-} as required with the second also staying unchanged. The resulting ZQ terms are

$$\begin{aligned} & \frac{1}{4}S c^4 (\hat{I}_{1\mp}\hat{I}_{2\pm}\hat{I}_{3\beta} + \hat{I}_{1\mp}\hat{I}_{2\beta}\hat{I}_{3\pm}) \exp [\mp i(\Omega_1 + \pi J_{12} + \pi J_{13})t_1] \\ & \frac{1}{4}S c^4 (\hat{I}_{1\mp}\hat{I}_{2\pm}\hat{I}_{3\alpha} - \hat{I}_{1\mp}\hat{I}_{2\beta}\hat{I}_{3\pm}) \exp [\mp i(\Omega_1 + \pi J_{12} - \pi J_{13})t_1] \\ & \frac{1}{4}S c^4 (-\hat{I}_{1\mp}\hat{I}_{2\pm}\hat{I}_{3\beta} + \hat{I}_{1\mp}\hat{I}_{2\alpha}\hat{I}_{3\pm}) \exp [\mp i(\Omega_1 - \pi J_{12} + \pi J_{13})t_1] \\ & \frac{1}{4}S c^4 (-\hat{I}_{1\mp}\hat{I}_{2\pm}\hat{I}_{3\alpha} - \hat{I}_{1\mp}\hat{I}_{2\alpha}\hat{I}_{3\pm}) \exp [\mp i(\Omega_1 - \pi J_{12} - \pi J_{13})t_1]. \end{aligned}$$

The final β pulse now produces an interesting result. The highest-intensity terms are those for which the spin represented by \hat{I}_{i-} remains unchanged; the \hat{I}_{j+} operator must therefore be transformed into either \hat{I}_{ja} or \hat{I}_{jb} . The result is that the ZQ coherence contributes only to the diagonal peaks in the N-type spectrum, and only to the cross peaks in the P-type spectrum.

The resulting observable operators in the N-type spectrum are

$$\begin{aligned} & \frac{1}{8}iS^2c^8 (\hat{I}_{1-}\hat{I}_{2\alpha}\hat{I}_{3\beta} + \hat{I}_{1-}\hat{I}_{2\beta}\hat{I}_{3\alpha} - 2\hat{I}_{1-}\hat{I}_{2\beta}\hat{I}_{3\beta}) \exp [-i(\Omega_1 + \pi J_{12} + \pi J_{13})t_1] \\ & \frac{1}{8}iS^2c^8 (\hat{I}_{1-}\hat{I}_{2\alpha}\hat{I}_{3\alpha} + \hat{I}_{1-}\hat{I}_{2\beta}\hat{I}_{3\beta} - 2\hat{I}_{1-}\hat{I}_{2\beta}\hat{I}_{3\alpha}) \exp [-i(\Omega_1 + \pi J_{12} - \pi J_{13})t_1] \\ & \frac{1}{8}iS^2c^8 (\hat{I}_{1-}\hat{I}_{2\alpha}\hat{I}_{3\alpha} + \hat{I}_{1-}\hat{I}_{2\beta}\hat{I}_{3\beta} - 2\hat{I}_{1-}\hat{I}_{2\alpha}\hat{I}_{3\beta}) \exp [-i(\Omega_1 - \pi J_{12} + \pi J_{13})t_1] \\ & \frac{1}{8}iS^2c^8 (\hat{I}_{1-}\hat{I}_{2\alpha}\hat{I}_{3\beta} + \hat{I}_{1-}\hat{I}_{2\beta}\hat{I}_{3\alpha} - 2\hat{I}_{1-}\hat{I}_{2\alpha}\hat{I}_{3\alpha}) \exp [-i(\Omega_1 - \pi J_{12} - \pi J_{13})t_1]. \end{aligned}$$

The P-type spectrum comprises two cross-peak multiplets. The multiplet between

spins one and two is

$$\begin{aligned} & \frac{1}{8}iS^2c^8(\hat{I}_{1\alpha}\hat{I}_{2-}\hat{I}_{3\beta} - \hat{I}_{1\beta}\hat{I}_{2-}\hat{I}_{3\beta})\exp[+i(\Omega_1 + \pi J_{12} + \pi J_{13})t_1] \\ & \frac{1}{8}iS^2c^8(\hat{I}_{1\alpha}\hat{I}_{2-}\hat{I}_{3\alpha} - \hat{I}_{1\beta}\hat{I}_{2-}\hat{I}_{3\alpha})\exp[+i(\Omega_1 + \pi J_{12} - \pi J_{13})t_1] \\ & \frac{1}{8}iS^2c^8(-\hat{I}_{1\alpha}\hat{I}_{2-}\hat{I}_{3\beta} + \hat{I}_{1\beta}\hat{I}_{2-}\hat{I}_{3\beta})\exp[+i(\Omega_1 - \pi J_{12} + \pi J_{13})t_1] \\ & \frac{1}{8}iS^2c^8(-\hat{I}_{1\alpha}\hat{I}_{2-}\hat{I}_{3\alpha} + \hat{I}_{1\beta}\hat{I}_{2-}\hat{I}_{3\alpha})\exp[+i(\Omega_1 - \pi J_{12} - \pi J_{13})t_1], \end{aligned}$$

and the multiplet between spins one and three is

$$\begin{aligned} & \frac{1}{8}iS^2c^8(\hat{I}_{1\alpha}\hat{I}_{2\beta}\hat{I}_{3-} - \hat{I}_{1\beta}\hat{I}_{2\beta}\hat{I}_{3-})\exp[+i(\Omega_1 + \pi J_{12} + \pi J_{13})t_1] \\ & \frac{1}{8}iS^2c^8(-\hat{I}_{1\alpha}\hat{I}_{2\beta}\hat{I}_{3-} + \hat{I}_{1\beta}\hat{I}_{2\beta}\hat{I}_{3-})\exp[+i(\Omega_1 + \pi J_{12} - \pi J_{13})t_1] \\ & \frac{1}{8}iS^2c^8(\hat{I}_{1\alpha}\hat{I}_{2\alpha}\hat{I}_{3-} - \hat{I}_{1\beta}\hat{I}_{2\alpha}\hat{I}_{3-})\exp[+i(\Omega_1 - \pi J_{12} + \pi J_{13})t_1] \\ & \frac{1}{8}iS^2c^8(-\hat{I}_{1\alpha}\hat{I}_{2\alpha}\hat{I}_{3-} + \hat{I}_{1\beta}\hat{I}_{2\alpha}\hat{I}_{3-})\exp[+i(\Omega_1 - \pi J_{12} - \pi J_{13})t_1]. \end{aligned}$$

Within each spectrum, the ZQ artefacts have the same phase as the wanted peaks. However, when the two datasets are summed, the artefacts in the N-type spectrum have no counterparts in the P-type spectrum with which to combine (and *vice versa*) and so the artefacts appear in the final spectrum with the phase-twist lineshape. It is for this reason that the ZQ coherence must be suppressed if we wish to acquire a clean spectrum.

4.1.2 The diagonal-peak multiplet

In the case of the diagonal peaks, the analysis above shows that each product operator that is present prior to t_1 gives only one operator during t_2 . The position of each peak in ω_1 is the same as the ω_2 position, except that *all* the coupling terms have the *opposite* sign. This arises because all the passive spins have the opposite spin polarization in t_2 to the one they had during t_1 ; there is a high probability that the first mixing pulse (of flip angle $\pi + \beta$) will flip the spin states, and the second pulse (of flip angle β) will leave the polarization unaffected. The peaks therefore all lie on the counter-diagonal, as shown in Figure 4.2 (a).

This multiplet contains a complete separation of the offsets and J -couplings: the frequency dimension that is parallel to the diagonal contains only the offset information, and the frequency dimension along the counter-diagonal contains only

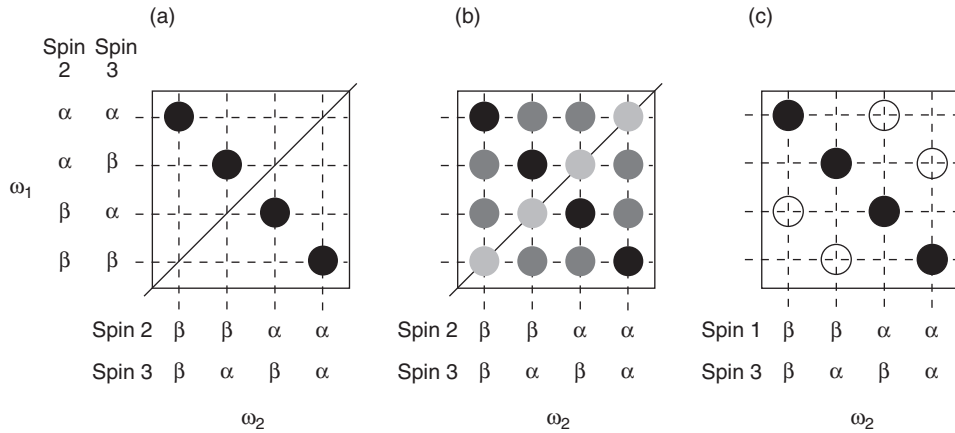


Figure 4.2: Schematic diagonal- and cross-peak multiplets in the anti z -COSY spectrum of a three-spin system. The diagonal-peak multiplet of spin one is shown in (a); the spin states of the two passive spins are given in both dimensions. The only peaks that are present with significant intensity are those for which the passive spins are in different states in each dimension. As a result, all the peaks lie along the counter-diagonal. The full form of the diagonal-peak multiplet is shown in (b), in which the three types of peak are coloured with a different shade of grey. Type 1 peaks are black, type 2 peaks are dark grey, and the peaks of type 3 are light grey. The cross-peak multiplet between spins one and two is shown in (c). It is assumed that $J_{12} > J_{13} = J_{23}$. Filled circles represent peaks of positive intensity, and unfilled circles represent peaks of negative intensity.

Table 4.1: The positions and intensities of the three types of peak in the diagonal-peak multiplet of the anti z -COSY spectrum of a three-spin system. $S = \sin \beta$, $c = \cos \frac{1}{2}\beta$, and $s = \sin \frac{1}{2}\beta$.

peak type	description	complex intensity
1	counter-diagonal peak	$-\frac{1}{4}iS^2(c^8 + 2c^4s^4 + s^8)$
2	off-diagonal peak	$-\frac{1}{2}iS^2(c^6s^2 + c^2s^6)$
3	on-diagonal peak	$-iS^2c^4s^4$

the coupling information. Hence, the projection of this multiplet onto the diagonal is a proton-decoupled proton spectrum.

A more detailed calculation, which does not discard any of the lower-intensity population terms, gives a complete analysis of the diagonal-peak multiplet. The set of intensities is given in Table 4.1, from which it is seen that there are three types of diagonal peak. They are illustrated in Figure 4.2 (b).

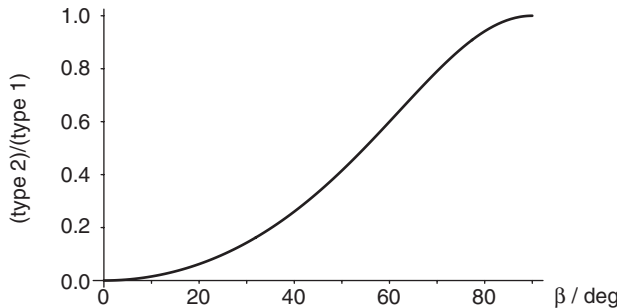


Figure 4.3: The intensity of the unwanted type 2 peaks relative to the type 1 peaks as a function of flip angle β .

The type 1 peaks lie on the counter-diagonal, and are the ones we require. They are made up of the following three terms. The term that varies as c^8 is due to the fraction of passive spins whose spin states are unaffected by *both* the β pulses, and therefore has the greatest intensity. The second term varies as $2c^4s^4$ and corresponds to one passive spin being flipped by the first β pulse, and then being flipped back by the second. The third term, s^8 , is due to both spins being flipped by both pulses.

The peaks of type 3 lie on the main diagonal. Their intensities are given by $4c^4s^4$, which arise from each spin being flipped once by either of the two pulses, and are negligible for small β . They therefore do not need to be considered further.

The peaks of type 2 are more intense, as the leading term is $2c^6s^2$ which is due to only one spin being flipped by either of the mixing pulses. The less intense term, $2c^2s^6$ is due to a process in which both spins are flipped by one of the pulses, and one is flipped back by the other pulse. The ratio of the intensity of these unwanted peaks to the intensity of the type 1 peaks is given by

$$\frac{\text{type 2}}{\text{type 1}} = \frac{4}{3 + \cos 2\beta} - 1,$$

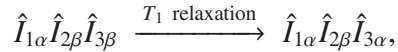
and is plotted in Figure 4.3.

For a flip angle of $\beta = 20^\circ$, this ratio is 0.062, or type 1 : type 2 = 16 : 1. If $\beta = 10^\circ$, the relative intensity is 0.015, or 65:1. The peaks that do not lie on the counter-diagonal will give unwanted peaks in the projection, and so they must be suppressed. This is done by reducing the value of β , but there is a limit to this. The intensities of all the peaks have a multiplicative factor of $\sin^2 \beta$ which is also reduced by decreasing β . Therefore, a compromise must be reached in which β is small enough

to reduce the unwanted peaks sufficiently, but large enough to retain adequate intensity in the counter diagonal peaks. Generally, a flip angle between 10° and 20° achieves a satisfactory compromise.

The effects of longitudinal relaxation

It proves necessary to account for longitudinal relaxation during the z -filter when considering the structures of the diagonal-peak multiplets. During t_z , relaxation mechanisms will cause transformations such as



which can be interpreted as a transition from the $|\alpha\beta\beta\rangle$ state to the $|\alpha\beta\alpha\rangle$ state.

In this case, spin three has flipped during t_z , and so does not experience an *overall* change of polarization. Therefore relaxation leads to an increase in the intensity of the unwanted peaks (here of type 2). This effect can be minimized by using as short a delay t_z as possible; in practice, this means that t_z is long enough to accommodate the ZQ suppression element and homospoil. Using standard lengths for the swept pulse and homospoil, for example the values of 24 ms and 5 ms that are used in this Chapter, T_1 relaxation has a negligible effect on the peak intensities for small- to medium-sized molecules.

4.1.3 The cross-peak multiplets

Each cross-peak multiplet contains eight components, which are divided into two *anti-phase square arrays*. This is illustrated in Figure 4.2 (c) for the spin one–two multiplet. The only peaks that have significant intensity are those for which the spin that is passive in both dimensions has a different polarization in t_1 and t_2 .

4.1.4 Strongly-coupled spin systems

It is necessary to determine how strong coupling affects the form of the spectrum, which can be done by using the approach outlined in Section 1.9. However, the calculation rapidly becomes very unwieldy, and so it will be restricted to a two-spin system in which the only terms that are retained are up to $O(\beta^2)$ and $O(\theta)$. This latter restriction is applicable only if the degree of strong coupling is not too high, so that θ is small. It will be shown that strong coupling does not introduce any phase errors into the spectrum [56].

The results of the density matrix calculation for the P-type spectrum are presented

Table 4.2: The peak positions and intensities in the anti *z*-COSY spectrum of a strongly-coupled two-spin system. The multiplets are labelled according to whether the coherence was predominantly present on spin one or two during t_1 or t_2 . Therefore, ‘D1’ refers to the diagonal peak mainly associated on spin one, and ‘C12’ refers to a cross peak where the coherence was mainly present on spin one during t_1 , and spin two during t_2 .

peak type	ω_1 frequency	ω_2 frequency	complex intensity
D1	$\frac{1}{2}(\Omega_1 + \Omega_2 + C + 2\pi J_{12})$	$\frac{1}{2}(\Omega_1 + \Omega_2 + C - 2\pi J_{12})$	$-\frac{1}{4}iS^2c^4(1 + \theta)$
	$\frac{1}{2}(\Omega_1 + \Omega_2 + C - 2\pi J_{12})$	$\frac{1}{2}(\Omega_1 + \Omega_2 + C + 2\pi J_{12})$	$-\frac{1}{4}iS^2c^4(1 - \theta)$
	$\frac{1}{2}(\Omega_1 + \Omega_2 + C + 2\pi J_{12})$	$\frac{1}{2}(\Omega_1 + \Omega_2 + C + 2\pi J_{12})$	$-\frac{1}{4}iS^2c^4\theta$
	$\frac{1}{2}(\Omega_1 + \Omega_2 + C - 2\pi J_{12})$	$\frac{1}{2}(\Omega_1 + \Omega_2 + C - 2\pi J_{12})$	$\frac{1}{4}iS^2c^4\theta$
D2	$\frac{1}{2}(\Omega_1 + \Omega_2 - C + 2\pi J_{12})$	$\frac{1}{2}(\Omega_1 + \Omega_2 - C - 2\pi J_{12})$	$-\frac{1}{4}iS^2c^4(1 - \theta)$
	$\frac{1}{2}(\Omega_1 + \Omega_2 - C - 2\pi J_{12})$	$\frac{1}{2}(\Omega_1 + \Omega_2 - C + 2\pi J_{12})$	$-\frac{1}{4}iS^2c^4(1 + \theta)$
	$\frac{1}{2}(\Omega_1 + \Omega_2 - C + 2\pi J_{12})$	$\frac{1}{2}(\Omega_1 + \Omega_2 - C + 2\pi J_{12})$	$\frac{1}{4}iS^2c^4\theta$
	$\frac{1}{2}(\Omega_1 + \Omega_2 - C - 2\pi J_{12})$	$\frac{1}{2}(\Omega_1 + \Omega_2 - C - 2\pi J_{12})$	$-\frac{1}{4}iS^2c^4\theta$
C12	$\frac{1}{2}(\Omega_1 + \Omega_2 + C + 2\pi J_{12})$	$\frac{1}{2}(\Omega_1 + \Omega_2 - C + 2\pi J_{12})$	$\frac{1}{8}iS^2c^4(1 + 2\theta)$
	$\frac{1}{2}(\Omega_1 + \Omega_2 + C + 2\pi J_{12})$	$\frac{1}{2}(\Omega_1 + \Omega_2 - C - 2\pi J_{12})$	$-\frac{1}{8}iS^2c^4(1 - 6\theta)$
	$\frac{1}{2}(\Omega_1 + \Omega_2 + C - 2\pi J_{12})$	$\frac{1}{2}(\Omega_1 + \Omega_2 - C + 2\pi J_{12})$	$-\frac{1}{8}iS^2c^4(1 + 6\theta)$
	$\frac{1}{2}(\Omega_1 + \Omega_2 + C - 2\pi J_{12})$	$\frac{1}{2}(\Omega_1 + \Omega_2 - C - 2\pi J_{12})$	$\frac{1}{8}iS^2c^4(1 - 2\theta)$
C21	$\frac{1}{2}(\Omega_1 + \Omega_2 - C + 2\pi J_{12})$	$\frac{1}{2}(\Omega_1 + \Omega_2 + C + 2\pi J_{12})$	$\frac{1}{8}iS^2c^4(1 - 2\theta)$
	$\frac{1}{2}(\Omega_1 + \Omega_2 - C - 2\pi J_{12})$	$\frac{1}{2}(\Omega_1 + \Omega_2 + C - 2\pi J_{12})$	$-\frac{1}{8}iS^2c^4(1 + 6\theta)$
	$\frac{1}{2}(\Omega_1 + \Omega_2 - C - 2\pi J_{12})$	$\frac{1}{2}(\Omega_1 + \Omega_2 + C + 2\pi J_{12})$	$-\frac{1}{8}iS^2c^4(1 - 6\theta)$
	$\frac{1}{2}(\Omega_1 + \Omega_2 - C - 2\pi J_{12})$	$\frac{1}{2}(\Omega_1 + \Omega_2 + C - 2\pi J_{12})$	$\frac{1}{8}iS^2c^4(1 + 2\theta)$

in Table 4.2. The peaks are labelled according to whether they are diagonal or cross peaks, and the spin with which they are predominantly associated. There is a set of complementary peaks for the N-type spectrum.

A simulated spectrum for the two-spin system is shown in Figure 4.4. There are three features that are immediately apparent about this spectrum. Firstly, all the peaks have the same phase, which is a consequence of the observable signal being produced by a *z*-filter immediately before acquisition. Secondly, the cross-peak and diagonal-peak multiplets exhibit a roofing effect in which the intensities of the individual components are distorted. Thirdly, the intensities of the on-diagonal components of the diagonal-peak multiplets are much greater than for weakly-coupled spins. They

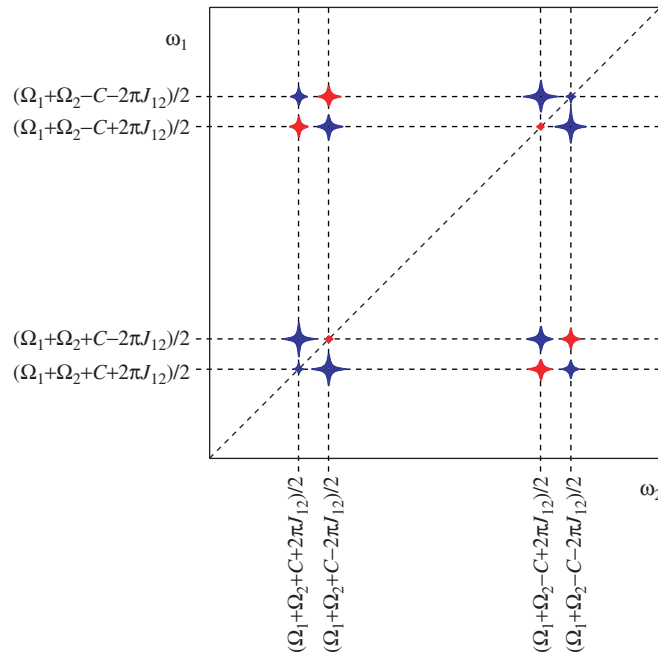


Figure 4.4: Simulated anti *z*-COSY spectrum of a strongly-coupled two-spin system. The value of θ is 3.6° .

could be problematic as they would result in extra unwanted peaks appearing in the decoupled spectrum.

4.2 Separation of chemical shifts and couplings

As has been explained, the decoupled spectrum can be calculated by projecting the diagonal peaks onto the main diagonal. There are two ways in which we can obtain the projection in practice. Firstly, we can rotate the spectrum by 45° so that the main diagonal is parallel to the ω_2 axis, and then project onto this axis. Secondly, we can shear the spectrum so that the multiplets are aligned in the correct way, and then project as before.

Both methods are equivalent; however, it is conceptually easier to start with the rotation, whereas in practice the shear is used. The shear is used in practice because it is both computationally easy to implement, and allows us to process spectra that have been folded, as is described in Section 4.3.

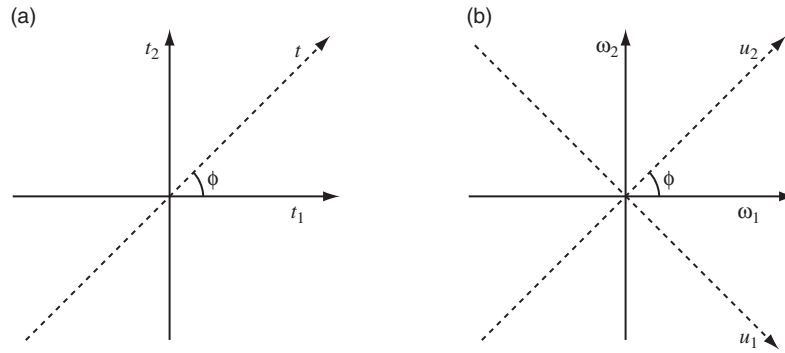


Figure 4.5: Illustration of the axis system used in rotating the anti *z*-COSY spectrum. The time domain is shown in (a), and the frequency domain is shown in (b). The angle of rotation ϕ is 45° .

4.2.1 Rotating the spectrum

The axis system that is used for the rotation is given in Figure 4.5. The time domain is shown in (a), and the frequency domain is shown in (b). Mathematically, the projection onto the axis u_2 is calculated by rotating the spectrum by $\pi/2 - \phi$ so that u_2 coincides with ω_2 , and then integrating over u_1 . The frequency coordinate transformation is

$$\begin{aligned} u_1 &= \omega_1 \sin \phi - \omega_2 \cos \phi \\ u_2 &= \omega_1 \cos \phi + \omega_2 \sin \phi. \end{aligned}$$

When $\phi = \pi/4$, as is the case here, the transformation becomes

$$u_1 = \frac{1}{\sqrt{2}}\omega_1 - \frac{1}{\sqrt{2}}\omega_2 \quad (4.2)$$

$$u_2 = \frac{1}{\sqrt{2}}\omega_1 + \frac{1}{\sqrt{2}}\omega_2. \quad (4.3)$$

4.2.2 Shearing the spectrum

In order to transform the spectrum in such a way as to achieve the offset-coupling separation, two shears are needed. The process is illustrated for a simulated spectrum of a three-spin system in Figure 4.6.

The original spectrum in (a) is sheared parallel to ω_1 with a shear rate of $\kappa_1 = -1$, which gives spectrum (b). The frequency space is transformed into a coordinate

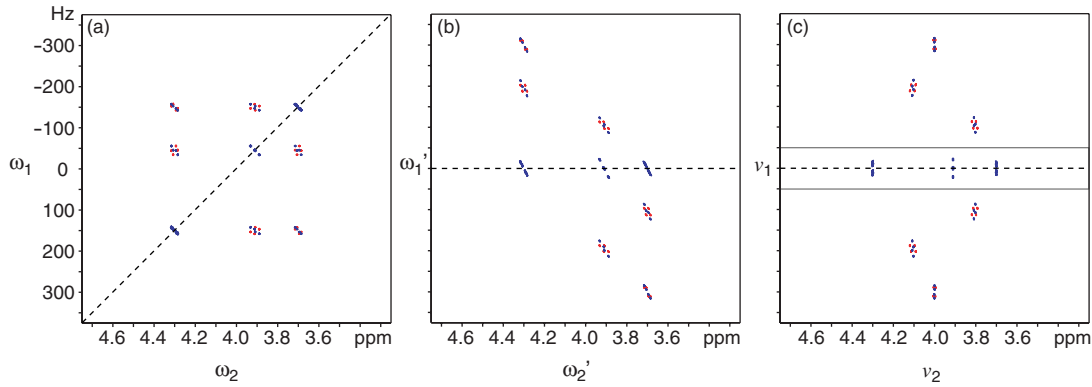


Figure 4.6: The effect of the two shears on the simulated anti *z*-COSY spectrum of a three-spin system. The main diagonal is indicated by the dashed line. See text for details of the shear operations that relate (b) to (a), and (c) to (b).

system (ω'_1, ω'_2) , which is defined as

$$\begin{aligned}\omega'_1 &= \omega_1 + \kappa_1 \omega_2 \\ &= \omega_1 - \omega_2 \\ \omega'_2 &= \omega_2.\end{aligned}$$

The diagonal is now parallel to ω'_2 , but the multiplets are still tilted with respect to ω'_1 . To rectify this, a second shear is applied parallel to ω'_2 , with a shear rate of $\kappa_2 = +\frac{1}{2}$, which gives a spectrum with the coordinate system (v_1, v_2) :

$$\begin{aligned}v_1 &= \omega'_1 \\ &= \omega_1 - \omega_2\end{aligned}\tag{4.4}$$

$$\begin{aligned}v_2 &= \omega'_2 + \kappa_2 \omega'_1 \\ &= \frac{1}{2}\omega_1 + \frac{1}{2}\omega_2.\end{aligned}\tag{4.5}$$

This gives the spectrum in (c) in which we have achieved a complete separation of offsets and *J*-couplings.

On comparing Equations 4.2 and 4.3 with Equations 4.4 and 4.5, it is seen that

$$\begin{aligned}v_1 &= \sqrt{2}u_1 \\ v_2 &= \frac{u_2}{\sqrt{2}}.\end{aligned}$$

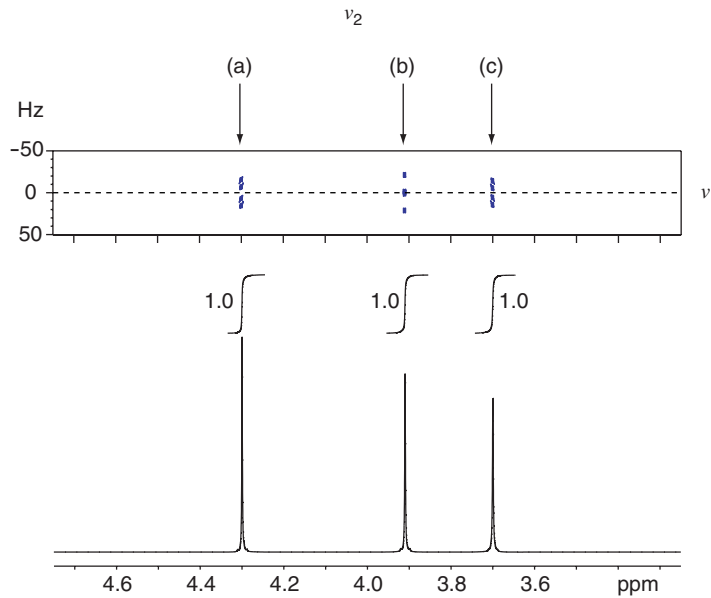


Figure 4.7: The region of the spectrum in Figure 4.6 (c) that is projected. The projection itself is shown below along with the integrals for the three peaks. The values of T_2 that were used are in the ratio 2:1.33:1. The three arrows labelled (a)–(c) indicate the positions at which the vertical cross-sections in Figure 4.8 were taken.

Hence, the combination of these two shears is equivalent to a 45° rotation followed by a scaling operation that is parallel to each of the two rotated axes. The scaling is entirely trivial as both the linewidth and frequency axes are scaled in the same way. The resolution is therefore the same.

The projection of the diagonal peaks of the sheared spectrum onto v_2 gives a broadband proton-decoupled proton spectrum. This projection is calculated by selecting the region of the spectrum which contains only the diagonal-peak multiplets (as shown by the grey box in Figure 4.6 (c)) and summing over the data points in the v_1 dimension. The projected region is shown in Figure 4.7 along with the decoupled spectrum.

In addition, a cross-section that is taken parallel to v_1 at the spin offset in v_2 gives the structure of the associated multiplet. The relevant cross-sections from Figure 4.7 are shown in Figure 4.8 (a)–(c). It should be noted that, as a result of the scaling in the v_1 dimension, the width of a multiplet in this dimension is actually *twice* the width in the conventional spectrum. This is because the stretch factor of $\sqrt{2}$ is multiplied by

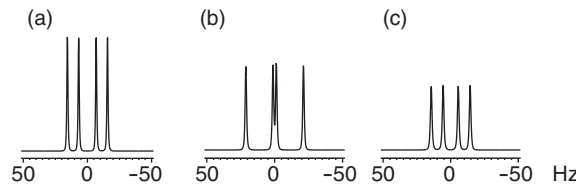


Figure 4.8: The cross-sections of the sheared anti *z*-COSY spectrum of the three-spin system. The three cross-sections were taken at positions (a), (b), and (c) in Figure 4.7, and give the structures of the multiplets.

a second factor of $\sqrt{2}$ that arises because the separation of the peaks measured along the counter-diagonal is larger by a factor of $\sqrt{2}$ than the same separation measured in either the ω_1 or ω_2 dimensions. Therefore, the coupling constants measured from the cross-sections will be twice their actual value.

4.2.3 Lineshapes in the decoupled spectrum

In this Section, it will be shown that the lines in the projection have the absorption-mode lineshape with a linewidth that is the average of the ω_1 and ω_2 linewidths.

The easiest way to calculate the lineshape in the projection is to apply the projection-slice theorem [16] to a spectrum that contains a single absorption-mode line. As discussed in Section 1.12.4 we cannot use the real FID, and so we will use the following fictitious time domain-function,

$$s(t_1, t_2) = \frac{1}{4} \exp(i\Omega^{(1)}t_1) \exp(-|t_1|/T_2^{(1)}) \exp(i\Omega^{(2)}t_2) \exp(-|t_2|/T_2^{(2)}), \quad (4.6)$$

which is defined for both positive and negative times. The factor of $\frac{1}{4}$ is required for normalization. The two-dimensional Fourier transform of this function is the double absorption-mode Lorentzian, with no imaginary part:

$$S(\omega_1, \omega_2) = \mathcal{A}_{\Omega^{(1)}}(\omega_1) \mathcal{A}_{\Omega^{(2)}}(\omega_2).$$

The projection of this lineshape onto the main diagonal (with $\phi = \pi/4$) can be calculated by setting $t_1 = t \cos \phi$ and $t_2 = t \sin \phi$ in Equation 4.6 and calculating the Fourier transform. The resulting one-dimensional slice is

$$s(t/\sqrt{2}, t/\sqrt{2}) = \frac{1}{4} \exp\left[i\frac{1}{\sqrt{2}}(\Omega^{(1)} + \Omega^{(2)})t\right] \exp\left[-|t|\frac{1}{\sqrt{2}}(1/T_2^{(1)} + 1/T_2^{(2)})\right],$$

and the Fourier transform of this is

$$\begin{aligned} P(u_2) &= 2\pi \int_{-\infty}^{\infty} s(t/\sqrt{2}, t/\sqrt{2}) \exp(-iu_2 t) dt \\ &= \frac{\pi T'_2}{1 + (u_2 - \Omega')^2 T'_2^2}, \end{aligned}$$

where Ω' and T'_2 are the effective offset and decay time constant for the line in the projection. They are given by:

$$\begin{aligned} \Omega' &= \frac{1}{\sqrt{2}} (\Omega^{(1)} + \Omega^{(2)}) \\ \frac{1}{T'_2} &= \frac{1}{\sqrt{2}} \left(\frac{1}{T_2^{(1)}} + \frac{1}{T_2^{(2)}} \right). \end{aligned}$$

In practice, we shear the spectrum rather than rotate it, and so the lineshape in the projection is modified to account for the scaling. This gives the following absorption-mode lineshape in the projection:

$$P(v_2) = \frac{\pi T_2^{(p)}}{1 + (v_2 - \Omega^{(p)})^2 T_2^{(p)2}},$$

where

$$\Omega^{(p)} = \frac{1}{2} (\Omega^{(1)} + \Omega^{(2)}), \quad (4.7)$$

and

$$\frac{1}{T_2^{(p)}} = \frac{1}{2} \left(\frac{1}{T_2^{(1)}} + \frac{1}{T_2^{(2)}} \right).$$

The peak in the projection is therefore an absorption-mode Lorentzian whose linewidth is the average of the linewidths in both the ω_1 and ω_2 dimensions.

4.2.4 Sensitivity

In this Section the sensitivity of the anti z -COSY spectrum will be compared with that of the J -spectrum in which the time domain is not weighted. This can be done by comparing the SNR of a singlet in the two spectra. To make the comparison meaningful, the two experiments must be acquired using the same experiment time. It will be seen in the next Section that the spectral width in the anti z -COSY spectrum can be reduced significantly, thus reducing the number of increments that are required to obtain a particular t_1^{\max} . We can therefore record both spectra out to the same t_1^{\max}

using the same number of increments M_1 . In addition t_2^{\max} , the number of scans n , and therefore the experiment times are the same.

The ratio of the SNRs is given by the ratio of the magnitudes of the coefficients in front of the observable terms that arise from the product operator calculations:

$$\frac{\text{SNR } (z\text{-COSY})}{\text{SNR } (J\text{-spectrum})} = \frac{1}{2} \sin^2 \beta.$$

For a flip angle of $\beta = 20^\circ$, the SNR of the anti z -COSY spectrum is 5.8% of the SNR of the J -spectrum, while if $\beta = 10^\circ$, the ratio is 1.5%. The SNR of the latter is comparable to that of the J -spectrum in which the time domain is shaped to a pseudo echo; however anti z -COSY has the advantage that, as no strong weighting functions are used, there are no intensity distortions.

4.3 Anti z -COSY spectra with reduced ω_1 spectral width

It was shown in Section 4.2.3 that the linewidth in the projection is the average of the linewidths in the ω_1 and ω_2 dimensions. This means that we must acquire a large enough number of t_1 increments such that the linewidth in this dimension is not limited by insufficient sampling. The resolution obtained in a given total experiment time can be increased by reducing the ω_1 spectral width. The size of the t_1 increment is thus increased, and so fewer increments are required to achieve a given t_1^{\max} .

Reducing the spectral width also results in the peaks folding in the ω_1 dimension. However, it will be shown that, in the sheared spectrum, the diagonal peaks will always be present in the same positions whether or not they have folded. Therefore, reducing the spectral width does not affect the calculation of the projection. The cross peaks are more problematic, and they may fold into the region we wish to project. However, it will be shown that on folding they acquire different symmetry properties which enable them to be removed in a straightforward way.

4.3.1 The diagonal peaks

When the ω_1 spectral width is reduced, the diagonal is folded into discrete sections, as shown in Figure 4.9 (a). In this diagram, the central section of the diagonal has not folded, and is left in its normal position. The two sections immediately either side have folded once in ω_1 ; the left-hand section has folded from a more negative offset, and the right-hand section has folded from a more positive frequency. The two outer

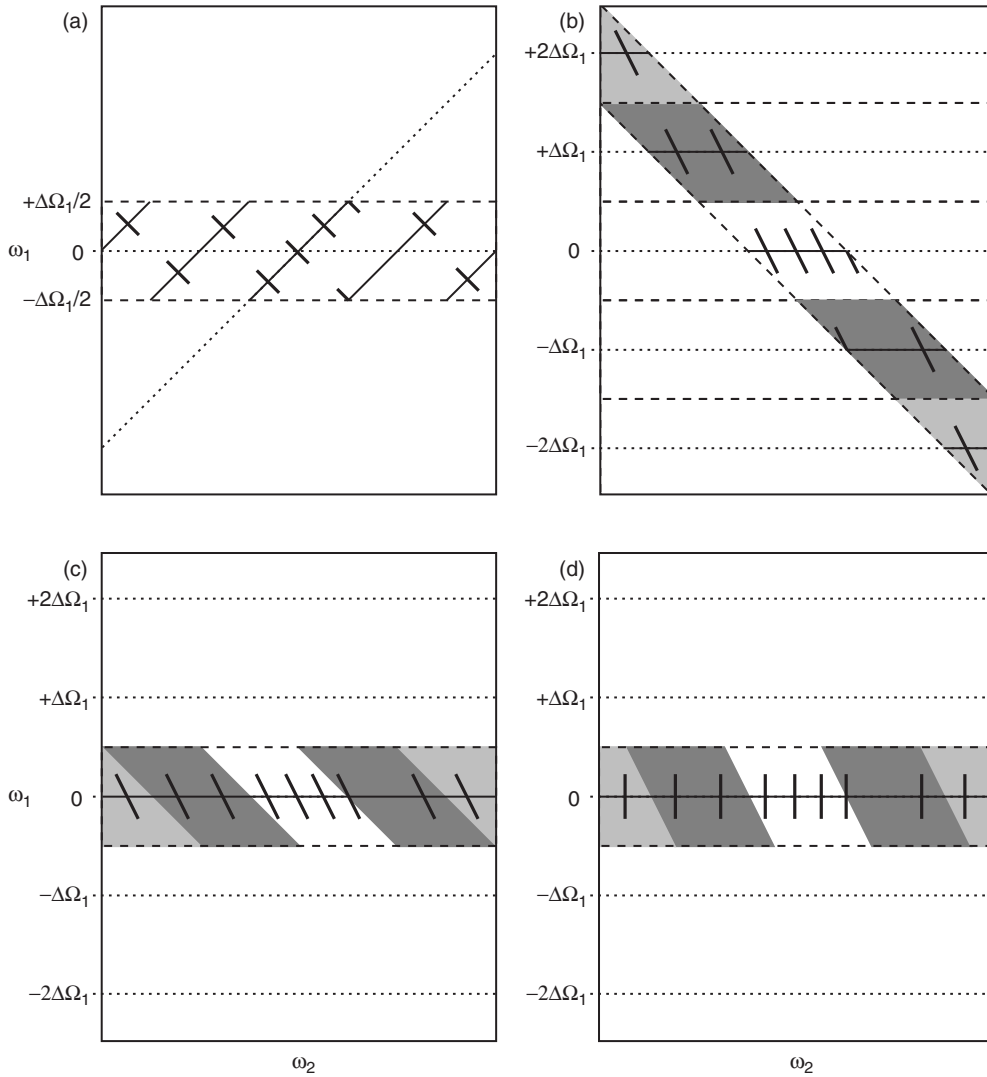


Figure 4.9: An illustration of the effect of shearing on the diagonal-peak multiplets of a folded spectrum. The positions of the multiplets in a folded spectrum are given in (a). The boundaries of the spectral window are given by the widely-spaced dashed lines. The true diagonal, which is represented by the closely-spaced dashed line, is folded into a series of discrete sections, which are represented by the solid lines. This spectrum is sheared parallel to ω_1 with a shear rate of -1 , which gives the spectrum in (b), in which the rectangular spectral window is transformed into a parallelogram. Any regions that were shifted outside the original window are shaded grey. These are wrapped back inside to give the spectrum in (c). Finally the second shear, which is parallel to ω_2 with a shear rate of $+1/2$, gives the spectrum in (d). This second shear also involves a wrapping process, but this is not important in the present discussion, as explained in the text.

sections have each folded twice.

The first shear gives the spectrum in (b). The central section of the diagonal is transformed onto $\omega_1 = 0$ as usual. As to the other sections, there will be two that have folded q times in (a) (one either side of the central section), where q is a positive integer. One will be sheared onto $\omega_1 = +q\Delta\Omega_1$, and the other will be sheared onto $\omega_1 = -q\Delta\Omega_1$. All the multiplets are tilted at an angle of $\tan^{-1} \frac{1}{2}$ to the ω_1 axis.

The rectangular spectral window has been transformed into a parallelogram. It is conventional to translate any sections of the spectrum that lie outside the original window back inside the original rectangle, which is a process that is referred to as wrapping. Each section is translated back by a multiple of $\Delta\Omega_1$; for example, a section that was sheared onto $\omega_1 = -q\Delta\Omega_1$ is translated by $+q\Delta\Omega_1$ so that it now lies on $\omega_1 = 0$. This is shown in the spectrum in (c). Considering only the diagonal peaks, the spectrum is the same after wrapping as the one we would have obtained if the original spectrum had not been folded.

Finally, the second shear aligns the multiplets so that they are parallel to the ω_1 axis as shown in (d). There is also a wrapping process involved with this shear, but provided that $\Delta\Omega_2$ is wide enough to accommodate the whole spectrum, this process is unimportant.

4.3.2 The cross peaks

It can be seen from Figure 4.6 and Equation 4.7 that a cross-peak multiplet between spins i and j will be sheared so that in ν_2 it is centred on the average of Ω_i and Ω_j . Furthermore, since the $i-j$ cross peaks are mirror images of the $j-i$ cross peaks across the diagonal, they will be symmetrically placed about $\nu_1 = 0$ in the sheared spectrum. This is shown for the case of a two-spin system in Figure 4.10 (a); the original spectrum, and the spectrum after each shear are shown. However, if the spectral width is reduced to the extent shown in (b) (by 12% in this case) the cross peaks wrap during the first shear. They are shifted outside the spectral window, and are translated back to different positions compared to (a). The second shear subsequently moves them to non-symmetrical positions. It should be noted that, in this case, the peaks have *not* folded during acquisition; this effect is due solely to the shear.

A similar situation is seen in the spectrum in (c), in which the spectral width has been reduced further still. The amount by which the cross peaks wrap after the first shear is different, and so they are closer to the diagonal.

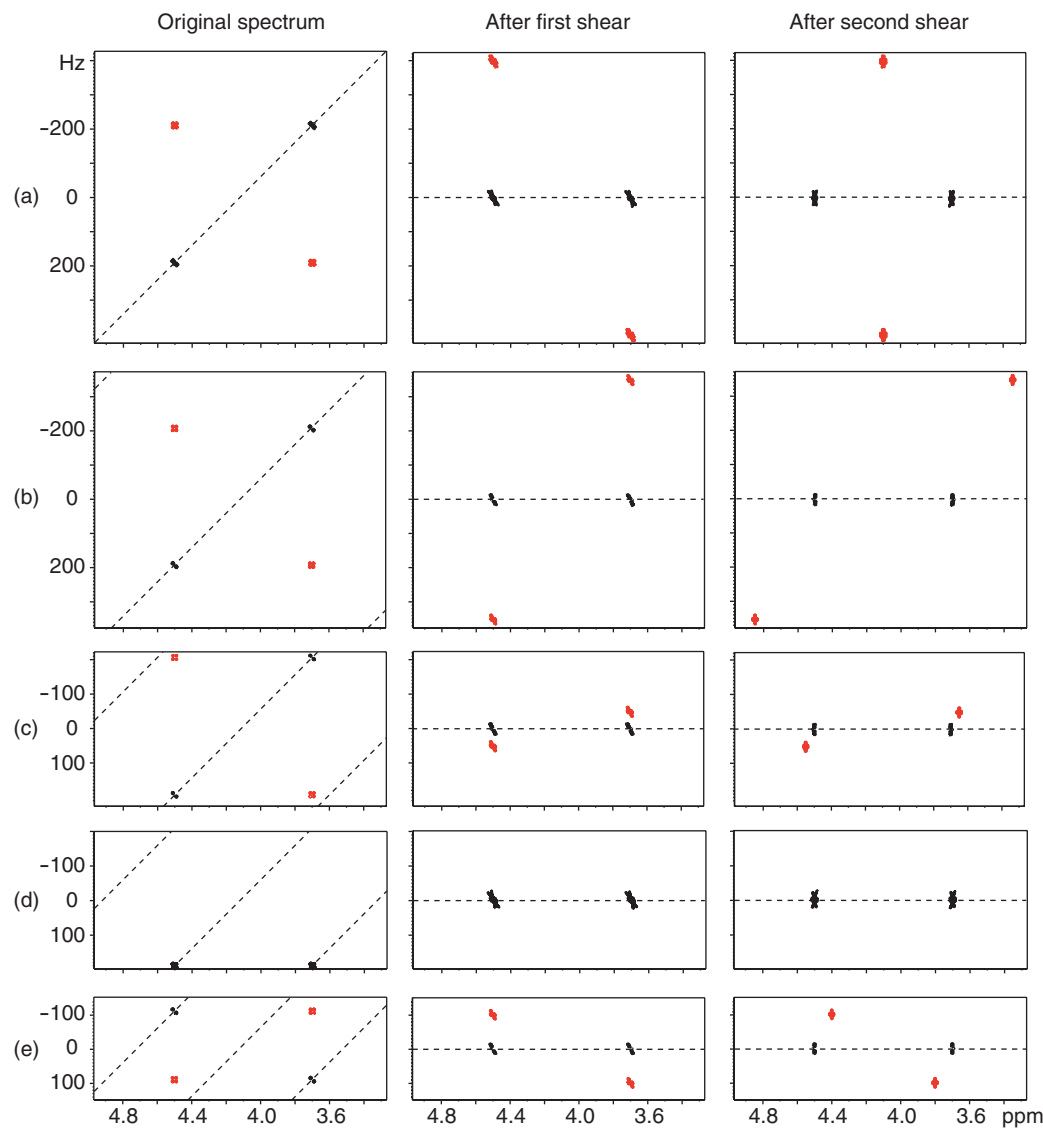


Figure 4.10: Simulated anti *z*-COSY spectra of a two-spin system (at 500 MHz) with different spectral widths in the ω_1 dimension. The ω_2 spectral width is 850 Hz in all cases. The ω_1 spectral width takes the following values: (a) 850 Hz, (b) 750 Hz, (c) 450 Hz, (d) 400 Hz, and (e) 300 Hz. The diagonal is shown as a dashed line. Where they are clearly separated from the diagonal peaks, the cross peaks are coloured red.

In spectrum (d), the cross- and diagonal-peak multiplets at the top of the spectrum have been folded to the bottom, and lie directly on top of the other peaks. Using the method of suppressing the cross peaks that is described in this Section there is, in this case, no way of removing the cross peaks and leaving the diagonal peaks intact. Unfortunately, for a given cross-peak multiplet, there will be an ω_1 spectral width at which the cross peaks will fall directly on top of the diagonal peaks. However, unless the former are perfectly symmetrically related about $v_1 = 0$, it will be possible to at least reduce their intensity.

In the last spectrum (e), all the peaks have folded during acquisition. However as expected, the diagonal peaks still shear to the same positions as before and the cross peaks are, once again, moved to unsymmetrical positions.

In general, the $i-j$ cross-peak multiplet will be unsymmetrically related to its partner provided the spectral width $\Delta\Omega_1$ is small enough for the following relationship to apply:

$$|\Omega_i - \Omega_j| > \frac{1}{2}\Delta\Omega_1.$$

This inequality is proved by applying simple geometry.

4.3.3 Removal of the cross peaks by symmetrization

For a weakly-coupled spin system, the diagonal-peak multiplets in the sheared spectrum are symmetrically distributed about $v_1 = 0$. The cross peaks, if they are folded in ω_1 or wrapped during the first shear, are not symmetrically-related to their partners. They can therefore be removed by applying a simple symmetrization procedure. The intensity at (v_1, v_2) is compared with the intensity at $(-v_1, v_2)$; the higher absolute value is replaced by the lower absolute value, while retaining the original sign.

If there is no accidental overlap between the cross peaks and diagonal peaks, this procedure removes all the cross peaks that have folded or wrapped differently from their partners. It is therefore remarkably effective at ‘cleaning up’ the spectrum, as shown in Figure 4.11.

Cross peaks that have not wrapped differently will still be symmetrically-related to their partners, and so will not be removed by symmetrization. Such cross-peak multiplets necessarily lie close to the diagonal. They are not due to strong coupling *per se*, but are analogous to the strong-coupling artefacts in two-dimensional *J*-spectra.

If an individual cross peak falls directly on top of an individual diagonal peak, the

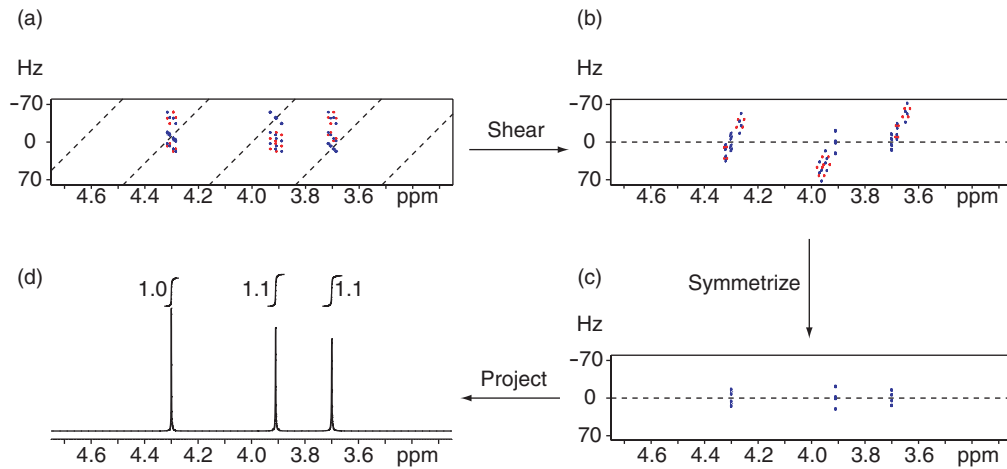


Figure 4.11: Illustration of the shearing and symmetrization processes on the simulated spectrum of a three-spin system with reduced ω_1 spectral width. The folded spectrum in (a) is sheared to give the spectrum in (b). Symmetrization removes the cross peaks to give the spectrum in (c), which is projected onto v_2 to give (d). The integrals are given with the projection.

intensity of the latter will be perturbed in a way that may or may not be removed by symmetrization. If the intensity of the diagonal peak is increased by the overlap, the symmetrization will restore the correct intensity. If, on the other hand, the diagonal peak is reduced in intensity, the perturbation will be transferred to its symmetrically-related counterpart.

The result of all this is that, even after symmetrization, the folding of cross peaks into the region occupied by the diagonal peaks may lead to intensity perturbations that will affect the projection and the multiplets. This is seen in Figure 4.11 (d) in the form of perturbations of the integrals.

A further consideration is how symmetrization affects the diagonal-peak multiplets of strongly-coupled spin systems. It was shown in Section 4.1.4 that the diagonal peaks of such systems display the characteristic roofing effect. Hence, the two peaks within a given symmetrically-related pair will have different intensities, and symmetrization will therefore reduce the intensity of the largest peak so that it matches that of the lower intensity peak.

If the linewidths in the two dimensions are the same, the symmetrization will affect neither the lineshape nor the linewidth in the projection. This is shown in Figure 4.12 (a). If the ω_1 linewidth is greater than the ω_2 linewidth, which may result from

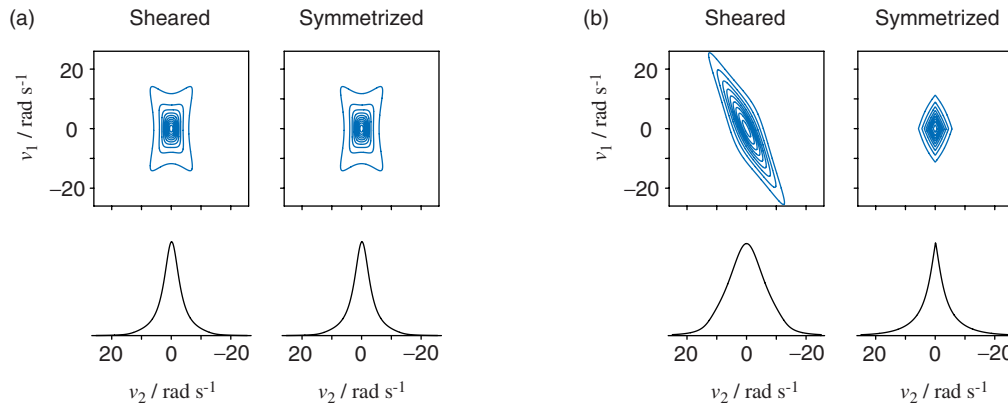


Figure 4.12: The effect of symmetrization on the sheared spectrum of a singlet in which the ω_1 linewidth is greater than the ω_2 linewidth. In both cases, the ω_2 linewidth is 1 Hz. In (a), the ω_1 linewidth is the same as the linewidth in ω_2 (1 Hz), while in (b) it is 4 Hz. The sheared two-dimensional spectra are shown before and after symmetrization, and the projection of each is given below. The spectrum in (a) is unaffected by symmetrization, and so the two projections are the same. On the other hand, the peak in (b) is distorted as the broader parts of the line are removed. The projection of the symmetrized spectrum has a somewhat lower linewidth, but retains the broad base.

restricted sampling in t_1 followed by the application of a decaying weighting function, symmetrization will result in changes to the lineshape, as shown in (b). One effect that is observed is a reduction of the linewidth in the projection. Generally speaking the FWHM is close to the ω_2 value, while the base in the lineshape reflects the broader line in ω_1 . Therefore, there is little real improvement in resolution.

4.4 Direct suppression of the cross peaks

Rather than relying on symmetrization alone to remove the cross peaks, it is desirable to have a pulse-sequence based method for suppressing them. This is termed ‘direct suppression’ of the cross peaks.

Suppressing the cross peaks, and retaining the diagonal peaks, in *z*-COSY poses essentially the same problem as the suppression of ZQ coherence during a *z*-filter [33–35], or the removal of strong-coupling artefacts from a *J*-spectrum [8]. In both of these cases, the wanted and unwanted terms in the density operator follow the same CTP, and so cannot be removed by conventional phase-cycling or gradient-selection methods. However, there is a difference between the density operator terms that

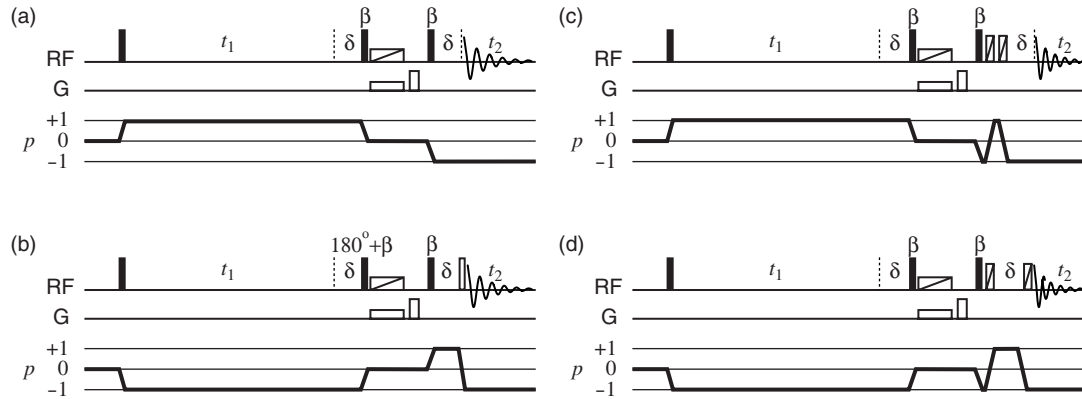


Figure 4.13: Anti *z*-COSY pulse sequences incorporating the multiple-scan cross-peak suppression scheme. The required CTPs are also shown. The sequence in (a) gives the N-type spectrum, and the sequence in (b) gives the P-type spectrum. Sequences (c) and (d) also give the N- and P-type spectra respectively, but have been modified to include a pair of swept-frequency 180° pulses (represented by the open rectangles with diagonal strokes after the second β pulse). In (a) and (c), both the first mixing pulse and receiver are phase cycled according to $[0, \pi/2, \pi, 3\pi/2]$. The receiver phase takes the same values in the P-type sequences of (b) and (d), but the first mixing pulse is cycled according to $[0, 3\pi/2, \pi, \pi/2]$.

produce the cross peaks and diagonal peaks that allows the former to be suppressed. The cross peaks are generated by coherence transfer during the *z*-filter, and so evolve at a different offset either side of the mixing period. The diagonal peaks, on the other hand, evolve at the same offset.

This feature is exploited in the pulse sequences shown in Figure 4.13. A delay δ is inserted either side of the mixing period, and a CTP is selected so that the coherence order is of *opposite* sign during the two delays. For a diagonal peak, the phase acquired during the first delay is equal and opposite to the phase acquired during the second delay, and as a result the diagonal peaks acquire no overall phase. In contrast, an operator giving rise to a cross peak between spins *i* and *j* will evolve at the offset of spin *i* during the first delay and acquire a phase $-\Omega_i\delta$ (in the case of the sequence in (a)). During the second delay, the operator acquires a phase $+\Omega_j\delta$. Therefore, the cross peak acquires an overall phase of $(\Omega_i - \Omega_j)\delta$, and so can be suppressed by the co-addition of several spectra with different values of δ .

In order that the magnetization giving rise to the diagonal peaks acquires no overall phase, it is essential that the coherence order must be ± 1 during the first delay, and ∓ 1

during the second delay. The N-type and P-type spectra must therefore be recorded with separate sequences, and the data combined in the usual way to give absorption-mode lineshapes. The two variants of the pulse sequence, which give the N-type and P-type spectra, are given in Figure 4.13 (a) and (b). The inclusion of the 180° pulse just prior to t_2 in the latter ensures that the coherence order of +1 is converted to -1 for acquisition.

4.4.1 Analysis of the pulse sequences

The pulse sequences in Figure 4.13 (a) and (b) will be analyzed for a two-spin system, which is sufficient as such a spin system illustrates all the relevant properties. Starting from equilibrium magnetization on spin one, the density operator at the start of t_1 is $-\hat{I}_{1y} = \frac{1}{2}i(\hat{I}_{1+} - \hat{I}_{1-})(\hat{I}_{2\alpha} + \hat{I}_{2\beta})$. Ultimately, the operators containing \hat{I}_{1+} produce the N-type spectrum, and those containing $-\hat{I}_{1-}$ produce the P-type spectrum. For simplicity, we will calculate the evolution of a single operator from each: that is, the evolution of $\hat{I}_{1+}\hat{I}_{2\alpha}$ during sequence (a), and the evolution of the complementary operator $-\hat{I}_{1-}\hat{I}_{2\alpha}$ during sequence (b). Initially, it is assumed that $\delta \ll 1/|J_{12}|$, so that the evolution of the J -coupling can be ignored during the delays δ .

In sequence (a), the operator $\hat{I}_{1+}\hat{I}_{2\alpha}$ evolves to give the following term just prior to the mixing period:

$$\hat{I}_{1+}\hat{I}_{2\alpha} \exp[-i(\Omega_1 + \pi J_{12})t_1] \exp[-i\Omega_1\delta].$$

The first β pulse produces the following population terms:

$$\frac{1}{2}iS c^2 (\hat{I}_{1\alpha}\hat{I}_{2\alpha} - \hat{I}_{1\beta}\hat{I}_{2\alpha}) \exp[-i(\Omega_1 + \pi J_{12})t_1] \exp[-i\Omega_1\delta],$$

which are inverted by the swept pulse to give

$$\frac{1}{2}iS c^2 (\hat{I}_{1\beta}\hat{I}_{2\beta} - \hat{I}_{1\alpha}\hat{I}_{2\beta}) \exp[-i(\Omega_1 + \pi J_{12})t_1] \exp[-i\Omega_1\delta].$$

The second β pulse gives the following observable terms:

$$-\frac{1}{4}S^2 c^4 (2\hat{I}_{1-}\hat{I}_{2\beta} + \hat{I}_{1\beta}\hat{I}_{2-} - \hat{I}_{1\alpha}\hat{I}_{2-}) \exp[-i(\Omega_1 + \pi J_{12})t_1] \exp[-i\Omega_1\delta],$$

which comprise one diagonal peak, and two cross peaks. Finally, evolution during the

second delay δ gives the following terms prior to acquisition:

$$\begin{aligned} & -\frac{1}{2}S^2c^4 \exp[-i(\Omega_1 + \pi J_{12})t_1] \hat{I}_{1-}\hat{I}_{2\beta} \\ & -\frac{1}{4}S^2c^4 \exp[i(\Omega_2 - \Omega_1)\delta] \exp[-i(\Omega_1 + \pi J_{12})t_1] \hat{I}_{1\beta}\hat{I}_{2-} \\ & +\frac{1}{4}S^2c^4 \exp[i(\Omega_2 - \Omega_1)\delta] \exp[-i(\Omega_1 + \pi J_{12})t_1] \hat{I}_{1\alpha}\hat{I}_{2-}. \end{aligned}$$

The cross peaks, which are the second and third terms, acquire a phase that depends on δ , whereas the diagonal peak does not.

In the P-type experiment in (b), the operator $-\hat{I}_{1-}\hat{I}_{2\alpha}$ produces the following observable terms:

$$\begin{aligned} & -\frac{1}{2}S^2c^4 \exp[+i(\Omega_1 + \pi J_{12})t_1] \hat{I}_{1-}\hat{I}_{2\beta} \\ & -\frac{1}{4}S^2c^4 \exp[-i(\Omega_2 - \Omega_1)\delta] \exp[+i(\Omega_1 + \pi J_{12})t_1] \hat{I}_{1\beta}\hat{I}_{2-} \\ & +\frac{1}{4}S^2c^4 \exp[-i(\Omega_2 - \Omega_1)\delta] \exp[+i(\Omega_1 + \pi J_{12})t_1] \hat{I}_{1\alpha}\hat{I}_{2-}. \end{aligned}$$

Again, the cross peaks have acquired a phase that depends on δ .

The cross peaks of a two-spin system can be suppressed by acquiring two experiments, the first with $\delta = 0$, and the second with $\delta = \pi/|\Omega_1 - \Omega_2|$. This ensures that the cross peaks have the opposite sign in each experiment, whereas the diagonal peaks are unaffected. If there are several cross-peak multiplets that need to be suppressed, the experiment is repeated a number of times with a systematic variation in the value of δ . The attenuation factor A_{cross} is given by

$$A_{\text{cross}} = \frac{1}{N} \left| \sum_{n=0}^{N-1} \exp[i(\Omega_1 - \Omega_2)\delta_n] \right|,$$

where δ_n is the value of δ in the n th experiment, and there are N experiments acquired in total. The value of A_{cross} gives the reduction in the intensity of a cross peak relative to its intensity in a spectrum that is acquired with $\delta = 0$.

Two representative attenuation curves are plotted as a function of $\Omega_1 - \Omega_2$ in Figure 4.14. The curve in (a) is plotted for eight equally-spaced values of δ between 0 and 10 ms. It has a similar form to the multiple-scan ZQ suppression curves in Figure 2.12 (a), which reflects the similarity of the two suppression schemes. In this case, the summation can be simplified to give

$$A_{\text{cross}} = \frac{1}{N} \left| \frac{1 - \exp[i(\Omega_1 - \Omega_2)\delta_{N-1}N/(N-1)]}{1 - \exp[i(\Omega_1 - \Omega_2)\delta_{N-1}/(N-1)]} \right|,$$

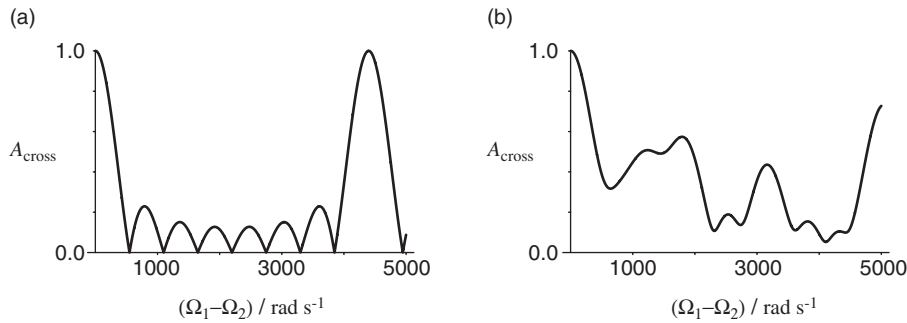


Figure 4.14: Attenuation curves for the multiple-scan cross-peak suppression scheme. The curve in (a) was generated using eight values of δ that were equally-spaced between 0 and 10 ms. Plot (b) is the result of eight random values between 0 and 10 ms.

where δ_{N-1} is the maximum value of δ . The nulls are located at the following frequencies:

$$\Omega_1 - \Omega_2 = 2m\pi \frac{N-1}{N\delta_{N-1}}, \quad (4.8)$$

where m is an integer which is *not* a multiple of N . If m is an integer multiple of N , the cross peaks acquire the same phase in each scan, and $A_{\text{cross}} = 1$.

The curve plotted in (b) was generated with eight random values of δ between 0 and 10 ms. From these plots it can be seen that, generally, systematic variation gives better suppression than random variation for a larger range of offsets, and so this was the scheme that was employed.

The effect of J-modulation

The lowest value of $\Omega_1 - \Omega_2$ for which the cross-peak multiplet is completely suppressed is located at the first null in the attenuation curve, as given by Equation 4.8 with $m = 1$. The best way of ensuring that cross peaks closer to the diagonal are completely suppressed is to increase the maximum value of δ , so that this null occurs for smaller values of the difference in the offsets. However, it is likely that δ will then extend to values such that the J -modulation cannot be ignored, and it is important that we calculate the effect of this on the diagonal peaks in both the N-type and P-type experiments.

In the N-type experiment, the operator $\hat{I}_{1+}\hat{I}_{2\alpha}$ evolves during the first delay δ to give

$$\hat{I}_{1+}\hat{I}_{2\alpha} \exp [-i(\Omega_1 + \pi J_{12})\delta].$$

The z -filter comprises two small flip angle pulses and one 180° pulse, the overall effect of which is to change the polarization of the passive spin. The resulting diagonal-peak term is therefore

$$-\frac{1}{2}S^2c^4\hat{I}_{1-}\hat{I}_{2\beta}\exp[-i(\Omega_1 + \pi J_{12})\delta],$$

which evolves during the second delay δ to give

$$\begin{aligned} & -\frac{1}{2}S^2c^4\hat{I}_{1-}\hat{I}_{2\beta}\exp[-i(\Omega_1 + \pi J_{12})\delta]\exp[+i(\Omega_1 - \pi J_{12})\delta] \\ & = -\frac{1}{2}S^2c^4\hat{I}_{1-}\hat{I}_{2\beta}\exp[-2i\pi J_{12}\delta]. \end{aligned}$$

As has been mentioned before, selecting the CTP so that the coherence order is of opposite sign during the two delays ensures that the offset is refocused. However, in addition, the passive spin has been flipped which results in the J -coupling evolving for 2δ . Hence, this sequence behaves in the same way as a standard spin echo experiment.

In the P-type experiment, the complementary operator $-\hat{I}_{1-}\hat{I}_{2\alpha}$ evolves during the first delay to give

$$-\hat{I}_{1-}\hat{I}_{2\alpha}\exp[+i(\Omega_1 + \pi J_{12})\delta].$$

The z -filter now comprises two small flip angle pulses, and *two* 180° pulses (as the first mixing pulse has flip angle $\beta + 180^\circ$). Each 180° pulse changes the polarization of the passive spin, and so the overall result is that the spin does *not* flip. The diagonal-peak term is therefore

$$-\frac{1}{2}S^2c^4\hat{I}_{1+}\hat{I}_{2\alpha}\exp[+i(\Omega_1 + \pi J_{12})\delta].$$

This term evolves during the second delay δ to give

$$\begin{aligned} & -\frac{1}{2}S^2c^4\hat{I}_{1+}\hat{I}_{2\alpha}\exp[+i(\Omega_1 + \pi J_{12})\delta]\exp[-i(\Omega_1 + \pi J_{12})\delta] \\ & = -\frac{1}{2}S^2c^4\hat{I}_{1+}\hat{I}_{2\alpha}. \end{aligned}$$

Once again, the offset is refocused as the coherence order is of opposite sign during the two delays. However, the passive spin has *not* been flipped by the z -filter, and so the J -coupling is also refocused.

The J -modulation which occurs in the N-type experiment, but not in the P-type, will lead to a phase distortion in the diagonal peaks of the spectrum when the two sets of data are combined. Neither the two-dimensional spectrum, nor the projection will be in the absorption mode. It is therefore concluded that this method cannot be used

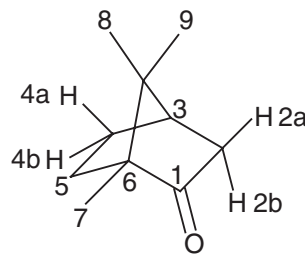


Figure 4.15: The chemical structure of camphor with the labels used for the assignment of the spectrum.

to suppress the cross peaks that lie close to the diagonal, as the values of δ that would be required lead to significant phase errors.

A second disadvantage that arises from using large values of δ is that the degree by which the signal decays due to transverse relaxation will be significant. The peak heights will be reduced by a factor of $\exp(-2\delta/T_2)$, which depends on T_2 . The integrals will therefore be weighted by relaxation, and so the spectrum will no longer be quantitative.

4.5 Experimental verification

The method for obtaining the separation of offsets and couplings is illustrated experimentally with the spectra of camphor (dissolved in CDCl_3), whose structure is shown in Figure 4.15.

All the spectra were recorded at 500 MHz for ^1H on a Bruker Avance DRX500 spectrometer. Both the mixing pulses in the z -filter had the same flip angle of 10° . Removal of coherences of non-zero coherence order during the z -filter was achieved using a homospoil gradient that was shaped to a half-sine bell, of duration 5 ms, and with a maximum strength of 50% of the maximum intensity of 55.8 G cm^{-1} *. The suppression of the ZQ coherences was achieved with a CHIRP pulse with an RF field strength of 1.7 kHz (the first and last 10% of the amplitude profile were smoothed), and which swept through a range of frequencies of 24 kHz in 24 ms [22–24]; the accompanying gradient had a relative strength of 4% [34]. The basic pulse sequence

*The absolute gradient strength was determined by measuring the diffusion constant of HOD in a sample of 1% H_2O in D_2O which was doped with 1 mg/ml of GdCl_3 . The literature value for this constant is $19.0 \times 10^{-6} \text{ cm}^2 \text{ s}^{-1}$ at 25°C [57].

which incorporates both the homospoil and ZQ suppression scheme is shown in Figure 4.1 (b).

A two-step phase cycle in which the phases of both the first pulse and receiver were changed by 180° was used to suppress the axial peaks, i.e. peaks resulting from z -magnetization that was produced by longitudinal relaxation during t_1 and subsequently converted into observable magnetization by the mixing period. The spectral width in ω_2 is 1085 Hz, and the acquisition time in t_2 was 1.89 s.

Further experimental parameters that are relevant to specific experiments are given in the relevant sections.

4.5.1 Anti z -COSY with full spectral width

The anti z -COSY spectrum with the full ω_1 spectral width of 1085 Hz is shown in Figure 4.16 (a). Frequency discrimination and absorption-mode lineshapes were achieved by using the SHR method [15]. The number of t_1 increments acquired was 760, giving a t_1^{\max} of 0.7 s. This is sufficient to ensure that the time-domain data for the multiplets are not truncated, barring the three methyl groups. However, for the present discussion, the methyls are the least interesting part of the spectrum.

The region of the doubly sheared spectrum that is projected is shown in (b). The projection itself is shown in Figure 4.17 (b), with the conventional spectrum in (a) for comparison.

The multiplet structures of the first seven camphor multiplets (starting at the largest chemical shift) obtained from the vertical cross sections taken at the offsets of the spins are shown in Figure 4.18 (a)–(g). The multiplets shown in (f) and (g) are of particular interest as they overlap in the conventional one-dimensional spectrum, making it impossible to distinguish their form. This overlap is removed by the separation of offsets and couplings, giving a clear view of the multiplets.

The cross-peak multiplets between the diagonal-peak multiplets that are centred on 1.35 and 1.42 ppm lie very close to the diagonal, and so are included in the region that is projected. They project to give the set of peaks with the apparent anti phase structure. It is possible to leave these peaks out of the projection by projecting over a smaller range of ω_1 frequencies. A series of such ‘limited projections’ is shown in Figure 4.19 (a)–(c). This approach produces projections in which the integrals are distorted, as not all the diagonal-peak components are included. Nevertheless, these limited projections may be of interest as they avoid contributions from the cross peaks.

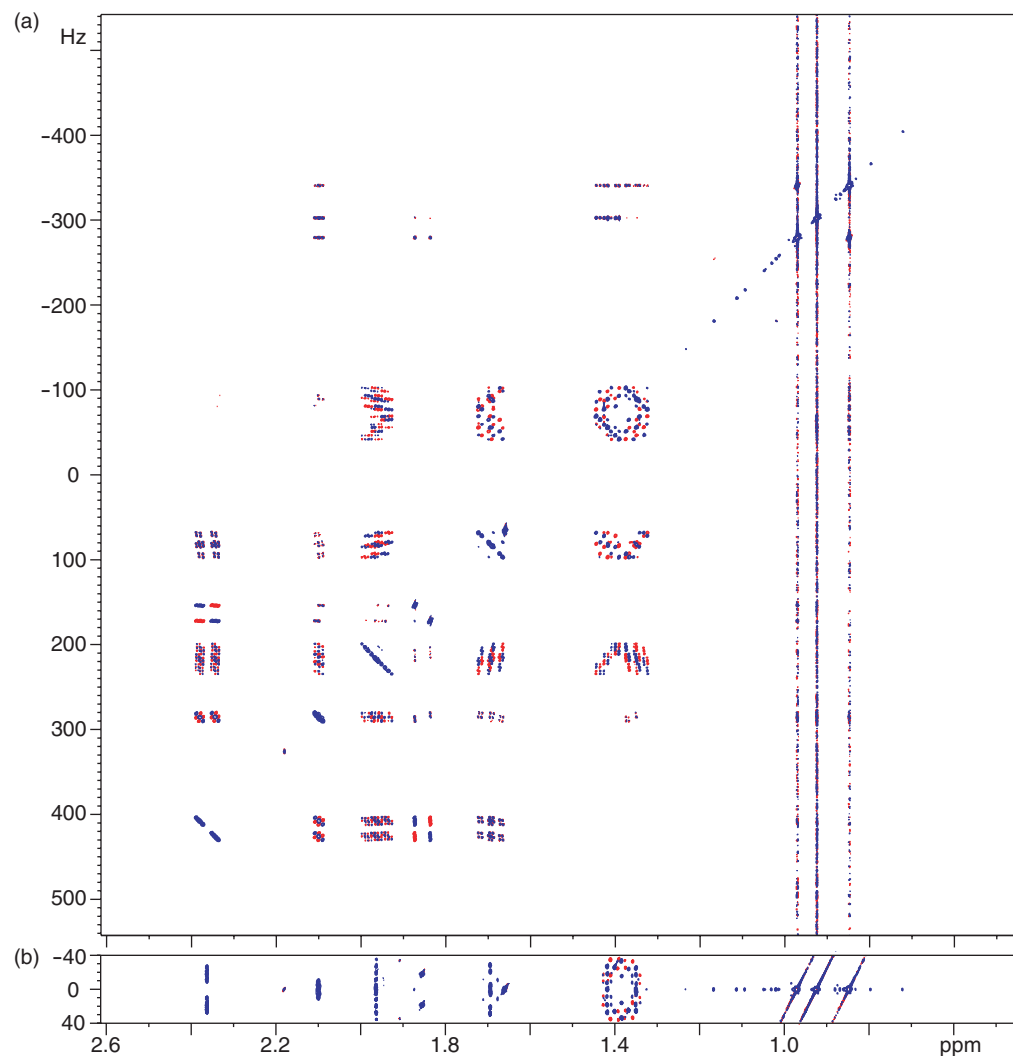


Figure 4.16: The anti z -COSY spectrum of camphor dissolved in CDCl_3 . The spectrum with the full spectral width is shown in (a). This is sheared, and the central region, shown in (b), is projected to give the decoupled spectrum. The region between 1.35 and 1.42 ppm contains two cross-peak multiplets that lie very close to the diagonal, and so they are included in the projected region. Some t_1 noise is visible at the shifts of the three methyl groups between 0.8 and 1.0 ppm [58].

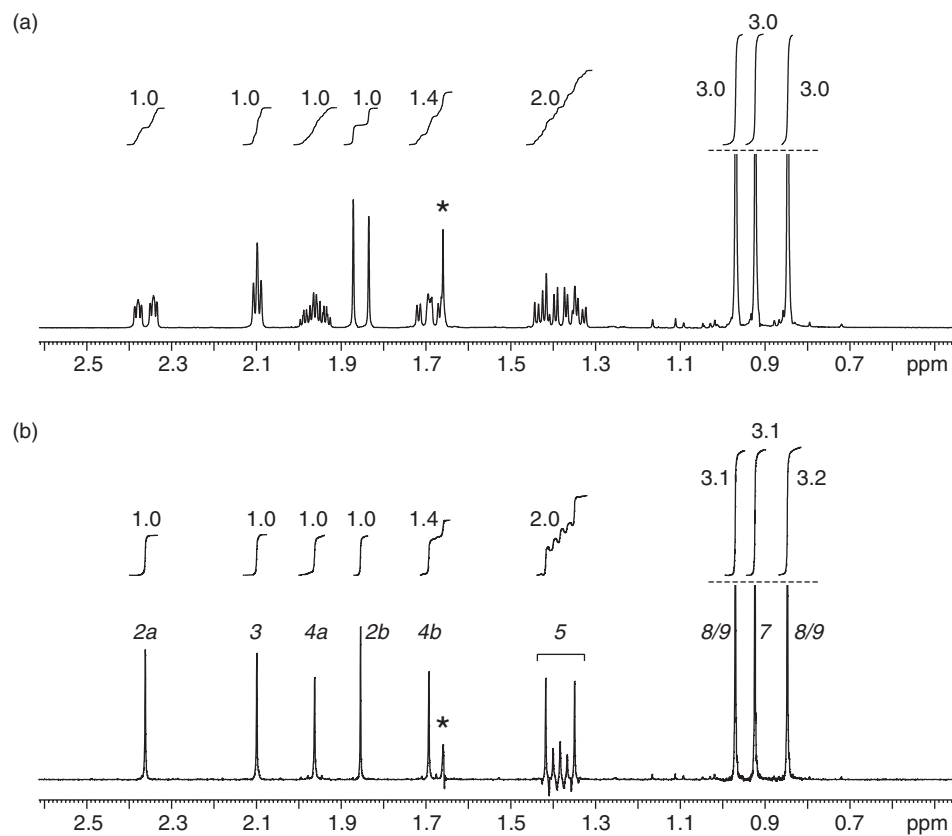


Figure 4.17: The one-dimensional spectra of camphor dissolved in CDCl_3 . The conventional spectrum is shown in (a), and the decoupled spectrum (calculated from the projection of Figure 4.16 (b)) is shown in (b). In both cases, the integrals of each resonance are given relative to the resonance at 2.36 ppm. The peak at 1.66 ppm is due to H_2O dissolved in the CDCl_3 , and is marked with an *. The two peaks at 1.35 and 1.42 ppm are due to spins that are strongly coupled to each other, resulting in the cross peaks lying very close to the diagonal (see Figure 4.16). These cross peaks project to give the set of anti-phase peaks between the two singlets. The numbers in italics give the assignment corresponding to the labels in Figure 4.15.

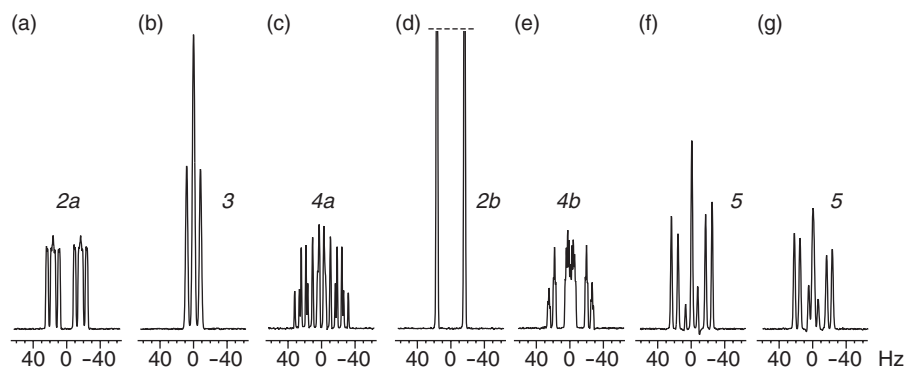


Figure 4.18: The cross-sections taken from Figure 4.16 (b) giving the structures of the seven camphor multiplets with the largest chemical shifts. They are taken at the following shifts in ppm: (a) 2.36, (b) 2.10, (c) 1.96, (d) 1.85, (e) 1.69, (f) 1.42, and (g) 1.35. The assignment is given by the italicized numbers.

4.5.2 Anti *z*-COSY with reduced spectral width

Figure 4.20 (a) shows an anti *z*-COSY spectrum in which the ω_1 spectral width is reduced to 100 Hz. The number of t_1 increments that were acquired is 70, giving a t_1^{\max} of 0.7 s, which is the same as for the spectrum in Figure 4.16 (a). The sheared spectrum is shown in (b), from which it can be seen that the diagonal peaks have moved to their usual positions. However, the cross peaks now lie all over the spectrum, but are mostly removed by symmetrization to give the spectrum shown in (c). The cross peaks that lie close to the diagonal (between 1.35 and 1.42 ppm) have not folded/wrapped differently to their partners, and so are not removed by the symmetrization procedure.

4.5.3 Anti *z*-COSY spectra with direct cross-peak suppression

Direct suppression of the cross peaks was achieved using the pulse sequences in Figure 4.13 (c) and (d) to give separate N-type and P-type data. These sequences make use of the BIPs to achieve broadband inversion of the passive spins as they have a greater tolerance to RF inhomogeneity than conventional hard pulses. The specific pulses that were used are designated BIP-720-25-40, and had a duration of 100 μ s and B_1 field of 20 kHz [27]. Two such pulses were used so that the phase errors generated by the first were refocused by the second.

The cross-peak suppression scheme employed eight values of the delay δ that were equally-spaced between 0 and 10 ms. The smallest frequency difference for which there is a null in the corresponding attenuation curve is 87.5 Hz. Selection of the CTP

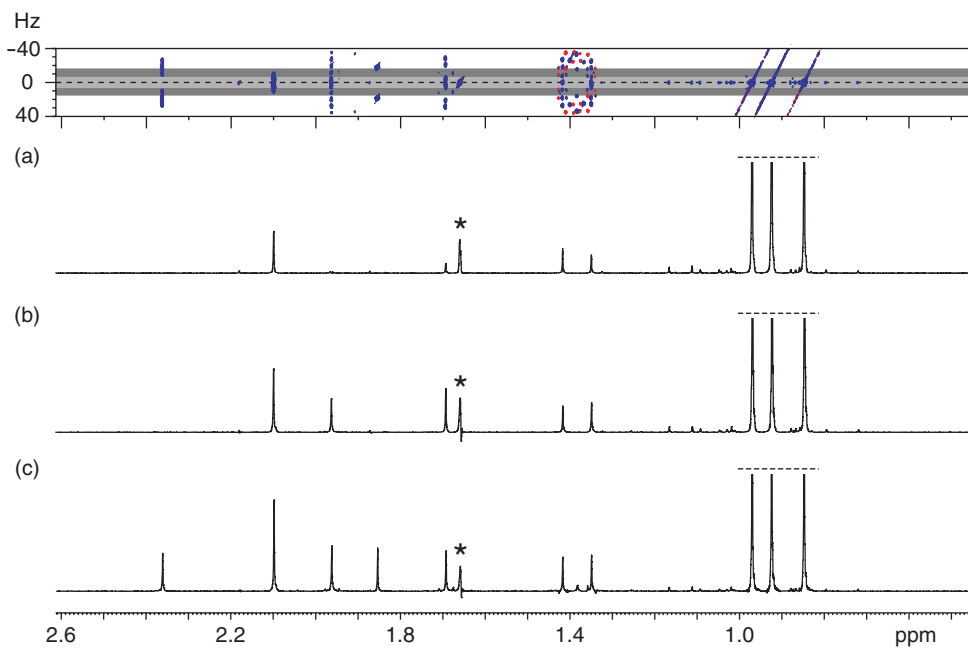


Figure 4.19: A selection of limited projections of the region containing the diagonal-peak multiplets from the anti z -COSY spectrum of camphor dissolved in CDCl_3 . Spectrum (a) is the single row at $\omega_1 = 0$ (the dashed line). The close-lying cross peaks do not contribute any intensity. However, some of the diagonal-peak multiplets do not contribute either as they have zero intensity in this row. Widening the range of the limited projection to 11 Hz (range indicated by the area that is shaded light grey) includes more of the diagonal-peak intensity, giving the spectrum in (b). Increasing the range to 33 Hz (dark grey region) is sufficient to include intensity from all the diagonal-peak multiplets, as shown in (c), but some of the close-lying cross peaks are also included. The peak labelled with an * is due to H_2O .

to give either the echo or anti-echo was achieved with a four-step phase cycle. The first mixing pulse took the values $[0, \pi/2, \pi, 3\pi/2]$ in the N-type experiment, and $[0, 3\pi/2, \pi, \pi/2]$ in the P-type experiment; in both cases the receiver phase took the values $[0, \pi/2, \pi, 3\pi/2]$, which ensured that $\Delta p = -1$ was selected in the former, and $\Delta p = +1$ was selected in the latter.

The anti z -COSY spectrum that was acquired with the full spectral width in ω_1 is shown in Figure 4.21. There is a significant reduction in the intensities of the cross peaks, although the close-lying cross peaks between 1.35 and 1.42 ppm are only partially suppressed on account of the small difference between the offsets of the coupled spins.

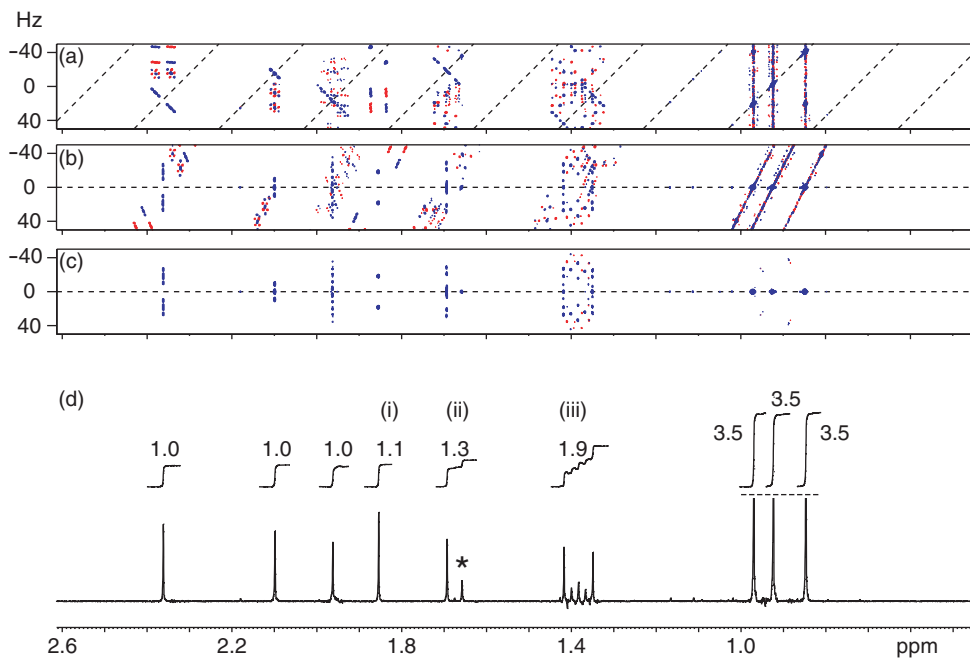


Figure 4.20: The anti *z*-COSY spectrum of camphor, dissolved in CDCl_3 , with reduced spectral width. The spectrum is shown in (a), which is sheared to give (b). Symmetrization gives (c), from which we obtain the decoupled spectrum in (d). The integrals are still in good agreement with the conventional spectrum, but there is some deviation for the integrals labelled (i)–(iii) and the methyls. The cross peaks lying close to the diagonal are still present after symmetrization since they are symmetrically-distributed in the sheared spectrum. The H_2O peak is labelled with an *.

This method of cross-peak suppression requires recording the spectrum with multiple values of δ , which results in a large minimum experiment time. The resolution that can be obtained in ω_1 is therefore severely limited: only 70 t_1 increments could be acquired in 16 hours of experiment time, giving a small t_1^{\max} of 64 ms.

As before, this problem can be solved by reducing the spectral width in the indirect dimension. The resulting spectrum is shown in Figure 4.22 (a), which also shows an excellent degree of cross-peak suppression. The sheared spectrum is shown in (b), and this is projected to give (c). There is some deviation in the values of the integrals, which is attributed to transverse relaxation during the delays δ . It can also be seen that the residual cross-peak intensity leads to distortions near the bases of the peaks. This residual intensity can be removed by symmetrization, and then projecting to give the cleaner spectrum in (d).

If there is any overlap between a cross peak and diagonal peak, the intensity of the

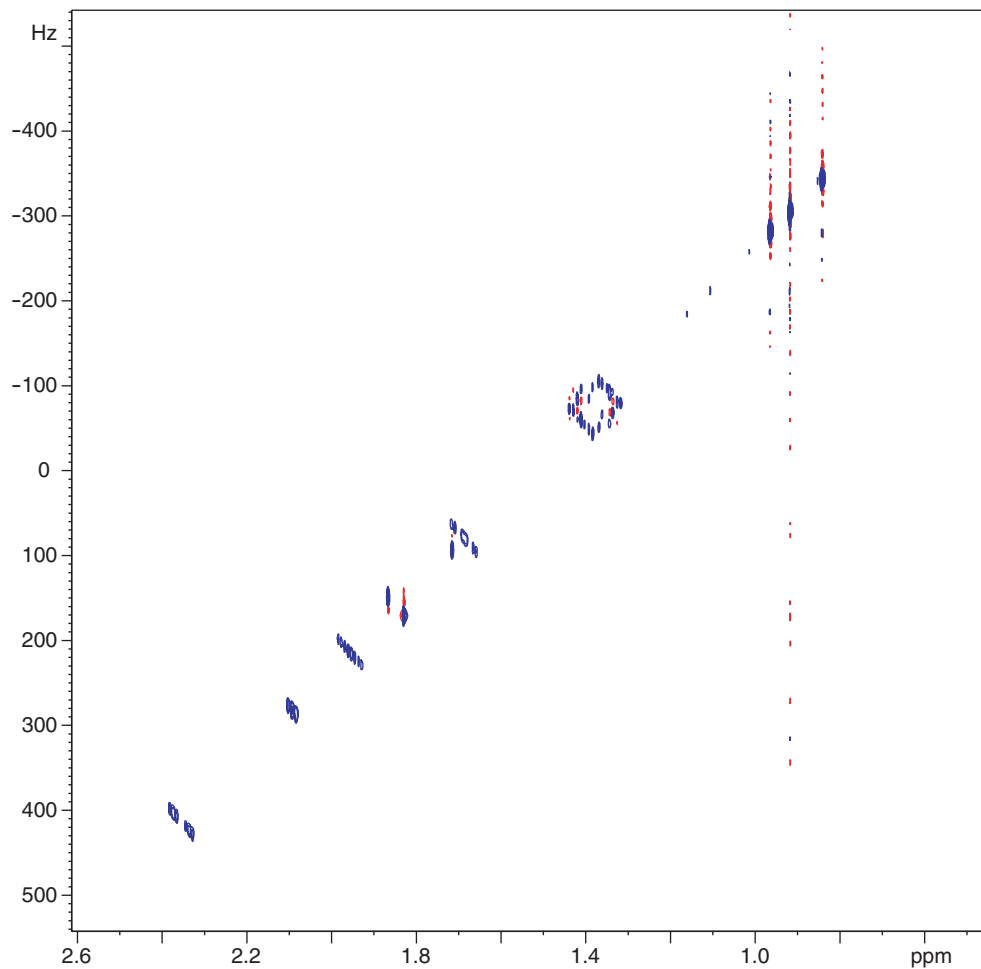


Figure 4.21: The anti z -COSY spectrum of camphor in CDCl_3 that was recorded using the modified pulse sequences to suppress the cross peaks. All of the cross peaks that lie well away from the diagonal have been suppressed significantly. The close-lying cross peaks between 1.35 and 1.42 ppm are, however, still present. A Gaussian weighting function was used in the indirect dimension.

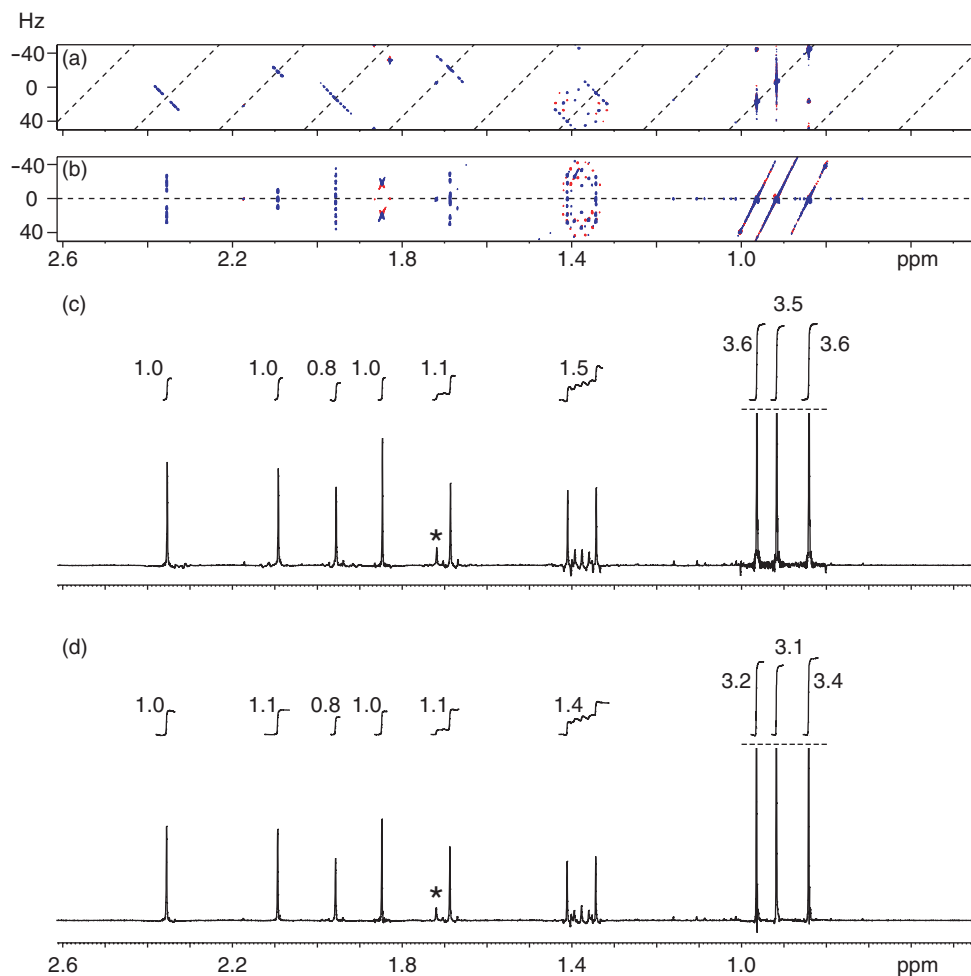


Figure 4.22: The anti *z*-COSY spectrum of camphor in CDCl_3 recorded with reduced ω_1 spectral width, and variable-delay cross-peak suppression. The spectrum is shown in (a), which is sheared to give (b). Spectrum (b) is projected to give the decoupled spectrum in (c). The deviation in the integrals is due to differential relaxation during the delays δ . In addition, some intensity distortions are seen near the peak bases, which are due to the residual cross-peak intensity. This is removed by symmetrizing (b), and then projecting to give (d). The H_2O peak is labelled with an *; note that it is in a different position to the corresponding peak in Figure 4.16.

latter may be distorted on symmetrizing the spectrum. This effect is reduced when the cross peaks have been suppressed directly.

4.6 Application to diffusion-ordered spectroscopy

In this Section, the way in which anti *z*-COSY can be applied to the measurement of molecular self-diffusion constants will be discussed. The basic method, which is referred to as diffusion-ordered spectroscopy (DOSY), involves recording a number of one-dimensional ^1H spectra in which the intensities of the peaks are attenuated by diffusion to different degrees. The intensities are then fitted to a decay curve, and the diffusion coefficient is extracted. If there is no overlap in the spectrum, this method can be used to determine the diffusion constants very easily; however, if neighbouring multiplets do overlap the fitting becomes more complicated, and will not necessarily give the correct result. One way to solve this problem is to attack the source of the overlap problem by removing the splittings due to the *J*-couplings, which is the approach adopted here.

Similar work has been carried out by Nilsson and Morris using the Zanger–Sterk experiment (which is described in Section 5.1) to achieve the decoupling [59].

4.6.1 The stimulated-echo experiment

The discussion about diffusion is here restricted to *molecular self-diffusion*, in which the molecules move in the absence of a concentration gradient. On moving, a molecule collides with other molecules causing it to change direction, and so over time it will be displaced from its original position. The total displacement is given by the vector sum of the distances travelled between each collision.

The rate of diffusion in an NMR sample can be measured by using a gradient-based pulse sequence, such as that shown in Figure 4.23 (a), which is known as the *stimulated-echo* (STE). It comprises a *z*-filter which is flanked by two gradients of equal strength G and duration δ , which are separated by a delay Δ . These two gradients ensure that the CTP is of opposite sign either side of the *z*-filter; the evolution of the offset during the first PFG is hence refocused by the evolution during the second.

The sequence can be analyzed for a one-spin system using the single-element operators. The equilibrium density operator \hat{I}_z is transformed into $\frac{1}{2}\text{i}(\hat{I}_+ - \hat{I}_-)$ by the first 90° pulse. Coherence order +1, corresponding to the operator \hat{I}_+ , is selected and

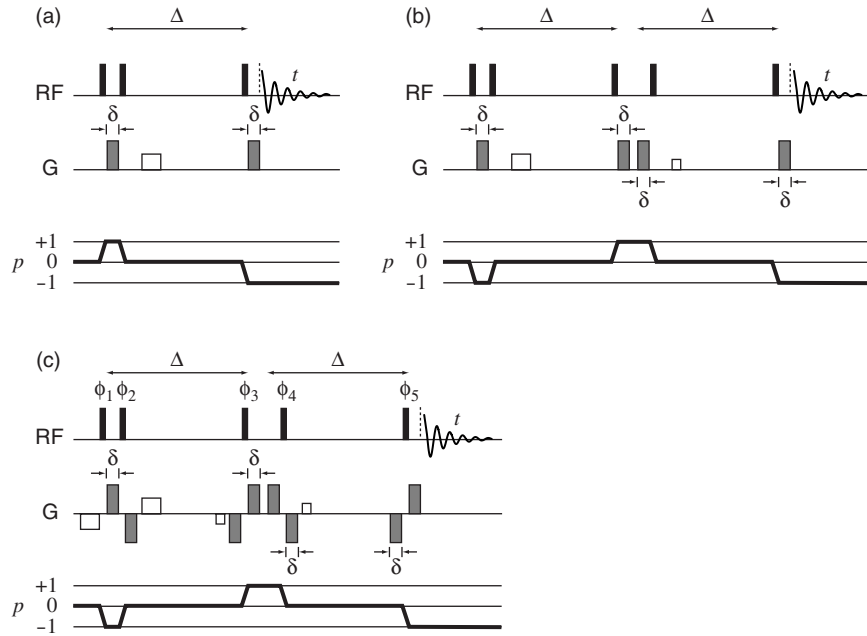


Figure 4.23: Pulse sequences used for measuring diffusion coefficients. The basic STE pulse sequence is shown in (a), which comprises a single z -filter that is flanked by two gradients (coloured grey). The third gradient is a homospoil. The DSTE, which is shown in (b), comprises two consecutive echoes. Unlike the STE, the DSTE compensates for the effects of convection. The sequence in (c) is a DSTE in which the eddy currents are reduced by compensation gradients. The phase cycle is: $\phi_1 = [0, 0, 0, 0, \pi, \pi, \pi, \pi]$, $\phi_2 = \phi_3 = [0, \pi/2, 0, \pi/2, 0, \pi/2, 0, \pi/2]$, $\phi_4 = \phi_5 = [0, 0, \pi/2, \pi/2, 0, 0, \pi/2, \pi/2]$, and $\phi_{\text{rec}} = [0, \pi, \pi, 0, \pi, 0, 0, \pi]$.

evolves during the first PFG to give

$$\frac{1}{2}i\hat{I}_+ \exp[-i(\Omega - \gamma Gz)\delta].$$

The second 90° pulse generates the following population terms:

$$-\frac{1}{4}(\hat{I}_\alpha - \hat{I}_\beta) \exp[-i(\Omega - \gamma Gz)\delta].$$

During the subsequent delay $\Delta - \delta$, molecular self-diffusion acts to displace the spins along z by an amount δz .

The final 90° pulse gives a mixture of $+1$ and -1 coherences. Only the latter is selected according to the CTP, which acquires a spatially-dependent phase during the

second PFG that depends on the new position $z + \delta z$.

$$\begin{aligned} & \frac{1}{4}i\hat{I}_- \exp[-i(\Omega - \gamma Gz)\delta] \exp[+i(\Omega - \gamma G(z + \delta z))\delta] \\ & = \frac{1}{4}i\hat{I}_- \exp[-iyG(\delta z)\delta]. \end{aligned}$$

Therefore, molecular self-diffusion results in incomplete refocusing of the spatially-dependent phases. The signal attenuation is calculated by summing over all the values of δz . This analysis does not account for diffusion that takes place *during* the PFGs; this will be dealt with in the following discussion.

The Stejskal–Tanner equation

The mathematical form of the signal intensity S is given by the Stejskal–Tanner equation [60]. For an ensemble of uncoupled spins, this equation can be derived from a modified form of the Bloch equations [61], giving

$$S = S_0 \exp \left[-D\gamma^2 \int_0^t dt' \left(\int_0^{t'} dt'' p(t'') G(t'') \right)^2 \right],$$

where D is the molecular self-diffusion coefficient, and S_0 is the peak height in the absence of diffusion.

This equation can be used to predict the signal attenuation resulting from the experiments of Figure 4.23. For example, if the diffusion gradients both have shape factor s , the Stejskal–Tanner equation has the following form for the STE:

$$S = S_0 \exp(-D\gamma^2 s^2 G^2 \delta^2 \Delta_r), \quad (4.9)$$

where Δ_r is a reduced diffusion time that accounts for the diffusion that takes place during the PFGs. If rectangular gradients are used, $s = 1$, and $\Delta_r = \Delta - \delta/3$. On the other hand if half-sine bells are used, $s = 2/\pi$, and $\Delta_r = \Delta - \delta/4$.

The rate of diffusion is measured by recording several spectra using the STE sequence with different gradient strengths G ; the peak heights are fitted to Equation 4.9, which enables D to be extracted.

4.6.2 Convection

It has so far been assumed that the motion of the spins in the sample is due only to self-diffusion. However, this may not be the case in practice, and it becomes necessary

to consider other mechanisms that may interfere with diffusion measurements. The most important of these is convection, which will be discussed here.

The density of a solvent is related to its temperature, and so if there is a temperature gradient across the sample, there will be a variation of the density. Gravity causes the cooler, denser regions to fall to the bottom of the sample, and less dense regions rise to the top; this is referred to as convection. It differs from diffusion in that the motion of the spins is coherent, that is spins in one region of the sample tend to move in the same direction.

The effect of convection can be calculated by adding a further term to the Bloch equations to account for coherent flow. Assuming that there is a single flow velocity v in the z -direction, the Bloch equations can be solved to give the following signal intensity

$$S = S_0 \exp \left[-D\gamma^2 \int_0^t dt' \left(\int_0^{t'} dt'' p(t'') G(t'') \right)^2 \right] \exp \left[i\gamma v \int_0^t dt' \int_0^{t'} dt'' p(t'') G(t'') \right].$$

For the STE sequence, the intensity loss is given by

$$S = S_0 \exp(-D\gamma^2 s^2 G^2 \delta^2 \Delta_r) \exp(+iv\gamma s G \delta \Delta). \quad (4.10)$$

Convection acts to change the phase of the signal. If there is a distribution of velocities in the sample, the phase factors combine to impose an additional decay on the signal. For a modest degree of convection, the decay will still be exponential, but with a greater apparent diffusion coefficient. In extreme cases, the decay will no longer be exponential, and it will not be possible to fit the data.

Methods of convection compensation

There are three methods which can be used to compensate for the effects of convection. The most simple is to turn off the sample heater that is used to maintain the sample temperature. This ensures that there is no temperature gradient, and hence no convection is possible. However, this method has the disadvantage that the temperature will fluctuate with the temperature of the surroundings, which itself will lead to a change in the diffusion coefficients. The second method is to rotate the sample tube about the z -axis during the experiment [62, 63].

The third method, which is the approach used in this work, is to use a *double stimulated-echo* (DSTE) pulse sequence, as shown in Figure 4.23 (b) [64]. During

the first echo, the coherence has order -1 and $+1$ during the two PFGs respectively. For the second echo, the coherence orders during the two PFGs are swapped, which crucially allows the linear velocity term in Equation 4.10 to be cancelled. The overall signal attenuation is given by the product of the attenuation factors arising from each echo; it is given by

$$\begin{aligned} S &= S_0 \exp(-D\gamma^2 s^2 G^2 \delta^2 \Delta_r) \exp(-iv\gamma s G \delta \Delta) \exp(-D\gamma^2 s^2 G^2 \delta^2 \Delta_r) \exp(+iv\gamma s G \delta \Delta) \\ &= \exp(-2D\gamma^2 s^2 G^2 \delta^2 \Delta_r). \end{aligned} \quad (4.11)$$

It can be seen that the effect of convention has been completely cancelled. This form of compensation only works if each spin maintains a constant velocity throughout the recording of each individual scan.

4.6.3 Eddy currents

As was explained in Section 2.3.2, the application of PFGs often results in eddy currents which tend to distort the spectrum. In addition to using shaped pulse profiles, it was found to be necessary to modify the pulse sequence so as to include compensation gradients [65, 66]. Each PFG is followed or preceded by a second PFG of equal strength and duration, but opposite sign. This results in the partial cancellation of the eddy currents that are generated by the two pulses. However, the second pulse must be included so that it does not refocus an unwanted CTP.

The sequence that was used to record the DOSY spectra is the modified DSTE, which includes compensation gradients. It is shown in Figure 4.23 (c).

4.6.4 Homonuclear decoupling

If the spectrum contains no overlap in the chemical shift dimension, the peak heights can be fitted to Equation 4.11, enabling the diffusion constant to be calculated. However, in the proton spectra of mixtures it is frequently the case that multiplets from different components of the mixture overlap. In the case of overlap between two components, the attenuation of the peak height will actually be described by the sum of two exponentials (referred to as a biexponential decay); fitting such a decay to Equation 4.11 will give an apparent diffusion coefficient with a value that is intermediate between the true coefficients.

One way of solving this problem is to reduce the overlap between neighbouring multiplets. Spectral resolution can be improved by three-dimensional DOSY, in which

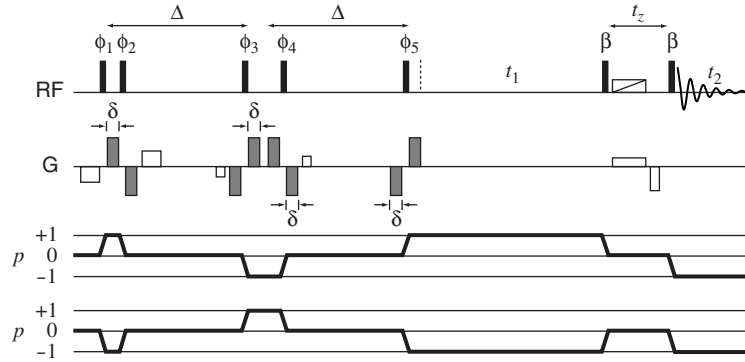


Figure 4.24: The pulse sequence used to record a series of diffusion-weighted anti *z*-COSY spectra. The two CTPs are for the N-type and P-type spectra respectively, and are acquired simultaneously. The phase cycle is as for the sequence in Figure 4.23 (c).

diffusion weighting is added to a two-dimensional experiment [67–73]. The method that is used here is to collapse the multiplet structure to a single line per chemical shift [54, 59]. Although the experiment is essentially three-dimensional, the series of spectra that are processed to obtain the diffusion coefficient is one-dimensional.

The pulse sequence used to record the diffusion-weighted anti *z*-COSY spectra is shown in Figure 4.24 with the required CTPs. The sequence represents a concatenation of the DSTE with the standard anti *z*-COSY experiment, and so is compensated for the effects of convection. Gradient-compensation in the DSTE part of the pulse sequence is achieved in exactly the same way as for the DSTE in Figure 4.23 (c). It is also necessary to compensate for the gradients in the *z*-filter with the small flip angle pulses immediately before t_2 . This is most easily achieved by arranging the gradient strengths so that the area under the homospoil is equal and opposite to the area under the gradient used to suppress the ZQ coherence. The latter has a rectangular profile, and so this condition can be expressed as

$$G_{ZQ}t_p + s_{HS}G_{HS}\tau_{HS} = 0,$$

where G_{ZQ} is the gradient strength used to suppress the ZQ coherence and s_{HS} , G_{HS} , and τ_{HS} are the shape factor, strength, and duration of the homospoil. It should be noted that the two gradients do *not* refocus unwanted CTPs, even though they are equal and opposite. The reason for this is that the swept-pulse imparts a phase to the transverse magnetization that varies as Ω^2 ; in the presence of a gradient, the spatially-

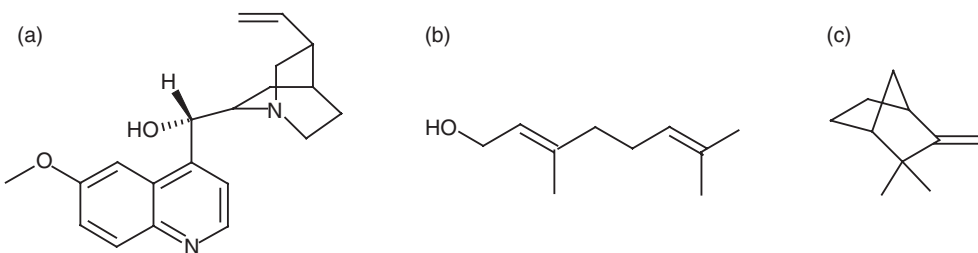


Figure 4.25: The chemical structures of the components of the mixture. Quinine is shown in (a), geraniol is shown in (b), and camphene is in (c).

dependent phase has a term that is proportional to z^2 , which can never be refocused by the homospoil.

4.6.5 Experimental examples

The new DOSY experiment was tested on a mixture of 15.4 mg of quinine, 10.8 mg of geraniol, and 13.0 mg of camphene (the structures of which are shown in Figure 4.25) dissolved in 0.7 ml of deuterated methanol; the concentrations of the three compounds were in the ratio 1:1.49:2.02.

The temperature of the sample was maintained at 298 K by a flow of heated gas, the flow rate of which was 400 l hr⁻¹. The STE sequence was found to give larger values of the diffusion coefficient than the DSTE sequence. The increased values were attributed to the effects of convention, and so the DSTE sequence was subsequently employed.

The duration of the diffusion PFGs δ and diffusion delay Δ were 2 ms and 75 ms respectively. Ten values of the diffusion gradients were used that varied linearly from 10% to 74% of the maximum intensity. The two homospoils were of duration 2.7 ms, and had strengths of 61% and 19% respectively; all PFGs were shaped to a half sine bell. The spectral width and acquisition time were 4496 Hz and 1.82 s. A peak-picking algorithm located the peaks, whose heights were fitted to Equation 4.11 using a Levenberg–Marquardt procedure [74].

In the anti *z*-COSY sequence of Figure 4.24, β was set to 20° since sensitivity was at a premium. The swept-frequency 180° pulse covered a range of offsets of 24 kHz in 24 ms with a B_1 field of 1.7 kHz. The accompanying gradient was applied for 24.3 ms with a relative strength of 4%. The homospoil was a rectangular pulse of strength -18.34%, and was applied for 4.3 ms to compensate for the eddy currents generated

by the ZQ gradient. The spectral width in ω_1 was set to 82 Hz, and 57 increments were acquired, giving a t_1^{\max} of 0.68 s. The data were acquired and processed using the SHR method [15]. The ten two-dimensional anti *z*-COSY time domains were multiplied by an exponentially-decaying weighting function with 1 Hz of line broadening in each dimension to enhance the SNR. Each spectrum was then sheared, symmetrized and projected, and the peak intensities were fitted to Equation 4.11.

The standard DOSY spectrum that was acquired with the gradient-compensated DSTE is shown in Figure 4.26. The two-dimensional representation shows the diffusion constant of each peak that results from the fit; the error bars indicate the standard error. The multiplets located at shifts greater than 2.2 ppm are well-resolved, and so the components of the mixture are easily separated. The average diffusion constants that were calculated from these resonances are indicated on the plot by the dashed lines: the values for quinine, geraniol, and camphene are 6.8, 10.2, and $14.5 \times 10^{-6} \text{ cm}^2 \text{ s}^{-1}$. Below 2.2 ppm there is significant overlap, and there are several peaks that do not return the correct value of D . This can be seen in Figure 4.27 which shows an expansion of the crowded spectrum.

The degree of overlap is alleviated by recording the DOSY spectrum with the anti *z*-COSY pulse sequence in Figure 4.24. The complete spectrum is shown in Figure 4.28. Some of the cross peaks lie close to the diagonal, and so are included in the projection. However, they are not included in the fitting procedure. The crowded region is shown in Figure 4.29. This region is much better resolved than the corresponding spectrum in Figure 4.27, and so most of the peaks are centred at their correct positions in the diffusion dimension.

4.6.6 Discussion

Applying anti *z*-COSY to diffusion measurements is potentially a useful method for obtaining a better separation of the components of a mixture. The main drawbacks are that the sensitivity is much lower than for the standard DSTE experiment, and because it is necessary to acquire several two-dimensional spectra the data are more time-consuming to acquire. For example, the total set of diffusion-weighted anti *z*-COSY spectra took 42 hours to acquire, whereas the DSTE experiment required just 10 minutes.

The quality of the fit is affected by two factors. Firstly, the lower SNR means that the calculated value of D will be affected by the noise to a greater degree. This is

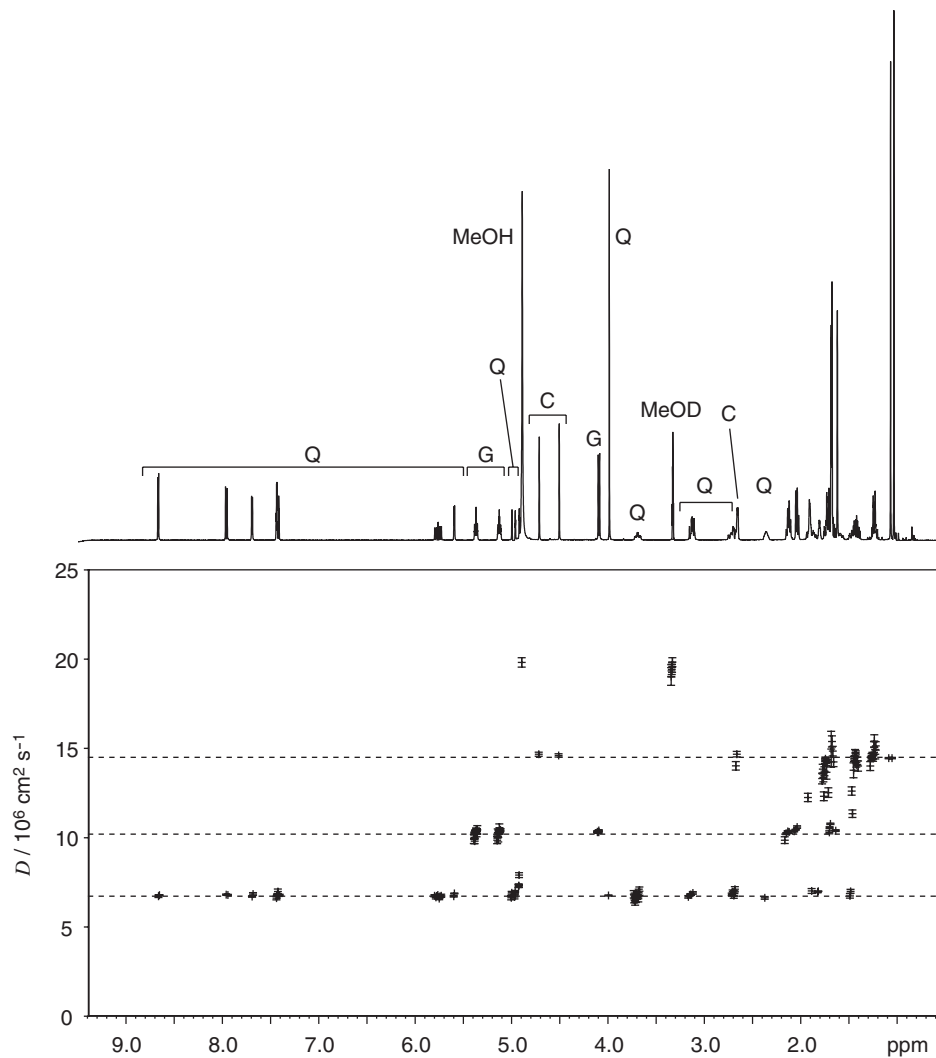


Figure 4.26: The DOSY spectrum of the mixture. The points in the two-dimensional spectrum give the value of D that was calculated for each chemical shift; the error bars indicate the standard error of the fit. The spectrum acquired with the lowest diffusion gradient (10%) is shown above, with the assignment of the well-resolved peaks to each component of the mixture (Q for quinine, G for geraniol, and C for camphene). The dashed lines indicate the average values of D for the three compounds, as calculated from the well-resolved resonances: the values for quinine, geraniol, and camphene are 6.8, 10.2, and $14.5 \times 10^{-6} \text{ cm}^2 \text{ s}^{-1}$.

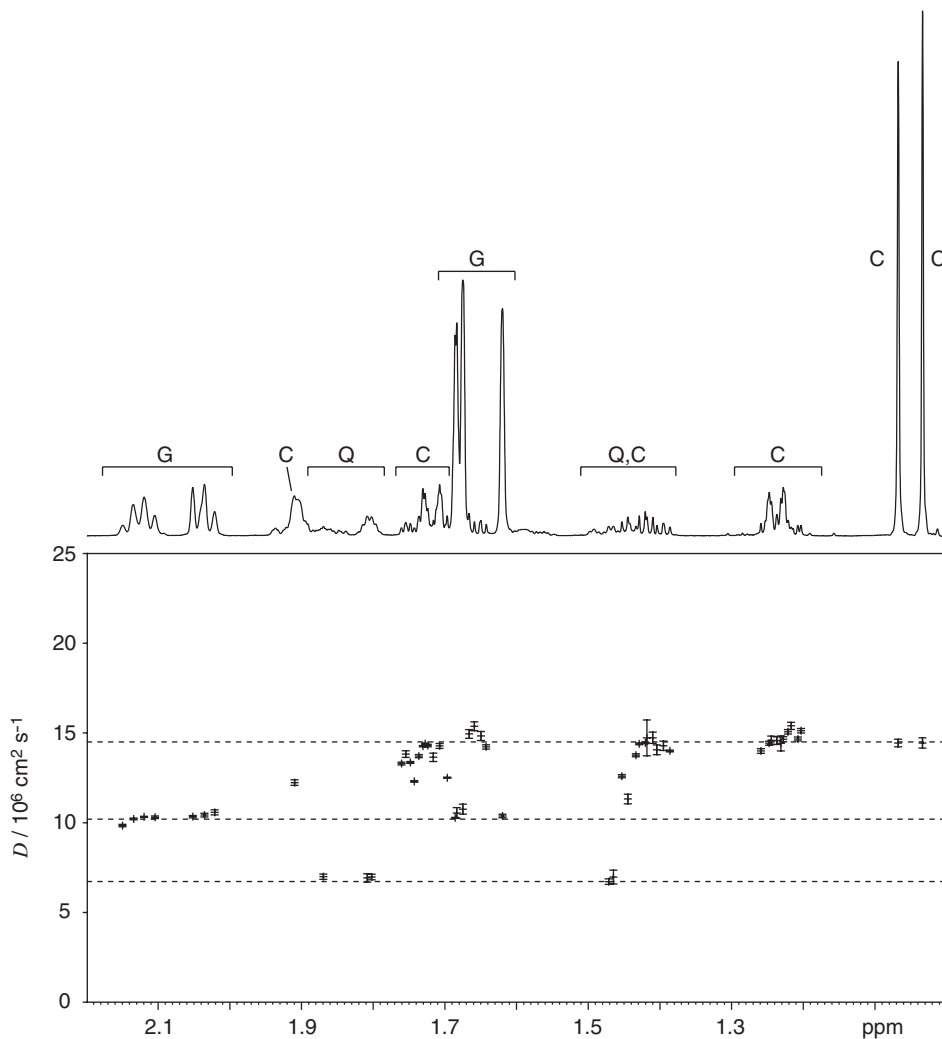


Figure 4.27: The crowded region of the DOSY spectrum between 1.0 and 2.2 ppm. The spectrum that was acquired with the lowest diffusion gradient is shown at the top, with the assignment of the peaks to each component of the mixture.

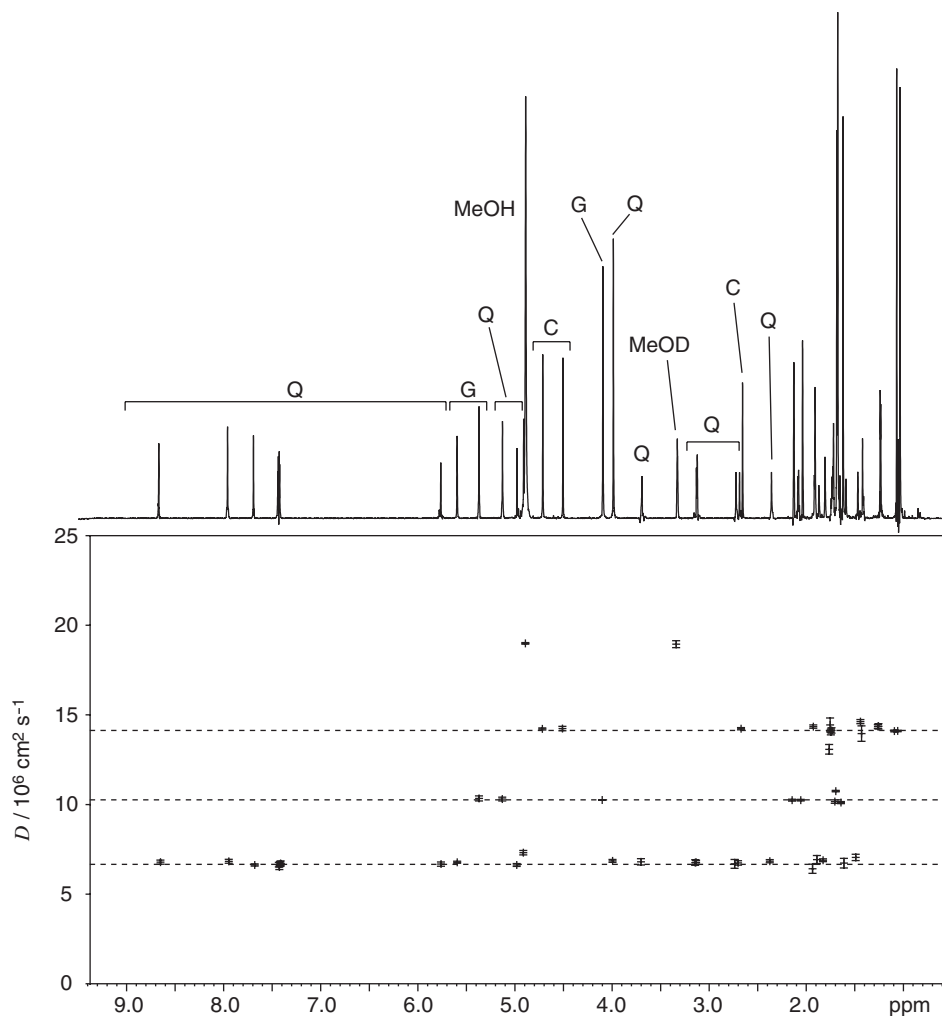


Figure 4.28: The decoupled DOSY spectrum of the mixture. The two-dimensional spectrum is a plot of the diffusion constant against the chemical shift. The projection acquired with the lowest diffusion gradient (10%) is shown above, with the assignment of the well-resolved peaks to each component of the mixture. The dashed lines indicate the average values of D for the three compounds, as calculated from the well-resolved resonances: the values for quinine, geraniol, and camphene are 6.7, 10.3, and $14.2 \times 10^{-6} \text{ cm}^2 \text{ s}^{-1}$.

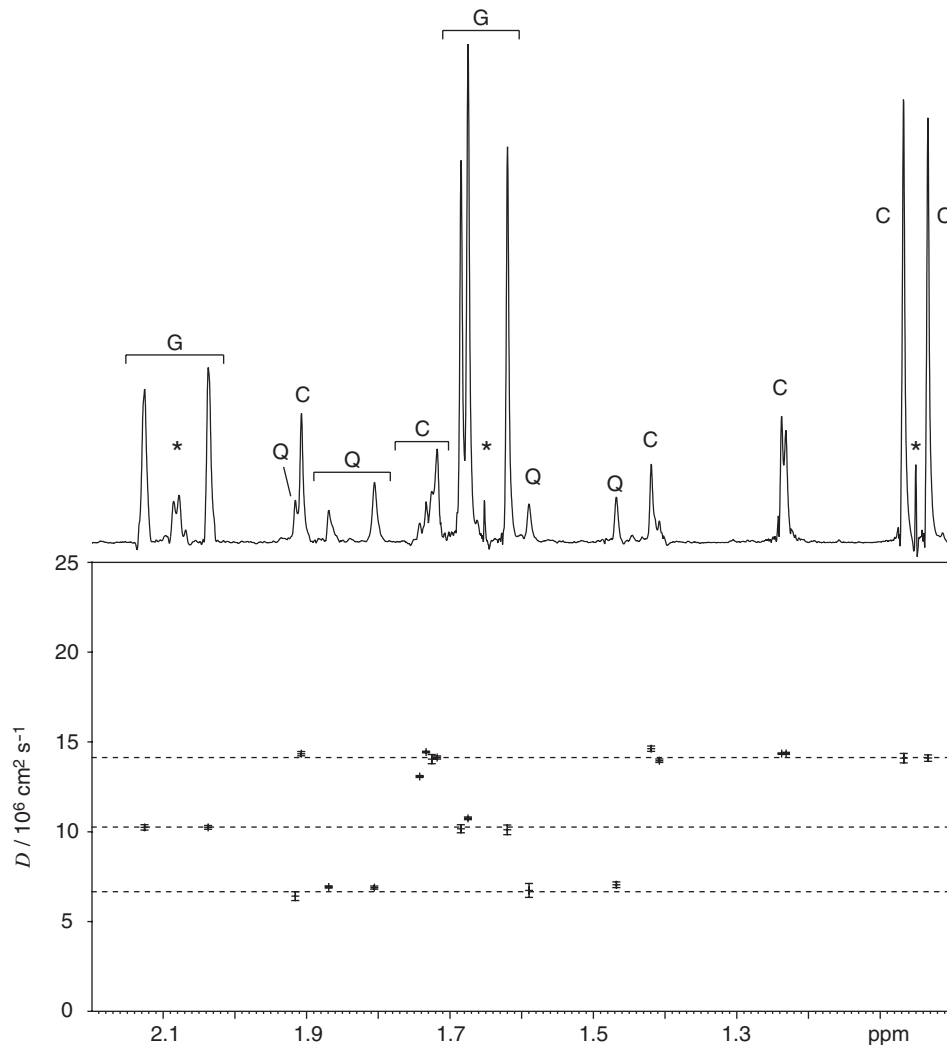


Figure 4.29: The crowded region of the decoupled DOSY spectrum below 2.2 ppm. The projection that was acquired with the lowest diffusion gradient is shown at the top with the assignment of the peaks to each component of the mixture. Extra peaks are present which correspond to cross peaks that lie close to the diagonal. They are marked with an *.

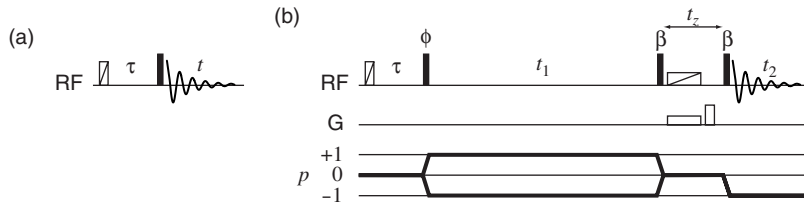


Figure 4.30: Inversion–recovery pulse sequences used to determine T_1 . The most basic sequence is shown in (a), which is used to record a series of one-dimensional spectra with peak heights that are weighted by longitudinal relaxation during τ . The sequence and CTP in (b) are used to record a series of relaxation-weighted anti z -COSY spectra, which can be processed to give a series of decoupled spectra. The inversion pulse is a BIP [27]. The axial peaks are suppressed by phase cycling the pulse labelled ϕ and the receiver according to $[0, \pi]$.

reflected in the larger standard errors that are obtained (up to an order of magnitude) than for the standard DSTE. Secondly, the extended length of the experiment results in spectrometer instabilities, particularly the inhomogeneity of the B_0 field, having a greater influence on the quality of the spectra.

4.7 Application to longitudinal relaxation measurements

The measurement of the time constant T_1 that characterizes longitudinal relaxation is made in an analogous way to the measurement of diffusion coefficients. A series of one-dimensional spectra are recorded, in which the peak intensities are weighted by relaxation to different degrees. The heights are then fitted to an equation, from which T_1 is determined.

4.7.1 The inversion–recovery experiment

The rate of longitudinal relaxation can be measured by using the inversion–recovery pulse sequence in Figure 4.30 (a). The equilibrium z -magnetization is inverted by the 180° pulse, and is then allowed to relax during a delay τ . The z -magnetization is then rotated to the y -axis by the 90° pulse, so that it can be observed during acquisition. Several such spectra are recorded with different values of τ , and the peak heights are fitted to a relaxation curve. A BIP was used to obtain uniform inversion over the whole spectrum. The short duration of such a pulse enables us to ignore any relaxation that occurs during the pulse.

The form of the relaxation curve can be derived very easily. After time τ , the

z-magnetization is given by Equation 1.24 with $t = \tau$ and $M_z(0) = -M_0$, which gives

$$M_z(\tau) = M_0 [1 - 2 \exp(-\tau/T_1)].$$

The peak height in the spectrum $S(\tau)$ is proportional to $M_z(\tau)$, and so the intensities are given by

$$S(\tau) = S(0) [2 \exp(-\tau/T_1) - 1], \quad (4.12)$$

where $S(0)$ is the (negative) peak height for $\tau = 0$. Equation 4.12 can be rearranged to give

$$\ln \left[\frac{S(\tau) + S(0)}{2S(0)} \right] = -\frac{\tau}{T_1},$$

from which T_1 can be calculated by plotting $\ln [(S(\tau) + S(0))/2S(0)]$ against τ .

A problem arises if the spectrum contains two overlapping multiplets with different values of T_1 , as the relaxation curve for two overlapping peaks will not be described by Equation 4.12. This is exactly the same problem as we encountered in DOSY of overlapping multiplets.

The overlap can be removed by eliminating the multiplet structure in the spectrum. The relevant pulse sequence is shown in Figure 4.30 (b), which is simply a standard anti *z*-COSY experiment in which a 180° pulse and delay τ have been inserted before the first 90° pulse. A sequence of such spectra are recorded with a systematic variation of τ ; these are then sheared, symmetrized, projected, and the peak heights are fitted to Equation 4.12.

4.7.2 Experimental examples

The pulse sequence in Figure 4.30 (b) was tested on camphor. The inversion pulse was BIP-720-25-40, and had a duration of $100 \mu\text{s}$ and B_1 field of 20 kHz [27]. The delay τ took eight values that are equally-spaced between 0 and 3.5 s. All the other experimental parameters in the anti *z*-COSY experiment are the same as for the spectra in Section 4.5.2.

Figure 4.31 shows the values of T_1 , and their standard errors, that were obtained for the camphor multiplets using the standard inversion-recovery experiment. The eight one-dimensional spectra were obtained in 2 minutes of acquisition time. The values of T_1 that were obtained using anti *z*-COSY to decouple the spectrum are shown in Figure 4.32. These data were recorded in 11 hours.

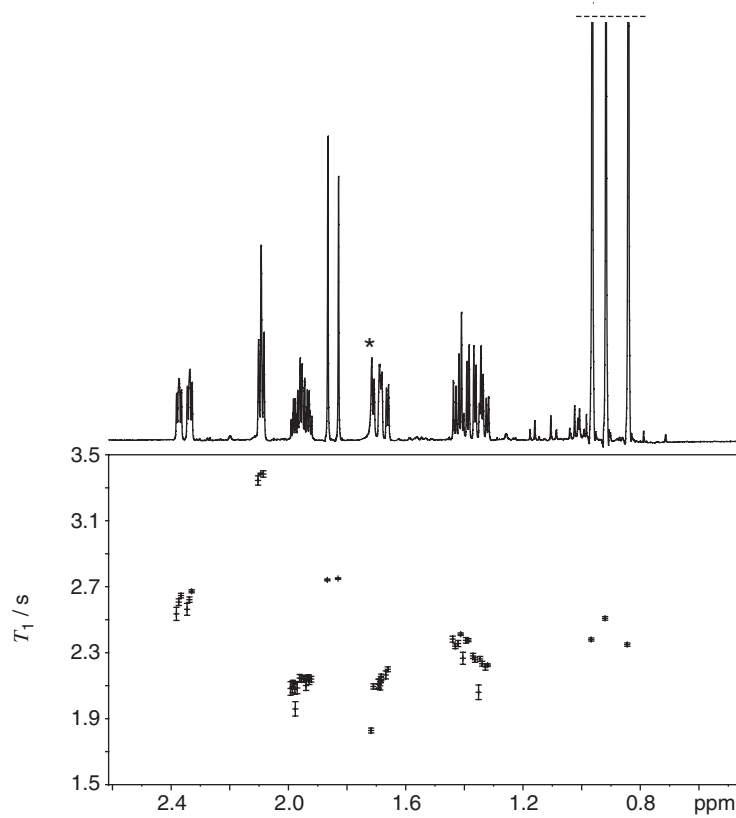


Figure 4.31: Values of T_1 for the camphor multiplets that were obtained by inversion–recovery. The trace at the top is the spectrum obtained for $\tau = 0$, which has been phased to positive absorption. The peak marked with an * is due to H_2O , which has a comparatively low T_1 of 1.8 s.

4.8 Application to complex mixtures

The final application of broadband proton-decoupled proton spectra that is presented is in the studies of complex mixtures that arise from metabolomics or metabolomics studies. It is common to use multivariate statistical methods, such as principal component analysis, to analyze the proton spectra of such mixtures and identify the metabolites that are present [75]. However, the standard proton spectra often show considerable overlap in certain chemical shift regions, especially the aliphatic region. In such cases, conventional J -spectroscopy has proved useful in simplifying the spectra and is widely used, despite the shortcomings of the experiment [76–80]. It is therefore expected that the new method for recording decoupled spectra will be useful in this field.

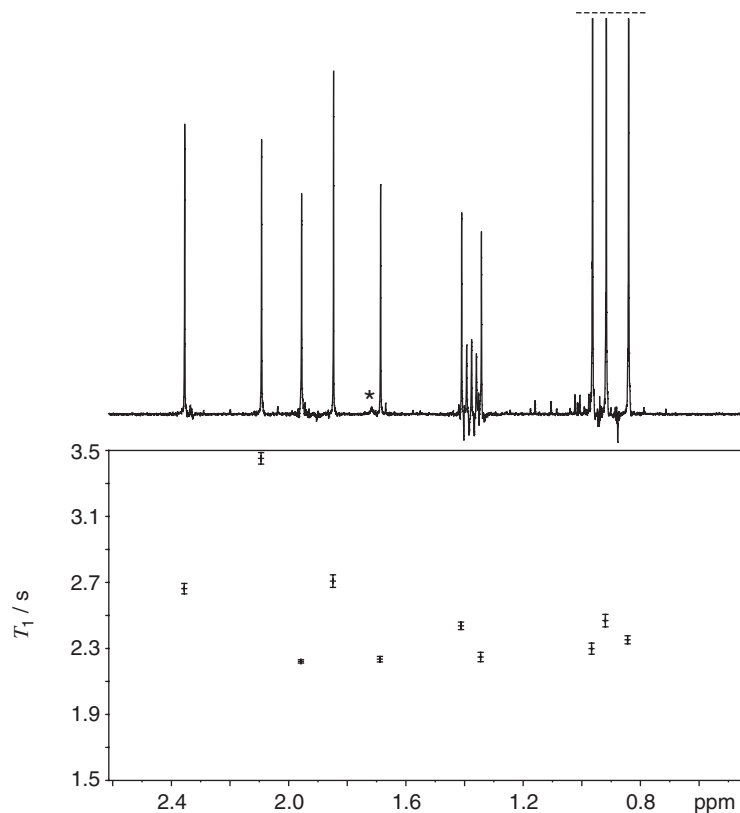


Figure 4.32: Values of T_1 for the camphor multiplets obtained with the anti z -COSY pulse sequence of Figure 4.30 (b). The trace at the top is the projection of the spectrum with $\tau = 0$, which has been phased to positive absorption. The H_2O peak is marked with an *.

4.8.1 Experimental example

The application of the anti *z*-COSY method to metabonomics is demonstrated with the spectra of a sample of a KG1a (AML cancer model) cell extract (dissolved in D₂O) that was supplied by Dr Ulrich Günther of the University of Birmingham.

Sensitivity was at a premium, and so the spectra were recorded at 500 MHz for ¹H on a DRX500 Bruker spectrometer that is equipped with a cryoprobe. The flip angle β was set to 20°, and 80 scans were acquired per increment. The spectral widths in ω_1 and ω_2 are 100 and 5000 Hz respectively, and the acquisition time in t_2 was 0.8 s. The number of increments that was acquired in the indirect dimension was 40, giving a t_1^{\max} of 0.4 s. The residual water signal was suppressed by presaturation. An exponentially-decaying weighting function with 1.3 Hz of line broadening was employed in both dimensions, and the spectrum was processed using the SHR method [15] before shearing, symmetrizing, and projecting.

The conventional spectrum is shown in Figure 4.33 (a), and the decoupled spectrum is shown in (b). The former was recorded in 3 minutes, compared to the 16 hours required for the latter. Nevertheless, the region between 0.5 and 4.4 ppm is very crowded, and so the analysis of this region benefits significantly from the simplification obtained by decoupling. Expansions of this region are shown in Figure 4.34 (a) and (b).

4.9 Conclusion

The anti *z*-COSY pulse sequence is an appealing alternative to conventional *J*-spectroscopy for separating the offsets and *J*-couplings of the proton spectrum. The principal advantages of the former are that the peaks have the absorption-mode line-shape, and the spectrum is quantitative. However, it has been shown that the presence of the cross peaks is problematic, and so it is essential that they be suppressed. The two methods that were proposed for the removal of the cross peaks are very effective, but can have unwanted side effects. A related problem is that cross peaks that lie close to the diagonal (and are therefore analogous to the strong coupling artefacts in *J*-spectra) cannot be removed by these methods.

Nevertheless, the results that were obtained are clearly superior to conventional *J*-spectra, and in particular the application to DOSY should prove very useful for the separation of the individual components of a mixture.

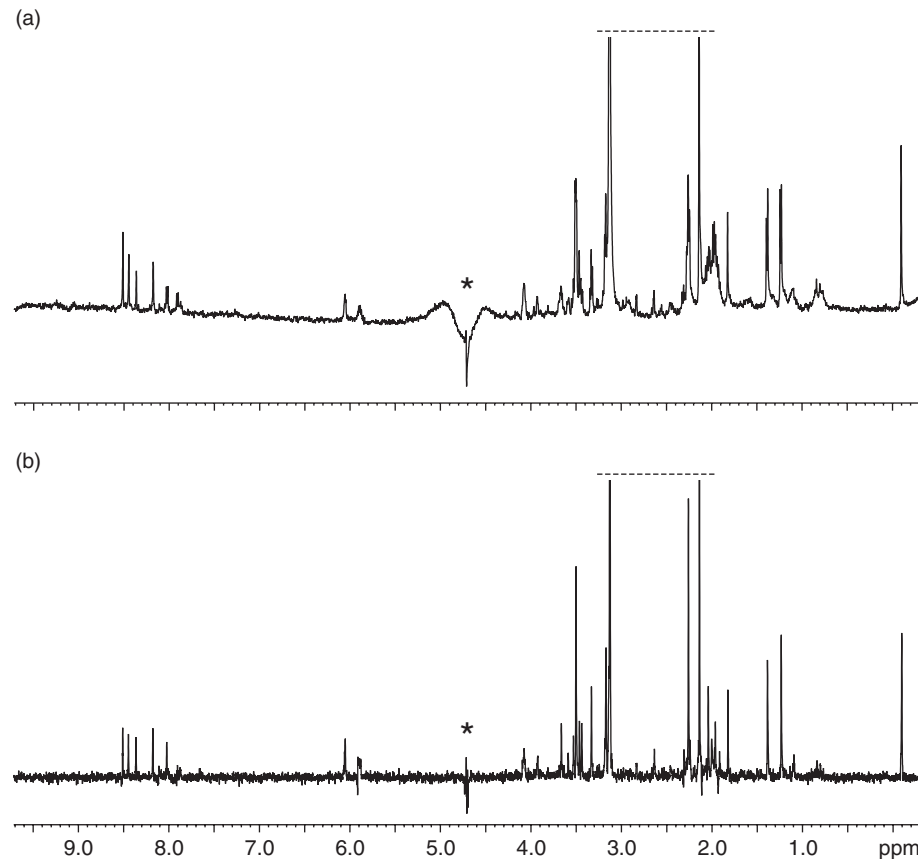


Figure 4.33: Broadband proton-decoupled proton spectra of the cancer model cell extract in D_2O . The conventional proton spectrum is shown in (a), and the projection of the anti z -COSY spectrum is shown in (b). Both spectra were recorded with presaturation of the water signal; the residual water signal can still be seen on-resonance, and is marked with an *.

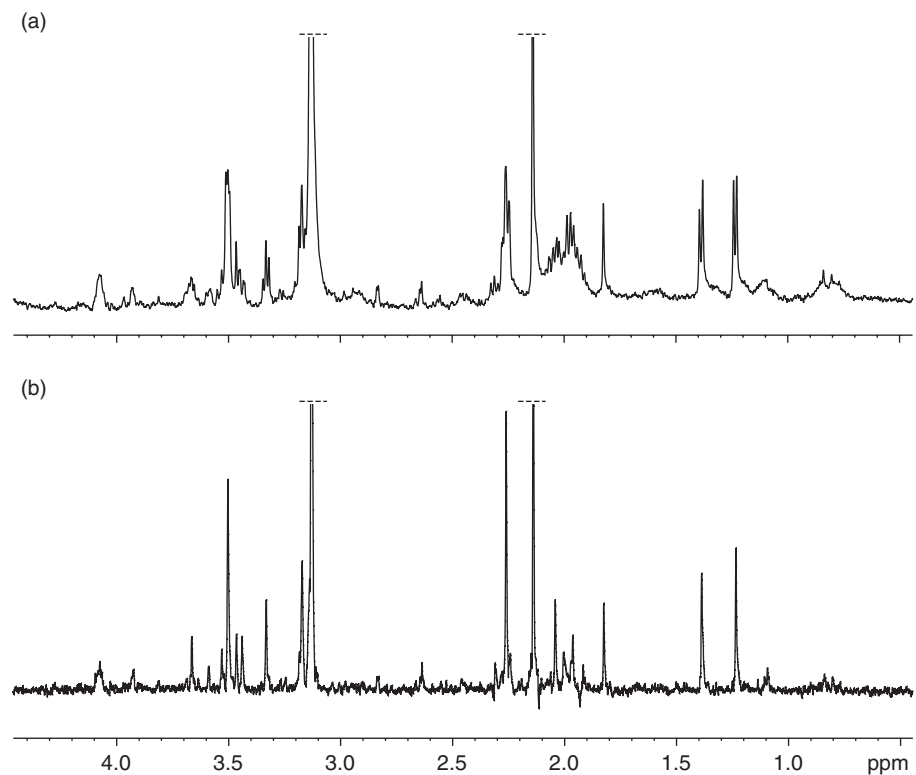


Figure 4.34: The crowded regions of the spectra shown in Figure 4.33. The conventional spectrum is shown in (a), and the decoupled spectrum is shown in (b).

Chapter 5

Two-dimensional *J*-spectra with absorption-mode lineshapes

THE WORK PRESENTED IN CHAPTER 4 described how a separation of offsets and *J*-couplings can be obtained using anti *z*-COSY. The advantage of this new method over conventional *J*-spectroscopy is that the peaks in the spectrum have the absorption-mode lineshape and the natural intensities. The disadvantage is that the spectrum also contains cross-peak multiplets, which must be suppressed if we are to obtain a clean separation of offsets and couplings.

One of the most appealing aspects of conventional *J*-spectroscopy is its simplicity, and so it is a very attractive prospect to be able to record an absorption-mode spectrum using essentially the same pulse sequence. In this Chapter, a new spectroscopic method for obtaining a *J*-spectrum with absorption-mode lineshapes is presented.

The new pulse sequence is closely related to an ingenious experiment that was proposed by Zanger and Sterk [81] which can be used to obtain a broadband proton-decoupled proton spectrum. The most important part of this sequence is an element that selectively decouples different spins in different parts of the sample. The inclusion of this Zanger–Sterk pulse-sequence element is the key to the new method for obtaining absorption-mode *J*-spectra. It will therefore prove useful to describe in detail how the Zanger–Sterk experiment works, as many of the issues that arise from this experiment directly affect the new *J*-spectroscopy pulse sequence.

A very useful side effect of the new experiment is that, although the extra peaks due to strong coupling are present in the two-dimensional spectrum, their intensities mostly cancel on calculating the projection. This is especially useful as no special measures are required to suppress them.

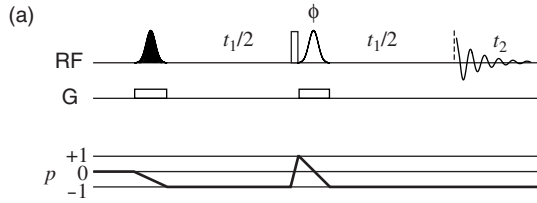


Figure 5.1: The pulse sequence and CTP of the Zanger–Sterk pulse sequence. The two Gaussian-shaped profiles represent the selective pulses; the filled profile is a pulse with a 90° flip angle on-resonance, and the unfilled profile is a 180° pulse. All pulses are applied along the x -axis, with the exception of the selective 180° pulse; the phase ϕ takes the values $[0, \pi/2, \pi, 3\pi/2]$, and the receiver is phase-cycled according to $[0, \pi, 0, \pi]$. Any additional CTP selection that may be needed for the other pulses has been omitted.

5.1 The Zanger–Sterk experiment

The Zanger–Sterk experiment will be described in this Section, commencing with an analysis of the pulse sequence. All the properties of the sequence are illustrated with the spectrum of a two-spin system.

5.1.1 Analysis of the pulse sequence

The pulse sequence and CTP are shown in Figure 5.1. The key features of the experiment are the selective pulses, which are applied in the presence of a weak gradient. As will be seen in Section 5.1.3, the gradient ensures that different spins are selectively excited in different parts of the sample. For the present discussion, we will initially analyze the sequence in the part of the sample where spin one is excited, and then repeat the calculation for spin two. It is not necessary for the first pulse to be soft, as the necessary selectivity is introduced by the selective 180° pulse; indeed, it can be the source of an unwanted frequency-dependent phase across the spectrum, and so is best replaced by a hard 90° pulse with no gradient. However it was included in the original experiment, and so is retained here [81].

The first selective pulse has a flip angle of 90° , and is applied to spin one in the first part of the sample. Coherence order -1 is selected immediately after this pulse, and so there are only two density operator terms that are excited, which are

$$-\frac{1}{2}i\hat{I}_{1-}\hat{I}_{2\alpha} - \frac{1}{2}i\hat{I}_{1-}\hat{I}_{2\beta}.$$

During the first half of t_1 , both operators evolve at their characteristic frequencies to

give

$$-\frac{1}{2}i\hat{I}_{1-}\hat{I}_{2\alpha} \exp [i(\Omega_1 + J_{12})t_1/2] - \frac{1}{2}i\hat{I}_{1-}\hat{I}_{2\beta} \exp [i(\Omega_1 - J_{12})t_1/2].$$

There now follows the combination of a hard 180° pulse, followed by a selective 180° pulse that is applied to spin one. The hard pulse changes the coherence order of spin one, and flips the spin state of spin two to give

$$-\frac{1}{2}i\hat{I}_{1+}\hat{I}_{2\beta} \exp [i(\Omega_1 + J_{12})t_1/2] - \frac{1}{2}i\hat{I}_{1+}\hat{I}_{2\alpha} \exp [i(\Omega_1 - J_{12})t_1/2].$$

The selective pulse then changes the coherence order of spin one back to -1 , resulting in

$$-\frac{1}{2}i\hat{I}_{1-}\hat{I}_{2\beta} \exp [i(\Omega_1 + J_{12})t_1/2] - \frac{1}{2}i\hat{I}_{1-}\hat{I}_{2\alpha} \exp [i(\Omega_1 - J_{12})t_1/2].$$

The two pulses have had the effect of keeping spin one unchanged, and flipping the spin state of the passive spin. This is crucial, because during the second half of t_1 , the phase acquired due to the offset will be the same as for the first half of t_1 , as the spin one coherence order is still -1 . The coupling terms, however, will have the *opposite* sign as the passive spin is now in the *other* spin state. The result is that the evolution of the coupling in the second half of t_1 completely cancels the evolution during the first half, giving

$$\begin{aligned} & -\frac{1}{2}i\hat{I}_{1-}\hat{I}_{2\beta} \exp [i(\Omega_1 + J_{12})t_1/2] \exp [i(\Omega_1 - J_{12})t_1/2] \\ & -\frac{1}{2}i\hat{I}_{1-}\hat{I}_{2\alpha} \exp [i(\Omega_1 - J_{12})t_1/2] \exp [i(\Omega_1 + J_{12})t_1/2] \\ = & -\frac{1}{2}i\hat{I}_{1-}\hat{I}_{2\beta} \exp [i\Omega_1 t_1] - \frac{1}{2}i\hat{I}_{1-}\hat{I}_{2\alpha} \exp [i\Omega_1 t_1]. \end{aligned}$$

Finally, the two operators evolve during t_2 to give

$$-\frac{1}{2}i\hat{I}_{1-}\hat{I}_{2\beta} \exp [i\Omega_1 t_1] \exp [i(\Omega_1 - J_{12})t_2] - \frac{1}{2}i\hat{I}_{1-}\hat{I}_{2\alpha} \exp [i\Omega_1 t_1] \exp [i(\Omega_1 + J_{12})t_2].$$

Repeating the calculation, this time with the selective pulses applied to spin two, gives the following operators:

$$-\frac{1}{2}i\hat{I}_{1\beta}\hat{I}_{2-} \exp [i\Omega_2 t_1] \exp [i(\Omega_2 - J_{12})t_2] - \frac{1}{2}i\hat{I}_{1\alpha}\hat{I}_{2-} \exp [i\Omega_2 t_1] \exp [i(\Omega_2 + J_{12})t_2].$$

The resulting spectrum is shown in Figure 5.2. As is the case for *J*-spectroscopy, the absence of a mixing period means that the number of peaks is the same as for the conventional proton spectrum, i.e. four in this case. The combination of the hard and

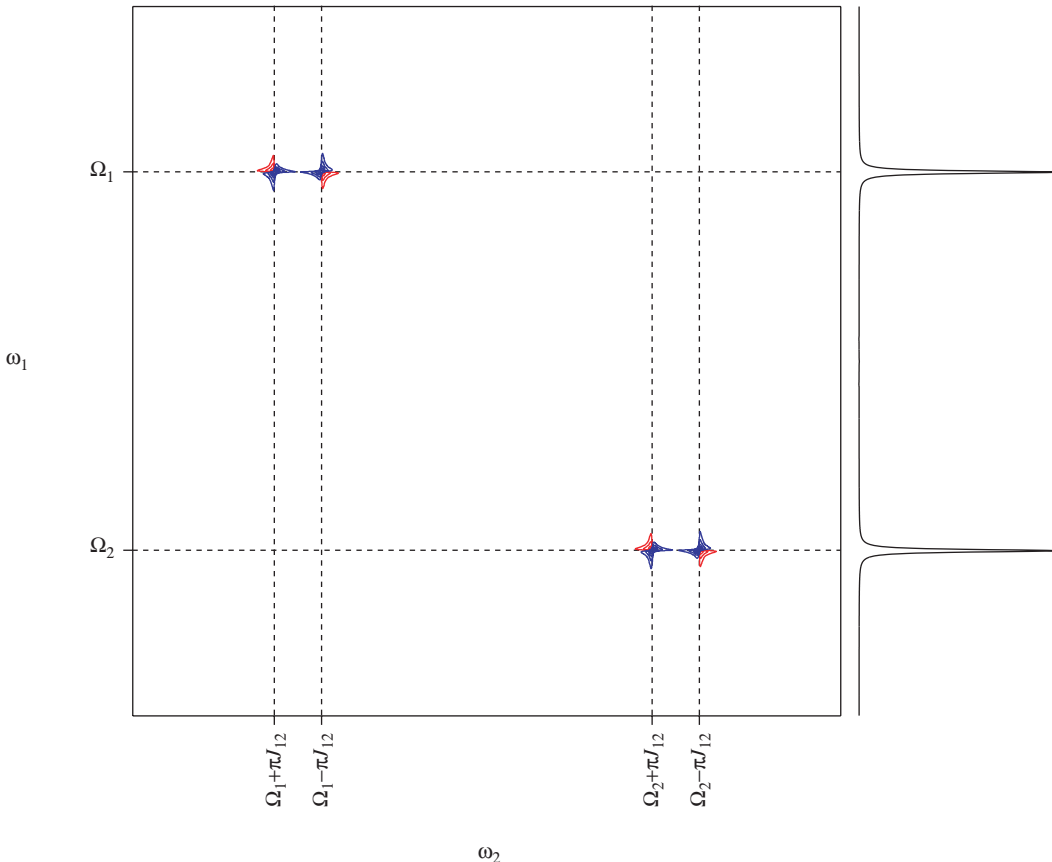


Figure 5.2: A simulated Zanger–Sterk spectrum of a weakly-coupled two-spin system. The components of each multiplet are aligned at the offset of the active spin in ω_1 ; there is no splitting in this dimension. The projection onto ω_1 , shown at the right, is therefore a decoupled spectrum. Note that the peaks in the two-dimensional spectrum have the phase-twist lineshape.

soft 180° pulses during t_1 refocused the coupling, with the result that the t_1 evolution of each operator depends only on the offset of the active spin. It can be seen that the result of this is that each component of a particular multiplet lies at the same frequency in ω_1 , namely the offset of the active spin. Therefore, the projection of this spectrum onto the ω_1 axis is a decoupled spectrum.

5.1.2 Lineshapes and the projection

A single CTP is acquired in t_1 , and so the time-domain data are phase-modulated in this dimension; the peaks in the two-dimensional spectrum therefore have the phase-twist lineshape. However, this does not affect the calculation of the projection, in

contrast to the case of J -spectra, as the spectrum is projected onto ω_1 and not onto the anti-diagonal. According to the projection–slice theorem, this projection is found by extracting from the time domain the slice that lies along the t_1 axis, and calculating its Fourier transform. For a spectrum that contains a single singlet, the time-domain data are

$$s(t_1, t_2) = \exp(i\Omega t_1) \exp(-t_1/T_2) \exp(i\Omega t_2) \exp(-t_2/T_2).$$

The slice that lies along the t_1 axis, which is known as the first interferogram, is given by setting $t_2 = 0$ to give

$$s(t_1, 0) = \exp(i\Omega t_1) \exp(-t_1/T_2).$$

The Fourier transform of this is an absorption-mode line in the real part of the spectrum*:

$$P(\omega_1) = \pi \mathcal{A}_\Omega(\omega_1).$$

The projection–slice theorem shows us that the projection can be obtained simply by acquiring the first interferogram of the time domain; that is, we repeat the experiment and increment t_1 as usual, but it is only necessary to acquire the first complex data point at $t_2 = 0$ for each increment. This observation saves the inconvenience of having to process the whole two-dimensional spectrum.

In principle a cross-section taken parallel to the ω_2 axis, through the offset of spin i in ω_1 , gives the structure of the associated multiplet just as in the case of conventional J -spectroscopy. However in order to extract this information in practice, it is necessary to eliminate the dispersive component of the lineshape, which can be done by applying the combination of pseudo-echo weighting and absolute value processing [38].

5.1.3 Spatially-selective decoupling

In order to acquire the complete spectrum the whole experiment, in principle, needs to be repeated with the selective pulses applied to each multiplet in turn. For most molecules, this will lead to a prohibitively long experiment. However, Zanger and Sterk proposed an ingenious solution to this problem, which is to apply a weak magnetic field gradient at the same time as the selective pulses. The offsets therefore become position-dependent, and so the selective pulse affects different spins in *different parts*

*The factor of π arises from the integration over ω_2 (c.f. Equation 1.35).

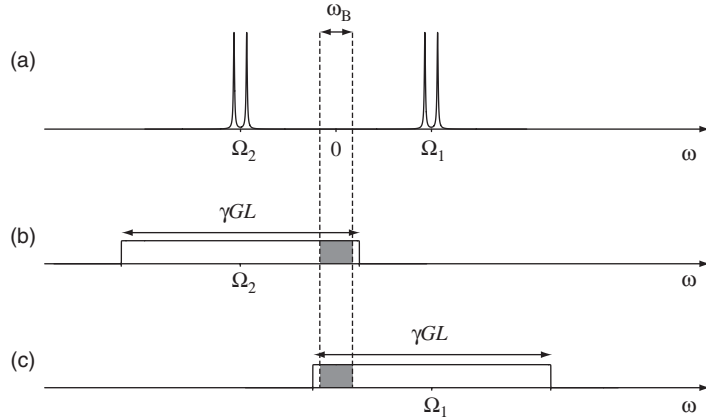


Figure 5.3: Illustration of how selective decoupling is achieved for different spins in different parts of the sample. A typical spectrum of a two-spin system is shown in (a). The application of a gradient broadens each multiplet into an image of the sample that is centred on the offset. The image from spin two is shown in (b), and the image from spin one is shown in (c). The selective pulse, of bandwidth ω_B and at offset zero, excites each spin in completely different parts of the sample; these slices are indicated in (b) and (c) by the grey regions.

of the sample. This combination of selective pulse and gradient is referred to as the Zanger–Sterk pulse-sequence element.

Exactly how this works is illustrated for a two-spin system in Figure 5.3. For simplicity, it is assumed that the selective 180° pulse has a simple rectangular inversion profile $f_{\text{refoc}}(\Omega)$, which uniformly inverts spins whose offsets lie within a bandwidth ω_B , and leaves spins that lie outside this range unaffected. In the presence of the gradient each multiplet in the spectrum shown in (a) is broadened into an image of the sample, of width γGL , that is centred on the offset of the spin. If the gradient strength is sufficiently large, the two images will overlap with each other; for simplicity, the images from each multiplet are shown separately in (b) and (c).

The pulse is then applied on resonance. The key to the method is that, on account of the offsets now being dependent on z , *spins with different offsets are on-resonance in different slices of the sample*. This is illustrated in Figure 5.3 (b) and (c), where the regions of the sample where spins one and two are affected by the pulse are shaded grey. The selective pulse only affects spin two near the bottom of the sample, where it is on-resonance as shown in (b). *In the same part of the sample* spin one has an offset of $\Omega_1 - \Omega_2$, which lies outside the bandwidth of the pulse, and so is unaffected. Hence,

spin two has been flipped by the pulse, leaving the spin one to which it is directly coupled unchanged. Likewise, spin one is on-resonance near the top of the sample, as shown in (c), and spin two is offset by $-(\Omega_1 - \Omega_2)$. So, it can be seen that it is possible to apply a selective pulse to all of the spins simultaneously.

In general, spin i will be on-resonance at position $z_0^{(i)} = \Omega_i/(\gamma G)$. Therefore, this spin will be excited inside a slice of thickness $\Delta z = \omega_B/(\gamma G)$ that is centred at $z = z_0^{(i)}$. The condition for exciting spin one and spin two separately is that the two slices within which they are affected by the pulse must not overlap, i.e. $|z_0^{(1)} - z_0^{(2)}| \geq \Delta z$ which is equivalent to $|\Omega_1 - \Omega_2| \geq \omega_B$; that is the selectivity is determined solely by the bandwidth of the pulse.

The value of the gradient has no bearing on the selectivity of the experiment; although increasing G decreases the width of the slice that is excited, it also decreases the separation between neighbouring slices by the same amount. However, the gradient does determine the range of offsets that are excited by the selective pulse and gradient combination. If the peak corresponding to the largest offset in the spectrum, Ω_{\max} , is to contribute at all to the Zanger–Sterk spectrum, the degree of gradient-broadening must be sufficiently large for there to be a slice of the sample where this peak is on-resonance. From reference to Figure 5.3 it can be seen that, if the slice is to contribute its maximum intensity to the spectrum, the following inequality must be satisfied:

$$\frac{1}{2}\gamma GL \geq \Omega_{\max} + \frac{1}{2}\omega_B,$$

where it has been assumed that $\Omega_{\max} > 0$. This condition can be approximated as

$$\gamma GL \geq \Delta\Omega,$$

i.e. the gradient broadening must be greater than or equal to the spectral width. We therefore have two conditions that we need to impose on the pulse-gradient pair. Firstly, the pulse must have a low enough bandwidth to select between the two coupled spins with the smallest difference in offsets, and secondly the gradient must be large enough so that the broadening of the lines is comparable to the spectral width.

Sensitivity

The use of selective decoupling in different parts of the sample, while essential for the feasibility of the experiment, does have consequences for the sensitivity. For each resonance only a fraction of the sample contributes to the signal that is observed,

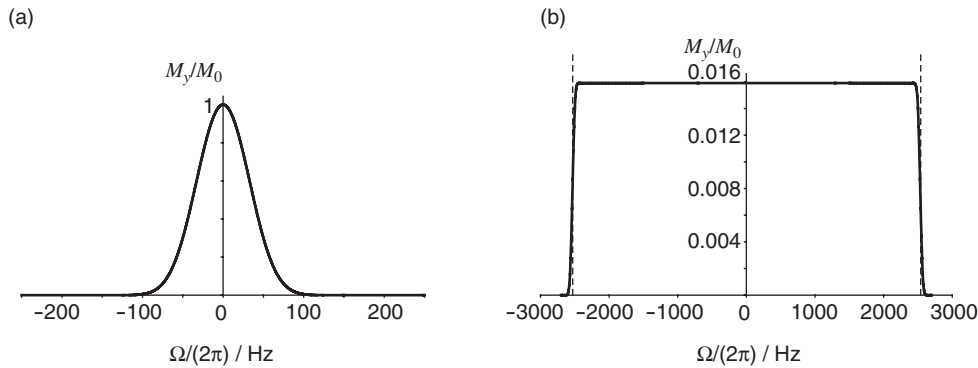


Figure 5.4: Simulated excitation profile of the Zanger–Sterk experiment. The plot in (a) is the profile in the absence of a gradient. The selective 180° pulse is a Gaussian with a duration of 20 ms. Applying a gradient of strength 1.19 G cm^{-1} simultaneously to this pulse gives the profile in (b). The dashed lines represent the boundaries of the region that would be covered by a standard gradient-broadened image.

which means that the SNR is greatly reduced compared to that of a conventional proton spectrum. The SNR in the Zanger–Sterk spectrum, compared to the conventional spectrum, is

$$\frac{\Delta z}{L} = \frac{\omega_B}{\gamma GL}.$$

The larger the gradient, or the more selective the pulse, the lower the sensitivity. In practice, it will therefore be necessary to find a compromise between fulfilling the two selectivity conditions we have imposed on the selective pulse and gradient, and obtaining a sufficiently high SNR.

Simulation of the excitation profile

The excitation profile of the Zanger–Sterk pulse-sequence element was simulated using the SPINEVOLUTION [20]. The pulse sequence that was used is a modified form of the Zanger–Sterk sequence in Figure 5.1; the selective 90° pulse and gradient were replaced by a hard 90° pulse. The first increment, $t_1 = 0$, was simulated for a range of offsets of a single spin, and the y -magnetization was calculated in each case; the x -magnetization was zero as applying EXORCYCLE to the selective pulse removed any phase errors.

The results are shown in Figure 5.4. The selective pulse was a Gaussian with a duration of 20 ms whose $B_1(t)$ profile was truncated at 1% of the maximum field. The excitation profile in the absence of the gradient is shown in (a). A gradient of strength

1.19 G cm⁻¹ was then applied; the sample length was set to 1.0 cm, giving an image broadening of 5067 Hz. The gradient was implemented by dividing the sample into 101 slices, calculating the result of the sequence for each, and summing the results. This gives the plot shown in (b). The dashed lines enclose the region of the gradient-broadened image; their positions are given by $\pm\gamma GL/(4\pi) = \pm2533$ Hz. The gradual decrease of M_y at these boundaries occurs because the width of the excited slice is truncated by the edge of the sample. The maximum value of M_y is 0.0159 which gives an estimated bandwidth of the pulse of 81 Hz. This corresponds approximately to the region within which $M_y/M_0 > 0.5$ for the excitation profile in (a), and so is smaller than the total width of the profile as measured from the breadth of its base. The sensitivity of the experiment is rather low; in the simulation given here only 1.6% of the total available signal is retained by the spatially-selective pulse.

Linewidths

The use of spatial selectivity to achieve decoupling across the spectrum has a very beneficial side-effect on the linewidth and lineshape in the decoupled spectrum. In conventional spectroscopy, the linewidth is the sum of a homogeneous part, and an inhomogeneous part that arises due to the spatial non-uniformity of the B_0 field. However, in the Zangerer–Sterk experiment, the signal from each resonance is acquired from a comparatively small region of the sample, where the local inhomogeneity of the magnetic field is lower than for the whole sample. The linewidths in the Zangerer–Sterk spectrum may therefore be close to the homogeneous values.

5.1.4 Spatial inhomogeneity of the gradient and RF field

It has so far been assumed that gradient and RF field are spatially uniform, by which it is meant that both $\partial G/\partial z$ and $\partial B_1/\partial z$ are zero throughout the sample. In practice, however, this may not be true. Since different resonances are acquired from different parts of the sample, it may be necessary to take the effects of spatial inhomogeneity into account. The intensities of the resonances are affected by three different factors which are described below.

Firstly, the gradient is spatially inhomogeneous, which means that different slices of the sample experience a slightly different gradient intensity. The result of this is that the image that is recorded from a region of the sample where the gradient is greater than the average will be stretched, whereas regions where the gradient is lower

will give a compressed image. A slice-selective pulse with a given bandwidth will therefore excite a smaller slice of the sample where the gradient is higher than the nominal value, than for regions where the gradient is lower. Therefore, the intensities of the peaks across the spectrum will be non-uniform.

Secondly, the non-uniform B_1 field produces two effects: the bandwidth of the selective pulse and its flip angle will vary throughout the sample. As has been discussed, the larger the bandwidth the greater the width of the slice that is excited and the greater the intensity of the resonance. The spatial variation of the flip angle also affects the intensity. From Equation 1.20, the intensity of the transformation of \hat{I}_+ to \hat{I}_- is

$$\sin^2 \frac{1}{2}(\pi + \varepsilon(z)) = \cos^2 \frac{1}{2}\varepsilon(z),$$

where $\varepsilon(z)$ is the spatially-dependent deviation from the nominal flip angle of 180° .

Finally, we also need to take into account the non-uniformity of the coupling to the receiver coil. The different slices of the sample do not contribute equally to the total FID. It is found that the size of the signal becomes lower as we move from the middle of the active region of the sample to the edge.

The result of all this is that the spatial variation of the signal will affect the intensities of the peaks in the spectrum. The exact form of the variation is very difficult to predict, as it depends on the coils that generate the pulses and detect the signal, and the coils that produce the magnetic field gradient. However, it can be determined experimentally by recording the first increment of the Zanger-Sterk experiment a number of times on a one-spin system whilst varying the offset of the selective 180° pulse, thus acquiring the signal from different slices in each experiment. The sample that was used to determine the excitation profile was 1% H_2O in D_2O that was doped with 0.1 mg/ml of $GdCl_3$ to give a T_1 of 195 ms. The selective pulse was a Gaussian of length 57.6 ms, and was truncated at 1% of its maximum intensity. The accompanying gradient had a relative strength of 3%; this corresponds to an absolute gradient of 1.7 G cm^{-1} , and so the width of the gradient-broadened image is 7.1 kHz.

The water peak was placed on-resonance, and the offset of the selective pulse was varied from -2500 to $+2500$ Hz. This is equivalent to keeping the pulse on-resonance, and varying the offset of the peak from $+2500$ to -2500 Hz, i.e. in the *opposite direction*. Each one-dimensional spectrum was Fourier transformed, and the integral of the peak was computed. The plot of the integral I , relative to the maximum

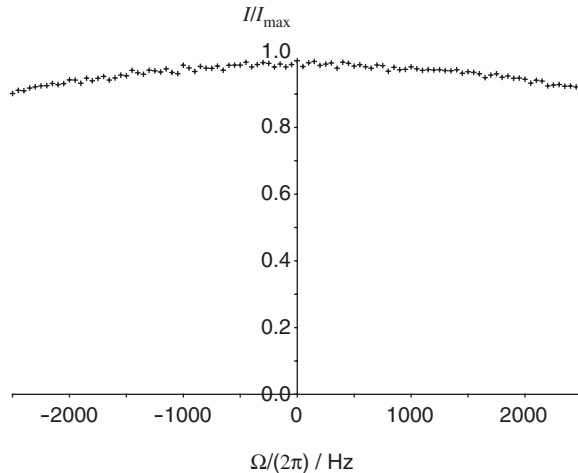


Figure 5.5: Experimental excitation profile of the Zanger–Sterk pulse-sequence element. The points on the plot give the integral I of the singlet at various offsets, relative to the maximum integral I_{\max} .

integral that was measured I_{\max} , is plotted against the *peak offset* in Figure 5.5. The size of the integrated signal drops off towards larger (positive and negative) offsets, which reflects the variation of the coupling to the receiver coil. The largest drop in intensity was 9.8% of the maximum, which was measured at the largest offsets.

5.1.5 Strong coupling and close-lying multiplets

The analysis of the Zanger–Sterk pulse sequence has so far assumed that the passive spins are unaffected by the selective 180° pulse. This is certainly true if the difference between the offsets of the passive and active spins is large enough so that the former lies outside the bandwidth of the pulse, as was discussed in Section 5.1.3. However, this will not necessarily be the case for two reasons. Firstly, the available SNR dictates the lower limit to which the bandwidth may be set. This may not be sufficient to decouple two spins with close-lying multiplets. Secondly, in the case of very significant strong coupling where the two multiplets overlap with each other, it may not be possible to decouple the two spins regardless of how selective the pulse is.

A typical example of a spectrum in which the two spins are not affected separately by the selective pulse is shown in Figure 5.6. The spectrum is a result of a SPINEVOLUTION simulation of the Zanger–Sterk sequence applied to a two-spin system [20]. The difference between the offsets of the two spins is 50 Hz, and the J -coupling constant is 10 Hz giving a strong coupling parameter of $\theta = 5.7^\circ$. The

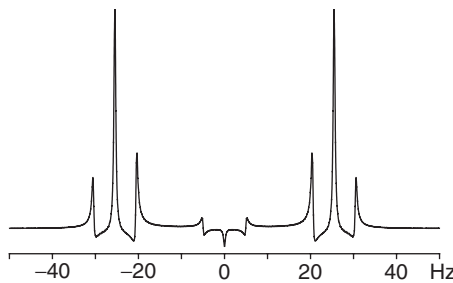


Figure 5.6: Simulation of the Zanger–Sterk spectrum of two closely-spaced spins. The offsets are -25 and $+25$ Hz, and $J_{12} = 10$ Hz. Details of the selective pulse and gradient are given in the text.

selective pulse is a Gaussian of 20 ms, which is truncated at 1% of the maximum field. The width of the excitation profile (as measured from its base) is approximately 200 Hz, and so the pulse cannot differentiate between the two spins. This pulse was applied simultaneously to a gradient of 1.19 G cm^{-1} . Once again, the first 90° pulse is non-selective. The resulting spectrum takes a peculiar form, in which each resonance is the superposition of a singlet and the doublet that would be observed in the conventional spectrum. There is also a set of peaks centred at the average of the two offsets. The form of the spectrum can be rationalized as follows.

The splitting of the singlet resonance arises because the slices of the sample in which the two spins are affected by the selective pulse overlap with each other. It is not a strong coupling effect *per se*, in that the spins do not need to be strongly coupled for this effect to be observed. This can be seen from Figure 5.7 (a)–(f) which show a singlet resonance from a series of simulated Zanger–Sterk spectra for a two-spin system. The difference between the offsets has been progressively increased from (a) to (f) by the same factor as the coupling constant, so that the strong coupling parameter θ is the same for each. As the multiplets move further apart we observe a sharpening of the resonance as the doublet becomes less intense until, in (e) and (f), only the singlet remains. The form of the spectrum in Figure 5.6 can therefore be rationalized by considering two weakly-coupled spins.

It must be recognized that the transformation caused by the selective pulse is more complicated than the simple instantaneous 180° rotation of the active spin, as was described in Section 2.4. In the part of the sample where the spin is on-resonance, the overall rotation experienced by the spin will be of 180° about the x -axis. On the other hand, in the slices where the spin is not on-resonance the actual rotation will be

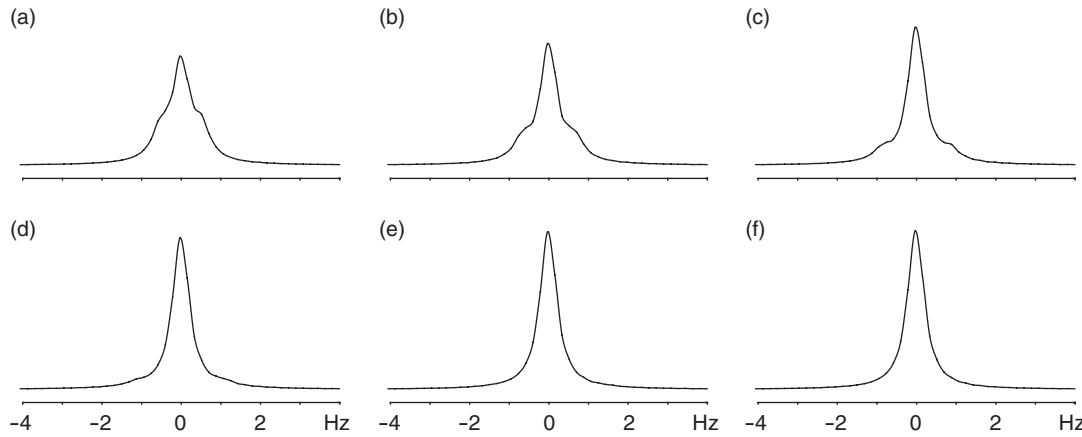


Figure 5.7: A series of simulated Zanger–Sterk spectra of a two-spin system in which the separation between the offsets is progressively increased. The spin two resonance is shown. Spin two is on-resonance in all of the spectra, whilst the offset of spin one is varied. The coupling constant is also varied so that the strong coupling parameter θ is the same for each simulation. The chosen parameters ($\Omega_1/(2\pi), J_{12}$) in Hz are: (a) (50.00, 1.00), (b) (64.58, 1.29), (c) (83.41, 1.67), (d) (107.72, 2.15), (e) (139.13, 2.78), and (f) (179.69, 3.59). In all cases $\theta = 0.57^\circ$ and the natural linewidth is 0.5 Hz.

about an axis that is tilted away from the transverse plane, and through a flip angle that depends upon the effective field ω_{eff} . For the present discussion however we will assume that a spin i is simply rotated about x through an angle α_i that is equal to 180° on-resonance, and which decreases to zero with increasing offset.

If we only consider the operators that represent -1 coherence on spin one, the density operator at the end of the first half of the evolution period t_1 is

$$-\frac{1}{2}i\hat{I}_{1-}\hat{I}_{2\alpha} \exp [i(\Omega_1 + J_{12})t_1/2] - \frac{1}{2}i\hat{I}_{1-}\hat{I}_{2\beta} \exp [i(\Omega_1 - J_{12})t_1/2].$$

The hard 180° pulse transforms these terms into

$$-\frac{1}{2}i\hat{I}_{1+}\hat{I}_{2\beta} \exp [i(\Omega_1 + J_{12})t_1/2] - \frac{1}{2}i\hat{I}_{1+}\hat{I}_{2\alpha} \exp [i(\Omega_1 - J_{12})t_1/2].$$

We now model the selective pulse as a rotation of the spin-one operators through an angle α_1 , followed by a rotation of the spin-two operators by an angle α_2 . After the

evolution during the second half of t_1 the resulting terms of coherence order -1 are:

$$\begin{aligned} & -\frac{1}{2}is_1^2c_2^2\hat{I}_{1-\beta}\exp[i\Omega_1t_1] - \frac{1}{2}is_1^2c_2^2\hat{I}_{1-\alpha}\exp[i\Omega_1t_1] \\ & -\frac{1}{2}is_1^2s_2^2\hat{I}_{1-\alpha}\exp[i(\Omega_1 + \pi J_{12})t_1] - \frac{1}{2}is_1^2s_2^2\hat{I}_{1-\beta}\exp[i(\Omega_1 - \pi J_{12})t_1] \\ & + \frac{1}{8}iS_1S_2\hat{I}_{1\alpha}\hat{I}_{2-}\left\{\exp\left[i\left(\frac{1}{2}(\Omega_1 + \Omega_2) + \pi J_{12}\right)t_1\right] - \exp\left[i\frac{1}{2}(\Omega_1 + \Omega_2)t_1\right]\right\} \\ & + \frac{1}{8}iS_1S_2\hat{I}_{1\beta}\hat{I}_{2-}\left\{\exp\left[i\left(\frac{1}{2}(\Omega_1 + \Omega_2) - \pi J_{12}\right)t_1\right] - \exp\left[i\frac{1}{2}(\Omega_1 + \Omega_2)t_1\right]\right\}, \end{aligned}$$

where $c_i = \cos \frac{1}{2}\alpha_i$, $s_i = \sin \frac{1}{2}\alpha_i$, and $S_i = \sin \alpha_i$. The first two terms are modulated in t_1 by the offset Ω_1 and not the coupling J_{12} , so they combine to give the singlet in the decoupled spectrum. The second two terms are modulated by both Ω_1 and J_{12} . Therefore, they produce the doublet that is superimposed upon the spin-one singlet. The last four terms are produced from a coherence transfer to spin two. The effective offset at which the evolution during t_1 is modulated is the average of the offsets of both spins, $\frac{1}{2}(\Omega_1 + \Omega_2)$. They therefore give the three peaks that are centred on this frequency.

In the Zanger–Sterk spectrum of a strongly-coupled spin system, there will also be a mixing effect due to the hard 180° pulse. This effect is the same as is encountered in conventional J -spectroscopy where a coherence that is mainly present on one spin is transferred to a coherence that is mainly present on the other spin. However the resulting peak will also have an effective offset of $\frac{1}{2}(\Omega_1 + \Omega_2)$, and so the process is indistinguishable from the coherence transfer described above.

5.1.6 Speeding up acquisition

The main drawback of the Zanger–Sterk experiment as it has been so far described is that the linewidth in the decoupled spectrum is equal to the linewidth in the ω_1 dimension. In order to obtain high resolution in this dimension, many t_1 increments are required. This is the same situation that was encountered with anti z -COSY, except that in the latter case the problem was somewhat less serious as the linewidth in the projection also depended on the ω_2 linewidth.

The problem therefore has a similar solution, which is to increase the increment Δt_1 , so that the same resolution can be achieved with fewer increments. As with anti z -COSY, the spectrum will fold in ω_1 , but the true offsets can be restored by employing the following method. The value of Δt_1 is set to be an integer multiple n of the dwell time in t_2 , i.e. $n\Delta t_2$, and for each increment we acquire the first n complex data points

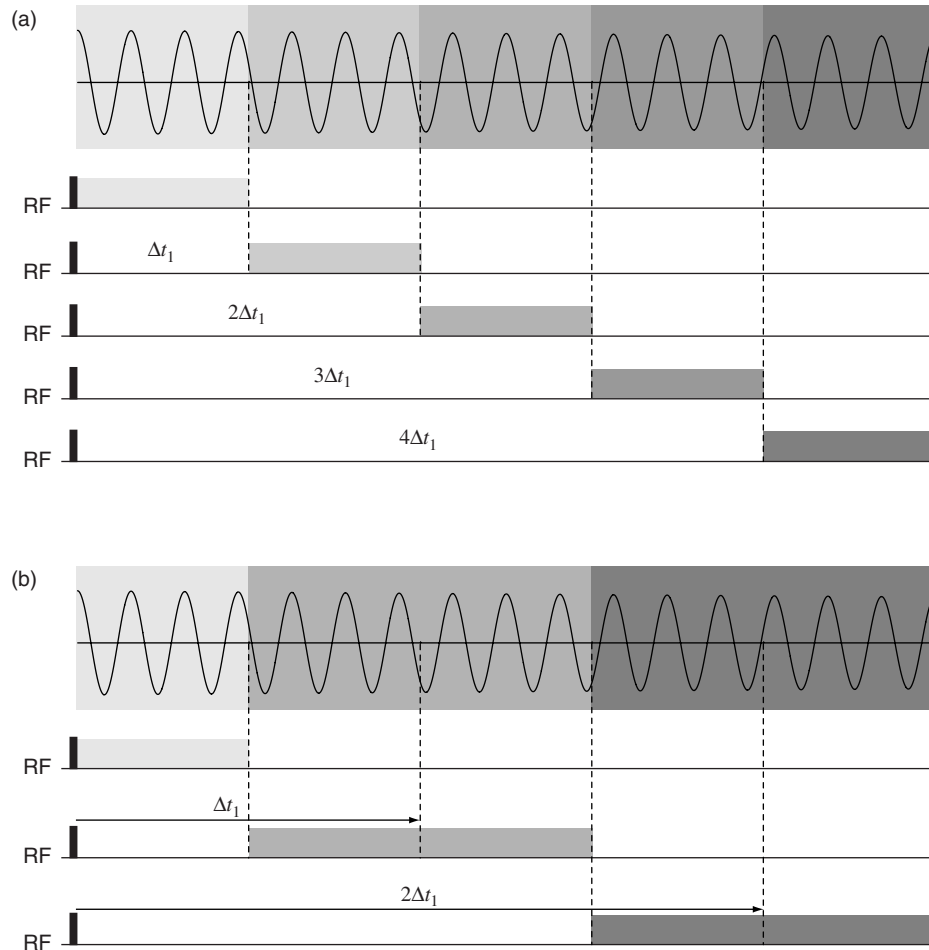


Figure 5.8: Illustration of the acquisition schemes used in the Zanger–Sterk experiment. The original scheme is shown in (a) [81]. The constructed FID is shown at the top, and is separated into the blocks that are acquired individually; each is coloured with a different shade of grey. The five blocks are recorded by the five sequences shown below, each corresponding to the first five increments of the pulse sequence; the parts of the sequence where the n data points are acquired are shaded grey ($\Delta t_1 = n\Delta t_2$ where n is an integer). Note that the pulses in the middle of t_1 are omitted for clarity. The modification of the scheme in (a) is shown in (b) [59]. The increment Δt_1 is now $2n\Delta t_2$. In each block, the first n points are acquired before the end of t_1 , and the second n points are acquired from the start of t_2 .

in t_2 , rather than just the first point. The chunks of data are then combined in sequence to give the FID, the Fourier transform of which is a decoupled spectrum. The process is illustrated in Figure 5.8 (a).

The evolution of the offset is properly represented in the constructed FID since it

evolves uninterrupted throughout the sequence after the initial 90° pulse. The peaks will therefore be located at their correct offsets in the spectrum. In order for the FID to give a decoupled spectrum, there must be no evolution of the coupling during t_2 . This is obviously not the case, but the experiment can be conducted in a way so that the evolution of the coupling is negligible. Since the coupling is refocused at the end of t_1 , every n th complex point in the constructed FID, counting from the first point, is independent of the coupling constant J . In addition, if $n\Delta t_2 |J| \ll 1$, the evolution of the coupling can also be ignored for all the other points.

Recently, Nilsson and Morris proposed a modification of this acquisition method that decreases the total experiment time by approximately a factor of two [59]. The value of Δt_1 is set to $2n\Delta t_2$, and we acquire the first n points *before* the end of t_1 and the first n points after the end of t_1 in a single block, with the exception that the first n data points of the FID are acquired in the same way as before. The process is shown in Figure 5.8 (b). The evolution of the coupling can be ignored as before, despite doubling the number of points that are acquired in a single block; this is because the coupling is refocused at the halfway point in each acquisition block.

5.1.7 Comparison of the anti z -COSY and Zanger–Sterk pulse sequences

Despite the pulse sequences for anti z -COSY and the Zanger–Sterk experiment appearing very different at first sight, they actually share a striking similarity. Both experiments achieve decoupling by changing the polarization of a fraction of the spins in the sample, and selecting only the coherences resulting from these spins. Anti z -COSY accomplishes this by the use of two small flip angle pulses and a 180° pulse. This combination changes the polarization of a small fraction of the spins which are distributed uniformly throughout the sample. In the Zanger–Sterk experiment, on the other hand, the passive spins are flipped with 100% probability by the combination of the non-selective and selective 180° pulses, but only in a small region of the sample.

The 45° projection of the absorption-mode anti z -COSY spectrum gives the decoupled spectrum. However, this projection can also be calculated by projecting N-type spectrum onto the $\omega_2 = -\omega_1$ anti-diagonal, projecting the P-type spectrum onto the $\omega_2 = \omega_1$ diagonal, and summing the two results. The form of both projections can be calculated by using the projection–slice theorem.

The projection of the N-type spectrum is calculated from the Fourier transform of the one-dimensional slice that is extracted along $t_2 = -t_1$ from the N-type time

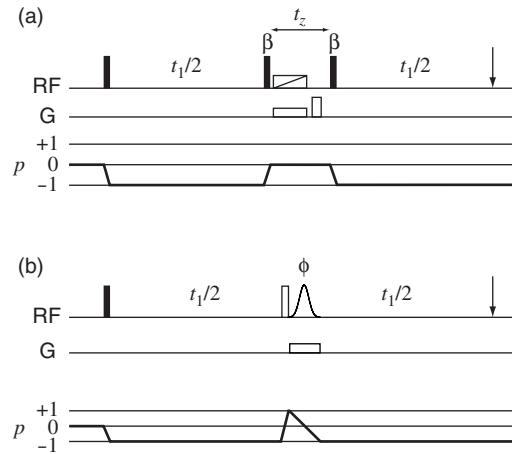


Figure 5.9: Comparison of the anti z -COSY and Zanger–Sterk pulse sequences. The sequence shown in (a) is used to record the 45° projection of the P-type anti z -COSY spectrum which, considering only the diagonal peaks, is a decoupled spectrum. The arrow at the end of the sequence indicates the acquisition of a single complex data point. The Zanger–Sterk pulse sequence is shown in (b) for comparison.

domain. However, just as in the case of conventional J -spectroscopy, there is no data for negative times, and so this projection is zero. On the other hand, the projection of the P-type spectrum is calculated by extracting the $t_2 = t_1$ slice from the P-type time domain, the Fourier transform of which gives an absorption-mode line in the real part of the spectrum.

Therefore, in order to obtain the decoupled spectrum, we only need to record the P-type spectrum, and project this onto the diagonal. In fact, the whole two-dimensional time domain is not needed, and it is sufficient to increment the times t_1 and t_2 in concert, and acquire a single complex data point at the beginning of the detection period. The pulse sequence can therefore be simplified as shown in Figure 5.9 (a). The Zanger–Sterk sequence is shown in (b). If we consider only the diagonal peaks of the former experiment, the two sequences differ only in form of the pulse-sequence element that inverts the passive spins during t_1 . It should be noted that it is possible to insert either pulse-sequence element into the evolution period of an arbitrary two-dimensional pulse sequence to achieve decoupling in the ω_1 dimension, thus reducing the overlap in crowded two-dimensional spectra [81, 82].

One significant advantage of the anti z -COSY method over the Zanger–Sterk experiment is that the former also provides the structures of the multiplets, where the

latter does not. However, it will be shown in the next Section that it is possible to exploit the Zanger–Sterk pulse-sequence element in conventional J -spectroscopy to obtain a two-dimensional J -spectrum with the absorption-mode lineshape [83].

5.2 Two-dimensional J -spectra with absorption-mode lineshapes

In this Section, a new method for obtaining absorption-mode J -spectra is presented. In contrast to other methods [38–50], this new experiment is very simple to implement, requires no specialized data processing, and retains the natural intensities of the lines.

It was shown in Section 1.12.1 that an N-type and P-type spectrum can be combined to give an absorption-mode spectrum [13, 14]. Both spectra have the phase-twist lineshape, but if the ω_1 axis of the former is reversed, and this spectrum is added to the latter, the dispersive parts of the lineshape cancel.

In terms of the CTP, the N-type spectrum is acquired by selecting the +1 pathway during t_1 , and the P-type spectrum is acquired by selecting the −1 pathway. For the conventional J -spectroscopy pulse sequence, shown in Figure 3.1 (a), the coherence order changes sign in the middle of t_1 , and so it is not possible to classify this experiment as either N-type or P-type. However, it is still the case that symmetrical pathways must be acquired. Normally, we can switch between the two pathways simply by changing either the phase cycle, or one or more of the PFGs. However, this is not possible in conventional J -spectroscopy as there is no mixing period in the sequence.

The pulse sequence which is used to record the complementary J -spectrum is shown in Figure 5.10 (b). We refer to the spectrum that is acquired by this sequence as the *anti J-spectrum*. The coherence order is −1 during the first half of t_1 , and +1 for the second half. It is therefore necessary to include an element at the end of this period to convert the +1 coherence into a −1 coherence that can be observed during the detection period. It will be seen that this can only be accomplished by selectively flipping the active spin from \hat{I}_+ to \hat{I}_- , and leaving *all the passive spins unaffected*. For this reason, a hard 180° pulse cannot be used, and so the Zanger–Sterk pulse-sequence element is used instead. The Zanger–Sterk element also has the effect of reducing the sensitivity of the spectrum. So, in order to obtain a comparable conventional J -spectrum, the standard pulse sequence also has to be

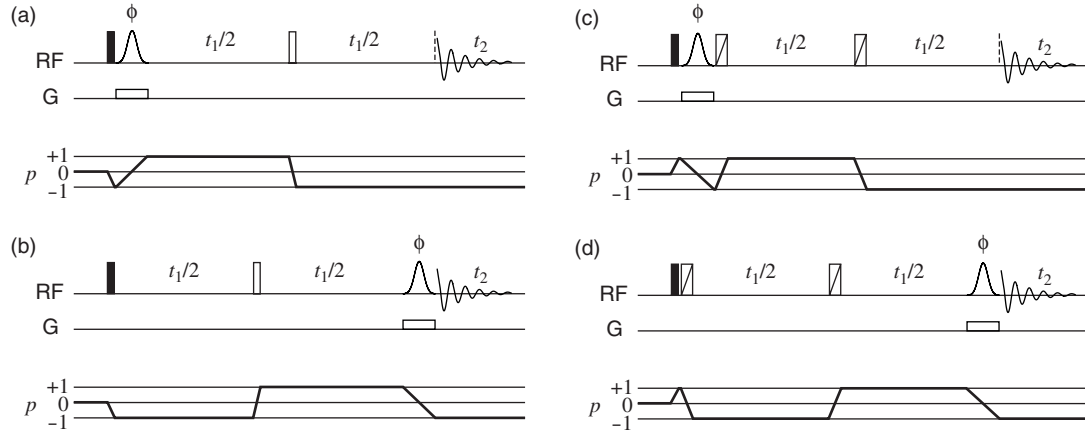


Figure 5.10: Pulse sequences used to record J -spectra with absorption-mode lineshapes. The sequence in (a) is a modified conventional J -spectroscopy pulse sequence. The Zangger–Sterk pulse-sequence element at the beginning of t_1 ensures that the resulting spectrum has the correct intensity weighting. The sequence in (b) includes the same pulse-sequence element immediately prior to acquisition, and so produces the anti J -spectrum. The sequences in (c) and (d) have been modified to include a pair of BIPs, rather than the single hard 180° pulse. All pulses are applied along x , with the exception of those marked ϕ . The phase ϕ is phase cycled as $[0, \pi/2, \pi, 3\pi/2]$, and the receiver phases are $[0, \pi, 0, \pi]$.

modified. The Zangger–Sterk pulse-sequence element is included immediately before t_1 , where it weights the intensities appropriately, but does not affect the multiplets in the final spectrum. This sequence is shown in (a). The idea of inserting a 180° pulse at the end of t_1 to obtain the complementary spectrum has already been utilized in the case of heteronuclear J -spectroscopy [13, 84].

5.2.1 Analysis of the pulse sequences

The features of the experiment can be fully-described by using a two-spin system, as is the case for conventional J -spectroscopy. The conventional sequence in Figure 5.10 (a) will be analyzed first. Starting from equilibrium magnetization on spin one, the 90° pulse creates the following density operator terms of coherence order -1 :

$$-\frac{1}{2}i\hat{I}_{1-}\hat{I}_{2\alpha} - \frac{1}{2}i\hat{I}_{1-}\hat{I}_{2\beta}.$$

The Zangger–Sterk pulse-sequence element changes the coherence order of spin one to $+1$ in a particular slice of the sample, and leaves the passive spin in the same slice unaffected. Ignoring the factor that accounts for the loss of intensity (which is common

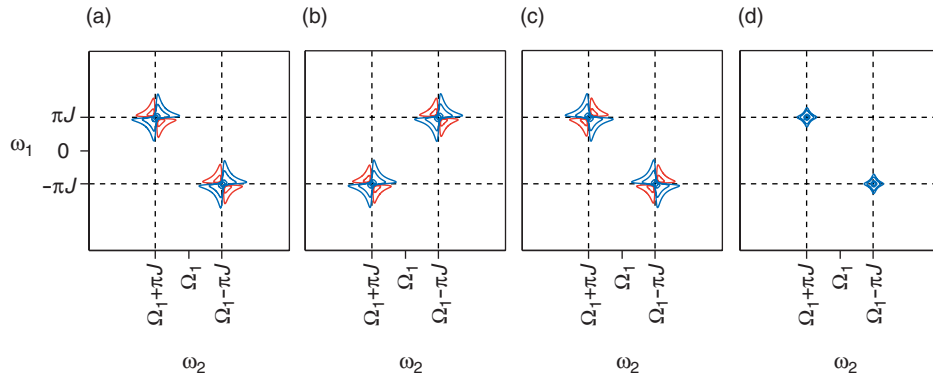


Figure 5.11: Simulated spin-one doublet in the J -spectra of a weakly-coupled two-spin system. The conventional J -spectrum is shown in (a), in which the doublet is aligned parallel to the main diagonal. The doublet in (b) is taken from the anti J -spectrum and is aligned parallel to the anti-diagonal. Reversing the ω_1 axis of (b) gives the spectrum in (c), in which the doublet is aligned parallel to the doublet in (a). However, the dispersive parts of the peaks have opposite sign, and so when (c) is added to (a), they cancel giving the absorption-mode spectrum in (d).

for all spins across the spectrum) the density operator is now

$$-\frac{1}{2}i\hat{I}_{1+}\hat{I}_{2\alpha} - \frac{1}{2}i\hat{I}_{1+}\hat{I}_{2\beta}.$$

These two terms now evolve under coupling only during the spin echo in t_1 , and under both offset and coupling during t_2 . The final result is

$$-\frac{1}{2}i\hat{I}_{1-}\hat{I}_{2\beta} \exp[-i\pi J_{12}t_1] \exp[i(\Omega_1 - \pi J_{12})t_2] - \frac{1}{2}i\hat{I}_{1-}\hat{I}_{2\alpha} \exp[+i\pi J_{12}t_1] \exp[i(\Omega_1 + \pi J_{12})t_2],$$

which is essentially the same result that was found in Section 3.1.1. The resulting spin-one multiplet is shown in Figure 5.11 (a).

In the anti J -spectroscopy sequence in Figure 5.10 (b) the following operators are produced by the 90° pulse

$$-\frac{1}{2}i\hat{I}_{1-}\hat{I}_{2\alpha} - \frac{1}{2}i\hat{I}_{1-}\hat{I}_{2\beta},$$

which evolve during the spin echo to give

$$-\frac{1}{2}i\hat{I}_{1+}\hat{I}_{2\beta} \exp[+i\pi J_{12}t_1] - \frac{1}{2}i\hat{I}_{1+}\hat{I}_{2\alpha} \exp[-i\pi J_{12}t_1].$$

The Zanger–Sterk pulse-sequence element now changes the coherence order of spin one to -1 , leaving the passive spin unaffected, to give

$$-\frac{1}{2}i\hat{I}_{1-}\hat{I}_{2\beta} \exp[+i\pi J_{12}t_1] - \frac{1}{2}i\hat{I}_{1-}\hat{I}_{2\alpha} \exp[-i\pi J_{12}t_1].$$

Finally, evolution during t_2 gives

$$-\frac{1}{2}i\hat{I}_{1-}\hat{I}_{2\beta} \exp[+i\pi J_{12}t_1] \exp[i(\Omega_1 - \pi J_{12})t_2] - \frac{1}{2}i\hat{I}_{1-}\hat{I}_{2\alpha} \exp[-i\pi J_{12}t_1] \exp[i(\Omega_1 + \pi J_{12})t_2].$$

The multiplet is shown in Figure 5.11 (b). The spectrum has exactly the same form as a conventional J -spectrum, with the exception that the signs of the ω_1 frequencies have all been inverted. This is a result of the polarization of the passive spins being left unaffected by the Zanger–Sterk pulse-sequence element at the end of t_1 . If a hard 180° pulse is used, the passive spins would be inverted, and the subsequent evolution during t_2 would yield a spectrum that is identical to the conventional J -spectrum. Hence, the two spectra could not be combined to give the absorption-mode lineshape.

The multiplet in (b) is aligned parallel to the anti-diagonal. Reversing the ω_1 axis gives the spectrum in (c), in which the multiplet is now aligned parallel to the main diagonal, as is the case for the normal J -spectrum. However, the dispersive parts of the phase twists in (c) have the opposite sign to those in (a). Therefore when (a) and (c) are added the dispersive parts cancel, leaving the absorption-mode spectrum in (d).

5.2.2 Linewidths in the decoupled spectrum

The linewidth in the projection can be calculated in the same way as for the projection of the anti z -COSY spectrum in Section 4.2.3. The shear in the ω_1 dimension can be described by adopting the following coordinate transformation:

$$\begin{aligned} v_1 &= \omega_1 \\ v_2 &= \omega_2 + \kappa\omega_1 \\ &= \omega_2 - \omega_1. \end{aligned}$$

In this coordinate system, the two-dimensional absorption-mode Lorentzian is

$$S(\omega_1, \omega_2) = \mathcal{A}_{\Omega^{(1)}}(v_1) \mathcal{A}_{\Omega^{(2)}}(v_1 + v_2).$$

The projection is calculated by integrating over the v_1 dimension. It is given by

$$P(v_2) = \frac{\pi T_2^{(p)}}{1 + (v_2 - \Omega^{(p)})^2 T_2^{(p)2}},$$

where

$$\Omega^{(p)} = \Omega^{(2)} - \Omega^{(1)},$$

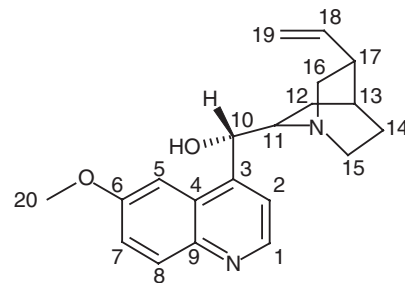


Figure 5.12: The structure of quinine with the labels used for the assignment of the spectrum.

and

$$\frac{1}{T_2^{(p)}} = \frac{1}{T_2^{(1)}} + \frac{1}{T_2^{(2)}}.$$

The linewidth in the projection is therefore the sum of the linewidths in the two dimensions. In practice, this means that the linewidth is equal to twice the homogeneous contribution plus the inhomogeneous contribution.

5.3 The absorption-mode *J*-spectrum of quinine

The new *J*-spectroscopy experiment was tested on a sample of quinine in DMSO, using the pulse sequences in Figure 5.10 (c) and (d) in which the hard 180° pulse is replaced with a pair of BIPs [27]. The second BIP refocuses the frequency-dependent phase errors that are introduced by the first. The structure of quinine is shown in Figure 5.12 with the labels used for the assignment of the NMR spectra. The spectra were recorded at 500 MHz for protons, with 36 scans per t_1 increment. The selective pulse was a Gaussian of length 57.6 ms, and was truncated at 1% of its maximum intensity. Such a pulse has an estimated bandwidth (the region over which the magnitude of the refocused magnetization is greater than $M_0/2$) of 26.5 Hz. The accompanying gradient had a relative strength of 3%; this corresponds to an absolute gradient of 1.7 G cm⁻¹, and so the width of the gradient-broadened image is 7.1 kHz. Therefore, the percentage of the total signal that is retained by the experiment is 0.4%. This represents a very drastic reduction in the SNR, and is a consequence of the high selectivity needed to decouple the vinyl protons (19) from each other.

The specific BIP that was used is designated BIP-720-25-40, and had a B_1 field and duration of 20 kHz and 100 μ s respectively. The spectral widths in ω_1 and ω_2 are

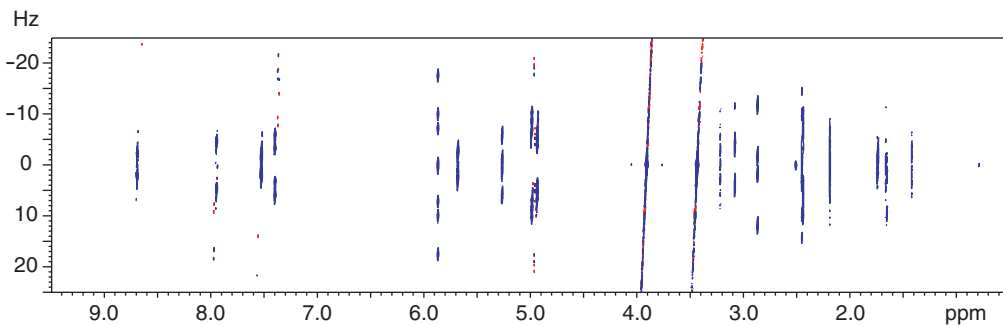


Figure 5.13: The sheared two-dimensional absorption-mode J -spectrum of quinine. The two intense resonances at 3.92 and 3.44 ppm contain visible t_1 noise. There are some strong-coupling artefacts that are visible at 7.98, 7.38, and 4.97 ppm.

50 and 4496 Hz respectively. The acquisition time in t_1 was 1.8 s, and 85 t_1 increments were recorded, giving a t_1^{\max} of 1.7 s. The total experiment time was 13 hours.

The two-dimensional J -spectrum is shown in Figure 5.13. The decoupled spectrum computed by projecting the two-dimensional spectrum is shown in Figure 5.14 with the conventional spectrum for comparison. The conventional and decoupled spectra of the aromatic and vinyl region are shown in (a) and (b), while the aliphatic region is shown in (c) and (d). The integrals of the peaks are in good agreement with those in the conventional spectrum, with the exception of the overlapping peaks around 1.7 ppm whose integral is substantially lower. These resonances are due to protons attached to carbons 12, 13, and 14 which are strongly coupled to each other. This deviation appears to be more important than that arising from considerations of the spatial inhomogeneity of the gradient and RF field as was discussed in Section 5.1.4. The latter effect was therefore ignored.

The structures of the multiplets that were taken from the sheared J -spectrum are shown in Figure 5.15 (a)–(t). The multiplets from the aromatic and vinyl region, shown in (a)–(j), were taken from the spectrum shown in 5.13. However, the multiplets in the aliphatic region had a lower SNR as the values of T_2 of these protons are lower than for the aromatic and vinyl protons. In order to obtain higher sensitivity, the J -spectrum of this region was re-recorded with a shorter acquisition time in t_2 (0.9 s) and fewer t_1 increments (45, giving a t_1^{\max} of 0.9 s). In addition, the number of scans per increment was 160. The resulting multiplets are shown in (k)–(t).

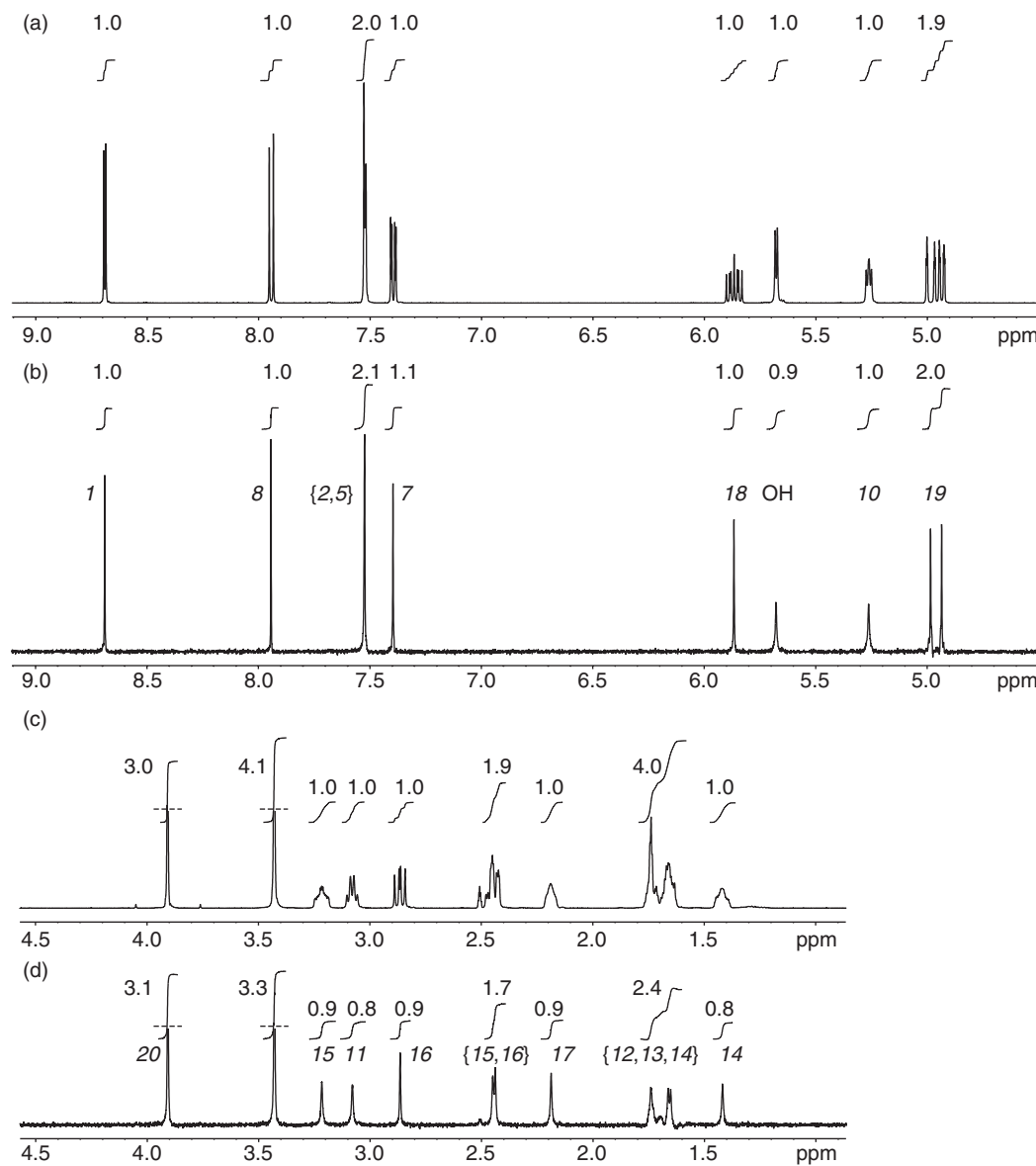


Figure 5.14: Conventional spectra and projections of the absorption-mode J -spectrum of quinine. The projection contains a single line at each offset, and so is decoupled. The spectra are shown in two parts: (a) and (b) are of the aromatic and vinyl region, and (c) and (d) are of the aliphatic region. The conventional spectra are shown in (a) and (c), and the projections are shown in (b) and (d). The numbers in italics give the assignment, and correspond to the labels in Figure 5.12. In each case, the integrals are given relative to the resonance at 8.69 ppm.

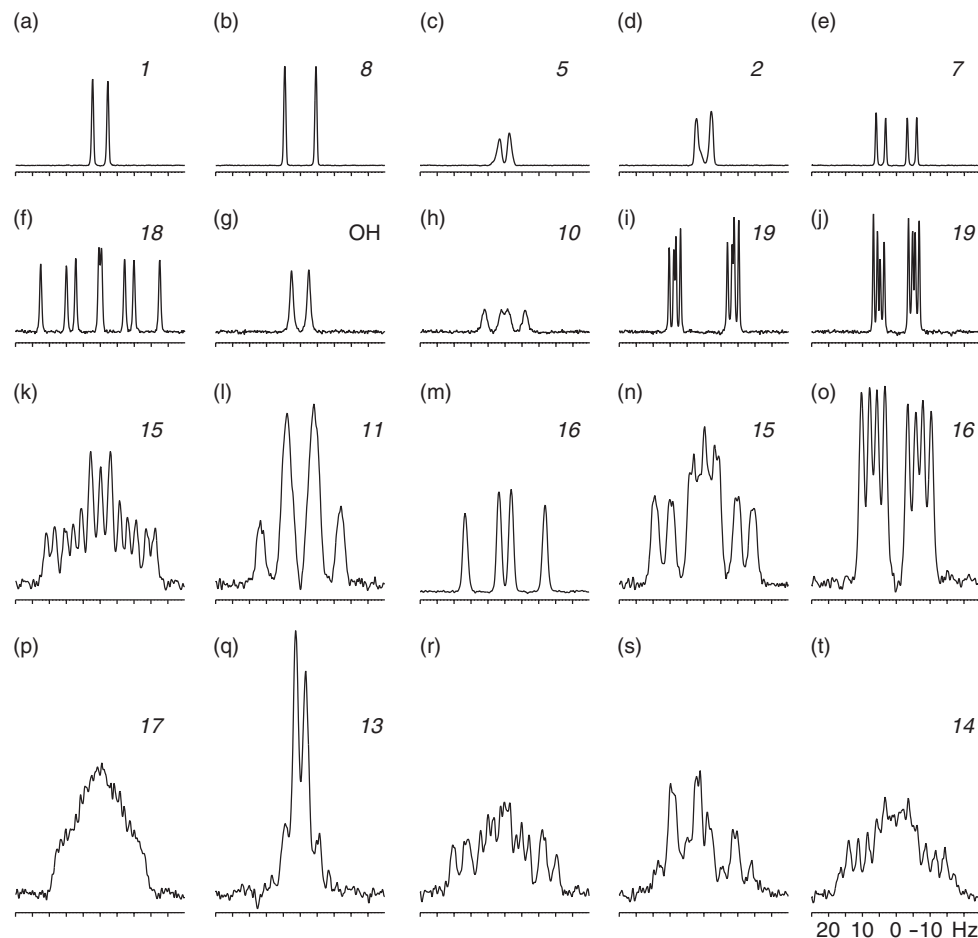


Figure 5.15: Cross-sections taken parallel to ω_1 from the sheared absorption-mode J -spectrum of quinine. Multiplets (a)–(e) are plotted on the same vertical scale, whereas (f)–(j) are five-fold expansions. The multiplets (k)–(t) are taken from a separate experiment, as described in the text. Multiplets (k), (l), and (n)–(t) are plotted on a scale that is expanded by five times relative to (m). The assignment is given by the italicized numbers; multiplets (r) and (s) are associated with protons 12 and 14, but the assignment of which is which is unclear.

5.4 The effects of strong coupling

The effects of strong coupling on the new J -spectroscopy experiment will now be considered. It will be shown that the J -spectra contain strong-coupling artefacts like the conventional J -spectra, but they cancel to a large degree on projecting.

If we assume that the selective pulse is able to differentiate between the two multiplets, then the source of the strong-coupling artefacts will be the hard 180° in the middle of t_1 . It was shown in Section 3.3 that this pulse causes a mixing effect that transfers a coherence that is mainly present on spin one to a coherence that is mainly present on spin two. The result is that there is magnetization whose offset is *not* refocused by the spin echo, and which therefore produces multiplets that are not centred on $\omega_1 = 0$.

The results of the density matrix calculation of the conventional J -spectrum of a strongly-coupled two-spin system are given in Table 3.1. The artefacts are grouped into two multiplets, one of which is centred on $\omega_1 = +\frac{1}{2}C$, the other being centred on $\omega_1 = -\frac{1}{2}C$. The splitting between the two components in each dimension is $2\pi J_{12}$. The important feature of these multiplets is that the two components in each have intensities of *opposite* sign; the intensity of the positive peak is $\frac{1}{2}i \sin 2\theta(1 + \sin 2\theta)$, and the intensity of the negative peak is $\frac{1}{2}i \sin 2\theta(-1 + \sin 2\theta)$. As has been already noted, the components line up at the same ω_2 frequency in the sheared spectrum. So, when the spectrum is projected, there is a cancellation of the positive and negative peaks; the intensity of the artefact in the decoupled spectrum is $2i \sin^2 2\theta$. For modest strong coupling (first order in θ) the artefacts cancel completely, whilst for more extreme cases, a small positive artefact is observed as can be seen in Figure 5.16 (b). This cancellation is not observed for conventional J -spectra as the phase information is lost in the magnitude calculation, and so the intensity of the artefact in the decoupled spectrum is greater, as is seen in (a).

5.5 The absorption-mode J -spectrum of dehydroisoandrosterone

The second test of the new experiment was the more complicated spectrum of the steroid dehydroisoandrosterone in CDCl_3 . The conventional J -spectrum in Figure 3.8 and its projection in Figure 3.9 show that there are numerous strong-coupling

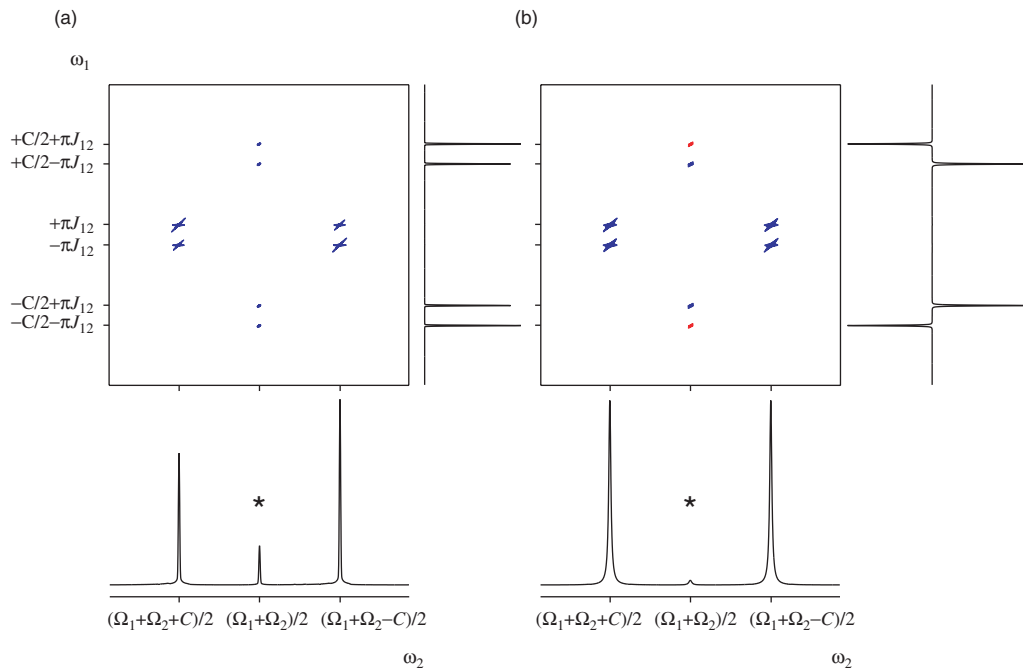


Figure 5.16: Simulated J -spectra of a strongly-coupled two-spin system. The conventional sheared magnitude spectrum is shown in (a), which has been processed with pseudo-echo weighting in both dimensions. The spectrum in (b) is in the absorption mode, and was simulated using the pulse sequences in Figure 5.10. To the right of each spectrum is shown the one-dimensional cross-section taken parallel to ω_1 through the strong coupling artefacts, i.e. the peaks at $\omega_2 = (\Omega_1 + \Omega_2)/2$. The projections are shown at the bottom, in which the artefacts are indicated with an *.

artefacts present. These artefacts are also present in the absorption-mode J -spectrum in Figure 5.17, although now they occur in pairs of opposite sign that lie at the same ω_2 frequency.

All experimental parameters regarding the spectral widths, acquisition times, number of increments, and the BIP are as given in Section 3.4. The selective pulse was a Gaussian of duration 57.6 ms, which was truncated at 1%; the accompanying gradient had a relative strength of 3%. The number of scans per increment was 44, giving a total experiment time of 1 day and 16 hours.

The projection of the sheared spectrum is shown in Figure 5.18 (b), with the conventional spectrum in (a) for comparison. The crowded regions of the spectra are shown in (c) and (d). The integrals in the projection are in good agreement with those in the normal spectrum.

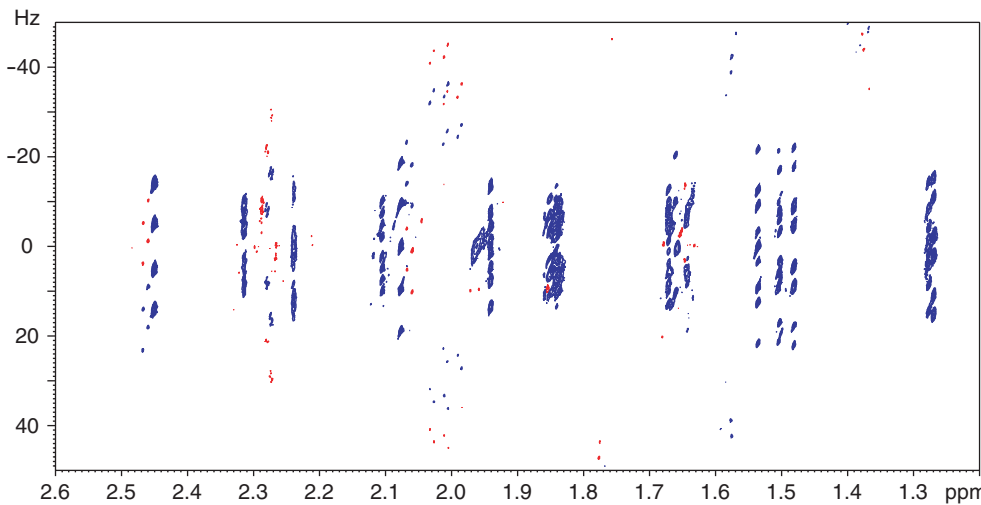


Figure 5.17: A region of the sheared absorption-mode J -spectrum of dehydroisoandrosterone. Note that the strong-coupling artefacts are in pairs of opposite sign that are lined up at the same ω_2 frequency.

The multiplets taken from the cross-sections are shown in Figure 5.19 (a)–(q). It can be seen that even in the crowded region, it is possible to obtain well-resolved multiplets.

5.6 Conclusion

The phase-twist lineshape is arguably the single most important factor that has limited the use of conventional J -spectroscopy, and so over the years a number of approaches has been taken with the aim of eliminating this lineshape [38–50]. It has been shown that the use of the Zangerer–Sterk pulse-sequence element in the standard pulse sequence makes it possible to record absorption-mode spectra with natural intensities [83].

The second problem that has long bedevilled conventional J -spectroscopy is the presence of strong-coupling artefacts. These have long been accepted as a ‘fact of life’ with the result that comparatively little effort has been invested in trying to suppress them. However, it was recently shown that they can be suppressed at the cost of an increase in experiment time and complexity, or a reduction in sensitivity [8]. In addition, if such methods are used, the pulse sequence cannot be modified to give absorption-mode lineshapes. The use of the Zangerer–Sterk element does not suppress

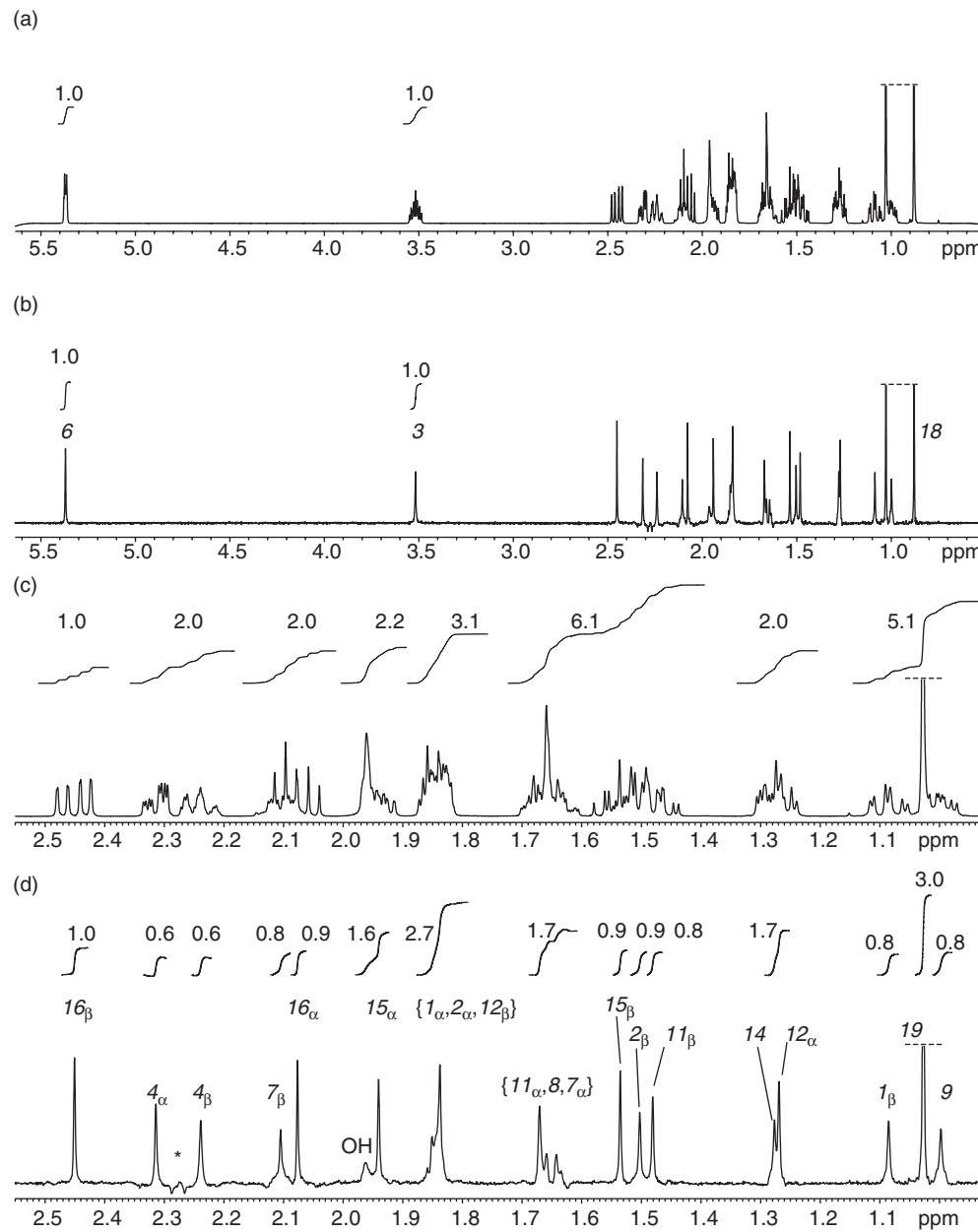


Figure 5.18: The conventional spectrum and projection of the absorption-mode J -spectrum of dehydroisoandrosterone. In (a) is shown the conventional spectrum of the full chemical shift range. The projection of the J -spectrum of the same region is shown in (b). Expansions of the crowded region of the normal and decoupled spectra are shown in (c) and (d). In the projection (d), the * indicates the position of a residual strong-coupling artefact. The assignment in (b) and (d) corresponds to the atom numbering in Figure 3.7.

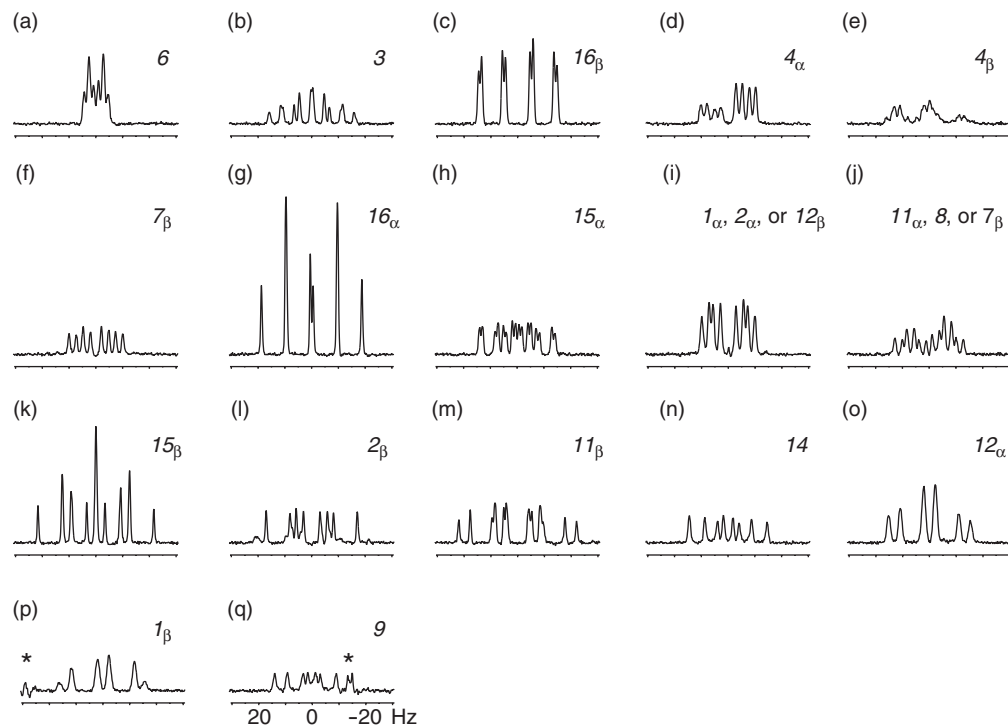


Figure 5.19: The cross sections taken from the spectrum in Figure 5.17 parallel to ω_1 . The assignment of each multiplet is given. The positions indicated by the * in (p) and (q) show disturbances due to the t_1 noise from the neighbouring methyl group.

the artefacts, but because the spectrum is now phase sensitive the unwanted peaks largely cancel on calculating the projection, giving a remarkably clean decoupled spectrum.

The price that must be paid for these improvements is a reduction in the sensitivity. However, the spectra are of such quality that this sensitivity reduction may be tolerable.

High-resolution heteronuclear correlation spectra using the Maximum Entropy Method

THE CONVENTIONAL METHOD for acquiring the increments in the indirect dimension of a two-dimensional NMR spectrum is uniform sampling. That is the value of t_1 is incremented by a constant amount, which is determined by the spectral width. The time-domain data are then processed by a Fourier transform in each dimension to give the two-dimensional spectrum. The disadvantage of uniform sampling is that it is very time-consuming to achieve a value of t_1^{\max} such that the data are not truncated. Very often the data in t_1 will be limited by sampling, leading to low resolution and sinc wiggles in the ω_1 dimension. The resolution that is attainable in a given experiment time can be increased by decreasing the ω_1 spectral width, as utilized in the work described in Chapter 4. However the resulting spectrum will fold in this dimension, and may therefore be impossible to interpret.

One solution to this problem, which was proposed many years ago, is to sample a subset of the required increments non-uniformly, so that the same t_1^{\max} is attained with fewer increments [85]. This method can be used to speed up acquisition considerably, but the data can no longer be processed with the conventional Fourier transform. We therefore apply an alternative processing algorithm that is referred to as the *Maximum Entropy Method* (MEM) [86–88]. A number of efficient maximum entropy processing algorithms have been developed [89–91] and applied to a variety of sparse sampling schemes [92]. However, the routine use of these methods has been limited partly because, unlike the Fourier transform, the MEM cannot be applied without significant input from the user.

Any situations to which the MEM is applied almost exclusively involve the processing of multi-dimensional NMR spectra of proteins. This study was aimed at ascertaining whether or not the maximum entropy processing of sparsely-sampled data introduces any significant benefits for the routine acquisition of two-dimensional spectra of small- to medium-sized molecules. Part of this involved determining under what situations the methodology works well and, just as importantly, when the ability to reconstruct the spectrum starts to break down.

The problem of limited sampling is exacerbated in single- and multiple-bond heteronuclear correlation spectra as the indirect dimension, which contains the spectrum of the heteronucleus, has a spectral width that is much larger than in the proton dimension. It was therefore decided to investigate the benefits and limitations of maximum entropy reconstruction of such spectra whose time domains have been sparsely sampled. There are two different pulse sequences that are commonly used to acquire a single-bond correlation. The choice of which experiment to use was made based on which spectrum has the highest intrinsic resolution in ω_1 ; how this choice was made is described in Section 6.1. The effect of the SNR in the time domain on the ability of the MEM to reconstruct the spectrum was also investigated. The methodology was then applied to multiple-bond correlation spectra.

The sampling scheme that is used can have a dramatic effect on the resolution, sensitivity, and the presence of any spectral artefacts. Therefore different schemes were employed to find an optimum sampling strategy. One aspect that is of interest is the minimum number of increments that can be sampled before spectrum degrades to point where it is no longer usable. With the single-bond correlations, it was found that the number of acquired increments can be reduced dramatically, by up to a factor of sixteen, without severely compromising the quality of the spectrum; this is due to the spectra being comparatively uncrowded. On the other hand multiple-bond correlation spectra are more complicated, and so pose a more difficult challenge. The specific algorithm that was used for the reconstruction of the spectra was the “Cambridge” algorithm [91], which is used by the Department of Biochemistry at the University of Cambridge for the processing of multi-dimensional spectra of proteins.

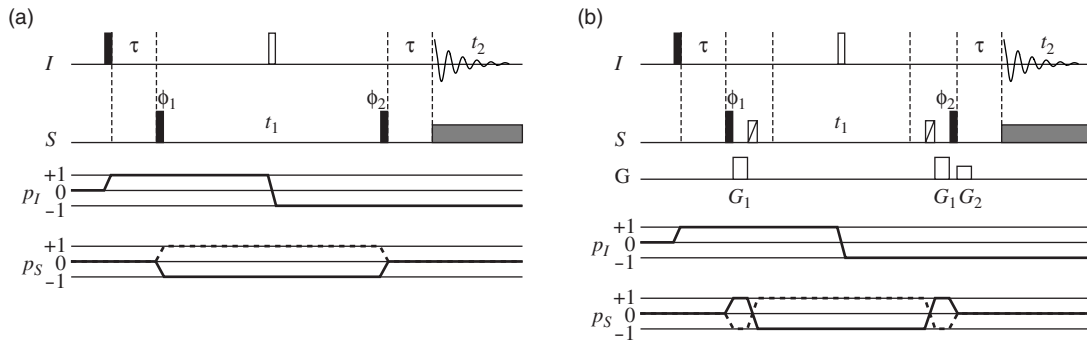


Figure 6.1: Pulse sequences and CTPs used for recording an HMQC. The basic sequence is shown in (a), where the grey rectangle on the S channel represents broadband heteronuclear decoupling. The sequence in (b) includes gradients to select the CTPs. For both sequences, the CTP for the S spin is indicated by the dashed line for the N-type experiment, and by the solid line for the P-type experiment. The following phase cycle is used: $\phi_1 = [0, \pi, 0, \pi]$, $\phi_2 = [0, 0, \pi, \pi]$, and $\phi_{\text{rec}} = [0, \pi, \pi, 0]$. See text for details about the gradient strengths.

6.1 Single-bond correlation experiments

A single-bond correlation experiment produces a spectrum in which the cross peaks indicate the presence of a bond between a proton and a heteronucleus. Such experiments employ inverse detection, that is the proton coherences are detected during acquisition rather than those of the heteronucleus, so as to maximize the sensitivity. There are two such experiments that are commonly used to aid the assignment of the spectra of small- to medium-sized molecules. These are the *heteronuclear multiple-quantum correlation* (HMQC) experiment [93] and the *heteronuclear single-quantum correlation* (HSQC) experiment [94]. Both sequences are analyzed in this Section to determine which has the highest intrinsic resolution in ω_1 , and therefore would benefit most from sparse sampling and maximum entropy reconstruction. The proton, which has a relatively high value of γ and 100% natural abundance, is represented by the I spin and the low- γ , low abundance heteronucleus is represented by the S spin.

6.1.1 HMQC of a two-spin system

The pulse sequence for the basic HMQC experiment is shown in Figure 6.1 (a), with the required CTPs for both the I spin and S spin. The pulse sequence will be analyzed initially for a system comprising a single I spin coupled to a single S spin.

The first 90° pulse rotates \hat{I}_z to $-\hat{I}_y$. This operator then evolves during the delay τ

under the free-precession Hamiltonian $\hat{\mathcal{H}}_{\text{free}}$, which is given by

$$\hat{\mathcal{H}}_{\text{free}} = \Omega_I \hat{I}_z + \Omega_S \hat{S}_z + 2\pi J_{IS} \hat{I}_z \hat{S}_z,$$

where Ω_I is the I -spin offset, Ω_S is the offset of the S spin, and J_{IS} is the one-bond heteronuclear coupling constant. The calculation can be simplified considerably by noting that the sequence of $\tau - t_1/2 - 180^\circ - t_1/2 - \tau$ on the I -spin channel is a spin echo; the evolution of the I -spin offset is therefore refocused at the start of acquisition, and so can be ignored. Therefore, during the delays τ , we need only consider the J -modulation.

Evolution of the coupling during τ gives the following mixture of in-phase and anti-phase terms:

$$-\hat{I}_y \cos(\pi J_{IS} \tau) + 2\hat{I}_x \hat{S}_z \sin(\pi J_{IS} \tau). \quad (6.1)$$

We now apply the first S -spin pulse. The in-phase term is unaffected, and is removed by the phase cycle. The anti-phase term, however, is transformed into a mixture of heteronuclear ZQ and DQ coherences:

$$-2\hat{I}_x \hat{S}_y \sin(\pi J_{IS} \tau).$$

We now need to consider the evolution during t_1 . This period is a spin echo, in which the 180° pulse is applied only to the I spins. The heteronuclear coupling is therefore refocused and so we need only consider the evolution of the S -spin offset, which gives

$$-2\hat{I}_x \hat{S}_y \sin(\pi J_{IS} \tau) \cos(\Omega_S t_1) + 2\hat{I}_x \hat{S}_x \sin(\pi J_{IS} \tau) \sin(\Omega_S t_1).$$

The second S -spin pulse is needed to rotate the transverse S -spin magnetization back to the z -axis. Only one observable term is produced, which is

$$-2\hat{I}_x \hat{S}_z \sin(\pi J_{IS} \tau) \cos(\Omega_S t_1).$$

Finally, this term evolves during the second delay τ to give the following at the beginning of t_2 :

$$-2\hat{I}_x \hat{S}_z \sin(\pi J_{IS} \tau) \cos(\pi J_{IS} \tau) \cos(\Omega_S t_1) - \hat{I}_y \sin^2(\pi J_{IS} \tau) \cos(\Omega_S t_1). \quad (6.2)$$

It is usual to employ broadband decoupling on the S spins during the acquisition period. This effectively removes the coupling term in the Hamiltonian, and therefore

the heteronuclear splitting is removed from the ω_2 dimension. As well as simplifying the multiplet structure of the in-phase term, the anti-phase term in Equation 6.2 is collapsed to zero, thus removing the phase distortion that would otherwise be present in ω_2 . In addition, collapsing the two components of the in-phase doublet onto each other gives an increase in the SNR. The final result is

$$-\hat{I}_y \sin^2(\pi J_{IS} \tau) \cos(\Omega_S t_1). \quad (6.3)$$

Under conditions of broadband decoupling, we therefore observe a single peak that is located at $(\omega_1, \omega_2) = (\Omega_S, \Omega_I)$.

The intensity of the signal is proportional to $\sin^2(\pi J_{IS} \tau)$. We need to maximize this factor in order to obtain the optimum sensitivity, which is done by setting $\tau = 1/(2J_{IS})$. This can be done across the spectrum very easily as the range of one-bond heteronuclear coupling constants is usually small compared to their magnitude. For example, the one-bond ^{13}C – ^1H coupling constants lie in the range 120–180 Hz.

Suppression of unwanted signals

In the HMQC experiment, the coherences that are detected during t_2 are present on the I spin, which has a natural abundance of 100%. However, the signal is only acquired from the fraction of the molecules that contain the NMR-active S spin; this fraction is 1.1% in the case of ^{13}C . It is therefore essential that we suppress the much larger signal arising from molecules that do not contain the S spin. This can be done by using either phase cycling, or PFG selection methods.

The phase cycle utilizes the fact that any magnetization from the I spins that are not coupled to the S spins will be independent of the phase of the S -spin pulses. Therefore, the experiment is recorded twice and the phase of one of the S -spin 90° pulses is inverted for the second scan; the second dataset is then subtracted from the first. The required signal adds up, whereas the unwanted signal cancels. The resulting phase cycle is given in the caption to Figure 6.1. The principle problem with this method is that the unwanted signal is much greater than the required signal, by a factor of 100 in the case of ^{13}C . In practice, it can prove difficult to obtain a clean subtraction.

A better degree of suppression can be achieved by inserting three PFGs into the sequence, as is shown in Figure 6.1 (b) [95]. The values of the gradients, G_1 and G_2 , are set to select the required CTPs. Any other signal, including that which arises from

I spins that are not coupled to S spins, is dephased in a single scan.

It should be noted that the spin system evolves under the free-precession Hamiltonian during the PFGs, and so the gradients should be introduced in such a way that no offset-dependent phase errors are acquired by the wanted coherences. One way of doing this is to incorporate the PFG as part of a spin echo, which is the method used for both the gradients with strength G_1 . One half of the echo contains the PFG, whilst the other half is a delay of equal duration. The 180° pulse on the S spins therefore refocuses the z -independent part of the S -spin offset and the heteronuclear coupling. The gradient G_2 , on the other hand, is included within an existing delay, and so the evolution during this PFG does not generate any phase errors.

The values of the gradients can be calculated from Equation 2.7. Assuming that both gradients have the same duration and shape factor, the refocusing condition for the N-type experiment is

$$(\gamma_I - \gamma_S)G_1 - (\gamma_I + \gamma_S)G_1 - \gamma_I G_2 = 0,$$

which simplifies to

$$\frac{G_1}{G_2} = -\frac{\gamma_I}{2\gamma_S}.$$

A second set of values is needed for the P-type experiment; these values are given by

$$\frac{G_1}{G_2} = +\frac{\gamma_I}{2\gamma_S}.$$

6.1.2 HSQC of a two-spin system

The pulse sequence of the HSQC experiment is very different to the HMQC sequence but, for a two-spin heteronuclear system, produces an identical spectrum. The sequence, which is shown in Figure 6.2 (a), will be analyzed in this Section.

The first 90° pulse rotates \hat{I}_z to $-\hat{I}_y$. During the subsequent spin echo the I -spin offset is refocused, but the heteronuclear coupling evolves throughout to give

$$\hat{I}_y \cos(2\pi J_{IS}\tau) - 2\hat{I}_x \hat{S}_z \sin(2\pi J_{IS}\tau).$$

There is now a sequence of a $90^\circ(y)$ pulse applied to I and a $90^\circ(x)$ pulse applied to S , which transfers the coherence from I to S . The in-phase operator is rotated onto z by the I pulse. It is removed by the phase cycle and so will henceforth be ignored. The anti-phase term, on the other hand, is transformed to

$$-2\hat{I}_z \hat{S}_y \sin(2\pi J_{IS}\tau).$$

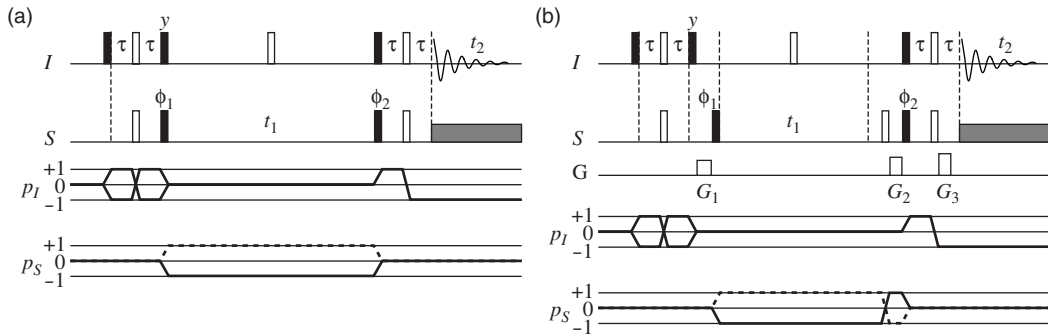


Figure 6.2: Pulse sequences and CTPs used for recording an HSQC. The basic sequence is shown in (a). The sequence in (b) includes gradients to select the CTPs. The following phase cycle is used: $\phi_1 = [0, \pi, 0, \pi]$, $\phi_2 = [0, 0, \pi, \pi]$, and $\phi_{\text{rec}} = [0, \pi, \pi, 0]$. See text for details about the gradient strengths.

As is the case with the HMQC experiment, the spin echo during t_1 refocuses the coupling, and so only the S -spin offset evolves. The density operator at the end of the evolution period is therefore

$$2\hat{I}_z\hat{S}_y \sin(2\pi J_{IS}\tau) \cos(\Omega_S t_1) - 2\hat{I}_z\hat{S}_x \sin(2\pi J_{IS}\tau) \sin(\Omega_S t_1).$$

The following pair of 90° pulses transfer the coherence back to the I spin. Only the first term gives rise to an observable operator, which is

$$-2\hat{I}_y\hat{S}_z \sin(2\pi J_{IS}\tau) \cos(\Omega_S t_1).$$

Finally, the coupling evolves during the spin echo to give

$$-2\hat{I}_y\hat{S}_z \sin(2\pi J_{IS}\tau) \cos(2\pi J_{IS}\tau) \cos(\Omega_S t_1) + \hat{I}_x \sin^2(2\pi J_{IS}\tau) \cos(\Omega_S t_1).$$

Once again, broadband heteronuclear decoupling is employed during the detection period and so, as is the case for the HMQC, we retain only the in-phase term:

$$\hat{I}_x \sin^2(2\pi J_{IS}\tau) \cos(\Omega_S t_1).$$

The spectrum is therefore identical to the HMQC spectrum in that there is a single peak at $(\omega_1, \omega_2) = (\Omega_S, \Omega_I)$. It is necessary to set the value of the delay τ so as to maximize the intensity of the detected signal. The optimal value is $\tau = 1/(4J_{IS})$.

Suppression of unwanted signals

As is the case with the HMQC, it is necessary to suppress the signals arising from I spins that are not coupled to S spins. Once again, this can be done by applying a two-step phase cycle to either of the S -spin 90° pulses in which both the pulse phase and receiver phase are inverted.

Alternatively, we can use gradient selection, as shown in Figure 6.2 (b) [95]. The first gradient G_1 acts as a homospoil, in that its sole purpose is to dephase any magnetization that is not aligned along z . After the $90^\circ(y)$ pulse that is applied to I , and before the first 90° pulse applied to S , the required term in the density operator expansion is $2\hat{I}_z\hat{S}_z \sin(2\pi J_{IS}\tau)$. This longitudinal two-spin order is unaffected by the gradient G_1 . On the other hand, any I -spin magnetization that is not coupled to S will be aligned along y after the first spin echo, and so will be unaffected by the $90^\circ(y)$ pulse. It is therefore dephased by the homospoil.

The presence of the gradients G_2 and G_3 ensure that any unwanted magnetization that is generated subsequently does not contribute to the signal. The required values are easily shown to be given by

$$\frac{G_2}{G_3} = -\frac{\gamma_I}{\gamma_S},$$

for the N-type experiment, and

$$\frac{G_2}{G_3} = +\frac{\gamma_I}{\gamma_S},$$

for the P-type experiment.

6.2 The effects of homonuclear coupling

In reality, the spin systems of the molecules that are studied by HMQC and HSQC experiments are more complicated than the simple heteronuclear spin pairs whose spectra have been calculated so far. One aspect in particular that has been ignored is the presence of couplings amongst the I spins. Therefore, we will now calculate the spectra of a spin system comprising two coupled I spins, I_1 and I_2 , the first of which is coupled to the S spin. This spin system is illustrated schematically in Figure 6.3.

6.2.1 HMQC of a three-spin system

The easiest way of including the effect of the evolution of the homonuclear coupling in the HMQC experiment is to note that, from the point of view of the I spins, the

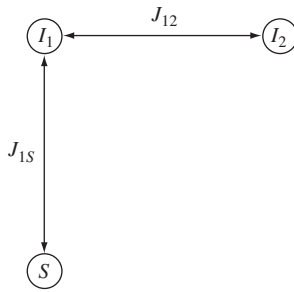


Figure 6.3: Illustration of the three-spin system used for the calculation of the HSQC and HMQC spectra in Section 6.2. The system comprises two I spins, I_1 and I_2 , and a single S spin. The couplings between them are indicated by the double-headed arrows.

pulse sequence is simply a spin echo. The coupling will therefore evolve throughout the sequence and is independent of the pulses applied to the S spin. Therefore, we can take the density operator that was calculated for the two-spin system at the beginning of t_2 , as given by Equation 6.2, and transform it under the Hamiltonian $2\pi J_{12}\hat{I}_{1z}\hat{I}_{2z}$. The density operator before the transformation is

$$-2\hat{I}_{1x}\hat{S}_z \cos(\pi J_{1S}\tau) \sin(\pi J_{1S}\tau) \cos(\Omega_S t_1) - \hat{I}_{1y} \sin^2(\pi J_{1S}\tau) \cos(\Omega_S t_1).$$

Including the evolution of the homonuclear coupling, we obtain

$$\begin{aligned} & -2\hat{I}_{1x}\hat{S}_z \cos(\pi J_{1S}\tau) \sin(\pi J_{1S}\tau) \cos(\Omega_S t_1) \cos(\pi J_{12}(2\tau + t_1)) \\ & - 4\hat{I}_{1y}\hat{I}_{2z}\hat{S}_z \cos(\pi J_{1S}\tau) \sin(\pi J_{1S}\tau) \cos(\Omega_S t_1) \sin(\pi J_{12}(2\tau + t_1)) \\ & - \hat{I}_{1y} \sin^2(\pi J_{1S}\tau) \cos(\Omega_S t_1) \cos(\pi J_{12}(2\tau + t_1)) \\ & + 2\hat{I}_{1x}\hat{I}_{2z} \sin^2(\pi J_{1S}\tau) \cos(\Omega_S t_1) \sin(\pi J_{12}(2\tau + t_1)). \end{aligned}$$

As before, the broadband decoupling that is applied during t_2 removes any terms that are anti-phase with respect to the I_1 - S coupling. This leaves

$$\begin{aligned} & - \hat{I}_{1y} \sin^2(\pi J_{1S}\tau) \cos(\Omega_S t_1) \cos(\pi J_{12}(2\tau + t_1)) \\ & + 2\hat{I}_{1x}\hat{I}_{2z} \sin^2(\pi J_{1S}\tau) \cos(\Omega_S t_1) \sin(\pi J_{12}(2\tau + t_1)). \end{aligned} \quad (6.4)$$

The multiplet structure

The easiest way to determine the form of the multiplet is to re-write Equation 6.4 in terms of the single-element basis operators. On setting $\tau = 1/(2J_{1S})$ we get the

following N-type spectrum:

$$\begin{aligned} & -\frac{1}{4}i \exp(+2i\pi J_{12}\tau) \exp(-i(\Omega_S - \pi J_{12})t_1) \hat{I}_{1-\hat{I}_{2\alpha}} \\ & -\frac{1}{4}i \exp(-2i\pi J_{12}\tau) \exp(-i(\Omega_S + \pi J_{12})t_1) \hat{I}_{1-\hat{I}_{2\beta}}, \end{aligned}$$

and the following P-type spectrum:

$$\begin{aligned} & -\frac{1}{4}i \exp(+2i\pi J_{12}\tau) \exp(+i(\Omega_S + \pi J_{12})t_1) \hat{I}_{1-\hat{I}_{2\alpha}} \\ & -\frac{1}{4}i \exp(-2i\pi J_{12}\tau) \exp(+i(\Omega_S - \pi J_{12})t_1) \hat{I}_{1-\hat{I}_{2\beta}}. \end{aligned}$$

The homonuclear coupling evolves throughout t_1 , and so it produces a splitting in the ω_1 dimension.

The details of the lineshapes can be worked out as follows. It can be seen that the ω_1 frequencies in the N-type spectrum are *not* equal to the negative corresponding frequencies in the P-type spectrum. Therefore, the dispersive components of the lineshapes will not cancel on combining the two spectra, and the final spectrum will contain the phase-twist lineshape. The two datasets do not combine properly because in both experiments the homonuclear coupling evolves to give the same sign of modulation during t_1 . This was expected since, as can be seen from Figure 6.1 (a), only a single I -spin CTP is acquired during t_1 .

Each peak also carries a phase error of $2\pi J_{12}\tau = \pi J_{12}/J_{1S}$ that is due to the evolution of the homonuclear J -coupling during the delays τ . However, this error is small as the one-bond heteronuclear coupling constants are usually large enough to satisfy $|J_{12}| / |J_{1S}| \ll 1$. The resulting multiplet is shown in Figure 6.4 (a).

6.2.2 HSQC of a three-spin system

Including the evolution of the homonuclear coupling throughout the HSQC experiment, the terms of the density operator that are in phase with respect to the I_1-S coupling at the start of t_2 are

$$\begin{aligned} & \hat{I}_{1x} \sin^2(2\pi J_{1S}\tau) \cos^2(2\pi J_{12}\tau) \cos(\Omega_S t_1) \\ & + 2\hat{I}_{1y}\hat{I}_{2z} \sin^2(2\pi J_{1S}\tau) \cos(2\pi J_{12}\tau) \sin(2\pi J_{12}\tau) \cos(\Omega_S t_1). \end{aligned} \quad (6.5)$$

The multiplet structure

It can be seen from Equation 6.5 that there is no splitting due to the homonuclear coupling in the ω_1 dimension. This is because the only operator that is present at the

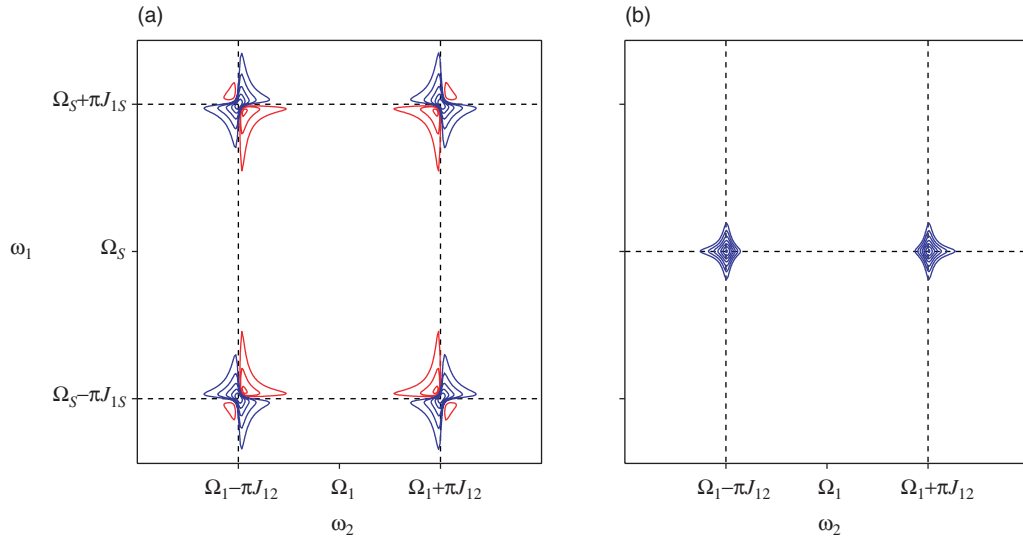


Figure 6.4: The multiplet structures in the I - S inverse correlation spectra of the three-spin system shown in Figure 6.3. The I_1 - S cross peak is shown in each. The HMQC spectrum is shown in (a), in which the multiplet is split by the I_1 - I_2 coupling constant in the ω_1 dimension. In addition, the N-type and P-type spectra do not combine properly, and so the final spectrum contains the phase-twist lineshape. The multiplet in (b) is taken from the HSQC spectrum. There is no splitting in the indirect dimension and, in the absence of phase errors, the peaks are in the absorption mode. In fact, in both spectra the peaks carry a phase error due to the evolution of the I_1 - I_2 coupling during the delays τ .

start of t_1 which produces observable signal during t_2 is

$$-2\hat{I}_{1z}\hat{S}_y \sin(2\pi J_{1S}\tau) \cos(2\pi J_{12}\tau).$$

This operator represents S -spin magnetization which does not evolve under the homonuclear coupling Hamiltonian $2\pi J_{12}\hat{I}_{1z}\hat{I}_{2z}$.

Expanding Equation 6.5 in terms of the single-element basis operators, we obtain the following N-type spectrum:

$$\begin{aligned} & \frac{1}{8} [1 + \exp(+4i\pi J_{12}\tau)] \exp(-i\Omega_S t_1) \hat{I}_{1-} \hat{I}_{2\alpha} \\ & + \frac{1}{8} [1 + \exp(-4i\pi J_{12}\tau)] \exp(-i\Omega_S t_1) \hat{I}_{1-} \hat{I}_{2\beta}, \end{aligned}$$

and the following P-type spectrum:

$$\begin{aligned} & \frac{1}{8} [1 + \exp(+4i\pi J_{12}\tau)] \exp(+i\Omega_S t_1) \hat{I}_{1-} \hat{I}_{2\alpha} \\ & + \frac{1}{8} [1 + \exp(-4i\pi J_{12}\tau)] \exp(+i\Omega_S t_1) \hat{I}_{1-} \hat{I}_{2\beta}. \end{aligned}$$

As is the case with the HMQC spectrum, there is a small phase factor that arises due to the evolution of the homonuclear coupling during the delays τ .

It can be seen that the P- and N-type spectra can be combined properly to eliminate the dispersive parts of the phase-twist lineshapes. The resulting multiplet is shown in Figure 6.4 (b).

6.2.3 Discussion

Part of the work described in this Chapter concerns the acquisition of a single-bond correlation spectrum with high resolution in the ω_1 dimension. In order to obtain the highest-possible resolution, it is obviously preferable to use the HSQC experiment, as the resolution is limited by the natural linewidth of the peak in the carbon spectrum. In contrast, the resolution in the HMQC is limited by both the size of the multiplet splitting in the ω_1 dimension, and the broadening introduced by the dispersive component of the lineshape. For these reasons, all the one-bond correlation spectra in this Chapter were recorded using the HSQC sequence.

6.3 Multiple-bond correlation experiments

Both the HMQC and HSQC sequences can be modified to obtain a heteronuclear correlation through multiple bonds. The principal change that is required is an increase in the value of τ , so as to allow the creation of a sufficient amount of anti-phase magnetization between the two coupled spins. In the case of the HMQC sequence, it was shown that the intensity of a cross-peak multiplet depends on the intensity factor $\sin(\pi J_{IS} \tau)$, which can be maximized by setting $\tau = 1/(2J_{IS})$. For a ^{13}C - ^1H correlation, a typical one-bond coupling constant is 140 Hz, which gives an optimal value of τ of 3.6 ms. By contrast, the multiple-bond coupling constants take values of up to only 20 Hz, and so we require τ to be an order of magnitude larger in order to obtain cross peaks of significant intensity. For example, a coupling constant of 10 Hz requires an optimal value of τ of 50 ms.

There are a number of additional issues arising from this experiment that must be addressed. Firstly, the larger value of τ increases the reduction in intensity due to transverse relaxation. For this reason, the second delay τ is usually omitted from the sequence, and the anti-phase signal is detected directly; no broadband decoupling is therefore used during t_2 . Secondly, the range of values of the long-range coupling

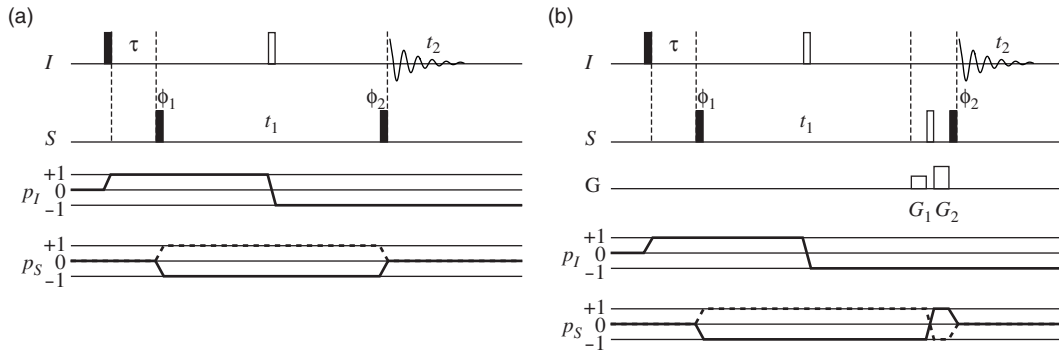


Figure 6.5: Pulse sequences and CTPs for recording an HMBC. The basic sequence is shown in (a), and the sequence in (b) includes gradients to select the CTPs. The following phase cycle is used: $\phi_1 = [0, \pi, 0, \pi]$, $\phi_2 = [0, 0, \pi, \pi]$, and $\phi_{\text{rec}} = [0, \pi, \pi, 0]$. See text for details about the gradient strengths.

constants, relative to the mean value, is much greater than for the one-bond coupling constants. Therefore no single value of τ will suffice and the peaks in the multiple-bond correlation will have a much larger range of intensities. It may be the case that some cross peaks are missing entirely. Furthermore, the peaks due to the single-bond correlations may also be present.

The basic pulse sequence that is based on the HMQC experiment is shown in Figure 6.5 (a). The resulting spectrum is referred to as a *heteronuclear multiple-bond correlation* (HMBC) [96].

6.3.1 HMBC of a two-spin system

The main difference between the sequence in Figure 6.5 (a) and Figure 6.1 (a) is that the I -spin offset is not refocused at the beginning of acquisition in the former, and so must be taken into account by the product operator calculation. Therefore in the HMBC experiment, the density operator at the end of the delay τ is

$$\begin{aligned} & -\hat{I}_y \cos(\Omega_I \tau) \cos(\pi J_{IS} \tau) + 2\hat{I}_x \hat{S}_z \cos(\Omega_I \tau) \sin(\pi J_{IS} \tau) \\ & + \hat{I}_x \sin(\Omega_I \tau) \cos(\pi J_{IS} \tau) + 2\hat{I}_y \hat{S}_z \sin(\Omega_I \tau) \sin(\pi J_{IS} \tau). \end{aligned}$$

The 90° pulse that is applied to the S spin now generates two multiple-quantum terms, one from each of the anti-phase terms above, which are given by

$$-2\hat{I}_x \hat{S}_y \cos(\Omega_I \tau) \sin(\pi J_{IS} \tau) - 2\hat{I}_y \hat{S}_y \sin(\Omega_I \tau) \sin(\pi J_{IS} \tau).$$

The offset of the I spin, and the heteronuclear J -coupling are refocused by the spin echo during t_1 . The operators therefore evolve only under the S -spin offset to give

$$\begin{aligned} & -2\hat{I}_x\hat{S}_y \cos(\Omega_I\tau) \sin(\pi J_{IS}\tau) \cos(\Omega_S t_1) + 2\hat{I}_x\hat{S}_x \cos(\Omega_I\tau) \sin(\pi J_{IS}\tau) \sin(\Omega_S t_1) \\ & + 2\hat{I}_y\hat{S}_y \sin(\Omega_I\tau) \sin(\pi J_{IS}\tau) \cos(\Omega_S t_1) - 2\hat{I}_y\hat{S}_x \sin(\Omega_I\tau) \sin(\pi J_{IS}\tau) \sin(\Omega_S t_1). \end{aligned}$$

Finally, the second 90° pulse applied to the S spin gives the following observable anti-phase terms:

$$-2\hat{I}_x\hat{S}_z \cos(\Omega_I\tau) \sin(\pi J_{IS}\tau) \cos(\Omega_S t_1) + 2\hat{I}_y\hat{S}_z \sin(\Omega_I\tau) \sin(\pi J_{IS}\tau) \cos(\Omega_S t_1). \quad (6.6)$$

Both terms are cosine-modulated during t_1 , and so the multiplet has the absorption-mode lineshape in the ω_1 dimension. However, the signal in t_2 is generated from two anti-phase terms that are 90° out of phase, the relative intensities of which are given by the factors $\cos(\Omega_I\tau)$ and $\sin(\Omega_I\tau)$. Therefore, the lineshape in the ω_2 dimension is a mixture of absorption and dispersion.

6.3.2 Suppression of unwanted signals using gradient selection

It is now necessary to include a set of gradient pulses which select the N-type and P-type CTPs, and dephase the magnetization due to I spins that are not coupled to S spins. Two such pulses, G_1 and G_2 , are added to the experiment to give the sequence in Figure 6.5 (b) [97]. They are included as part of a spin echo to refocus the evolution of the offset during the pulses. In the N-type experiment, the refocusing condition (for PFGs of equal durations) becomes

$$-(\gamma_I - \gamma_S)G_1 - (\gamma_I + \gamma_S)G_2 = 0,$$

and so the ratio of gradient strengths is

$$\frac{G_1}{G_2} = -\frac{\gamma_I + \gamma_S}{\gamma_I - \gamma_S}.$$

For the P-type experiment, the ratio is

$$\frac{G_1}{G_2} = -\frac{\gamma_I - \gamma_S}{\gamma_I + \gamma_S}.$$

6.3.3 HMBC of a three-spin system

The inclusion of a second I spin that is J -coupled to the first introduces the same problems into the HMBC spectrum as were discussed for the HMQC spectrum in Section 6.2.1. The multiplets are split in the ω_1 dimension by the homonuclear coupling, with the result that the N-type and P-type spectra are no longer equivalent.

The effects of the I_1 – I_2 coupling can be included by noting that the coupling will evolve throughout the sequence after the first 90° pulse; we therefore allow the operators in Equation 6.6 to evolve under the Hamiltonian $2\pi J_{12}\hat{I}_{1z}\hat{I}_{2z}$ during the delay $\tau + t_1$. The result is

$$\begin{aligned} & -2\hat{I}_{1x}\hat{S}_z \cos(\Omega_1\tau) \sin(\pi J_{1S}\tau) \cos(\pi J_{12}(\tau + t_1)) \cos(\Omega_S t_1) \\ & + 2\hat{I}_{1y}\hat{S}_z \sin(\Omega_1\tau) \sin(\pi J_{1S}\tau) \cos(\pi J_{12}(\tau + t_1)) \cos(\Omega_S t_1) \\ & - 4\hat{I}_{1y}\hat{I}_{2z}\hat{S}_z \cos(\Omega_1\tau) \sin(\pi J_{1S}\tau) \sin(\pi J_{12}(\tau + t_1)) \cos(\Omega_S t_1) \\ & - 4\hat{I}_{1x}\hat{I}_{2z}\hat{S}_z \sin(\Omega_1\tau) \sin(\pi J_{1S}\tau) \sin(\pi J_{12}(\tau + t_1)) \cos(\Omega_S t_1). \end{aligned}$$

The multiplet thus has a very complex splitting pattern in ω_2 , which is a superposition of four terms. These four terms form all possible combinations of in-phase or anti-phase splittings with respect to the homonuclear coupling, with the absorption and dispersion mode lineshapes.

6.4 Sparse sampling

For a given two-dimensional sequence, the experiment time is proportional to the number of t_1 increments that are recorded. In principle, the minimum experiment time is dictated by the number of increments that is required to obtain a value of t_1^{\max} that gives adequate resolution in the ω_1 dimension. In most practical situations, however, the available time is not sufficient to attain this goal and it is necessary to strike a compromise which results in the data being truncated.

For example, in a ^{13}C – ^1H correlation spectrum, a typical spectral width in the indirect (carbon) dimension is 18.75 kHz (150 ppm at 500 MHz for protons), which gives a Δt_1 of 53.3 μs . Therefore, 1875 increments are required to obtain a modest t_1^{\max} of 0.1 s if we employ uniform sampling of the time domain. If we record four scans per increment, each taking 10 s, and acquire separate N-type and P-type spectra, the total experiment time is approximately 55.5 hours.

It would therefore be advantageous to record fewer increments, but still acquire the data out to the same value of t_1^{\max} , thus obtaining the same resolution. This can be done by recording a subset of the increments in a non-uniform manner, which is a process that is referred to as sparse sampling. All of the spectra presented in this Chapter employ sparse sampling in the indirect dimension only.

6.4.1 On-grid and off-grid schemes

There are a number of sparse-sampling schemes that have been proposed for experiments that contain one or more frequency dimensions [92]. They can be divided into two groups, which are referred to as “off-grid” and “on-grid”. The term “on-grid” describes a sampling scheme in which the increments that are recorded correspond to values of t_1 which would be sampled by uniform sampling, whereas “off-grid” refers to the sampling of increments that do not. However, any off-grid scheme can be approximated by an on-grid scheme. All the sampling techniques described in this Chapter are on-grid, since this is a requirement for the method used to process the data, as described in Section 6.5.1.

6.4.2 Sensitivity of spectra constructed from sparsely-sampled data

Sparse sampling of the time domain produces a spectrum which has a lower SNR than the spectrum that would be obtained by uniform sampling out to the same maximum value of t_1 [92]. This observation can be rationalized by utilizing the expression for the SNR of a two-dimensional Fourier transform spectrum in Equation 1.34. The use of sparse sampling of the increments can be introduced by applying a weighting function $w(t_1, t_2)$ to the uniformly-sampled data. The weighting function is equal to one for the increments that are sampled and zero otherwise. The ratio of the SNRs of the two spectra is given by

$$\frac{\text{SNR(sparse)}}{\text{SNR(regular)}} = \frac{\overline{sw}}{\overline{s}(\overline{w^2})^{\frac{1}{2}}},$$

where the value of $\overline{w^2}$ is equal to the fraction of increments that is sampled. For data that have not decayed to within the level of the noise by t_1^{\max} , this fraction is always less than one which is as expected since sparse sampling has the effect of reducing the ‘volume’ of signal that is acquired in the time domain [98].

The details of how the sensitivity of the spectrum is affected depend upon the specific choice of sampling scheme. For instance, it is expected that if a large

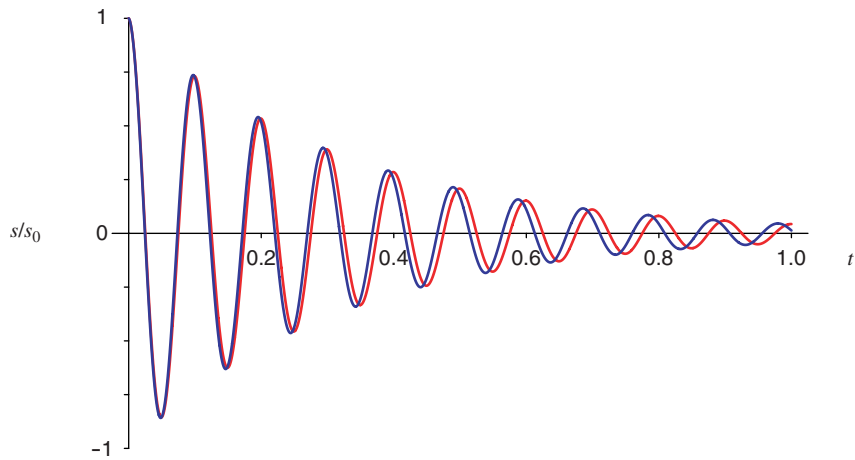


Figure 6.6: Two decaying cosine waves with similar frequencies. The red curve oscillates at 10 Hz, while the blue curve has a frequency of 10.2 Hz. Note that the two components are more easily distinguished at longer evolution times. Both components have the same decay time constant of $T_2 = 1/\pi$ s.

proportion of the selected increments correspond to a high intensity of the decay envelope, the sensitivity loss will be mitigated to a certain extent. By contrast if we select increments for which the envelope is of low intensity, the final spectrum will have lower sensitivity.

6.4.3 Resolution of spectra constructed from sparsely-sampled data

In order to be able to resolve two neighbouring peaks in the spectrum, it is necessary to be able to differentiate between the two corresponding components in the time domain. Figure 6.6 shows two decaying cosine functions with similar frequencies. Evidently, it is easier to distinguish between the two at longer evolution times. If we only sample increments at low values of t_1 it is harder to differentiate between similar frequencies, and we will obtain a spectrum with low resolution as is observed with truncated data. This suggests that the resolution can be increased by adopting a sparse sampling scheme that acquires a greater proportion of the increments at larger values of t_1 . However, the extent to which the maximum value of t_1 can be increased is limited by the rate of decay of the time-domain data. Components with a short T_2 may decay to within the level of the noise before they can be separated. Therefore, continuing to extend t_1 after the signal has decayed will only have the effect of acquiring a greater amount of noise, thus reducing the sensitivity.

6.4.4 Sampling schemes

The discussions in sections 6.4.2 and 6.4.3 have important consequences for the choice of sampling scheme. If the experiment produces data that decays exponentially in t_1 then it is apparent that the method of sampling that is chosen cannot optimize both the sensitivity and resolution simultaneously. The highest sensitivity will be obtained by sampling a large proportion of the increments at short evolution times, whereas it is expected that sampling many increments at long times will give better resolution. In addition, it should be noted that the exclusion of a proportion of the data has the effect of introducing so-called ‘sampling artefacts’ into the spectrum, the number and size of which can be reduced by the proper design of the scheme.

In order to calculate the increments that are selected by a particular method, we will refer to a ‘master’ dataset in which M_1 increments are sampled using uniform sampling. These increments are labelled using an index $i = 1, 2, 3, \dots, M_1$. The number of increments that are thus recorded provides the required resolution. Using the sparse-sampling method of acquisition, the same FID can be acquired with a smaller number of increments m_1 that are labelled with an index $j = 1, 2, 3, \dots, m_1$. This label corresponds simply to the order in which the increments are acquired. Of course, each of the second set of increments retains the label i that corresponds to the position of each increment in the master dataset.

Exponential sampling

A good compromise between sensitivity and resolution can be obtained by attempting to match the sampling scheme to the decay envelope of the time-domain data. For a signal that decays exponentially in t_1 , a suitable form of sampling is a scheme in which the density of the increments in the time domain decreases exponentially with increasing t_1 . This is referred to as exponential sampling, and was first proposed by Barna *et al* [85]. Most of the increments are acquired at small values of t_1 , which is supposed to give good sensitivity, with a small proportion acquired at larger times, which gives good resolution.

In order to obtain a dataset in which the m_1 increments are exponentially-sampled out to the same maximum time as the master dataset, the values of i that are selected are calculated according to

$$i = \text{floor} \{ \exp(\alpha(j - 1)) \} \quad \text{where} \quad \alpha = \frac{\ln(M_1)}{m_1 - 1}, \quad (6.7)$$

with the condition that neighbouring increments must have values of i that differ by at least one. The function $\text{floor}(x)$ gives the integer part of x .

Random sampling

There is an alternative sparse-sampling scheme that enables increments to be acquired with a more uniform sampling density. The increments to be recorded are selected at random from the master dataset. It has been shown that the use of such random selection can be useful for reducing the number and intensity of the sampling artefacts [99]. For example, if we wish to record half the increments of the master dataset, it is apparent that we cannot do so simply by recording every other increment. Such a strategy effectively halves the spectral width, and so the peaks in the spectrum will fold. However, the introduction of random ‘blurring’ in the selection of the increments removes this problem.

These methods of sparse-sampling are illustrated in Figure 6.7. Three sampling schemes are shown, in which a quarter of the increments is acquired. The uniform sampling method is shown in (a), in which the sampled increments have the lowest values of t_1 . This, of course, gives a dataset with a lower t_1^{\max} , and therefore lower resolution. The increments in (b) are selected by exponential sampling, using Equation 6.7. Finally, the scheme in (c) is pure random sampling.

In general, it is expected that exponential sampling will provide better sensitivity than random sampling, since a greater number of increments are sampled at lower values of t_1 where the signal intensity is highest. Conversely, random sampling will give rise to better resolution since a larger number of increments are sampled at longer times.

6.5 Spectral reconstruction from sparsely-sampled datasets

Time-domain data that have been sparsely sampled in the way that has been described in the previous Section cannot be processed with a conventional discrete Fourier transform. This is because the transform requires that the data are recorded with a regular sampling interval. Therefore an alternative processing algorithm is needed to construct the spectrum. The processing method that was used for producing the spectra in this Chapter is the Maximum Entropy Method (MEM) [86–88].

The principle of the MEM is to construct a series of spectra which are consistent

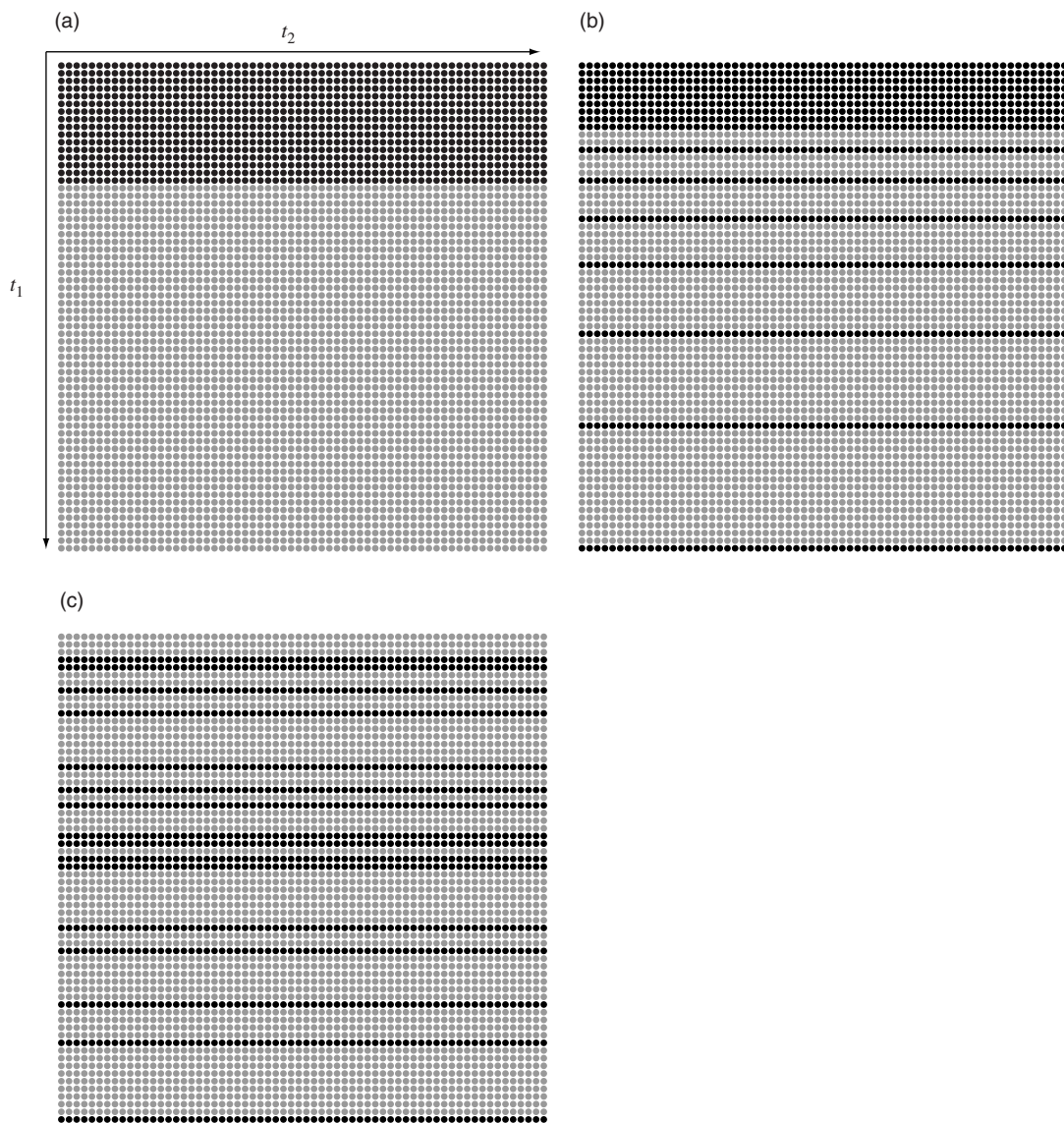


Figure 6.7: Sparse sampling schemes, in which a quarter of the increments are selected from the master dataset. Each data point in the master dataset is indicated by a circle, with each data point that is recorded using each scheme coloured black. Uniform sampling is shown in (a), in which the first quarter of the increments is acquired. Exponential sampling is shown in (b), and random sampling is shown in (c).

with the recorded time-domain data, and to select the spectrum which has the highest entropy. For the purposes of NMR the entropy can be viewed as a regularizing functional that produces spectra that do not contain artefacts for which there is no evidence in the time domain. Therefore maximizing the entropy gives the spectrum that contains the fewest artefacts, which is taken as being the ‘safest’ choice that is available. This feature of the MEM means that it is more likely to give spectra from which peaks are missing rather than include spurious artefacts, such as those that are introduced by the sparse-sampling scheme.

Another useful feature of the maximum entropy algorithm is that it does not make any assumptions about the form of the lineshapes in the reconstructed spectrum unlike, for example, the filter diagonalization method (FDM) which assumes that the FID is a sum of exponentially-decaying sinusoids [47, 48]. Therefore the MEM is able, in principle, to reconstruct a spectrum that contains arbitrary lineshapes.

6.5.1 The Maximum Entropy Method

An overview of the algorithm for maximum entropy reconstruction is as follows. The recorded time-domain data \mathbf{d} are taken to comprise m data points with intensities d_j , where $j = 1, 2, \dots, m$. These are used to construct a spectrum $\tilde{\mathbf{f}}$ that comprises N points, of which the intensities are \tilde{f}_k where $k = 1, 2, \dots, N$.

In the implementation of the MEM that was used for this work, the entropy S of the constructed spectrum is calculated using the following expression [91, 100]:

$$\begin{aligned} S &= \sum_{k=1}^N 2b \left[\sqrt{1 + \frac{\operatorname{Re}(\tilde{f}_k)^2}{4b^2}} - 1 - \frac{\operatorname{Re}(\tilde{f}_k)}{2b} \log \left(\frac{\operatorname{Re}(\tilde{f}_k)}{2b} + \sqrt{1 + \frac{\operatorname{Re}(\tilde{f}_k)^2}{4b^2}} \right) \right] \\ &\quad + \sum_{k=1}^N 2b \left[\sqrt{1 + \frac{\operatorname{Im}(\tilde{f}_k)^2}{4b^2}} - 1 - \frac{\operatorname{Im}(\tilde{f}_k)}{2b} \log \left(\frac{\operatorname{Im}(\tilde{f}_k)}{2b} + \sqrt{1 + \frac{\operatorname{Im}(\tilde{f}_k)^2}{4b^2}} \right) \right] \end{aligned}$$

where b is a scaling parameter. The entropy is maximized subject to the spectrum being consistent with the recorded data. This consistency is measured by computing the inverse Fourier transform to give a ‘mock’ time-domain dataset \mathbf{f} , which comprises the points f_j , and then calculating the following unweighted χ^2 statistic:

$$C = \sum_{j=1}^m |f_j - d_j|^2 .$$

It is in order to facilitate this comparison that the method of sparse sampling must follow an on-grid strategy. The spectrum is deemed to be consistent with the data when $C \leq C_0$, where C_0 is a threshold parameter that is estimated from the r.m.s. noise in the time-domain. This constrained optimization problem is transformed into an unconstrained optimization by the introduction of a Lagrange multiplier λ . We therefore maximize the value of Q , which is defined as

$$Q = S - \lambda C.$$

The algorithm is implemented as a numerical optimization in which a trial spectrum is iteratively improved, with a simultaneous change in the value of λ until the convergence criterion is satisfied. The initial spectrum is chosen to be flat, i.e. all the data points have the same intensity, which is given by the scaling factor b . There are three parameters which the user is able to vary: the scaling factor b , the estimate of the noise level (and hence the value of C_0), and the number of points N in the reconstructed spectrum. In the absence of the constraint the MEM produces a spectrum with the maximum possible entropy, in which all the data points \tilde{f}_k have zero intensity.

In addition to the ability to process sparsely-sampled data, the MEM enjoys a second advantage over the Fourier transform. If the signal in the time-domain is truncated, the application of the Fourier transform introduces sinc wiggles into the spectrum. These are troublesome as they tend to obscure genuine peaks of low intensity. It should be emphasized that they arise not because of the form of the time domain, but are due to the application of the Fourier transform. Therefore the MEM does not introduce them into the spectrum.

It should be noted that the SNR of the MEM spectrum is not a good indicator of the actual sensitivity. This is because any noise components in the time domain that have a lower intensity than the chosen threshold, as determined by C_0 , will have no effect on the algorithm, and so the SNR in the MEM spectrum will be artificially high. As we increase the value of C_0 , a greater proportion of the noise components are excluded, and we observe a corresponding increase in the SNR. However, any genuine signal components with intensities that are comparable to the noise level will also be discriminated against in the same way. Therefore, since the increase in the SNR does not allow us to better observe such signals, it cannot be claimed that it corresponds to an improvement in sensitivity.

It has been found that the intensities of the points in the MEM spectrum are scaled

down in comparison to those in the corresponding Fourier transform spectrum. This scaling is non-linear, in that low-intensity points are scaled down proportionally more than high-intensity values [101]. One consequence of this is that the noise near the baseline of the spectrum will be scaled down to a greater degree than the peaks whose intensities are much greater than the noise level. This is a second reason for the substantial increase in the apparent SNR. Once again, this does not correspond to an increase in sensitivity as the noise that is superimposed on the peaks is not scaled down by the same amount as the noise on the baseline. In addition low-intensity peaks are scaled down to a larger degree than high-intensity peaks, which gives a spectrum that is not quantitative.

6.5.2 Application of the MEM to two-dimensional spectra

All the sparse-sampling schemes that are used for two-dimensional experiments only apply sparse sampling to the t_1 dimension. This is because the data in the t_2 dimension are acquired in real time, and so are complete. It is necessary to acquire separate N-type and P-type data for each selected increment, so that the data can be processed to give absorption-mode lines and frequency discrimination.

The N-type and P-type datasets are processed as usual (including the Fourier transform in t_2) up until the Fourier transform in the t_1 dimension. The data now comprises a set of points whose intensities are given by the function $\exp(i\Omega^{(1)}t_1)\exp(-t_1/T_1^{(1)})\mathcal{A}_{\Omega^{(2)}}(\omega_2)$. The noise threshold level is estimated from this dataset, and then the maximum entropy algorithm is applied in the t_1 dimension.

6.6 HSQC of dehydroisoandrosterone

The use of the MEM in reconstructing an HSQC from sparsely-sampled data is illustrated with the spectrum of the steroid dehydroisoandrosterone in CDCl_3 . A master dataset was recorded using the pulse sequence in Figure 6.2 (b). The delay τ was optimized for a one-bond coupling of 145 Hz. The gradient strengths (relative to the maximum intensity) were $G_1 = 50\%$, $G_2 = 80\%$, and $G_3 = \mp 20.21\%$ where the minus sign is for the N-type experiment, and the plus sign is for the P-type experiment. All PFGs were shaped to a half-sine bell, and had durations of 1 ms. Four scans were acquired per increment, and four ‘dummy’ scans were performed at the beginning of the experiment in which no data were recorded. Decoupling during t_2 was achieved

with the GARP sequence with an RF field strength of 3.8 kHz [102].

The spectral widths in ω_1 and ω_2 are 18657 Hz and 2561 Hz respectively. The number of complex data points* acquired in t_2 was 4096, giving an acquisition time of 1.60 s in this dimension. The data in t_1 comprise 2048 increments that were sampled uniformly. The value of t_1^{\max} is therefore 0.11 s. The total experiment time for this acquisition was 1 day and 6 hours.

The spectrum of the master dataset was produced by a Fourier transform in both dimensions. The real part of the spectrum is composed of 8192 points in the ω_2 dimension, and 16384 points in ω_1 . Processing the data with a double Fourier transform required 30 s of CPU time. A region of this spectrum is shown in Figure 6.8, with the one-dimensional ^1H and broadband ^1H -decoupled ^{13}C spectra included along the top and right-hand side respectively. It can be seen that the time-domain in the t_1 dimension is truncated, resulting in the sinc wiggles running parallel to the ω_1 axis. Nevertheless, most of the multiplets in the two-dimensional spectrum are very well-resolved in ω_1 . However there is a part of the spectrum, shown in Figure 6.9, in which there are three ^{13}C resonances within a range of 20 Hz. Nevertheless, despite the linewidth in ω_1 being limited by the extent of the sampling, there is still a clear separation in the ω_1 dimension.

If the number of increments were reduced, and still sampled uniformly with the same value of Δt_1 , the linewidth would increase to the point where there is significant overlap in the ^{13}C dimension, and so sparse sampling combined with maximum entropy reconstruction was employed in an effort to reduce the experiment time and still obtain good resolution. Both exponential and random sampling strategies was used. In each case, the increments to be processed were extracted from the master dataset, and combined to form a smaller dataset; for each value of t_1 that was sampled, both the N-type and P-type increments were extracted and combined to give the cosine- and sine-modulated datasets as usual. Maximum entropy processing was performed using the Azara suite of programs provided by Wayne Boucher at the Department of Biochemistry in the University of Cambridge[†]. The specific implementation of the MEM code is the MemSys3 version of the “Cambridge” algorithm [91].

The resulting two-dimensional time-domain was processed with a Fourier trans-

*One complex point comprises one real and one imaginary point.

[†]The source code may be obtained by anonymous ftp to <http://www.bio.cam.ac.uk> in the directory `ftp/pub/azara`.

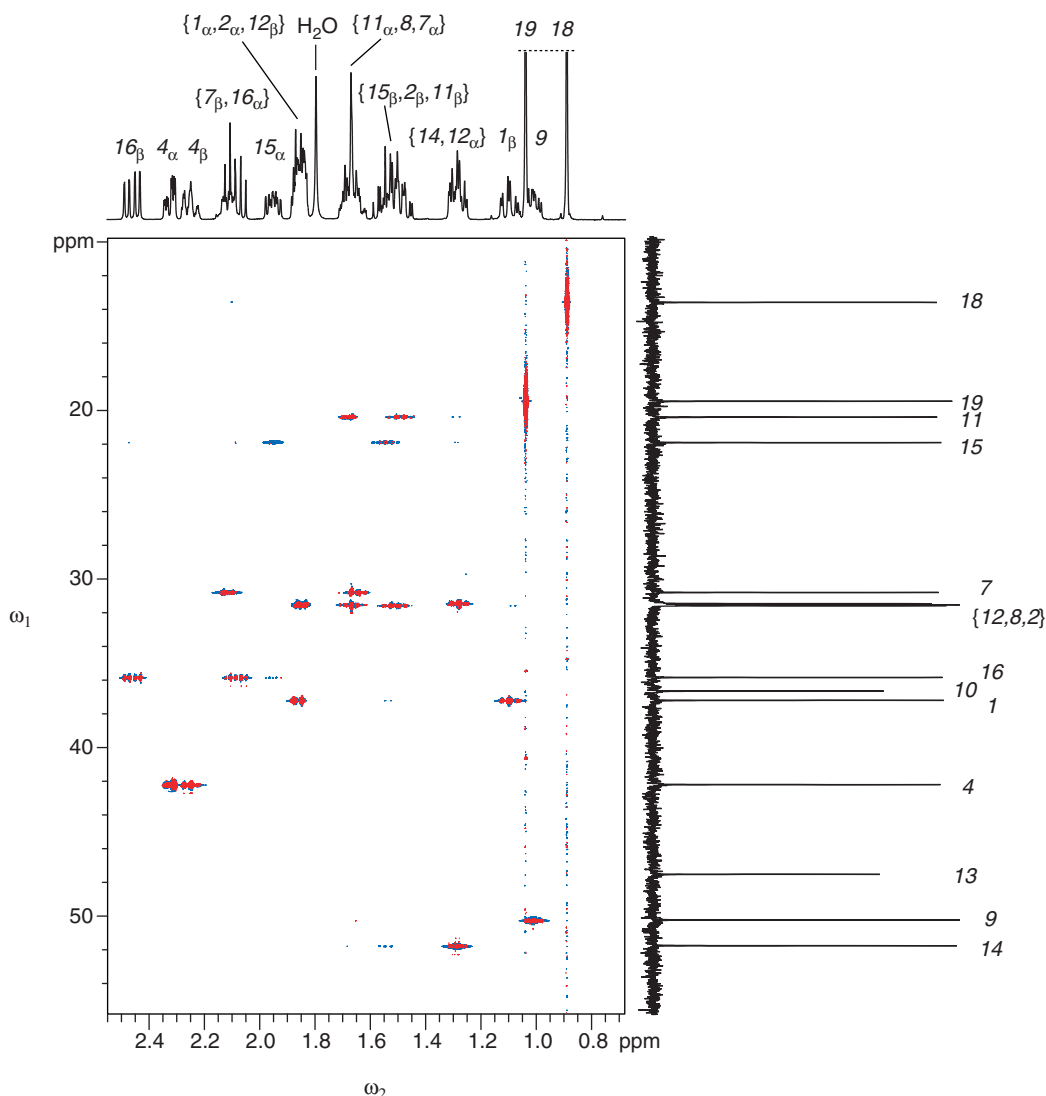


Figure 6.8: The HSQC of the steroid dehydroisoandrosterone. The spectrum was produced by a Fourier transform in both dimensions of the master dataset comprising 2048 increments. The ^{13}C dimension is along the vertical axis, and the ^1H dimension is along the horizontal: the conventional one-dimensional spectra are given as traces along the two axes, along with the assignment corresponding to the structure in Figure 3.7.

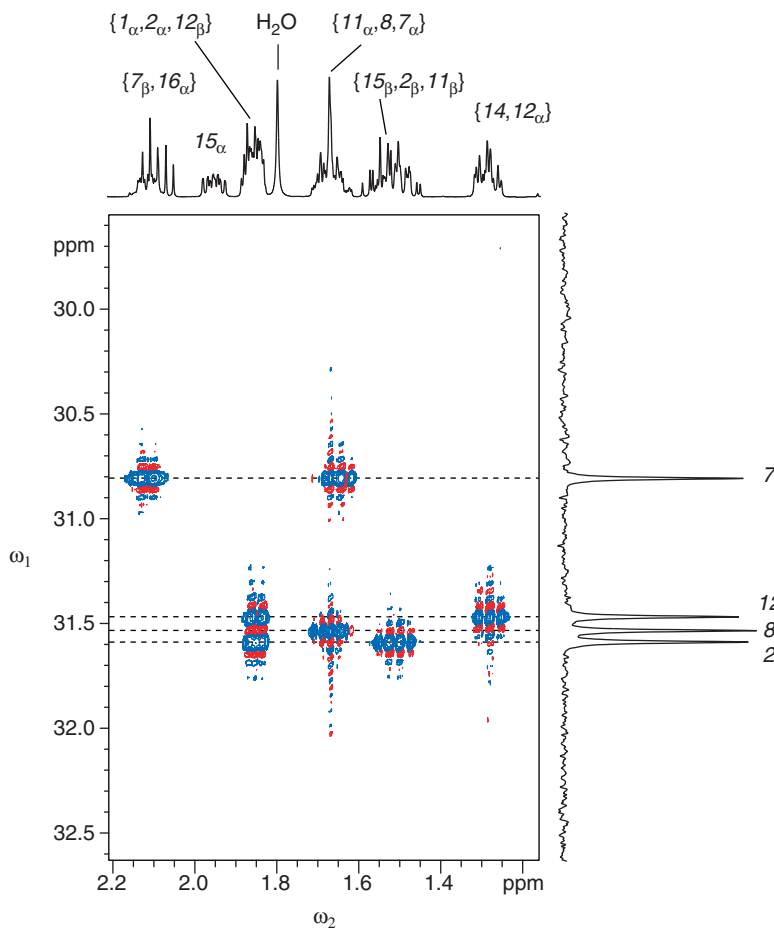


Figure 6.9: A region of the HSQC shown in Figure 6.8. The ^{13}C dimension contains three resonances that lie within a frequency range of 20 Hz.

form in t_2 using 8192 points in the ω_2 frequency dimension. Maximum entropy reconstruction was carried out in t_1 with the noise threshold level set to 0.7% of the intensity of the two methyl peaks in the first increment of the cosine-modulated dataset. The number of points in the ω_1 dimension was set to 16384. The required CPU time for complete processing of the data was 12 minutes, i.e. twenty-four times the time required for the double Fourier transform.

6.6.1 Exponential sampling

The increments were sampled exponentially out to the final increment in the master dataset (2048) using Equation 6.7. Datasets containing 1024, 512, 256, 128, 64, 32,

and 16 increments were produced in this way. The MEM spectrum of the master dataset is shown in Figure 6.10 (a). It is immediately apparent that, as expected, there is a significant reduction in the intensity of the sinc wiggles. The MEM spectra of the exponentially-sampled time-domains of (b) 1024, (c) 512, and (d) 256 increments are also shown. The remaining four spectra are shown in Figure 6.11, in which the number of increments is (a) 128, (b) 64, (c) 32, and (d) 16.

It can be seen that it is possible to reduce the number of recorded increments to as few as 128 without severely compromising the quality of the spectrum. This represents a substantial time saving as it is possible to obtain a high-resolution spectrum in under two hours rather than thirty. Any further reductions result in a rapid degradation of the quality of the spectrum in that genuine multiplets start to disappear, and extra artefacts are observed.

One reason for the lower intensities of the multiplets is that reducing the number of increments that are sampled causes a decrease in the sensitivity of the spectrum, as discussed in Section 6.4.3. This can be seen on examining the spectra that were processed with fewer than 128 increments. The effect is particularly pronounced for the resonances that are indicated by the box with the dashed border in Figure 6.11 (a). In addition the recorded time domain contains less information, and so the condition that the MEM spectrum is consistent with the recorded data becomes less restrictive. One consequence of this is that the spectral intensity in each cross-section parallel to ω_1 becomes more uniformly distributed, giving a greater number of low-intensity artefacts.

The crowded regions of the HSQC spectra are shown in Figure 6.12. The Fourier transform of all 2048 increments is shown in (a), and the MEM spectra are shown in (b)–(i). The MEM spectrum of the master dataset in (b) has a lower linewidth. On reducing the number of increments that are sampled it can be seen that there is an apparent reduction in the resolution. This is seen especially for the two multiplets with the ^1H chemical shift of 1.85 ppm (2_α and 12_β) which exhibit a greater degree of overlap on moving from (b) to (i). This is discussed more fully in the next Section.

6.6.2 Random sampling

The second method of sparse sampling that was employed was the random sampling of increments from the master dataset. Datasets containing 1024, 512, 256, 128, 64, 32, and 16 increments were constructed in this way. The MEM HSQC spectra are

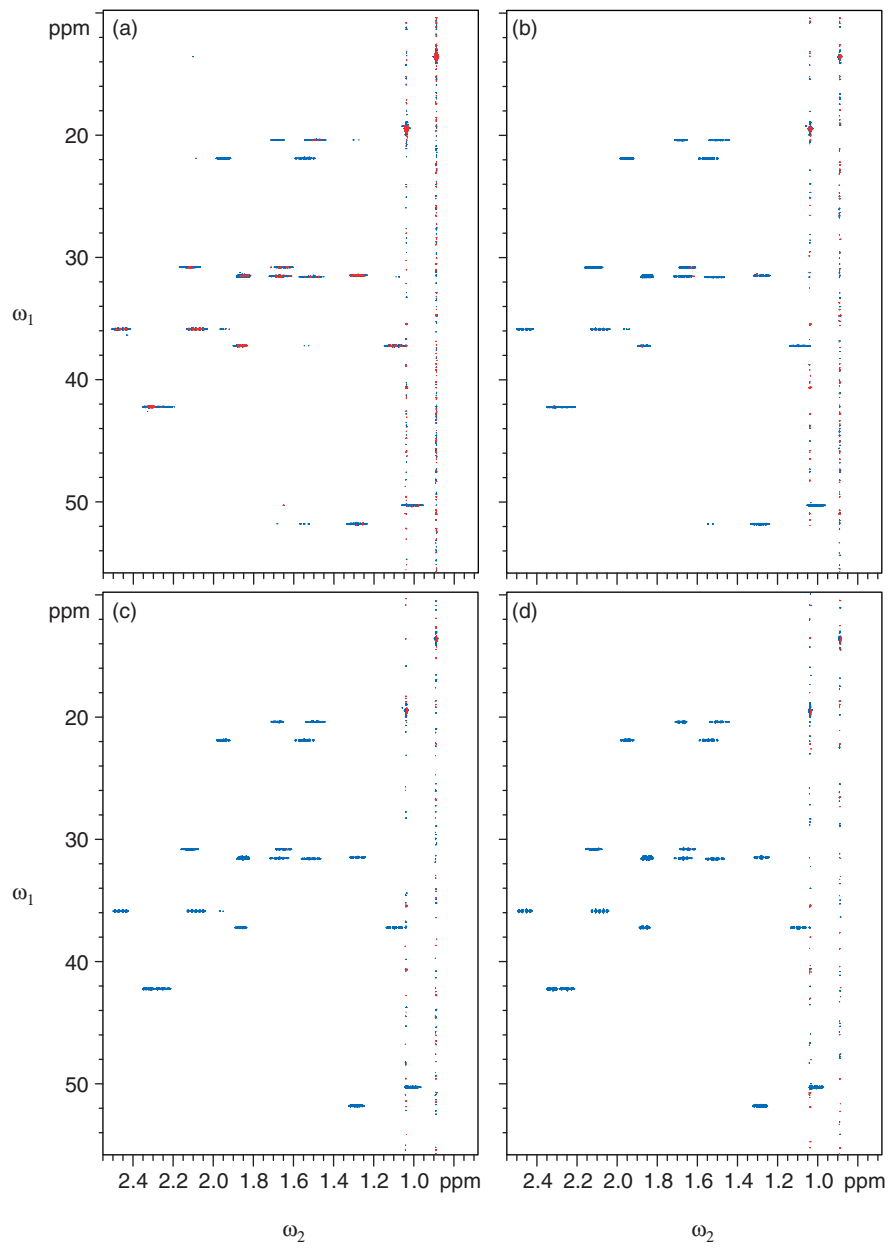


Figure 6.10: MEM HSQC spectra of the steroid in which the increments are sampled exponentially from the 2048 increments of the master dataset. The MEM spectrum of the master dataset is shown in (a). The other spectra were processed using the following number of increments: (b) 1024, (c) 512, and (d) 256.

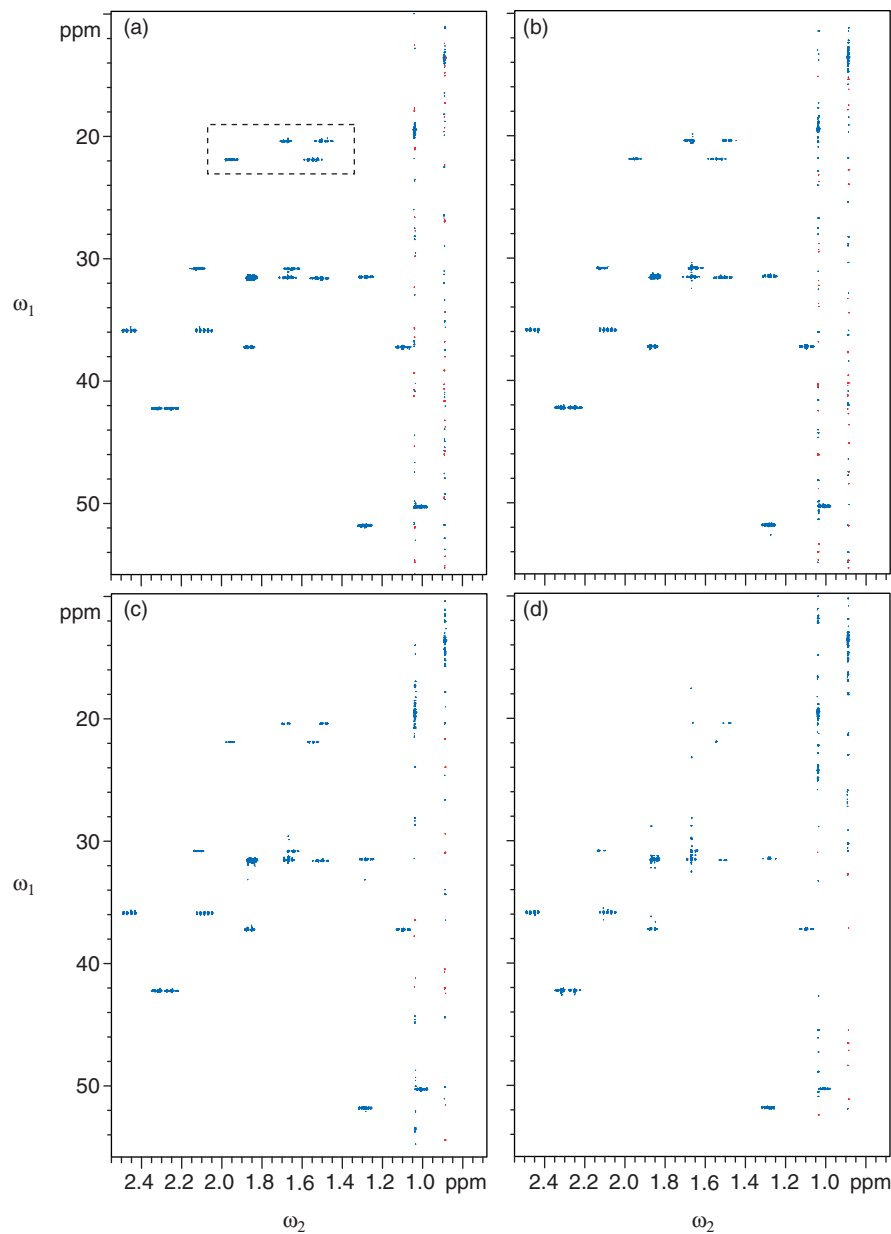


Figure 6.11: MEM HSQC spectra of the steroid in which the increments are sampled exponentially from the 2048 increments of the master dataset. The number of increments sampled is (a) 128, (b) 64, (c) 32, and (d) 16. The resonances that are surrounded by the dashed box exhibit a particularly pronounced loss of intensity on reducing the number of sampled increments.

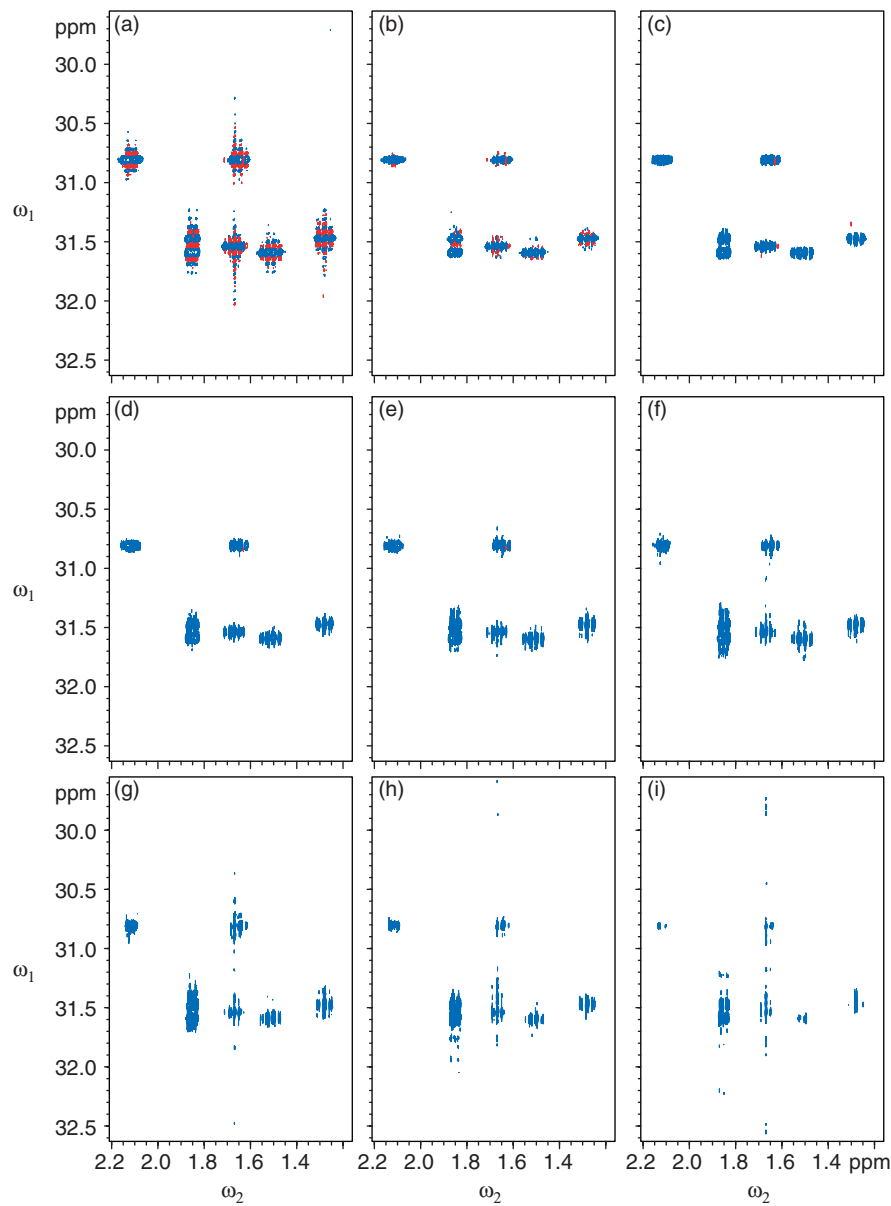


Figure 6.12: The crowded region of the HSQC spectrum of the steroid. The Fourier transform and MEM spectra of all 2048 increments are shown in (a) and (b). The remaining spectra are of exponentially-sampled datasets. The number of sampled increments is (c) 1024, (d) 512, (e) 256, (f) 128, (g) 64, (h) 32, and (i) 16.

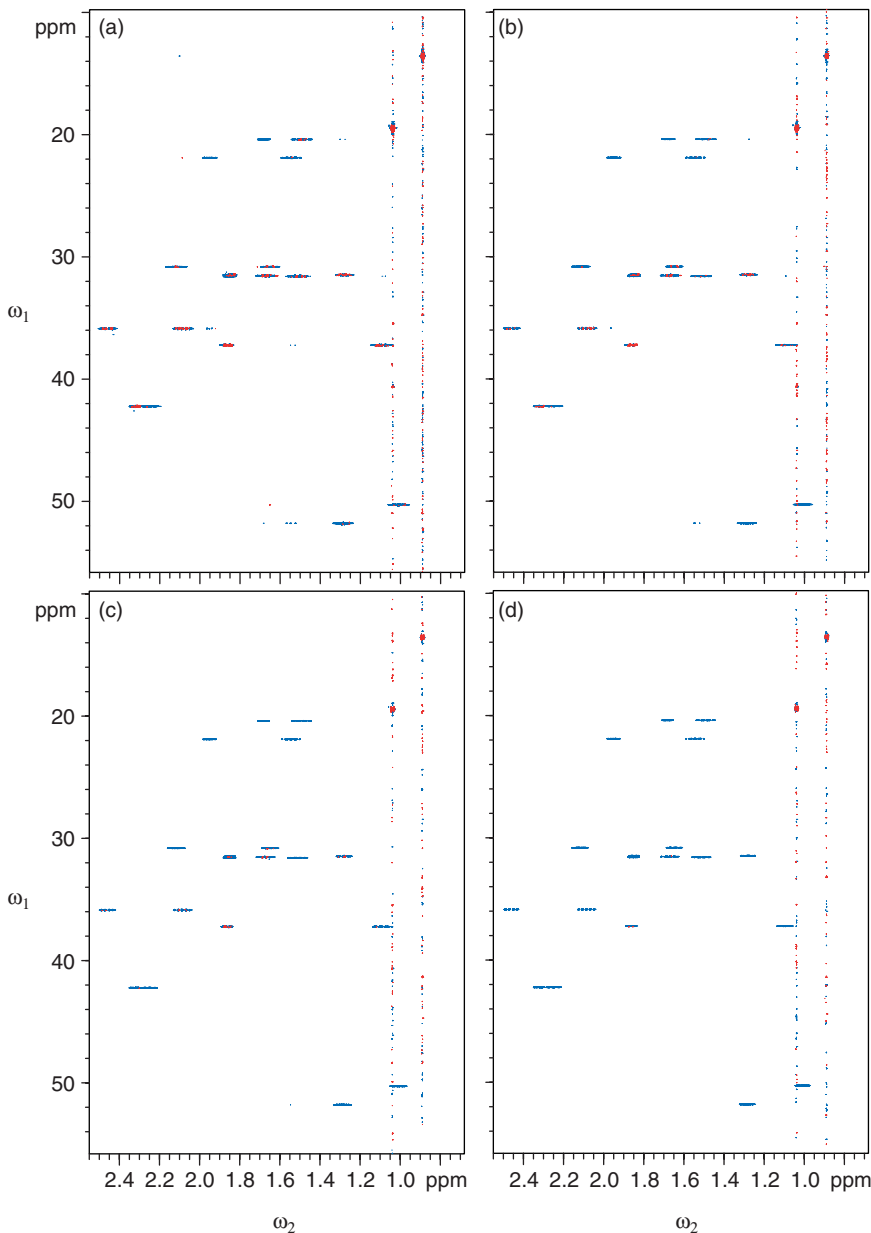


Figure 6.13: MEM HSQC spectra of the steroid in which the increments are sampled randomly from the 2048 increments of the master dataset. The MEM spectrum of the master dataset is shown in (a). The other spectra were processed using the following number of increments: (b) 1024, (c) 512, and (d) 256.

shown in Figures 6.13 and 6.14. The four spectra in the former were processed with (a) 2048, (b) 1024, (c) 512, and (d) 256 increments, and the four spectra in the latter

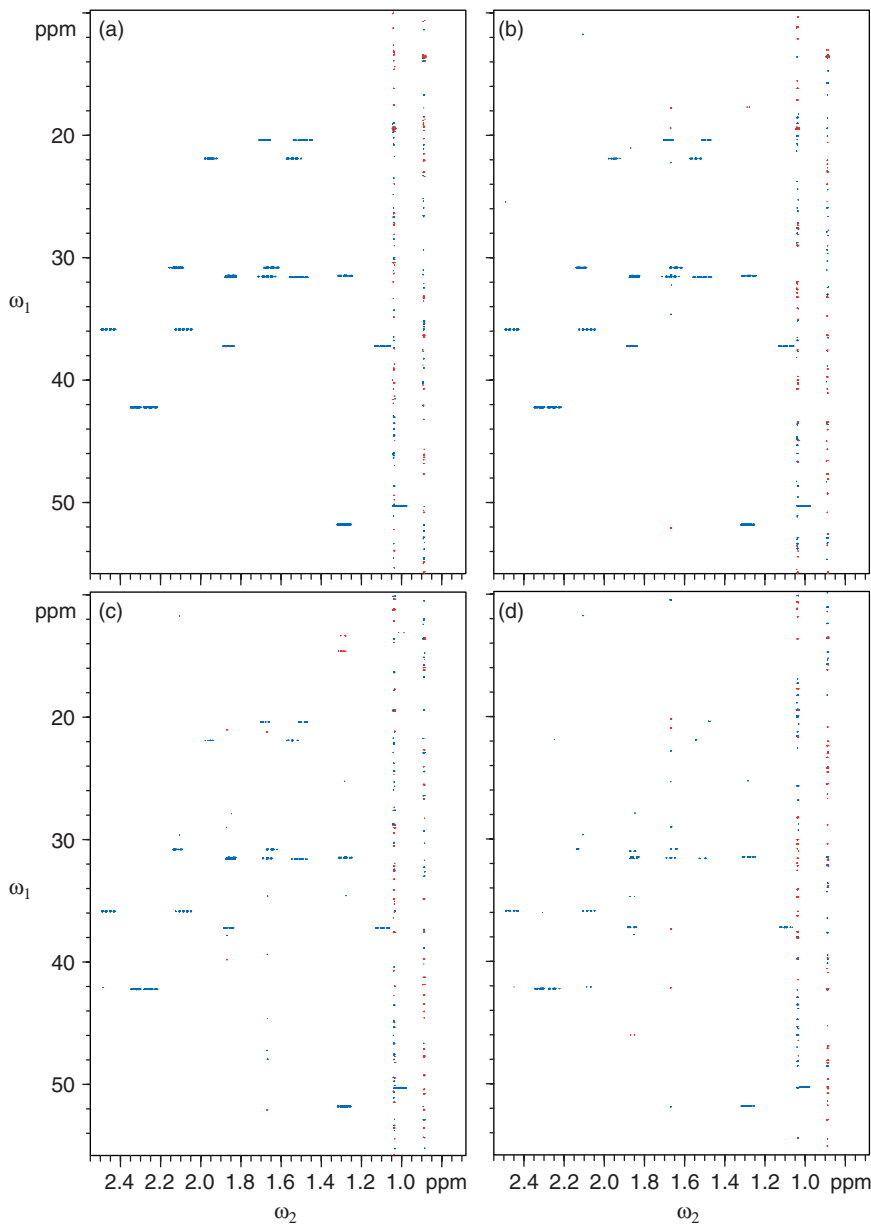


Figure 6.14: MEM HSQC spectra of the steroid in which the increments are sampled randomly from the 2048 increments of the master dataset. The number of increments sampled is (a) 128, (b) 64, (c) 32, and (d) 16.

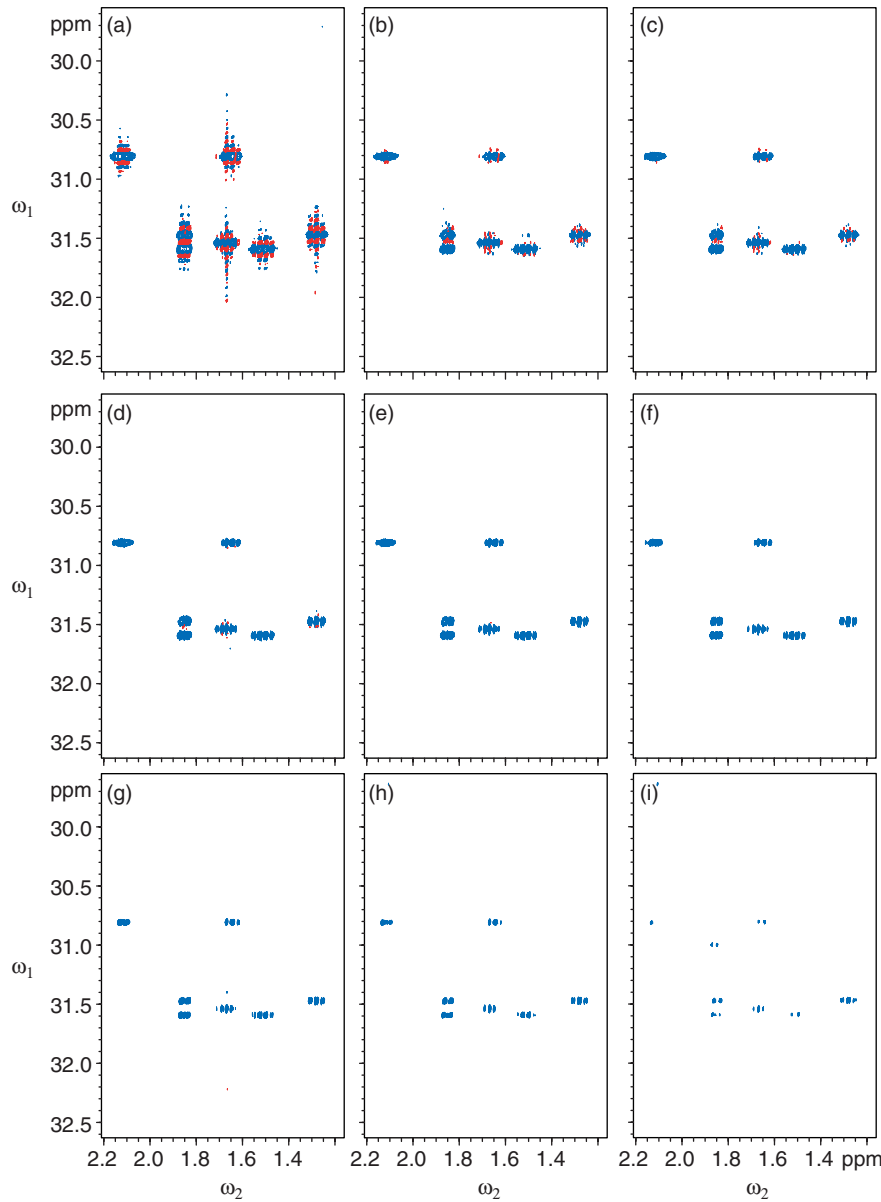


Figure 6.15: The crowded region of the HSQC spectrum of the steroid. The Fourier transform and MEM spectra of all 2048 increments are shown in (a) and (b). The remaining spectra are of randomly-sampled datasets. The number of sampled increments is (c) 1024, (d) 512, (e) 256, (f) 128, (g) 64, (h) 32, and (i) 16.

Figure were processed with (a) 128, (b) 64, (c) 32, and (d) 16 increments.

The crowded regions of these spectra are shown in Figure 6.15. The Fourier

transform is shown in (a), and the MEM spectra are shown in (b)–(i). These spectra exhibit lower linewidths when compared to the spectra that were obtained with exponential sampling of the same number of increments. This can be attributed to the random sampling scheme selecting a greater number of increments at larger values of t_1 than the exponential sampling scheme.

As was observed with the MEM spectra of the exponentially-sampled data, we are able to reduce the number of acquired increments to 128 and still obtain a usable spectrum. Any further reductions in the recorded data result in missing multiplets, and the presence of extra artefacts.

The resolution in the spectra that were obtained from the two sampling techniques can be compared more easily by taking one-dimensional cross-sections parallel to the ^{13}C dimension. Figure 6.16 shows the cross-sections taken through the overlapping resonances of the peaks assigned to protons 2_α and 12_β . The cross-section from the Fourier transform spectrum in (a) clearly exhibits the sinc wiggles and broadened central lobes that are expected from data that are truncated. In contrast the MEM suppresses the sinc wiggles, and also results in a reduced linewidth, as shown in (b). The traces in (c)–(i) each show two cross-sections, one from the MEM spectrum of the exponentially-sampled data, and one from the MEM spectrum of the randomly-sampled data which share the same number of increments. On reducing the number of increments used for exponential sampling, an increase in the linewidth is observed. This can be explained by noting the reduction in the number of increments that are acquired results a lower sampling density at larger values of t_1 , compared to the sampling density at lower values of t_1 . Reducing the number of increments in a random sampling scheme, on the other hand, preserves the resolution in the final spectrum as the sampling densities at low and high values of t_1 both decrease uniformly.

In the spectra that were acquired with random sampling, the peaks show a marked decrease in intensity on halving the number of increments from 64 to 32. This represents a decrease in the total ‘volume’ of signal acquired in the time domain and therefore a loss of sensitivity, as discussed in Section 6.4.2. The sensitivity loss is lower for the exponential sampling scheme, as the majority of the increments are sampled at low values of t_1 where the signal intensity is at its greatest. However, in the case of the spectra presented in this Section the largest value of t_1 is only 110 ms,

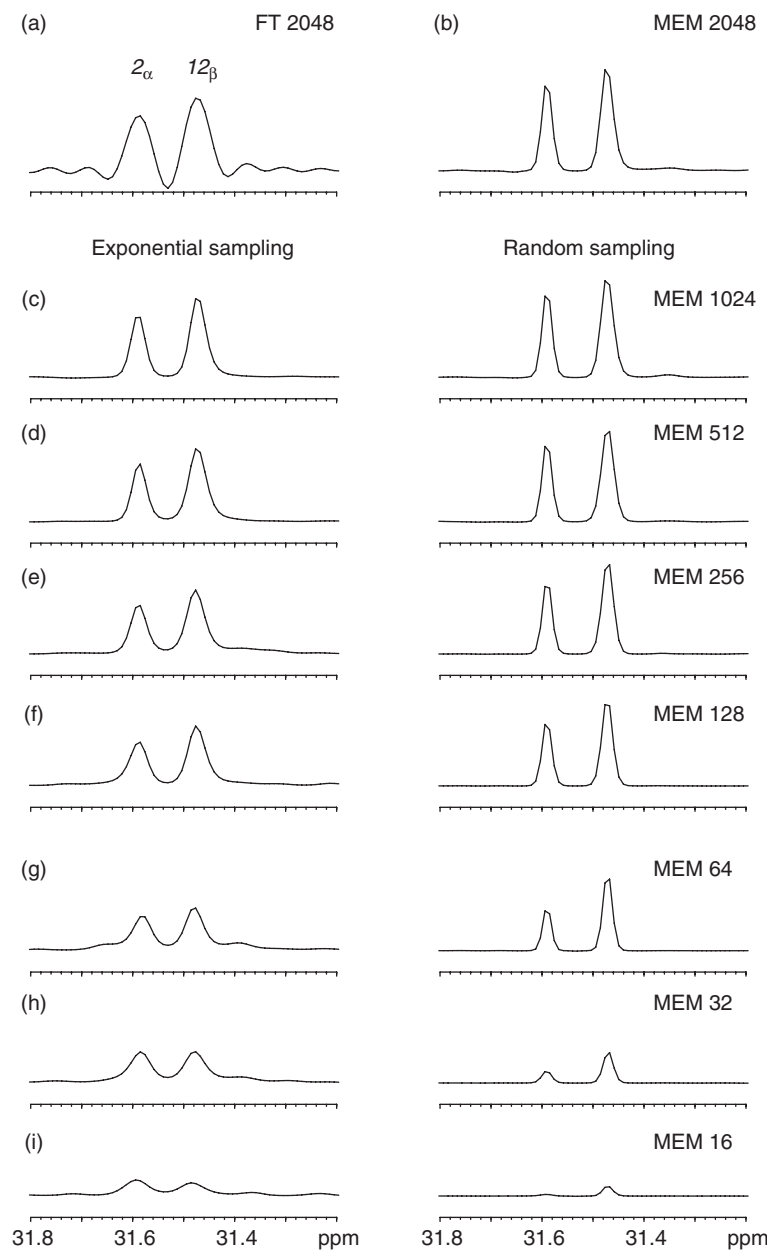


Figure 6.16: Cross-sections taken parallel to the ^{13}C dimension through the closely-spaced resonances 2_α and 12_β . The traces from the Fourier transform and MEM spectra of the master dataset are shown in (a) and (b) respectively. The cross-sections in (c)–(i) each show two traces taken from the spectra that were constructed from exponential and random sampling of the time domain.

and so the loss of signal intensity due to transverse relaxation is modest: 27% for a resonance with a linewidth of 1 Hz in the ^{13}C dimension.

6.6.3 Effect of the SNR on the MEM spectrum

The effect of a reduction in the SNR of the data on the ability of the MEM to reconstruct the spectrum was also investigated. Six HSQC spectra were recorded in which 128 increments were exponentially sampled out of a total of 2048. The flip angle of the first nominal 90° pulse on the ^1H channel was varied so as to alter the intensity of the signal; the flip angle took values between 15° and 90° in steps of 15°.

The six spectra are shown in Figure 6.17 (a)–(f) along with the first increments of each cosine-modulated dataset. As the SNR in the time domain is reduced, the MEM spectrum experiences a corresponding reduction in sensitivity. However, unlike the conventional Fourier transform spectrum, the sensitivity loss is not uniform for all resonances. This can be seen in Figure 6.18 (a)–(f) which shows a series of cross-sections extracted from the HSQC spectra parallel to the ^1H dimension. The two resonances are from protons 16_α and 16_β . In the spectrum that was recorded with a 15° flip angle, which is shown in (f), the latter resonance is seen to have lost more intensity than the former.

6.6.4 Discussion

In the case of the HSQC experiment, it has been shown that a combination of sparse sampling and the MEM can reduce the experiment time by up to a factor of sixteen. This dramatic reduction in the number of required increments can be attributed to such spectra being comparatively uncrowded. Even for a medium-sized molecule such as a steroid, there are generally at most two or three peaks in each slice taken parallel to ω_1 . In addition, the intensities are distributed over a small range. Therefore, a large reduction in the amount of the acquired information can be tolerated. With regard to which sampling scheme is employed, the choice of whether to use random or exponential sampling depends on whether resolution or sensitivity is the most important parameter.

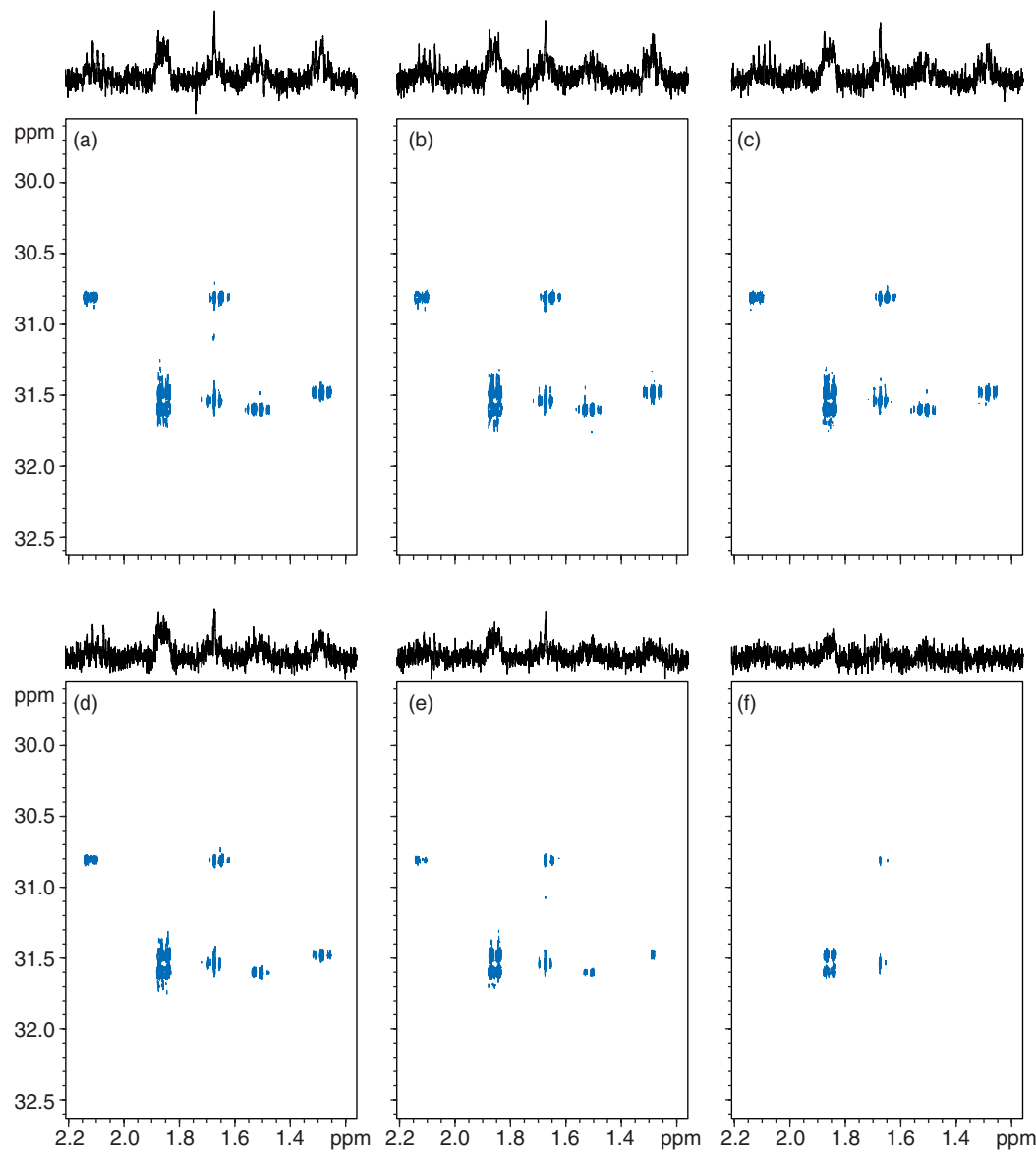


Figure 6.17: Six MEM HSQC spectra of the crowded region in which the first ^1H pulse of the sequence was varied. Each spectrum was acquired with exponential sampling of 128 increments out of 2048. Along the top of each is shown the first increment of the cosine-modulated time domain, to give an indication of the SNR. The flip angles used are (a) 90° , (b) 75° , (c) 60° , (d) 45° , (e) 30° , and (f) 15° .

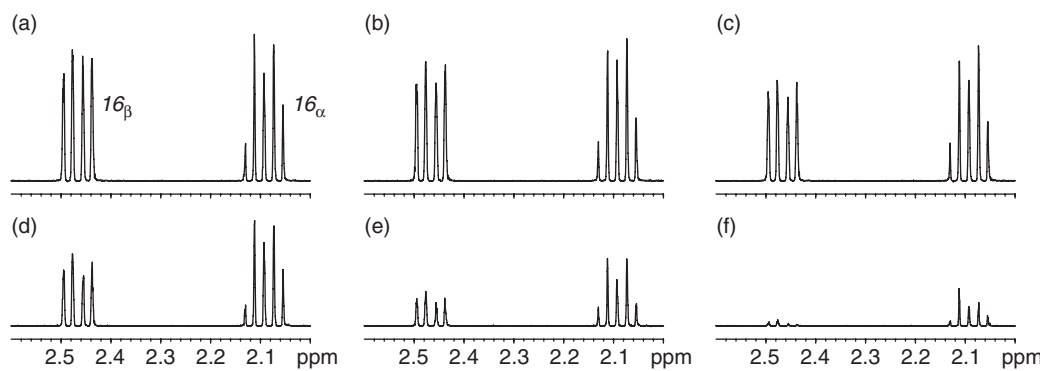


Figure 6.18: Cross-sections taken from the HSQC spectra in Figure 6.17. The cross-sections are taken parallel to ω_2 through the resonance of carbon 16. The flip angles used are (a) 90° , (b) 75° , (c) 60° , (d) 45° , (e) 30° , and (f) 15° .

6.7 HMBC of dehydroisoandrosterone

A more exacting test of the ability of the MEM to reconstruct a spectrum from sparsely-sampled data is the HMBC experiment. The added complexity of the spectrum can be summarized by four points. Firstly, each ^1H nucleus has long-range correlations to many different ^{13}C nuclei, and so there are many more peaks in each slice taken parallel to ω_1 than in the HSQC. Secondly, the multiplets have a very wide range of intensities, and so it should be noted that any peaks for which the SNR is very low may be excluded by the noise threshold. There is therefore an added difficulty in processing HMBC data in setting the value of this threshold. In the HSQC spectrum the range of intensities is comparatively small and so it is relatively easy to set the threshold without excluding any multiplets. In HMBC spectra, on the other hand, a small variation in the threshold could lead to the exclusion of any multiplets which have a low intensity. Thirdly, the cross-peak multiplets are split in the ω_1 dimension by the homonuclear coupling between the protons which adds further complexity to the spectrum in this dimension. Finally, the peaks have lineshapes with mixed phase, which is due to the evolution of the proton offset and couplings during the delay τ .

An HMBC spectrum was acquired using the sequence in Figure 6.5 (b). The spectral widths, number of data points and acquisition times in each dimension, and the number of scans were the same as for the HSQC spectrum. This master dataset is therefore composed of 2048 t_1 increments, and required a total experiment time of 1 day and 6 hours. The delay τ took the value 33.33 ms, which is optimized

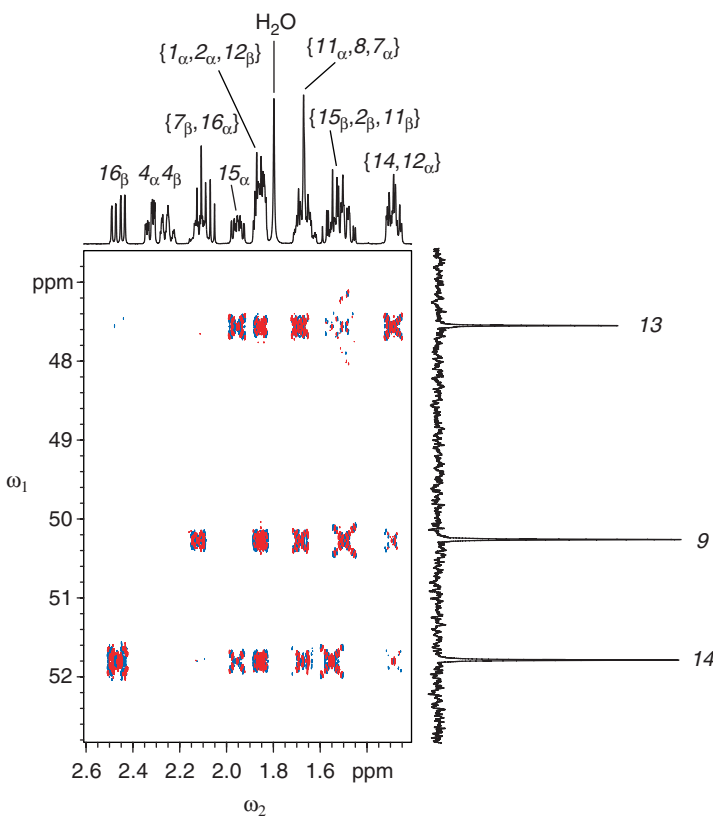


Figure 6.19: A region of the HMBC of the steroid dehydroisoandrosterone. The spectrum was produced by a Fourier transform in both dimensions of the master dataset comprising 2048 increments. The ^{13}C dimension is along the vertical axis, and the ^1H dimension is along the horizontal: the conventional one-dimensional spectra are given as traces along the two axes, along with the assignment corresponding to the structure in Figure 3.7.

for a 15 Hz coupling constant. The PFGs were all of 1 ms duration, and had relative strengths of $G_1 = 49.76\%$ and $G_2 = -29.76\%$ in the N-type experiment, and $G_1 = 29.76\%$ and $G_2 = -49.76\%$ in the P-type experiment.

A region of the Fourier transform spectrum of the master dataset is shown in Figure 6.19, with the one-dimensional ^1H and ^{13}C spectra displayed along the two axes. The mixed phase of the multiplets is clearly seen, along with their characteristic ‘St Andrew’s Cross’ structures, which are due to the splitting caused by the ^1H – ^1H J -coupling in both dimensions.

Sparsely-sampled datasets were constructed by extracting increments from the master dataset according to the same exponential and random sampling schemes that

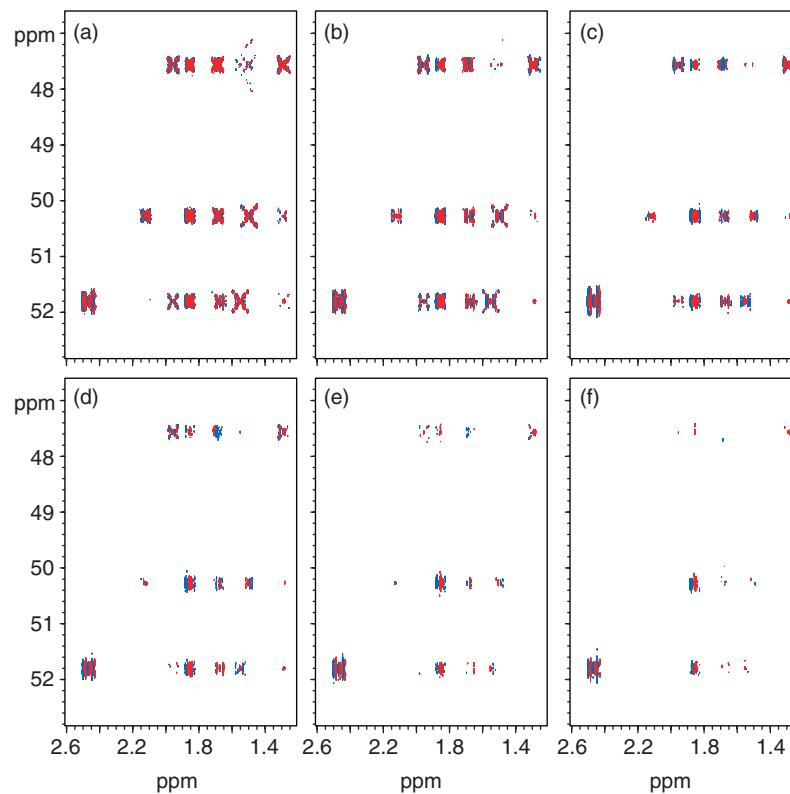


Figure 6.20: MEM HMBC spectra of dehydroisoandrosterone. The MEM spectrum of the master dataset is shown in (a). The remaining spectra were processed from time-domain data that were constructed by exponential sampling. The number of increments sampled is (b) 1024, (c) 512, (d) 256, (e) 128, and (f) 64.

were used for the HSQC. The spectra constructed from the exponentially-sampled data are shown in Figure 6.20. The MEM spectrum of the master dataset is shown in (a). The number of increments used for the remaining spectra is (b) 1024, (c) 512, (d) 256, (e) 128, and (f) 64.

Figure 6.21 shows the MEM spectra of the randomly-sampled data. The spectrum that was constructed from the master dataset is shown in (a), and the remaining spectra were constructed from the following number of increments: (b) 1024, (c) 512, (d) 256, (e) 128, and (f) 64. It can be seen for both sampling schemes that the HMBC spectra degrade more rapidly on reducing the number of sampled increments than do the HSQC spectra.

As before, the resolution can be compared by taking cross-sections parallel to ω_1

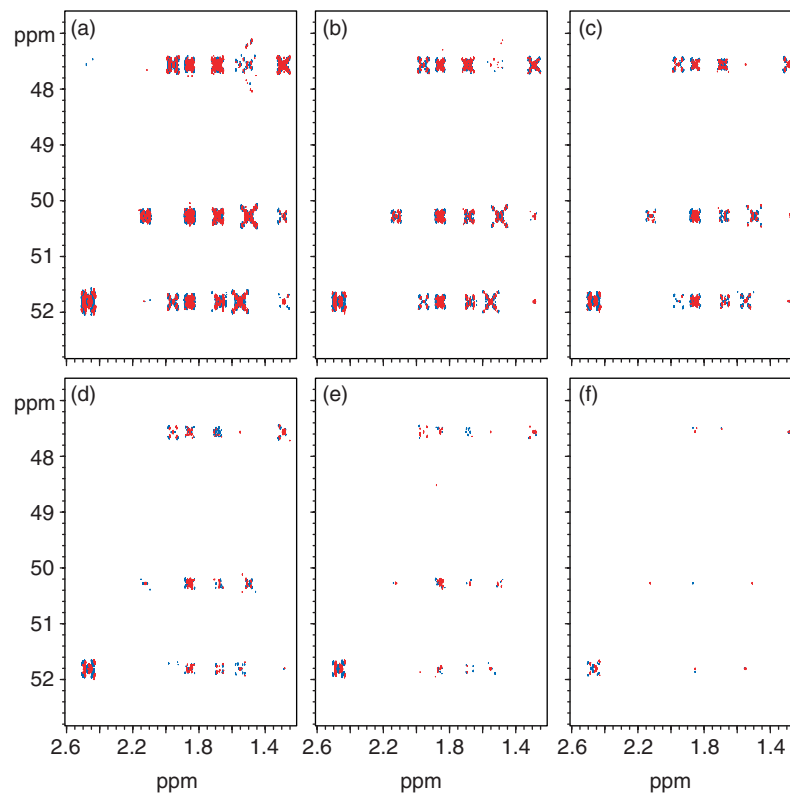


Figure 6.21: MEM HMBC spectra of dehydroisoandrosterone. The MEM spectrum of the master dataset is shown in (a). The remaining spectra were processed from time-domain data that were constructed by random sampling. The number of increments sampled is (b) 1024, (c) 512, (d) 256, (e) 128, and (f) 64.

through the cross peaks. Figure 6.22 shows cross-sections taken through the cross-peak multiplet that indicates the long-range coupling between ^{13}C 14 and ^1H 16 β . The Fourier transform spectrum, and the MEM spectrum of the master dataset are shown in (a) and (b) respectively. The splitting is due to the homonuclear coupling and is observed since the cross-section passes through both arms of the St Andrew's Cross. The MEM spectra of the sparsely sampled datasets are shown in (c)–(g); each shows the spectrum constructed from exponential and random sampling. The number of increments sampled in each case is (c) 1024, (d) 512, (e) 256, (f) 128, and (g) 64. The decrease in intensity is seen on reducing the number of increments in both schemes. In addition, exponential sampling also shows an increase in the linewidth owing to the reduction of the number of increments that is sampled at large values of t_1 .

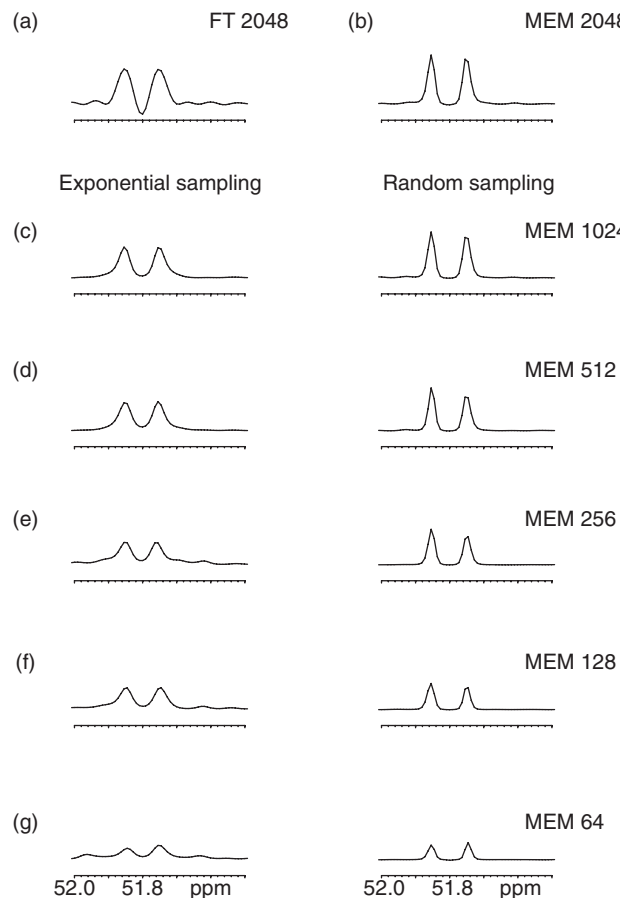


Figure 6.22: Cross-sections taken parallel to the ^{13}C dimension through the cross-peak multiplet that indicates the correlation between ^{13}C 14 and ^1H 16_β . There are two peaks because the cross-section passes through the two arms of the St Andrew's Cross structure of the multiplet, as is explained in the text. The traces from the Fourier transform and MEM spectra of the master dataset are shown in (a) and (b) respectively. The cross-sections in (c)–(g) each show two traces taken from spectra that were constructed from exponential and random sampling of the time domain.

6.8 Conclusion

Obtaining high resolution in the indirect dimension of two-dimensional spectra is very important for giving a clear separation of the resonances, and therefore facilitating the assignment. Using the conventional method of regular sampling and Fourier transform processing, the time required to obtain high resolution can only be reduced by decreasing the spectral width in ω_1 , which can give a spectrum that is impossible to assign.

By using sparse sampling of the time domain out to the same maximum value of t_1 and maximum entropy reconstruction, it is possible to obtain the same resolution in only a fraction of the experiment time. In the case of the HSQC experiment, it was shown that only a *sixteenth* of the increments need be acquired. However this represents an extreme case in that the spectrum is rather sparsely-populated with multiplets, and so it is possible to reproduce the spectrum with only a very small fraction of the total available information. For more complicated spectra, such as the HMBC, such a large reduction in experiment time is not possible without severely compromising the quality of the spectrum. In this case, the number of increments can only be reduced by a factor of four at most.

The time-saving thus obtained is paid for by the more complicated maximum entropy processing of the data. Unlike the Fourier transform, the MEM cannot be applied ‘blindly’ with minimal input from the user. The success of the method depends very strongly on the level to which the noise threshold is set. In addition, the MEM is computationally more intensive than the Fourier transform, with the result that the processing of data requires several minutes of CPU time rather than several seconds in the case of the Fourier transform. However, the experimental time-savings that are available with this method should increase its routine use in the NMR of small- to medium-sized molecules.

Appendix A

Angular momentum

IN THIS APPENDIX, the basic properties of the angular momentum operators and their matrix representations are summarized.

A.1 The spin angular momentum operators

The three Cartesian components of spin angular momentum are represented by the operators \hat{I}_x , \hat{I}_y , and \hat{I}_z . The operator for the square of the total spin $\hat{\mathbf{I}}^2$ is given by

$$\hat{\mathbf{I}}^2 = \hat{I}_x^2 + \hat{I}_y^2 + \hat{I}_z^2.$$

These operators satisfy the following commutation relations:

$$[\hat{I}_i, \hat{I}_j] = i\epsilon_{ijk}\hat{I}_k, \quad [\hat{\mathbf{I}}^2, \hat{I}_i] = 0, \tag{A.1}$$

where ϵ_{ijk} is the Levi–Civita symbol.

A.1.1 Eigenfunctions and eigenvalues

The commutation relations in Equation A.1 imply two properties of the eigenfunctions and eigenvalues of the spin operators. Firstly, the eigenfunctions of the \hat{I}_i are also eigenfunctions of $\hat{\mathbf{I}}^2$; secondly it is not possible to find simultaneous eigenfunctions of two of the Cartesian components of $\hat{\mathbf{I}}$.

For a single isolated spin, the eigenfunctions and eigenvalues are defined by two quantum numbers: the *nuclear spin angular momentum quantum number* I which takes integer or half-integer values for a given nucleus, and the *magnetic quantum number* M which takes values from $-I$ to $+I$ in integer steps. The eigenfunctions are denoted $|I, M\rangle$.

The eigenvalues of $\hat{\mathbf{I}}^2$ depend only on I :

$$\hat{\mathbf{I}}^2 |I, M\rangle = I(I+1) |I, M\rangle,$$

whilst the eigenvalues of \hat{I}_z depend only on M :

$$\hat{I}_z |I, M\rangle = M |I, M\rangle.$$

A.1.2 The raising, lowering, and polarization operators

The *raising and lowering operators*, \hat{I}_+ and \hat{I}_- , are defined as:

$$\hat{I}_+ = \hat{I}_x + i\hat{I}_y, \quad \hat{I}_- = \hat{I}_x - i\hat{I}_y.$$

These operators act to increase or decrease the value of M of the eigenfunctions $|I, M\rangle$ in the following way:

$$\begin{aligned}\hat{I}_+ |I, M\rangle &= \sqrt{I(I+1) - M(M+1)} |I, M+1\rangle \\ \hat{I}_- |I, M\rangle &= \sqrt{I(I+1) - M(M-1)} |I, M-1\rangle.\end{aligned}$$

It is thus possible to continue to act with these operators to step up and down a ladder of eigenfunctions. The eigenfunction at the ‘top’ of the ladder is $|I, I\rangle$, and has a magnetic quantum number of $M = +I$. Since there is no function with $M = I + 1$, acting on $|I, I\rangle$ with the raising operator simply gives zero. Likewise, the lowering operator returns zero when applied to the function at the bottom of the ladder, $|I, -I\rangle$.

There is a set of $2I + 1$ *polarization operators* \hat{I}_M , one for each value of M , which are defined as

$$\hat{I}_M = |I, M\rangle \langle I, M|.$$

They act on the eigenfunctions in the following way:

$$\hat{I}_M |I, M'\rangle = \delta_{MM'} |I, M\rangle,$$

where δ_{ij} is the Kronecker delta. They also satisfy the following equation:

$$\sum_{M=-I}^{M=+I} \hat{I}_M = \hat{E},$$

where \hat{E} is the identity operator. This is a *completeness relation*, which takes the more general form

$$\sum_i |i\rangle \langle i| = \hat{E}, \tag{A.2}$$

where $\{|i\rangle\}$ is a set of linearly independent basis functions.

A.1.3 Rotation operators

Nuclear magnetic resonance experiments are described in terms of rotations of operators. It will therefore prove useful to define a rotation operator $\hat{R}_i(\alpha)$ which rotates an operator \hat{A} about the axis i through an angle α to give a new operator \hat{A}' . This is represented by the ‘sandwich formula’

$$\hat{R}_i(\alpha) \hat{A} \hat{R}_i(\alpha)^{-1} = \hat{A}'.$$

The rotation operators are related to the spin angular momentum operators by the following expression:

$$\hat{R}_i(\alpha) = \exp(-i\alpha \hat{I}_i),$$

where \hat{I}_i is the operator for the component of the spin about the axis i .

A.2 Superposition states and matrix representations of operators

The wavefunction $|\psi(t)\rangle$ may be expressed as a linear combination, or superposition, of a set of n linearly independent basis functions $\{|i\rangle\}$:

$$|\psi(t)\rangle = \sum_{i=1}^n c_i(t) |i\rangle, \quad (\text{A.3})$$

where the $c_i(t)$ are a set of time-dependent, complex coefficients. The basis functions are usually defined to be orthonormal, that is $\langle i|j\rangle = \delta_{ij}$. For a system of N coupled spins- $\frac{1}{2}$, 2^N basis functions are required.

The basis can also be used to represent an operator \hat{A} in matrix form for which the matrix elements A_{ij} are defined as

$$A_{ij} = \langle i|\hat{A}|j\rangle. \quad (\text{A.4})$$

The eigenfunctions $|I, M\rangle$ form a complete orthonormal basis that is referred to as the Zeeman basis. For a single spin- $\frac{1}{2}$, there are two such basis functions which are conventionally denoted $|\alpha\rangle$ and $|\beta\rangle$:

$$|\alpha\rangle = |\frac{1}{2}, +\frac{1}{2}\rangle, \quad |\beta\rangle = |\frac{1}{2}, -\frac{1}{2}\rangle.$$

Using this basis, the spin angular momentum operators referred to above have the following matrix representations:

$$\begin{aligned} I_x &= \begin{pmatrix} 0 & \frac{1}{2} \\ \frac{1}{2} & 0 \end{pmatrix} & I_y &= \begin{pmatrix} 0 & -\frac{i}{2} \\ \frac{i}{2} & 0 \end{pmatrix} & I_z &= \begin{pmatrix} \frac{1}{2} & 0 \\ 0 & -\frac{1}{2} \end{pmatrix} \\ E &= \begin{pmatrix} 1 & 0 \\ 0 & 1 \end{pmatrix} & I_+ &= \begin{pmatrix} 0 & 1 \\ 0 & 0 \end{pmatrix} & I_- &= \begin{pmatrix} 0 & 0 \\ 1 & 0 \end{pmatrix} \\ I_\alpha &= \begin{pmatrix} 1 & 0 \\ 0 & 0 \end{pmatrix} & I_\beta &= \begin{pmatrix} 0 & 0 \\ 0 & 1 \end{pmatrix}, \end{aligned}$$

where \hat{I}_α and \hat{I}_β are the two polarization operators, which satisfy the following relationships:

$$\hat{I}_\alpha + \hat{I}_\beta = \hat{E} \quad \text{and} \quad \frac{1}{2}(\hat{I}_\alpha - \hat{I}_\beta) = \hat{I}_z.$$

The operators may also be written in terms of the basis functions. By inserting the completeness relation, Equation A.2, either side of the operator \hat{A} , and using the definition of the matrix representation in Equation A.4, we obtain:

$$\hat{A} = \sum_{i,j} |i\rangle \langle i| \hat{A} |j\rangle \langle j| = \sum_{i,j} A_{ij} |i\rangle \langle j|.$$

Using the spin- $\frac{1}{2}$ Zeeman basis, we obtain the following expressions for the spin angular momentum operators:

$$\begin{aligned} \hat{I}_x &= \frac{1}{2}(|\alpha\rangle\langle\beta| + |\beta\rangle\langle\alpha|) & \hat{I}_y &= \frac{1}{2i}(|\alpha\rangle\langle\beta| - |\beta\rangle\langle\alpha|) & \hat{I}_z &= \frac{1}{2}(|\alpha\rangle\langle\alpha| - |\beta\rangle\langle\beta|) \\ \hat{I}_+ &= |\alpha\rangle\langle\beta| & \hat{I}_- &= |\beta\rangle\langle\alpha| & \hat{I}_\alpha &= |\alpha\rangle\langle\alpha| \\ \hat{I}_\beta &= |\beta\rangle\langle\beta|. \end{aligned}$$

Using the matrix representations of the angular momentum operators, we can obtain the matrix representations of the rotation operators in the spin- $\frac{1}{2}$ Zeeman basis

[4]. They are:

$$R_x(\alpha) = \begin{pmatrix} \cos \frac{\alpha}{2} & -i \sin \frac{\alpha}{2} \\ -i \sin \frac{\alpha}{2} & \cos \frac{\alpha}{2} \end{pmatrix} \quad R_y(\alpha) = \begin{pmatrix} \cos \frac{\alpha}{2} & -\sin \frac{\alpha}{2} \\ \sin \frac{\alpha}{2} & \cos \frac{\alpha}{2} \end{pmatrix} \quad R_z(\alpha) = \begin{pmatrix} e^{-i\frac{\alpha}{2}} & 0 \\ 0 & e^{i\frac{\alpha}{2}} \end{pmatrix}. \quad (\text{A.5})$$

Bibliography

- [1] K. F. Riley, M. P. Hobson, and S. J. Bence. *Mathematical Methods for Physics and Engineering*. Cambridge University Press, Cambridge (1997).
- [2] M. Goldman. *Quantum Description of High-Resolution NMR in Liquids*. Oxford University Press, Oxford (1988).
- [3] A. Abragam. *Principles of Nuclear Magnetism*. Oxford University Press, Oxford (1961).
- [4] M. H. Levitt. *Spin Dynamics: Basics of Nuclear Magnetic Resonance*. John Wiley and Sons Ltd, Chichester (2001).
- [5] O. W. Sørensen, G. W. Eich, M. H. Levitt, G. Bodenhausen, and R. R. Ernst. *Prog. Nucl. Magn. Reson. Spectrosc.*, **16**, 163–192 (1984).
- [6] J. Keeler. *Understanding NMR Spectroscopy*. John Wiley and Sons Ltd, Chichester (2005).
- [7] E. L. Hahn. *Phys. Rev.*, **80**, 580–594 (1950).
- [8] M. J. Thrippleton, R. A. E. Edden, and J. Keeler. *J. Magn. Reson.*, **174**, 97–109 (2005).
- [9] M. H. Levitt, G. Bodenhausen, and R. R. Ernst. *J. Magn. Reson.*, **58**, 462–472 (1984).
- [10] J. Jeener. Ampere International Summer School, Basko Polje, Yugoslavia (1971).
- [11] W. P. Aue, E. Bartholdi, and R. R. Ernst. *J. Chem. Phys.*, **64**, 2229–2246 (1976).

- [12] G. Bodenhausen, R. Freeman, R. Niedermeyer, and D. L. Turner. *J. Magn. Reson.*, **26**, 133–164 (1977).
- [13] P. Bachmann, W. P. Aue, L. Müller, and R. R. Ernst. *J. Magn. Reson.*, **28**, 29–39 (1977).
- [14] J. Keeler and D. Neuhaus. *J. Magn. Reson.*, **63**, 454–472 (1985).
- [15] D. J. States, R. A. Haberkorn, and D. J. Ruben. *J. Magn. Reson.*, **48**, 286–292 (1982).
- [16] R. N. Bracewell. *The Fourier Transform and its Applications*. McGraw-Hill, New York (1965).
- [17] G. Bodenhausen, R. Freeman, and D. L. Turner. *J. Magn. Reson.*, **27**, 511–514 (1977).
- [18] M. Bak, J. T. Rasmussen, and N. C. Nielsen. *J. Magn. Reson.*, **147**, 296–330 (2000).
- [19] T. Vosegaard, A. Malmendal, and N. C. Nielsen. *Monatsh. Chem.*, **133**, 1555–1574 (2002).
- [20] M. Veshtort and R. G. Griffin. *J. Magn. Reson.*, **178**, 248–282 (2006).
- [21] C. Bauer, R. Freeman, T. Frenkel, J. Keeler, and A. J. Shaka. *J. Magn. Reson.*, **58**, 442–457 (1984).
- [22] J.-M. Böhlen, M. Rey, and G. Bodenhausen. *J. Magn. Reson.*, **84**, 191–197 (1989).
- [23] J.-M. Böhlen, I. Burghardt, M. Rey, and G. Bodenhausen. *J. Magn. Reson.*, **90**, 183–191 (1990).
- [24] J.-M. Böhlen and G. Bodenhausen. *J. Magn. Reson. Ser. A*, **102**, 293–301 (1993).
- [25] T.-L. Hwang, P. C. M. van Zijl, and M. Garwood. *J. Magn. Reson.*, **124**, 250–254 (1997).

- [26] M. Garwood and L. DelaBarre. *J. Magn. Reson.*, **153**, 155–177 (2001).
- [27] M. A. Smith, H. Hu, and A. J. Shaka. *J. Magn. Reson.*, **151**, 269–283 (2001).
- [28] P. T. Callaghan. *Principles of Nuclear Magnetic Resonance Microscopy*. Oxford University Press, Oxford (1991).
- [29] O. W. Sørensen, M. Rance, and R. R. Ernst. *J. Magn. Reson.*, **56**, 527–534 (1984).
- [30] S. Macura and R. R. Ernst. *Mol. Phys.*, **41**, 95–97 (1980).
- [31] L. Braunschweiler and R. R. Ernst. *J. Magn. Reson.*, **53**, 521–528 (1983).
- [32] H. Oschkinat, A. Pastore, P. Pfändler, and G. Bodenhausen. *J. Magn. Reson.*, **69**, 559–566 (1986).
- [33] S. Macura, Y. Huang, D. Suter, and R. R. Ernst. *J. Magn. Reson.*, **43**, 259–281 (1981).
- [34] M. J. Thrippleton and J. Keeler. *Angew. Chem. Int. Ed.*, **42**, 3938–3941 (2003).
- [35] K. E. Cano, M. J. Thrippleton, J. Keeler, and A. J. Shaka. *J. Magn. Reson.*, **167**, 291–297 (2004).
- [36] W. P. Aue, J. Karhan, and R. R. Ernst. *J. Chem. Phys.*, **64**, 4226–4227 (1976).
- [37] K. Nagayama, P. Bachmann, K. Wüthrich, and R. R. Ernst. *J. Magn. Reson.*, **31**, 133–148 (1978).
- [38] A. Bax, R. Freeman, and G. A. Morris. *J. Magn. Reson.*, **43**, 333–338 (1981).
- [39] B. Blümich and D. Ziessow. *J. Magn. Reson.*, **49**, 151–154 (1982).
- [40] A. J. Shaka, J. Keeler, and R. Freeman. *J. Magn. Reson.*, **56**, 294–313 (1984).
- [41] P. Xu, M.-L. Wu, and R. Freeman. *J. Magn. Reson.*, **95**, 132–148 (1991).
- [42] P. Xu, M.-L. Wu, and R. Freeman. *J. Am. Chem. Soc.*, **113**, 3596 (1991).
- [43] M. Woodley and R. Freeman. *J. Magn. Reson. Ser. A*, **109**, 103–112 (1994).

- [44] M. Woodley and R. Freeman. *J. Magn. Reson. Ser. A*, **111**, 225–228 (1994).
- [45] S. Simova, H. Sengstschmid, and R. Freeman. *J. Magn. Reson.*, **124**, 104–121 (1997).
- [46] L. Mahi, J. C. Duplan, and A. Briguet. *Magn. Reson. Chem.*, **36**, 515–519 (1998).
- [47] V. A. Mandelshtam, H. S. Taylor, and A. J. Shaka. *J. Magn. Reson.*, **133**, 304–312 (1998).
- [48] V. A. Mandelshtam, N. D. Taylor, H. Hu, M. Smith, and A. J. Shaka. *Chem. Phys. Lett.*, **305**, 209–216 (1999).
- [49] V. A. Mandelshtam, Q. N. Van, and A. J. Shaka. *J. Am. Chem. Soc.*, **120**, 12161–12162 (1998).
- [50] G. S. Armstrong, J. H. Chen, K. E. Cano, A. J. Shaka, and V. A. Mandelshtam. *J. Magn. Reson.*, **164**, 136–144 (2003).
- [51] G. Bodenhausen, R. Freeman, G. A. Morris, and D. L. Turner. *J. Magn. Reson.*, **31**, 75–95 (1978).
- [52] A. Kumar. *J. Magn. Reson.*, **30**, 227–249 (1978).
- [53] G. Wider, R. Baumann, K. Nagayama, R. R. Ernst, and K. Wüthrich. *J. Magn. Reson.*, **42**, 73–87 (1981).
- [54] A. J. Pell, R. A. E. Edden, and J. Keeler. *Magn. Reson. Chem.*, **45**, 296–316 (2007).
- [55] R. A. E. Edden. *New methods in NMR spectroscopy*. Ph.D. thesis, University of Cambridge (2005).
- [56] P. Pfändler and G. Bodenhausen. *J. Magn. Reson.*, **72**, 475–492 (1987).
- [57] R. Mills. *J. Phys. Chem.*, **77**, 685–688 (1973).
- [58] A. F. Mehlkopf, D. Korbee, T. A. Tiggelman, and R. Freeman. *J. Magn. Reson.*, **58**, 315–323 (1984).

- [59] M. Nilsson and G. A. Morris. *Chem. Commun.*, 933–935 (2007).
- [60] E. O. Stejskal and J. E. Tanner. *J. Chem. Phys.*, **42**, 288–292 (1965).
- [61] H. C. Torrey. *Phys. Rev.*, **104**, 563–565 (1956).
- [62] J. Lounila, K. Oikarinen, P. Ingman, and J. Jokisaari. *J. Magn. Reson.*, **118**, 50–54 (1996).
- [63] N. Esturau, F. Sánchez-Ferrando, J. A. Gavin, C. Roumenstand, M.-A. Delsuc, and T. Parella. *J. Magn. Reson.*, **153**, 48–55 (2001).
- [64] A. Jerschow and N. Müller. *J. Magn. Reson.*, **125**, 372–375 (1997).
- [65] G. Wider, V. Dötsch, and K. Wüthrich. *J. Magn. Reson. Ser. A*, **108**, 255–258 (1994).
- [66] C. S. Johnson. *Prog. Nucl. Magn. Reson. Spectrosc.*, **34**, 203–256 (1999).
- [67] M. Nilsson, A. M. Gil, I. Delgadillo, and G. A. Morris. *Chem. Commun.*, 1737–1739 (2005).
- [68] D. H. Wu, A. D. Chen, and C. S. Johnson. *J. Magn. Reson.*, **121**, 88–91 (1996).
- [69] L. H. Lucas, W. H. Otto, and C. K. Larive. *J. Magn. Reson.*, **156**, 138–145 (2002).
- [70] M. Nilsson, A. M. Gil, I. Delgadillo, and G. A. Morris. *Anal. Chem.*, **76**, 5418–5422 (2004).
- [71] H. Barjat, G. A. Morris, and A. G. Swanson. *J. Magn. Reson.*, **131**, 131–138 (1998).
- [72] M. J. Stchedroff, A. M. Kenwright, G. A. Morris, M. Nilsson, and R. K. Harris. *Phys. Chem. Chem. Phys.*, **6**, 3221–3227 (2004).
- [73] D. H. Wu, A. D. Chen, and C. S. Johnson. *J. Magn. Reson. Ser. A*, **123**, 215–218 (1996).
- [74] D. W. Marquardt. *J. Soc. Ind. Appl. Math.*, **11**, 431–441 (1963).

- [75] J. K. Nicholson and I. D. Wilson. *Prog. Nucl. Magn. Reson. Spectrosc.*, **21**, 449–501 (1989).
- [76] P. J. D. Foxall, J. A. Parkinson, I. H. Sadler, J. C. Lindon, and J. K. Nicholson. *J. Pharm. Biomed. Anal.*, **11**, 21–31 (1993).
- [77] P. J. D. Foxall, M. Spraul, R. D. Farrant, J. C. Lindon, G. H. Neild, and J. K. Nicholson. *J. Pharm. Biomed. Anal.*, **11**, 267–276 (1993).
- [78] S. H. Moolenaar, M. S. van der Knapp, U. F. H. Engelke, P. J. W. Pouwels, F. S. M. Janssen-Zijlstra, N. M. Verhoeven, C. Jakobs, and R. A. Wevers. *J. Pharm. Biomed. Anal.*, **11**, 267–276 (1993).
- [79] M. R. Viant. *Biochem. Biophys. Res. Commun.*, **11**, 267–276 (2003).
- [80] Y. Wang, M. E. Bolland, H. Keun, H. Antii, O. Beckonert, T. M. Ebbels, J. C. Lindon, E. Holmes, H. Tang, and J. K. Nicholson. *Anal. Biochem.*, **323**, 26–32 (2003).
- [81] K. Zanger and H. Sterk. *J. Magn. Reson.*, **124**, 486–489 (1997).
- [82] O. W. Sørensen, C. Griesinger, and R. R. Ernst. *J. Am. Chem. Soc.*, **107**, 7778–7779 (1985).
- [83] A. J. Pell and J. Keeler. *J. Magn. Reson.*, **189**, 293–299 (2007).
- [84] R. Freeman, S. P. Kempsell, and M. H. Levitt. *J. Magn. Reson.*, **34**, 663–667 (1979).
- [85] J. C. J. Barna, E. D. Laue, M. R. Mayger, J. Skilling, and S. J. P. Worrall. *J. Magn. Reson.*, **73**, 69–77 (1987).
- [86] S. F. Gull and G. J. Daniell. *Nature*, **272**, 686–690 (1978).
- [87] S. Sibisi, J. Skilling, R. G. Brereton, E. D. Laue, and J. Staunton. *Nature*, **311**, 446–447 (1984).
- [88] E. D. Laue, J. Skilling, J. Staunton, S. Sibisi, and R. G. Brereton. *J. Magn. Reson.*, **62**, 437–452 (1985).

- [89] J. Skilling and R. Bryan. *Mon. Not. R. Astron. Soc.*, **211**, 111–124 (1984).
- [90] P. Schmieder, A. S. Stern, G. Wagner, and J. C. Hoch. *J. Magn. Reson.*, **125**, 332–339 (1997).
- [91] S. F. Gull and J. Skilling. *Quantified Maximum Entropy: MemSys5 Users' Manual*. Maximum Entropy Data Consultants Ltd, South Hill, 42 Southgate Street, Bury St Edmunds, Suffolk (1999).
- [92] M. Mobli and J. C. Hoch. *Concepts Magn. Reson. A.*, **32**, 436–448 (2008).
- [93] A. Bax, R. H. Griffey, and B. L. Hawkins. *J. Magn. Reson.*, **55**, 301–315 (1983).
- [94] G. Bodenhausen and D. J. Ruben. *Chem. Phys. Lett.*, **69**, 185–189 (1980).
- [95] A. L. Davis, J. Keeler, E. D. Laue, and D. Moskau. *J. Magn. Reson.*, **98**, 207–216 (1992).
- [96] A. Bax and M. F. Summers. *J. Am. Chem. Soc.*, **108**, 2093–2094 (1986).
- [97] D. O. Cicero, G. Barbato, and R. Bazzo. *J. Magn. Reson.*, **148**, 209–213 (2001).
- [98] R. R. Ernst, G. Bodenhausen, and A. Wokaun. *Principles of Nuclear Magnetic Resonance in One and Two Dimensions*. Oxford University Press, Oxford (1987).
- [99] J. C. Hoch, M. W. Maciejewski, and B. Filipovic. *J. Magn. Reson.*, **193**, 317–320 (2008).
- [100] E. D. Laue, J. Skilling, and J. Staunton. *J. Magn. Reson.*, **63**, 418–424 (1985).
- [101] D. L. Donoho, I. M. Johnstone, A. S. Stern, and J. C. Hoch. *Proc. Natl. Acad. Sci. USA*, **87**, 5066–5068 (1990).
- [102] A. J. Shaka, P. B. Barker, and R. Freeman. *J. Magn. Reson.*, **64**, 547–552 (1985).